Technische Universität München
Institut für Energietechnik

Lehrstuhl für Thermodynamik

A Systems View on Non-Normal Transient Growth in Thermoacoustics

Ralf S. Blumenthal

Vollständiger Abdruck der von der Fakultät für Maschinenwesen der Technischen Universität München zur Erlangung des akademischen Grades eines

DOKTOR – INGENIEURS

genehmigten Dissertation.

Vorsitzender:
Univ.-Prof. Ph.-St. Koutsourelakis, Ph.D.
Prüfer der Dissertation:
Univ.-Prof. W. Polifke, Ph.D.
Prof. R. I. Sujith, Ph.D., Indian Institute of Technology Madras, Chennai / Indien

Die Dissertation wurde am 02.04.2015 bei der Technischen Universität München eingereicht und durch die Fakultät für Maschinenwesen am 22.06.2015 angenommen.

To me the very essence of education is
concentration of mind, not the collection of facts.

—Swami Vivekananda—

Kurzfassung

Die vorliegende Arbeit untersucht nicht-normales transientes Wachstum in einfachen thermoakustischen Systemen. Letztere werden aus einer systemischen Perspektive heraus betrachtet und als eine Ansammlung kontinuierlich miteinander in Wechselwirkung stehender Subsysteme behandelt. Der systemische Ansatz zeigt sich als robust und ganzheitlich, und ermöglicht einen frischen und klaren Blick auf thermoakustische Phänomene. Die beiden Subsysteme Wärmequelle und Akustik werden mithilfe von Modellen niedriger Ordnung beschrieben, die trotz ihrer kleinen Größe eine gute Annäherung der tatsächlichen Dynamik liefern. Für die Wärmequelle kommt ein filterbasiertes Modell mit verteilten Zeitverzügen zum Einsatz, welches aus experimentellen, numerischen oder semi-analytischen Daten gewonnen wird. Das 1-D homentropische akustische Feld beinhaltet ein mittleres Strömungsfeld und andere variierende mittlere Felder. Es wird numerisch durch eine Methode der gewichteten Residuen (Galerkin-Methode) angenähert, welche weitgehend frei von künstlichem nicht-normalen Wachstum ist. Es wird ferner argumentiert, dass die Energie des Ausgangs eines thermoakustischen Systems eine frei wählbare Größe darstellt, die lediglich die Art und Weise beeinflußt, wie die Ergebnisse zu interpretieren sind. Numerische Nicht-Normalität, welche von schlecht konditionierten diskretisierten Operatoren herrührt, wird physikalischer Nicht-Normalität gegenübergestellt. Die Dynamik und die Grundmechanismen von physikalischem optimalen nicht-normalem transienten Wachstum werden durch eine fluss- und quellenbasierte Bilanz erklärt. Optimales nicht-normales transientes Wachstum um einen stabilen Fixpunkt stellt sich als höchst unwahrscheinlich dar. Suboptimales transientes Wachstum kann hingegen vorkommen, ist aber klein und spielt beim Triggern eines linear stabilen thermoakustischen Systems zu einem stationären nichtlinearen Schwingungszustand keine bedeutende Rolle.

Abstract

The present thesis investigates the non-normal dynamics of a simple thermoacoustic system. Such a system is modeled in a systems framework and viewed and treated as a collection of subsystems that are in continuous feedback. The systems framework proves to be a robust and holistic approach, bringing along a beneficially fresh and clear perspective on thermoacoustics. Sophisticated low-order models for the subsystems heat source and acoustics are derived and analyzed. The heat source is modeled using a filter-based representation with distributed time lag characteristics stemming from experimental or numerical data or semi-analytical approaches. The 1-D homentropic acoustic field incorporates mean flow effects and varying mean quantities. It is numerically approximated by a method of weighted residuals (Galerkin method), which exhibits very little spurious non-normality. It is argued that the output energy of a thermoacoustic system is a matter of choice that merely prescribes the perspective from which the observed dynamics need to be interpreted. Spurious non-normality originating from ill-conditioned discretized operators or from model limitations is contrasted to physical non-normality. The dynamics and mechanisms of physical optimal non-normal transient growth are investigated and explained from an energy flux- and source-based perspective. The occurrence of optimal non-normal transient growth around a stable fix point is shown to be highly improbable. Despite the possibility of encountering suboptimal non-normal transient growth, its magnitude is small and may not play an important role in the process of triggering a linearly stable thermoacoustic system towards a nonlinear oscillating state.

Acknowledgments

This thesis has brought along an innumerable amount of enriching, uplifting and exciting moments, all adding to an unforgettable experience for which I am extremely thankful. By no means is it possible to depict my gratitude and happiness in words, and I would miserably fail at even attempting to write down every contributing event to such an intense nearly-five-year-long story, which played at so many offices, lawns and other outside places, couches and beds, chai stops, think tanks, trains, class and conference rooms, both seated behind and standing upfront, bars, airports, cafés, canteens, train stations, restaurants, cars and airplanes across three continents. Impossible also to name the vast amount of people who have, each in their own way, contributed to pushing my actions and especially my thoughts and perspective in a favorable direction. **Thank you!**

CONNY LILLY MY PARENTS WOLFGANG POLIFKE SUJITH ARUN PRIYA SEBASTIAN MY SIBLINGS MY PARENTS-IN-LAW ALEJANDRO ALP ANNA FISCHER CAMILO CARLO CHRISTOPH HIRSCH CONSTANZE TEMMLER DFG FAIDON-STELIOS KOUTSOURELAKIS HELGA HERBERT MANGESIUS JANNIS JÉRÔME HOEPFFNER JOSEF KILIAN LIPIKA LUCA MAGRI MATTHEW JUNIPER MARKUS SPINNLER MARTA MAX BAUMGÄRTNER MAX MEINDL MAXWELL MEENA MICHI MICHI SCHIFFNER PETER SCHMID SATHESH SIGRID SCHULZ-REICHWALD STEFAN JAENSCH STEFFI HOFMANN STEPHAN PARZINGER THOMAS EMMERT THOMAS FIALA THOMAS SATTELMAYER THOMAS STEINBACHER TOBI HOLZINGER TRAVIS TUM-IAS VINU VOLKER THE WERKSTATT MY AWESOME STUDENTS MY INSPIRING, HARD WORKING, SOCCER PLAYING, BBQING, FEND STÜBERL ADDICTED, HARD DISCUSSIONS LOVING, BOAZN DANCING, COFFEE SIPPING, CHRISTMAS PARTY SWINGING, GREAT FELLOW COLLEAGUES AT THE LEHRSTUHL

Wesentliche Teile der vorliegenden Dissertationsschrift wurden vom Autor bereits standardmäßig auf Konferenzen vorgetragen und als Konferenz- und Zeitschriftenbeiträge veröffentlicht [1, 10–14, 146, 147, 163]. Alle Vorveröffentlichungen sind entsprechend der gültigen Promotionsordnung ordnungsgemäß gemeldet. Sie sind deshalb nicht zwangsläufig im Detail einzeln referenziert. Vielmehr wurde bei der Referenzierung eigener Vorveröffentlichungen Wert auf Verständlichkeit und inhaltlichen Bezug gelegt.

Major parts of the present thesis have been presented by the author at conferences, and published in conference proceedings and journal papers [1, 10–14, 146, 147, 163]. All of the author's prior publications are registered according to the valid doctoral regulations. In the interest of clarity and comprehensibility of presentation, not all of the prior publications are explicitly cited throughout the present work.

Financial support was provided by the Technische Universität München – Institute for Advanced Study, funded by the German Excellence Initiative. I also gratefully acknowledge financial support by the German Research Foundation DFG, project PO 710/12-1.

Contents

List of Symbols

Abbreviations

ARX	autoregressive model with exogeneous input
ARMA	autoregressive moving average model
BIBO	bounded input bounded output
BJ	Box-Jenkins model
CFL	Courant number (Courant-Friedrichs-Lewy) [-]
dDDE	distributed delay differential equations
DNS	direct numerical simulation
FD	finite differences
FE	finite elements
FIR	finite impulse response
FRF	frequency response function
IR	impulse response
ITAF	intrinsic thermoacoustic feedback
LEE	linearized Euler equations
LNSE	linearized Navier-Stokes equations
LODI	local one-dimensional inviscid
LTI	linear time-invariant
MWR	method of weighted residuals
OE	output error model
ODE	ordinary differential equation
OIC	optimal initial condition
dDDE	distributed delay differential equations
PDE	partial differential equation
pdf	probability distribution function
RHS	right hand side

RK	Runge-Kutta scheme
SISO	single input single output
SSM	state space model
STL	single time lag
SVD	singular value decomposition
TF	transfer function
TVD	total variation diminishing

Latin Letters

a	advection velocity [m/s] (def. in Eq. (3.18a))
A	surface area [m^2] (def. in Eq. (3.4))
$\mathbf{A}$	system matrix of the discretized SSM (def. in Eq. (2.7a))
$\mathcal{A}$	continuous partial differential system operator (def. in Eq. (2.3a))
b	supply rate (def. in Eq. (2.10))
$\mathbf{B}$	input matrix of the discretized SSM (def. in Eq. (2.7a))
$\mathcal{B}$	continuous partial differential input operator (def. in Eq. (2.3a))
c	speed of sound [m/s] (def. in Eq. (4.3))
c_p	heat capacity at constant pressure [J/(kg K)] (def. following Eq. (4.1))
c_v	heat capacity at constant volume [J/(kg K)] (def. following Eq. (4.1))
$\mathbf{C}$	output matrix of the discretized SSM (def. in Eq. (2.7b))
$\mathcal{C}$	continuous partial differential output operator (def. in Eq. (2.3b))
d	displacement magnitude [m] (def. before Eq. (3.23))
$\mathbf{D}$	feedthrough matrix of the discretized SSM (def. in Eq. (2.7b))
$\mathbf{D}$	matrix of left-singular vectors (def. following Eq. (2.30))
$\mathcal{D}$	continuous partial differential feedthrough operator (def. in Eq. (2.1b))
E	output energy of the discretized SSM (def. in Eq. (2.8))
$\mathcal{E}$	output energy of the continuous partial differential SSM (def. in Eq. (2.6))
f	flux term (def. in Eq. (2.22))
f	rightward traveling characteristic wave [m/s] (def. in Eq. (4.5))
F	transfer function (def. following Eq. (2.18))
$\mathbf{F}$	transfer matrix (def. following Eq. (2.18))

$\mathscr{F}\{\cdot\}$	Fourier transform (def. in Eq. (2.21))
g	leftward traveling characteristic wave [m/s] (def. in Eq. (4.5))
g	Gibbs' free energy [J/kg] (def. in Eq. (5.7))
G	maximum normalized output energy of an autonomous system [-] (def. in Eq. (2.28))
$\mathcal{G}$	relative amplification of output energy [-] (def. in Eq. (2.26))
h	impulse response function (def. following Eq. (2.14))
H	maximum normalized output energy of a forced system [-] (def. in Eq. (2.34))
$\mathbf{H}$	impulse response matrix (def. in Eq. (2.13))
He	Helmholtz number [-] (def. following Eq. (6.6))
$\mathbf{I}$	identity matrix (def. following Eq. (2.24))
k	weighting function in revolution integral [m] (def. in Eq. (3.5))
K	non-dimensional strength of heat source [-] (def. in Eq. (4.10))
K_0	control parameter scaling the strength of heat source given by K [-] (def. in Eq. (4.10))
$\mathbf{K}$	finite element stiffness matrix (def. in Eq. (C.4))
L	length [m]
$\mathbf{L}$	time-marching operator (def. in Eq. (7.2))
$\mathscr{L}\{\cdot\}$	Laplace transform (def. in Eq. (2.20))
n	interaction index in STL model (def. in Sec. 3.3.3)
n	parameter of non-normality (def. in Sec. 1.1.1)
$\mathbf{n}$	normal vector (def. in Eq. (2.22))
N	number of states (def. following Eqs. (2.7) and (2.5))
N_p	number of random samples (def. in Sec. 7.3.2)
M	number of inputs (def. following Eqs . (2.7) and (2.5))
M	Mach number [-] (def. following Eq. (4.8))
$\mathbf{M}$	finite element mass matrix (def. in Eq. (C.3))
p	pressure [N/m^2]
P	number of outputs (def. following Eqs . (2.7) and (2.5))
P	probability (def. in Eq. (7.3))
$\mathbf{P}$	matrix of right-singular vectors (def. following Eq. (2.30))
$\dot{q}$	heat release rate [W] (def. in Eq. (3.4))
q_R	heat of reaction [J/kg] (def. in Eq. (3.4))
$\mathbf{Q}$	dissipation matrix (def. in Eq. (2.24))

R	frequency response function (def. following Eq. (2.21))
$\mathbf{R}$	frequency response matrix (def. following Eq. (2.21))
R_F	flame radius [m] (def. before Eq. (3.5))
s	complex-valued frequency $\lambda + j\omega$ (def. following Eq. (2.12))
s	specific source term (def. in Eq. (2.22))
S	integral source term (def. in Eq. (2.22))
$\mathbf{s}_f$	source term vector of body forces [N/kg] (def. in Eq. (4.1a))
s_m	source term of mass [N/(m^2 s)] (def. in Eq. (4.1b))
S_L	flame speed [m/s] (def. in Eq. (3.4))
$\mathbf{S}$	diagonal matrix of singular values (def. following Eq. (2.30))
$\mathcal{S}$	system (def. in Sec. 2.1)
Sr	Strouhal number [-] (def. in Eq. (6.6))
t	time [s]
T	temperature [K]
T	characteristic time scale [s]
$\mathbf{T}$	transformation matrix
$\mathcal{T}$	transformation operator
u	input vector of the continuous partial differential SSM (def. in Eq. (2.3a))
$\mathbf{u}$	input vector of the discretized SSM (def. in Eq. (2.7a))
$\mathbf{U}$	input vector of the discretized SSM in frequency domain (def. in Eq. (2.18))
$\mathcal{U}$	uniform random distribution (def. in Sec. 7.3.1)
v	velocity [m/s]
$\mathbf{v}$	velocity vector [m/s] (def. in Eq. (3.1))
V	Lyapunov function (def. in Sec. 2.2.1)
V	storage function (def. in Sec. 2.2.2)
$\mathbf{V}$	matrix of eigenvectors (def. before Eq. (2.12))
w	convective phase velocity of wrinkles in premixed flames [m/s] (def. in Eq. (3.10))
$\mathbf{W}$	energy weighting matrix (def. in Eq. (2.8))
$\mathcal{W}$	energy weighting operator (def. in Eq. (2.6))
x	state vector of the continuous partial differential SSM (def. in Eq. (2.3a))
$\mathbf{x}$	state vector of the discretized SSM (def. in Eq. (2.7a))

X	Set of spatial variables ξ (def. in Sec. 4.2)
$\mathbf{X}$	state vector of the discretized SSM in frequency domain (def. in Eq. (2.19))
y	output vector of the continuous partial differential SSM (def. in Eq. (2.3b))
$\mathbf{y}$	output vector of the discretized SSM (def. in Eq. (2.7b))
$\mathbf{Y}$	output vector of the discretized SSM in frequency domain (def. in Eq. (2.18))
z	support of a random variable (def. before Eq. (7.3))
Z	number of subsystems (def. in Sec. 2.1)

Greek Letters

α	flame angle [°] (def. following Eq. (3.8))
β	non-dimensional spatial temperature profile (def. in Eq. (4.8))
γ	heat capacity ratio [-] (def. in Eq. (4.1b))
δ_{ξ_F}	Dirac measure for heat addition to acoustic field [-] (def. in Eq. (4.11))
Δ_β	temperature incremental factor [-] (def. in Eq. (4.8))
ϵ	expansion parameter (def. in Eq. (3.7))
$\zeta_{1,2}$	modal damping coefficients (def. in Eq. (4.31))
ζ_p	pressure damping term [1/s] (def. in Eq. (4.7b))
ζ_v	velocity damping term [1/s] (def. in Eq. (4.7a))
η	flame displacement in laboratory-based reference [m] (def. in Eq. (3.3))
$\theta(\cdot)$	Heaviside step function
κ	ratio of kernel to output energy [-] (def. in Eq. (2.30))
λ	growth rate of complex-valued frequency (def. following Eq. (2.12))
λ	thermal conductivity [W/(K m)] (def. in Eq. (4.1b))
Λ	diagonal matrix of eigenvalues (def. before Eq. (2.12))
μ	ratio of convective to mean flow velocity w/v_0 (def. in Eq. (3.11))
μ	dynamic viscosity [(N s)/m^2] (def. following Eq. (4.1))
ξ	spatial variable [m]
ξ	flame displacement in flame-based reference [m] (def. following Eq. (3.11))
Π	ratio of convective to restorative time scale τ_c/τ_r [-] (def. in Eq. (3.26))

ρ	density [kg/m^3]
σ	entropy [J/(kg K)]
σ	standard deviation (def. following Eq. (C.23))
τ	history variable (def. in Eq. (3.18a))
τ	time constant/settling time [s]
τ	stress tensor [N/m^2] (def. in Eq. (4.1b))
ϕ	equivalence/fuel-to-air ratio [-] (def. in Sec. 3.1)
ϕ	dummy function
φ	probability distribution function (def. in Eq. (7.3))
ψ	volume function of heat addition [1/m^3] (def. in Eq. (4.1b))
ψ_q	1-D function of heat addition [1/m] (def. before Eq. (4.6))
ω	frequency of oscillation [rad/s] (def. following Eq. (2.12))
$\partial\Omega$	outer boundary
Ω	volume [m^3]

Subscripts

$\perp$	perpendicular to mean flow direction (y-direction in subsystem flame)
$\parallel$	parallel to flame sheet
A	acoustic
B	located at the flame base
c	convective
C	conical flame
d	downstream of heat source (hot)
f	rightward traveling characteristic wave
F	flame/heat source
FD	finite differences
FE	finite elements
g	leftward traveling characteristic wave
G	G-equation flame model
gen	general
IR	IR-based model
LTI	linear time-invariant

lyap	Lyapunov function
max	maximum
M	method of weighted residuals
N	full norm
r	restorative
ref	reference
s	settling
T	thermoacoustic
u	upstream of heat source (cold)
v	velocity model
W	wedge flame

Superscripts

$*$	optimal
$\check{}$	discretized
$\dagger$	kernel
$\hat{}$	estimated
$\tilde{}$	transformed; dimensional (only in App. B)
B	located at the flame base
H	Hermitian (complex-conjugate transpose)
T	Transpose

List of Figures

List of Tables

List of Supervised Works

Associated with the present thesis are a number of works carried out by undergraduate students at the Lehrstuhl für Thermodynamik in the framework of internships, term papers and Master and Diploma theses. The latter were all performed under the close supervision of the present author with regards to the full academic and professional breadth, and with respect to all context-related issues.

Name	Type	Year	Title
Maxwell Adams	DAAD-RISE Internship	2013	Nonlinear Models of Premixed Flames and Their Behavior in Thermoacoustic Limit Cycles
Marta Artacho Jiménez	Diploma thesis	2012	Using Adjoint Methods to Investigate Non-Normal Effects in Thermoacoustic Systems
Hendrik Börner	Term Paper	2013	Presentation, Evaluation and Application of Methods of Flame Transfer Function Identification and Thermoacoustic System Modeling
Abhishek Kumar Singh	Master thesis	2013	Effect of Non-Normality onto Triggering in Thermoacoustic Systems
Michael Schiffner	Term Paper	2013	A Solver for Thermoacoustic Systems with Distributed Heat Source Filters
Ellena Schubert	Term Paper	2012	An Experimental Investigation of the Lean Blow Off of a Conical Laminar Premixed Flame in a Dump Combustor
Travis Smith	DAAD-RISE Internship	2012	Time Domain Network Models of Thermoacoustic Systems
Gregory Stevens	IAESTE Internship	2012	Modeling and Visualization of Premixed Flames

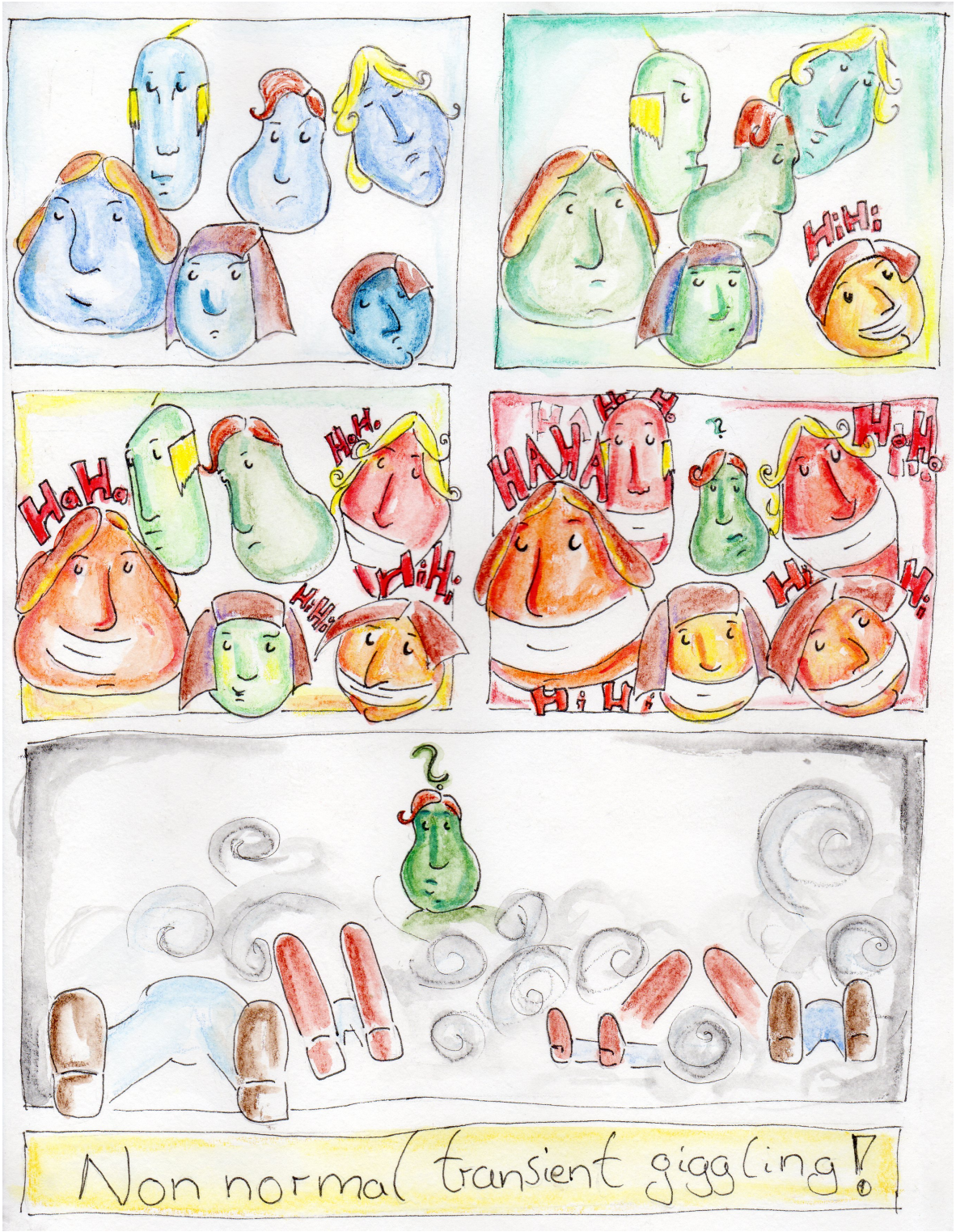

Special thanks to Constanze Temmler for the drawing

1 Introduction and Motivation

Stability is a ubiquitous aspect of life. It represents the foundation of many types of systems, a key requisite that many strive for, work for, or even fight for. Stability stands at the core of mankind, the development of social systems, religions and ideologies, all in the broader interest of creating a stable environment, which sets the stage for prosperous life and development. Examples are manifold: foreign policy is interested in conserving status quo; doctors try to preserve or to restore the health of their patients; engineers would like to design well-functioning devices; parents desire their children to develop in a sound environment; business developers look for opportunities to keep their companies going. More examples can be sought in nearly any area of life.

Many efforts in everyday life are thus concerned with maintaining stability against the destabilizing effect of a given set of perturbations. Foreign policy can be threatened by perturbations such as wars, revolutions or poverty; health is threatened by diseases; well-functioning devices may be perturbed by unforeseen operating conditions, noise or environmental stresses; childhood may be perturbed by anxiety, illnesses or lack of prospects; business development may be perturbed by financial sentiments or consumer moods.

Despite all efforts aimed at maintaining stability, a system may nonetheless become unstable. For example, even if the police outnumbers a crowd of hooligans, the crowd may build up unforeseen dynamics resulting in a big fight. Or, even if parents are sure to satisfy the needs of a group of children, they may develop into a fit of unbroken crying. Or finally, even if hundreds of engineers have designed a rocket to successfully reach space, it may fail right after takeoff. How do such unforeseen events of instability occur?

In some cases, events of instability occur due to a phenomenon called *triggering*. To explain this phenomenon, Fig. 1.1 schematically depicts the pos-

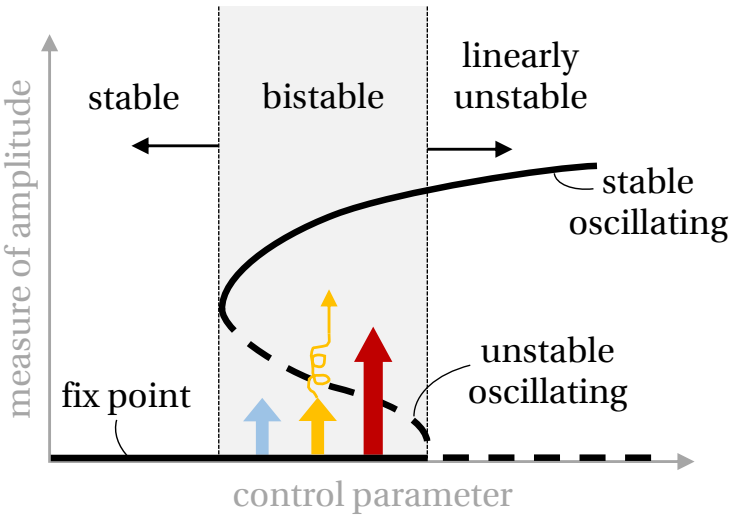

Figure 1.1: Sketch of the operating map of a dynamical system. Loss of stability through the event of triggering can happen in the bistable region of the control parameter due to the action of a large-amplitude perturbation (the red arrow), or a small-amplitude perturbation via the scenario of non-normal transient growth around an unstable oscillating limit cycle (the yellow arrow). The perturbation indicated by the blue arrow does not trigger the system.

sible operating map of a dynamical system. Below a certain threshold of the control parameter (typically some relevant parameter of the system dynamics, e.g. power output), the system is stable. It hence operates around a stable fix point and can withstand any finite-amplitude perturbation. Above an upper threshold of the control parameter, the system is linearly unstable. For any perturbation, even with infinitesimally small amplitude, the system moves towards the undesired operating point that oscillates at large amplitudes. Between both thresholds lies a bistable region, where the system can withstand a small-amplitude perturbation, as indicated by the blue arrow in the gray-shaded area in Fig. 1.1. However, if the perturbation is large in amplitude (see the red arrow), the system is pushed towards the undesired operating point. This process is called triggering.

If the dynamics of the dynamical system of interest is non-orthogonal (for example, a group of hooligans, a group of children, or a highly complex rocket

engine), triggering may also occur due to a phenomenon called *non-normal transient growth*. In this case, a small-amplitude perturbation to the system can transiently grow in magnitude. As the system is running in stable operation, it should be able to bear any such perturbation in the long run. However, if the transient amplification of the perturbation is sufficiently large, it may actuate higher-order effects that may push the system towards the unstable operating point, as indicated by the yellow arrow in Fig. 1.1.

The above scenario of triggering through non-normal transient growth is observed in laminar shear flows, which prematurely transition to turbulence (known as *bypass transition*) [149]. Other examples where non-normal transient growth is observed include population dynamics, nuclear reactors, Markov chains [173], astrophysical objects and circumterrestrial space [24], and weather phenomena [47]. Non-normal transient growth is known in the control community as *peaking phenomenon* [53, 75, 168].

The present study deals with the phenomenon of non-normal transient growth in thermoacoustics, where ideas of non-normality were introduced in recent years [4–6, 85, 118]. A thermoacoustic system is a system in which a heat source, an acoustic field and a flow field are in continuous interaction. Prominent examples are rocket engines, gas turbines or aircraft engines. However, any combustion-driven engine, such as motors or heaters, can be considered to be a thermoacoustic system.

Triggering a thermoacoustic system to self-sustained large-scale oscillations brings along disastrous effects and technical failure, as shown by the melted nozzle in Fig. 1.2. Triggering of a linearly stable thermoacoustic system may happen through a sufficiently large perturbation [185], which simply kicks the system away from the stable point of operation towards the stable oscillating limit cycle (analog to the red arrow in Fig. 1.1). However, triggering is also observed for small-amplitude perturbations of the order of the background noise [176, 177, 185]. There is some evidence that the latter cause for triggering may be through non-normal transient growth.

The present thesis investigates non-normal transient growth around a stable fix point. That is, the present study is concerned with an early phase of trig-

Figure 1.2: Image of a melted nozzle highlighting the possible impact of thermoacoustic oscillations. Image taken from [158].

gering, which is still entirely situated in the linear regime. Can non-normal transient growth around a stable fix point cause a sufficient amplification of perturbation amplitude such that the system can be attracted to an unstable oscillating limit cycle? Is it important which measure of perturbation amplitude is used? Commonly, one is interested in determining the conditions of optimal non-normal transient growth (optimal in the sense of largest). However, how likely is it to encounter any amount of optimal or suboptimal non-normal transient growth in the first place? In short, is non-normal transient growth a serious threat for thermoacoustic systems operating around a stable fix point?

In the following, the two main keywords of the present thesis, *non-normal transient growth* and *thermoacoustics*, which so far have been used in a rather loose manner, are introduced in greater depth. In Sec. 1.1, we give an introductory view on non-normal transient growth. The area of thermoacoustics is introduced in Sec. 1.2. Subsequently, we define the scope of the present work and contrast it to previous works in the field in Sec. 1.3. The structure of the present thesis is outlined in Sec. 1.4, where each chapter is briefly summarized and where we discuss the contributions and limitations of the present work.

1.1 An Introductory View on Non-Normality

The present section intends to convey some basic notions of non-normality: in Sec. 1.1.1, we define and interpret non-normality by way of example of a simple (2×2)-matrix. In Sec. 1.1.2, the concept is extended to non-normal transient growth, which is a time-dependent phenomenon.

1.1.1 Non-Normality of a Matrix

Non-normality is a property of linear systems described by a (linearized) matrix $\mathbf{L}$. Its mathematical definition is straightforward: $\mathbf{L}$ is non-normal, if it does not commute with its conjugate transpose, i.e., $\mathbf{L}\mathbf{L}^H - \mathbf{L}^H\mathbf{L} \neq \mathbf{0}$. If it does, $\mathbf{L}$ is a normal matrix. The concept applies in a similar manner to linear operators, which are non-normal if they do not commute with their Hermitian adjoint.

In the following, we give two interpretations of non-normality using the simple example of a (2×2)-matrix $\mathbf{L} \in \mathbb{R}^{2\times 2}$, which is inspired by the introductory example in [173],

$$\mathbf{L} = \begin{bmatrix} -1 & n \\ 0 & -2 \end{bmatrix},$$

where n is a parameter of non-normality. For $n = 0$, $\mathbf{L}$ is normal, while for $n \neq 0$, $\mathbf{L}$ is non-normal.

Initial research on non-normality was aimed at studying spectral aspects of ill-conditioned discretized numerical operators [60, 94, 174]. The first way to view non-normality is thus as a measure of how well-conditioned a matrix is. The condition number of a matrix is defined as the ratio of largest to smallest singular value of $\mathbf{L}$. Singular values are the square root of the eigenvalues of $\mathbf{L}\mathbf{L}^H$, and measure how much the action of a matrix can scale the space it is acting on [172]. The condition number thus indicates a normalized upper bound on the stretching action of a matrix.

For increasing condition numbers, the action of a matrix is increasingly sensitive to errors in the space it is acting on. The reason is because the error might

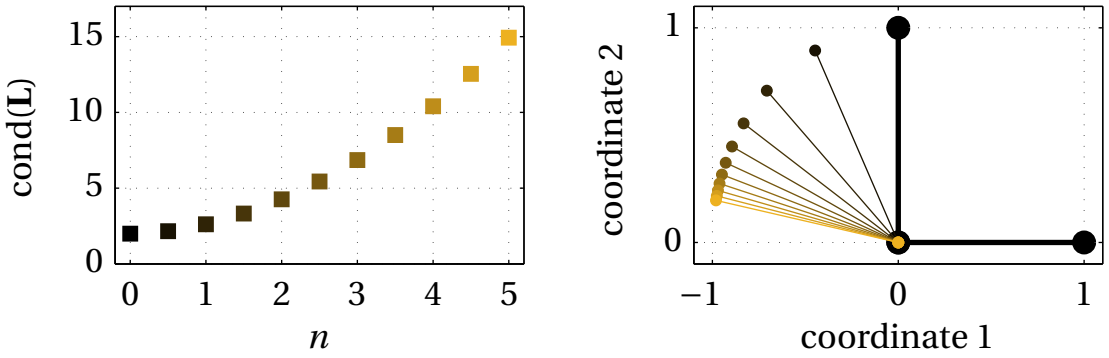

(a) Condition number. **(b)** Eigenvectors.

Figure 1.3: Stationary interpretations of non-normality: increasing the parameter of non-normality n leads to an increase in (a) the condition number, and (b) the non-orthogonality of the eigenvectors.

be more amplified (i.e., stretched) than the solution itself. This is the case for non-normal matrices. Non-normality may thus result from ill-conditioned matrices, which in turn depend on the chosen discretization scheme. This topic is addressed in the present work in Chap. 7.1. For normal matrices, singular values and eigenvalues are the same, and the condition number equals the ratio of largest to smallest eigenvalue. In Fig. 1.3(a), we plot the condition number of $\mathbf{L}$ as a function of the non-normal parameter n. It is visible that the condition of the matrix is best in the normal case for $n = 0$.

The second way to view non-normality is from a geometrical perspective. For normal matrices, the eigenvectors span an orthogonal basis. With increasing non-normality, the eigenvectors become non-orthogonal to one another. This is visible in Fig. 1.3(b). Since normal is a synonym for orthogonal, the term non-normality originates from this geometrical perspective.

1.1.2 Non-Normal Transient Growth

If a non-normal matrix or operator governs the time-dependent dynamics of a discrete or continuous model, respectively, this may lead to the occurrence of non-normal transient growth. As seen above, non-normality as such represents an inherent property of linear matrices and operators, and therefore

constitutes a necessary condition for non-normal transient growth. However, if the system dynamics is governed by a non-normal matrix or operator, this does not necessarily imply the occurrence of significant non-normal transient growth. For example, the observed behavior of Markov chains, which are known to be non-normal, does not differ significantly from the normal modal dynamics [173]. Non-normal transient growth depends on multiple other factors, which we will discuss below.

Suppose the above defined matrix $\mathbf{L}$ governs the time evolution of the ordinary differential equation

$$\frac{\mathrm{d}}{\mathrm{d}t}\begin{bmatrix} x_1 \\ x_2 \end{bmatrix} = \mathbf{L}\begin{bmatrix} x_1 \\ x_2 \end{bmatrix},$$

with energy $E = x_1^2 + x_2^2$. If $\mathbf{L}$ is non-normal, the maximum possible relative amplification of energy E over time can exceed unity. This is visible from Fig. 1.4(a), where the maximum amplification of E/E_0 is plotted over time for different non-normal parameters $n \in [0,5]$.

Above a certain parameter of non-normality n, the model admits non-normal transient growth at small times. Below this threshold (i.e., for small values of n), the energy E always decays exponentially. In a normal system with $n = 0$, which is excited at all frequencies, the exponential decay rate is given by the least stable eigenvalue of $\mathbf{L}$ *for all times*. This stands in contrast to the non-normal case, where the eigenvalues only dictate the asymptotic dynamics for $t \to \infty$. That is, whether the model is linearly stable or not is governed by the eigenvalues of $\mathbf{L}$, which is independent of non-normality. At small times, however, maximum energy amplification is governed by the singular values of $\mathbf{L}$ [148, 149, 173]. A classical linear stability analysis based on eigenvalues is therefore not able to capture the short-term dynamics of the model. This is precisely why interest in non-normality rose in the field of sheared flows, where results from classical linear stability analysis were not able to explain the transient development of flows observed in experiments [7, 43, 44, 47, 48, 74, 141, 149]. We will return to the topic of stability in the context of non-normality in Secs. 2.2 and 2.4.2.

The effect of non-normality is also visible in a stochastic framework. Assume an initial probability distribution (pdf) of energy φ_E at $t = 0$. If the propaga-

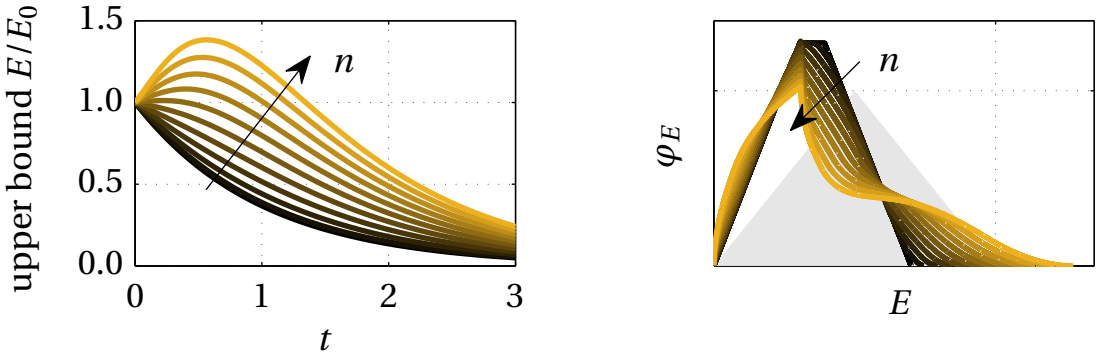

(a) Max. rel. amplification of E.

(b) Pdf of E after Δt.

Figure 1.4: Non-normality leads to (a) an increase in the maximum amplification of energy E/E_0, and (b) skewing a given initial energy probability distribution φ_E (indicated by the gray shaded triangle) after a given time interval Δt. The normal process for $n = 0$ (—) (a) only admits exponential decay, and (b) causes a scaling of the initial pdf, and conserves the general shape of the distribution (the smoothing of the tip results from numerical errors).

tor matrix $\mathbf{L}$ is normal, the action of $\mathbf{L}$ leads to a scaling of the pdf φ_E over time. However, the general shape of the initial distribution is preserved. This is visible from Fig. 1.4(b), where the black line indicates $\varphi_E(t = \Delta t)$ for $n = 0$ with respect to the initial pdf $\varphi_E(t = 0)$ given by the gray shaded triangle[1]. A significant skewing of the initial pdf is visible for $n > 0$. It is known that non-normality leads to an increase in variance of random processes [45, 46, 178].

Non-normal transient growth can be explained using the interpretations of non-normality given in the previous Sec. 1.1.1. From the interpretation of the condition of the matrix, the stretching action of non-normal matrices may lead to a co-domain that is enlarged and skewed with respect to the space the matrix is acting upon. From a geometrical point of view, the energy E corresponds to the resultant that is spanned by the eigenvectors. Although the latter are strictly decaying in time, the resultant may transiently increase in magnitude due to the non-orthogonality of the eigenvector space. However, this is only possible for a particular set of decay rates and angles between each

[1] Slight discrepancies at the tip of φ_E result from numerical errors.

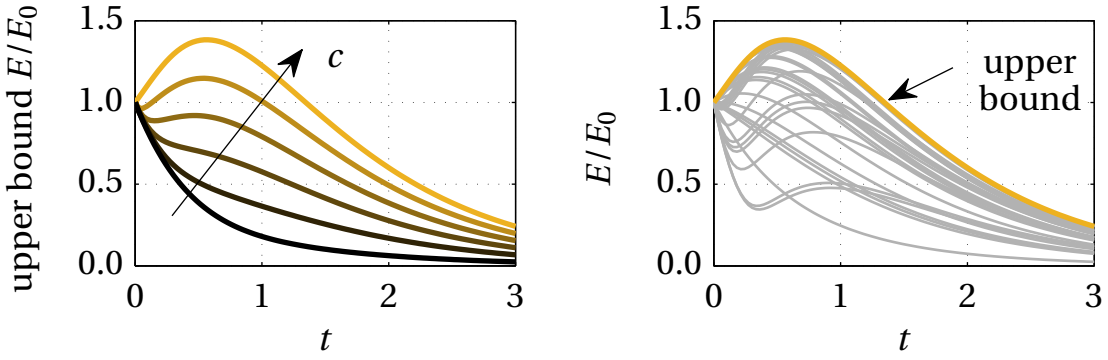

(a) Max. rel. amplification of E. **(b)** Different initial conditions.

Figure 1.5: Effect of (a) energy norm and (b) initial conditions on non-normal transient growth.

of the eigenvectors. As is visible from Fig. 1.4, the conditions for non-normal transient growth are not fulfilled for small values of n, even though the matrix $\mathbf{L}$ is non-normal. However, the skewing action of $\mathbf{L}$ is present even for small parameters of non-normality n (see Fig.1.4(b)).

As mentioned in the beginning of the present section, non-normal transient growth depends on other factors than solely on the non-normality of the underlying dynamics. In the plots shown so far, we have used the definition of energy $E = x_1^2 + x_2^2$. However, we are free to choose any other metric to quantify the system dynamics by a scalar measure. A different energy metric amounts to a change in perspective on the dynamics of the model.

In Fig. 1.5(a), we plot the maximum relative energy amplification for the non-normal case of $n = 5$. The energy is defined as a function of an energy scalar c, $E = c^2 x_1^2 + x_2^2$, with $c \in [0.1, 1]$. Non-normal transient growth is only visible for certain values of c. This example shows that the energy metric is crucial for the analysis of non-normal transient growth. Although it does not alter the level of non-normality contained in $\mathbf{L}$, it prescribes the way in which the dynamics is exhibited to the observer. We will return to this point in Chap. 5.

The second crucial factor for the analysis of non-normal transient growth consists in the initial condition from which the model is released. Until now, we have examined the maximum relative energy amplification E/E_0 (except for

in the stochastic framework in Fig. 1.4(b)). However, for every instant in time, there exists only one initial condition that reaches the maximum at precisely that instant in time. This initial condition is referred to as *optimal*, because it leads to the largest possible level of energy amplification at a given instant in time. How to compute such an *optimal initial condition* (OIC) will be treated in Sec. 2.4.2.

Figure 1.5(b) depicts the evolution of energy of 30 randomly computed initial conditions for the case of $n = 5$ and $c = 1$. The maximum energy amplification is overlaid in yellow. It can be seen that some initial conditions lead to non-normal transient growth, whereas others do not. That is, even if the dynamics of the model, together with the definition of energy metric, allow for non-normal transient growth, the initial condition needs to be conducive to energy amplification.

Analysis of the initial conditions leading to optimal growth may therefore shed light on the basic mechanisms of non-normal transient growth. However, a full analysis of non-normal transient growth also requires suboptimal conditions to be taken into account. This is done in the present work in Sec. 7.3, where we estimate the probability of encountering an initial condition leading to non-normal transient growth. To the author's best knowledge, an analysis on the likelihood of non-normal transient growth has so far only been carried out by Kim & Moehlis [91] for a low-order shear flow model.

In summary, the phenomenon of non-normal transient growth requires the beneficial combination of three ingredients. First, the matrix or operator governing the dynamics needs to be non-normal. This is definitely the case for most thermoacoustic systems [4, 5]. Second, the maximum energy amplification needs to exceed unity, which in turn depends on the choice of energy. This topic is addressed in the present study in Chap. 5. Third, the initial condition needs to be conducive to transient growth, which is treated in the present study in Chap. 7. Due to these factors, it is not always possible to observe transient growth, even if the underlying process is non-normal.

1.2 An Introductory View on Thermoacoustics

Thermoacoustics describes the interaction of a heat source, an acoustic and a flow field. The archetype of a thermoacoustic system, a so-called *Rijke tube*, consists of a straight duct open at both ends, which encloses a metal wire gauze in the lower part of the duct (see Fig. 1.6). The wire gauze acts as a heat source upon being heated by a candle or a lighter. A Rijke tube can develop self-excited and self-sustained oscillations, which are audible as a loud sound at about the fundamental frequency of the duct. This thermoacoustic phenomenon was discovered by the Dutch physicist Pieter Rijke in 1859 [143].

The basic mechanism of developing thermoacoustic oscillations is as follows. For a classical vertically-oriented Rijke tube, activating the heat source in the duct leads to a natural convective flow due to the increase in temperature. For a horizontal Rijke tube, the mean flow requires a mean pressure gradient across the duct. In turn, the heat addition to the flow depends on the flow velocity. Any minuscule acoustic perturbations alter the flow velocity, and thus lead to a local increase or decrease in the heat addition. These fluctuations in heat release rate are phase-delayed with respect to the acoustic velocity fluctuations. The same holds true for the acoustic pressure fluctuations, which locally compress and relax the air flow. Using the words of Lord Rayleigh published in 1878 [140], "if heat be given to the air at the moment of greatest condensation, or taken from it at the moment of greatest rarefaction, the vibration is encouraged." Thermoacoustic oscillations hence develop through the positive feedback between the acoustic and flow field and the heat source.

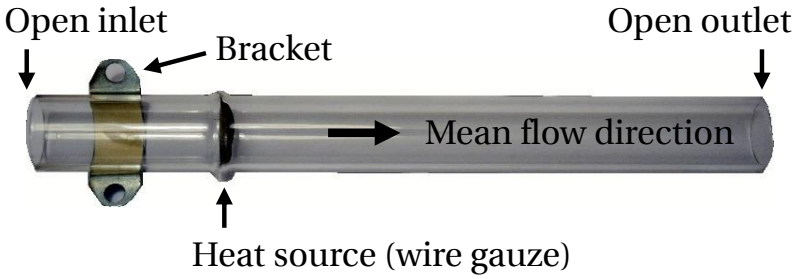

Figure 1.6: Image of a glass Rijke tube with a wire gauze acting as heat source. The classical Rijke tube is oriented vertically.

The acoustic perturbations grow by extracting energy from the heat source. In turn, the fluctuations in heat release rate are caused by the action of the acoustic and flow field.

Thermoacoustics is a multi-physics problem, which mainly consists of the three fields of combustion, acoustics and fluid dynamics. Each of these fields describes an entire research area for themselves, and therefore brings along a different point of view on thermoacoustics. For example, the combustion-based perspective on thermoacoustics is motivated by understanding the dynamics and mechanisms of heat release, and how the latter are altered by perturbations. The acoustics-based perspective treats thermoacoustics as an acoustic problem that is perturbed by a heat source [61, 92, 130, 142].

Analysis of thermoacoustic systems essentially amounts to investigating stability. From a design point of view, one is interested in determining whether a given thermoacoustic system will operate under stable conditions, or whether it is expected to attain a nonlinear oscillating limit cycle. From an understanding point of view, one is interested to find out why a thermoacoustic system may become unstable, and also to investigate the pertinent factors and parameters.

In the linear regime, a wide-spread approach to stability analysis consists in computing the complex-valued eigenfrequencies of a network of acoustic elements, such as ducts, flames, dampers, area changes or boundary conditions [144, 145, 161]. If the most unstable eigenfrequency possesses a negative growth rate (i.e., a positive decay rate), the system is *linearly stable*. This so-called *network model analysis* originates from an acoustics-based perspective on thermoacoustics. Each element is characterized by its acoustic scattering/response behavior in the frequency domain.

Frequency response functions of various elements can be determined from experiments [89, 127], by numerical simulations [25, 35, 70, 71, 80, 112, 129, 134] or from analytical and semi-analytical models [49, 138, 154]. The quality of results of a network model analysis crucially depends on how accurately each of the elements is described. Much research effort is thus aimed at the development of measuring techniques and sophisticated numerical codes

that allow to capture a precise picture of the dynamics of the element subject to acoustic excitation.

Extension of the network model-based approach to the nonlinear regime yields the so-called framework of describing functions [161]. There, the acoustic response behavior of an element is not only determined as a function of frequency as in the linear case, but also as a function of the amplitude of oscillation. The describing function framework is therefore capable of predicting amplitude and frequency of oscillation of nonlinear limit cycles [17, 38, 123, 137]. However, the predictions are limited to the asymptotic state of single-frequency harmonic limit cycles.

Frequency domain analysis is inherently aimed at analyzing the asymptotic dynamical behavior of a system. That is, frequency domain analysis yields insights into the long-term behavior. It is therefore not well suited for the analysis of transient processes. The latter are more conveniently investigated in the time domain. Full-scale numerical treatment of thermoacoustic problems in the time domain is frequent [131], but computationally expensive and time-consuming due to the necessary combination of small time and length scales, resulting from acoustics and combustion, respectively. Many time domain analyses in thermoacoustics therefore use low-order model descriptions. An extensive review on low-order modeling approaches to thermoacoustics can be found in [132].

A time domain approach to thermoacoustics offers benefits that are complementary to those of a frequency domain approach. For example, low-order time domain descriptions of different elements of a thermoacoustic system yield insight into the dominant response mechanisms each occurring at characteristic time scales [12, 93, 163]. Also, the linear stability bounds of an entire thermoacoustic system can be easily determined by a spectral eigenanalysis [16, 126, 151, 152]. This stands in contrast to the network model analysis mentioned above, where the eigenfrequencies are determined on a one-by-one basis using iterative root finding algorithms.

In the nonlinear regime, recent work in the time domain has shed light on the variety of stable and unstable limit cycles that a thermoacoustic system

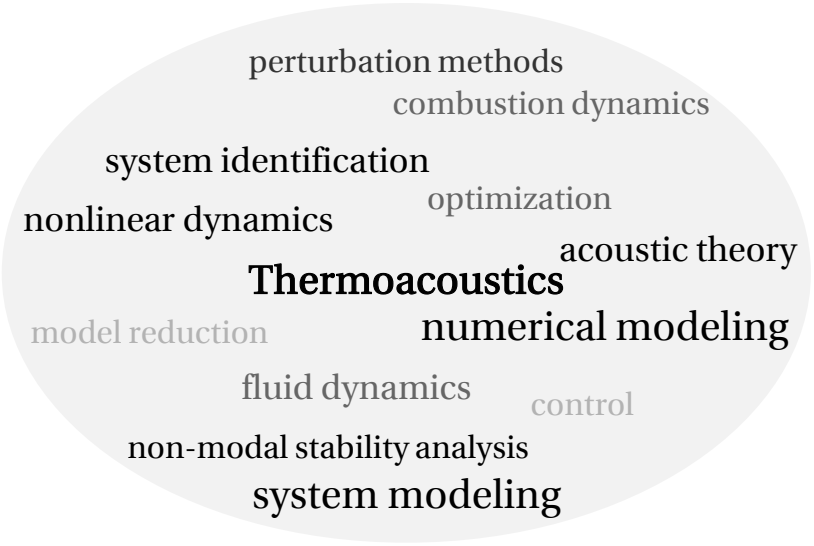

Figure 1.7: Schematic map of different fields of science and areas of research that are encountered when analyzing thermoacoustic systems.

can reach (for example, [79, 81, 84, 164, 166]). These studies contribute to a significantly better understanding and quantification of limit cycle behaviors. Nair & Sujith [119] have developed a method to infer an impeding loss of stable operation from time domain data by use of fractal methods. All these insights are not available from a frequency domain perspective.

Altogether, there are many possible approaches towards analyzing thermoacoustics, a multi-physics problem which combines aspects from various fields of science and areas of research. Depending on the desired flavor of the particular analysis, a time or frequency domain framework may prove beneficial. Each analysis requires the incorporation of different theories and the combination of information from different areas, which is schematically indicated by the map in Fig. 1.7.

Systems theory offers a robust platform to cope with such challenges. It homogenizes established thermoacoustic frameworks with ideas from other communities using a common language. Systems theory-based approaches are recent in thermoacoustics [105, 150, 151], and are currently on the rise. For example, some studies follow a system theory-based approach with the objective of applying active control to a thermoacoustic system [68, 126, 150, 152].

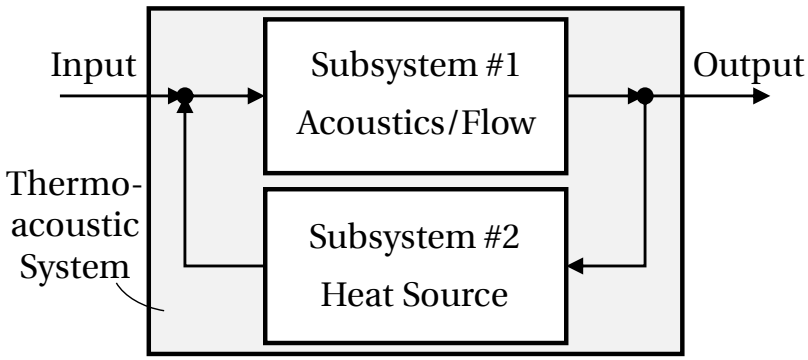

Figure 1.8: Schematic setup of a thermoacoustic system consisting of two subsystems in feedback: the subsystems acoustics/flow and heat source.

Or, using a systemic approach, a phenomenon called intrinsic thermoacoustic feedback (ITAF) describes potentially unstable thermoacoustic modes that have so far been overlooked by the traditional approach of adopting an acoustic perspective [15, 40]. The same is true for advances in soft-sensing and gray-box model system identification of flame response [72].

The present study also adopts a systems theory-based approach. This is done with the aim of gaining a fresh and clear perspective on the non-normal dynamics of a thermoacoustic system. As depicted in Fig. 1.8, we view a thermoacoustic system as a generic multi-physics problem of two subsystems in feedback: one subsystem for the acoustics and mean flow and one subsystem for the heat source. In the course of the present work, the subsystems are investigated in isolation before being assembled to a full thermoacoustic system.

The following section is intended to put the present work into context with previous work in the field of non-normal transient growth in thermoacoustics.

1.3 Non-Normal Transient Growth in Thermoacoustics

Studies on non-normal effects in thermoacoustics and their impact towards triggering can be found in recent thermoacoustic literature. Interest in this

field rose after different studies demonstrated that the interaction of an acoustic field with a heat source makes a thermoacoustic system non-normal [4, 5, 85, 118]. The analyses by Balasubramanian & Sujith [4, 5] were carried out for a duct enclosing a heat source, which was modeled as a diffusion flame and by a simple n-τ model. For the latter, it is assumed that the heat release rate impulsively follows the acoustic velocity by a constant delay τ (derived from a model proposed by [28]). The maximum relative energy amplification E/E_0 (see Sec. 1.1.2) is determined to be of the order of 10^0 (taking into account a later correction published in [104]). The same was shown by Mangesius & Polifke [105] for a state space model of a Rijke tube-like configuration with an n-τ model heat source.

In addition, Balasubramanian & Sujith [4, 5] presented evidence that non-normal transient growth around a stable fix point may be a cause for triggering a thermoacoustic system. This was also indicated by Subramanian & Sujith [165] in a low-order study of a duct enclosing a more sophisticated model of a premixed flame, and by Mariappan & Sujith [107] for a solid rocket motor. In both studies, the maximum E/E_0 is of the order of 10^2.

On the other hand, Juniper [76] shows for a Rijke tube-like configuration with an n-τ model heat source that the initial conditions leading to largest energy amplification found from optimizing the linearized governing equations are different from those found in a nonlinear analysis. He concludes that non-normal transient growth around a stable fix point is a rather theoretical option. In subsequent studies [77, 78], the focus is therefore pointed towards non-normal transient growth around an unstable limit cycle. Similar to bypass transition in turbulence, non-normal effects can transiently amplify perturbations of low energy around an unstable oscillating limit cycle, before they are repelled towards the undesired stable oscillating limit cycle by the action of nonlinearities. The scenario of triggering is thus through the combined effect of non-normality and nonlinearity, which both contribute to growth of perturbations. This is where triggering in thermoacoustics fundamentally differs to bypass transition to turbulence. For the latter, the nonlinear terms redistribute energy in a conservative manner, and growth is solely due to non-normal effects, which are entirely linear [55, 63, 149]. In thermoacoustics,

provided linear acoustics, the nonlinearity arises from the fluctuating heat source, which is a non-conservative source term.

Other studies in the field of non-normality in thermoacoustics deal with the question of appropriate energy norm. As seen in Sec. 1.1.2, the choice of energy has a strong effect on the observation of non-normal transient growth. Wieczorek *et al.* [179] report a difference in the optimal relative energy amplification of the order of 10^3 depending on whether or not entropy fluctuations are included in the definition of energy. We will return to this finding in Sec. 5.1. Other studies compare different energy norms as to their mathematical properties [56, 57, 59].

In view of the factors influencing non-normal transient growth as discussed in Sec. 1.1.2, previous studies on non-normal transient growth in thermoacoustics suffer from up to three critical points. First, some of the investigated low-order models and associated modeling assumptions tend to be restrictive in that they represent an oversimplified thermoacoustic configuration. Second, without exception, previous studies analyze non-normal transient growth subject to the energy defined as the L_2-norm of the state vector of the model. Results may thus be biased by the energy norm that follows from the chosen model structure. And third, non-normal transient growth and its impact towards triggering is examined with respect to optimal conditions of non-normal transient growth. The likelihood of encountering such optimal conditions, or whether suboptimal conditions may also prove dangerous, has so far only been addressed by [109] in a different context. We will discuss these three critical points in more detail in the following.

Common Low-Order Modeling Assumptions

There are good reasons to focus the analysis of non-normality on simple thermoacoustic systems inspired by the Rijke tube (see Fig. 1.6). As discussed in the previous Sec. 1.2, thermoacoustic problems are governed by the complex interaction of different subsystems, which may obscure the fundamental mechanisms of non-normal dynamics. Furthermore, one is required to solve an optimization problem to compute the optimal conditions leading to maxi-

heat source	approach	ϕ [-]	Sr [-]	M_u [-]	$T_{0,d}/T_{0,u}$ [-]	α [°]	$\lvert\zeta\rvert$ [-]
heated wire [50, 51, 100]	analytical, DNS	–	$\mathcal{O}(10^{-2})$	$\mathcal{O}(10^{-3})$	≈ 3.2	–	–
lam. premixed flame [79]	experimental	0.51	≈ 22	$\mathcal{O}(10^{-3})$	≈ 4.8	≈ 23	$0.04 \pm 10\%$
lam. premixed flame [84]	G-eq. model	0.85	≈ 2	0	1	≈ 8	$\mathcal{O}(10^{-2})$
lam. premixed flame [165]	G-eq. model	0.6...1	≈ 9	0	1	10...50	$\mathcal{O}(10^{-1}$ ...$10^{-3})$
generic [77, 78]	n-τ model	–	$\rightarrow 0$	0	1	–	very small

Table 1.1: Overview of a selection of parameters encountered in previous studies of laminar thermoacoustic systems: equivalence ratio ϕ, Strouhal number Sr, upstream Mach number M_u, ratio of downstream to upstream mean temperatures $T_{0,d}/T_{0,u}$, flame angle α, and absolute damping $|\zeta|$.

mum non-normal transient growth (see Sec. 1.1.2). In the interest of reducing computational cost, it is thus desirable to use low-order models with as few degrees of freedom as possible. Previous studies using low-order models are therefore all concerned with analyzing non-normal transient growth in simple thermoacoustic systems under laminar conditions. However, it is questionable whether the common low-order modeling assumptions addressed in the following paragraphs are reasonable. In Tab. 1.1, we give an overview on selected parameters used in previous studies of laminar thermoacoustic systems.

The assumption of zero mean flow does not account for the effect of mean flow onto the acoustic mode shapes (for example, [4, 5, 76–78, 105, 165]). Possible shortcomings of this assumption are discussed in [122]. Under laminar conditions, however, the upstream Mach number M_u is of the order of 10^{-3}. A zero Mach number assumption may therefore be tolerable.

On the other hand, the assumption of zero temperature jump across the heat

source neglects the actual effect of a heat source on its surroundings (for example, [4, 5, 76–78, 105, 165]). The temperature jump encountered in real setups, as for the experimental study published in [79], is significant (see Tab. 1.1). It should be expected that neglecting the jump in mean quantities strongly affects the results. This point will be addressed in Secs. 4.5 and 6.1.3.

Furthermore, the assumption of a very fast-reacting heat source does not reflect the slow nature of the response of most practical heat sources (for example, [5, 76–78]). The ratio of characteristic time scales between the heat source and the acoustic field is measured by the Strouhal number Sr. For premixed flames, $\mathrm{Sr} = \mathcal{O}(10^0 \dots 10^1)$, whereas $\mathrm{Sr} = \mathcal{O}(10^{-1} \dots 10^0)$ for heated wires [51]. Also, a heat source modeled by an n-τ model does not express the distributed manner of flame response. It is shown in [146, 163] and in Sec. 3.3.3 of the present work that an n-τ model is a poor representation of the heat source dynamics.

Altogether, the present study aims at investigating non-normal transient growth for a more sophisticated low-order model of a duct enclosing a heat source. As will be shown in Chaps. 3 and 4, respectively, the heat source is modeled by an impulse response-based filter model [12], and the model of the acoustic field incorporates a bulk mean flow and a jump in temperature, density and speed of sound at the position of the heat source.

The Choice of Energy Norm

As mentioned above, the question of proper energy norm for thermoacoustics is an ongoing matter of debate. Since thermoacoustic dynamics results from the combined effect of multiple subsystems in feedback, it is unclear which scalar measure is apt to give a meaningful quantification of the system behavior. Should the energy norm be a measure of only parts of the thermoacoustic dynamics, computing the optimal conditions leading to non-normal transient growth would necessitate semi-norm optimization algorithms, which so far have mainly been addressed in the framework of variational methods [52, 103].

Without exception, previous works in the field of non-normality in thermoacoustics define the energy as the L_2-norm of the state vector of the investigated low-order model. For example, the states of the thermoacoustic model of Mariappan & Sujith [107] resolve fluctuations in entropy and the model contains mean flow effects, such that they use Chu's norm [26] and Myer's norm [117], respectively. The thermoacoustic model of Juniper [76–78] consists of acoustic states without mean flow, and the energy norm is given by the acoustic energy. The acoustic energy, and Chu's and Myer's norms originate from first principles, and therefore correspond to generic forms of perturbation energy: kinetic, potential and internal perturbation energy. Other studies introduce additional states to model the heat source subsystem [4, 105, 165]. In these cases, the output energies do not necessarily correspond to a generic form of perturbation energy. For instance, Subramanian & Sujith [165] define the flame states such that the output energy can be interpreted as acoustic energy plus a contribution from acoustic monopole sources distributed along the flame surface.

In defining the energy as the L_2-norm of the state vector of the model, a given energy norm conditions the structure of the model, or vice versa. That is, the energy norm cannot be chosen independent of the model structure. This is a major drawback, because the energy norm has a significant effect on the observation of non-normal transient growth (see Sec. 1.1.2). It is therefore desirable to retain a maximum degree of flexibility in the choice of energy norm.

The present study aims at realizing the previously mentioned flexibility in the choice of energy metric. In Sec. 2.4.2, we propose an approach to perform semi-norm optimization using the singular value decomposition (i.e., without the need to resort to variational methods). We are thus able to analyze any energy metric independent of the particular low-order model structure in a straightforward manner. To the author's knowledge, the only other study related to this matter is a paper by Jiménez [73], where semi-norm optimization is used to investigate spatially localized energy amplification in turbulent channel flows.

Furthermore, adopting a systems theory-based perspective, we highlight that the selection of energy is a matter of choice. It merely prescribes the perspec-

tive in which results need to be interpreted (see Chap. 5). Any level of observable non-normal transient growth is unambiguously linked to the model and the choice of energy. However, the choice of energy does not alter the non-normal dynamics as such, because it is a property of the underlying linear(ized) dynamics. The choice of energy metric thus amounts to a matter of perspective.

Optimal vs. Suboptimal Non-Normal Transient Growth

With the exception of [109], previous studies on non-normal transient growth exclusively analyze the optimal conditions of maximum possible transient growth. While this approach certainly sheds light on the basic mechanisms, and thus on a deeper understanding of non-normal phenomena, it misses an important point: Even if optimal non-normal transient growth is relevant for triggering a thermoacoustic system, how common is it to encounter optimal conditions? Is optimal growth of theoretical nature or of practical relevance?

The present study intends to address this point by investigating the probability of encountering any level of non-normal transient growth (see Sec. 7.3). Similar to the experimental study of Mariappan *et al.* [109], we force the thermoacoustic system by a random linear combination of the first three thermoacoustic eigenmodes, which reflects the initial conditions that are controllable in an experiment. It is shown that although suboptimal non-normal transient growth is quite likely, it is highly improbable to encounter optimal non-normal growth conditions.

1.4 Summary, Contributions and Limitations

The body of the present work is divided into three main parts and consists of six chapters (Chaps. 2–7). The first part, given in the single Chap. 2, presents the theoretical foundations used throughout the thesis. In the second part, which spans the four subsequent Chaps. 3–6, the low-order thermoacoustic model is constructed and analyzed. The third part contains the core of the

present work, and can be found in Chap. 7. There, non-normal transient growth around a stable fix point is investigated using the previously constructed low-order model of a simple thermoacoustic system.

The present study applies to thermoacoustic systems in the absence of noise, with simple 1-D geometries, where mean flow effects are trivial and where the acoustic field is homentropic and dominated by planar waves. The limitations are evident, as the above assumptions towards noise, geometry, mean flow and acoustic field do not hold true for most practical thermoacoustic systems. Also, the non-modal analysis is restricted to non-normal transient growth around a stable fix point. Conclusions regarding the impact of non-normal transient growth onto triggering are thus limited, because the stable operating point of many practical thermoacoustic systems lies in a highly turbulent nonlinear regime to begin with. Also, the optimization procedures yielding the most dangerous initial states are limited to the linear regime. Finally, although it is reasonable to qualify the low-order models used throughout the present study as good approximations of the observed dynamics, the presented results lack a direct quantitative one-to-one validation to experimental data. For the largest part, this shortcoming is due to the academic nature of the present work. Generating experimental evidence of the effects treated here is difficult, if not impossible.

In the following, each of the chapters is summarized. Within the above limitations, we also discuss the contributions of the present work.

Chapter 2 conveys a systems theory-based approach to thermoacoustics and to non-modal stability analysis. A generic multi-physics system is defined as a family of different subsytems in feedback. We further define the notion of stability and introduce non-normal transient growth and tools for its analysis. The main contribution of Chap. 2 lies in defining a framework to perform semi-norm optimization in a simple and numerically efficient manner (using the singular value decomposition, without the need to resort to variational methods).

In **Chap. 3**, we derive and analyze models to represent the first building block of a thermoacoustic system, the heat source subsystem. The dynamics of the

heat source are thereby distilled into a generic low-order model structure in the time domain from semi-analytical and data-driven approaches. Chapter 3 highlights that low-order models in the time domain offer rich insights into the physical response mechanisms of the heat source subsystem. This is particularly visible for the convectively-driven response of premixed flames.

Chapter 4 treats the second building block of a thermoacoustic system, the acoustics subsystem. The equations governing the motion of an acoustic field are derived from first principles, and we define and analyze the one-dimensional reference duct configuration used in the present study. Different numerical approaches to approximate the governing equations for the reference configuration are introduced and discussed. A minor contribution of Chap. 4 consists in applying a numerical method of weighted residuals, often referred to as the Galerkin method, to a 1-D acoustic field with spatially varying profiles of mean flow and temperature.

The last building block of a thermoacoustic system, the definition of output energy, is discussed in **Chap. 5**. We contribute to the ongoing debate on appropriate energy norms in thermoacoustics by highlighting that the selection of output energy is a matter of choice, and that it merely defines the perspective that one wishes to adopt on the problem of interest. From a systems theory-based point of view, we then list a selection of physically motivated energy norms available for the treatment of thermoacoustic systems.

In **Chap. 6**, the outcomes of Chaps. 3–5 are combined to define and to analyze the full low-order model describing the simple thermoacoustic system treated in the present study. The temporal evolution of output energy is discussed with the aim of later identifying the causes of non-normal transient growth. We further perform a linear stability analysis. The contribution of Chap. 6 lies in highlighting the benefit of adopting a holistic view on thermoacoustic systems, which stands in contrast to approaching thermoacoustics as an acoustic problem that is slightly perturbed by a heat source.

Chapter 7 is dedicated to the analysis of the previously defined low-order model of a simple thermoacoustic system with regards to non-normal transient growth around a stable fix point. Spurious and inherent transient growth

resulting from ill-conditioned discretized numerical operators and model limitations, respectively, is contrasted to physical transient growth. We further investigate the dynamics of non-normal transient growth and make use of the semi-norm optimization technique defined in Chap. 2. The probability of encountering any level of non-normal transient growth is determined by random sampling techniques. Combining the results, we discuss the possible impact of non-normal transient growth onto triggering.

The first contribution of Chap. 7 is that non-normal transient growth is analyzed using semi-norm optimization, which allows for the treatment of more sophisticated models and also to retain flexibility in the choice of energy metric. Second, the non-modal analysis is not limited to optimal, but includes suboptimal transient energy amplification. Third, the present analysis quantifies the probability of encountering transient growth. Combining the contributions of Chap. 7 indicates that non-normal transient growth around a stable fix point does not seem to be a threat for triggering in simple thermoacoustic systems.

2 A Systems Theory Approach to Non-Modal Analysis

The present chapter serves as a compendium of the theory used throughout the thesis. Results and discussions of subsequent chapters are based on the definitions and concepts introduced in the following four sections. The systemic perspective adopted on a multi-physics problem such as thermoacoustics is laid out in Sec. 2.1. Stability of autonomous and forced systems is defined in Sec. 2.2. In Sec. 2.3, the definitions of stability are linked to the solution of the output of linear time invariant systems in the time and frequency domain. Section 2.4 brings together Secs. 2.2 and 2.3, and introduces the tools to analyze non-normal transient growth (*non-modal* stability analysis). While Secs. 2.1–2.3 mostly contain standard textbook material, Sec. 2.4 features results of the present thesis.

To simplify exposition, the present chapter exclusively deals with linear systems. The definitions on interconnected systems and on stability given in the first two Secs. 2.1–2.2 can be extended to the nonlinear regime in a straightforward manner. The sections on the output of linear time-invariant systems and on the non-modal analysis given in Secs. 2.3 and 2.4, respectively, are only valid in the linear regime. For enhanced homogeneity of presentation, the entire chapter is therefore limited to linear systems.

2.1 Formulation of a System of Interconnected Subsystems

A multi-physics problem such as thermoacoustics can be viewed as a collection of different systems in feedback. In the following, we define a generic system $\mathcal{S}$ consisting of Z interconnected subsystems $\mathcal{S}^{(i)}$, with $i \in \{1, 2, \ldots, Z\}$.

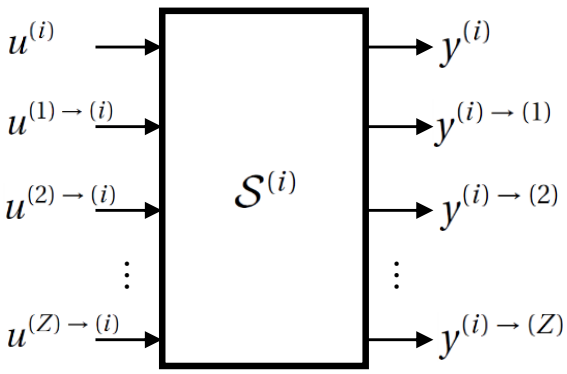

Figure 2.1: Sketch of the inputs and outputs to and from $\mathcal{S}^{(i)}$.

The dynamics of each subsystem is governed by a state and an output equation,

$$\frac{\partial x^{(i)}}{\partial t} = \mathcal{A}^{(i)}\, x^{(i)} + \mathcal{B}^{(i)}\, u^{(i)}\,, \tag{2.1a}$$

$$y^{(i)} = \mathcal{C}^{(i)}\, x^{(i)} + \mathcal{D}^{(i)}\, u^{(i)}\,. \tag{2.1b}$$

The state vector $x^{(i)}(t)$ consists of $N^{(i)}$ state functions defined for $t > 0$ on the system domain $\Omega^{(i)} \subset \mathbb{R}^3$ bounded by the system boundary $\partial\Omega^{(i)}$, so $x^{(i)} : \mathbb{R}_0^+ \times \Omega^{(i)} \to \mathbb{R}^{N^{(i)}}$. The vectors $u^{(i)}(t)$ and $y^{(i)}(t)$ denote input and output to the system, and are respectively defined on the input domain $\Omega_u^{(i)} \subset \mathbb{R}^\infty$ and system domain $\Omega^{(i)} \subset \mathbb{R}^3$. Thus, $u^{(i)} : \mathbb{R}_0^+ \times \Omega_u^{(i)} \to \mathbb{R}^{M^{(i)}}$ and $y^{(i)} : \mathbb{R}_0^+ \times \Omega^{(i)} \to \mathbb{R}^{P^{(i)}}$, with number of inputs and outputs, $M^{(i)}$ and $P^{(i)}$, respectively. The operators $\mathcal{A}^{(i)} : \mathbb{R}^{N^{(i)}} \to \mathbb{R}^{N^{(i)}}$, $\mathcal{B}^{(i)} : \mathbb{R}^{M^{(i)}} \to \mathbb{R}^{N^{(i)}}$, $\mathcal{C}^{(i)} : \mathbb{R}^{N^{(i)}} \to \mathbb{R}^{P^{(i)}}$, and $\mathcal{D}^{(i)} : \mathbb{R}^{M^{(i)}} \to \mathbb{R}^{P^{(i)}}$ are continuous partial differential operators of state, input, output and feedthrough, respectively.

The input $u^{(i)}$ and output $y^{(i)}$ consist of the stacked input and output vectors directly to and from $\mathcal{S}^{(i)}$, as well as to and from $\mathcal{S}^{(i)}$ to each of the other interconnected subsystems,

$$\begin{aligned} u^{(i)} = \Big[&\left(u^{(i)}\right)^T, \left(u^{(1)\to(i)}\right)^T, \left(u^{(2)\to(i)}\right)^T, \cdots, \left(u^{(i-1)\to(i)}\right)^T, \\ &\left(u^{(i+1)\to(i)}\right)^T, \left(u^{(i+2)\to(i)}\right)^T, \cdots, \left(u^{(Z)\to(i)}\right)^T \Big]^T, \end{aligned} \tag{2.2a}$$

$$y^{(i)} = \Big[\left(y^{(i)}\right)^T , \left(y^{(i)\to(1)}\right)^T , \left(y^{(i)\to(2)}\right)^T , \cdots , \left(y^{(i)\to(i-1)}\right)^T , \left(y^{(i)\to(i+1)}\right)^T , \left(y^{(i)\to(i+2)}\right)^T , \cdots , \left(y^{(i)\to(Z)}\right)^T \Big]^T . \tag{2.2b}$$

In this manner, it is ensured that each subsystem can be forced separately, can produce an independent output, and can act upon any other subsystem. Figure 2.1 schematically depicts the different input and outputs to $\mathcal{S}^{(i)}$.

Interconnection of subsystems is acquired by coupling the respective input and outputs. For example, the effect of subsystem $\mathcal{S}^{(q)}$ onto subsystem $\mathcal{S}^{(r)}$ is defined in the r-th model by $u^{(q)\to(r)} = y^{(q)\to(r)} = \mathcal{C}^{(q)\to(r)}\, x^{(q)}$. Feedthrough is neglected in the remainder of this work, $\mathcal{D}^{(i)} = 0$. Stacking all individual state vectors, and combining the dynamics of the individual subsystems and the interconnections, we obtain the governing equations of the full coupled system $\mathcal{S}$,

$$\dot{x} = \mathcal{A}\, x + \mathcal{B}\, u \,, \tag{2.3a}$$

$$y = \mathcal{C}\, x \,, \tag{2.3b}$$

with

$$x = \left[x^{(1)} , x^{(2)} , \ldots , x^{(Z)} \right]^T , \tag{2.4a}$$

$$u = \left[u^{(1)} , u^{(2)} , \ldots , u^{(Z)} \right]^T , \tag{2.4b}$$

$$y = \left[y^{(1)} , y^{(2)} , \ldots , y^{(Z)} \right]^T , \tag{2.4c}$$

and

$$\mathcal{A} = \begin{bmatrix} \mathcal{A}^{(1)} & \mathcal{B}^{(1)\to(2)}\mathcal{C}^{(1)\to(2)} & \cdots & \mathcal{B}^{(1)\to(Z)}\mathcal{C}^{(1)\to(Z)} \\ \mathcal{B}^{(2)\to(1)}\mathcal{C}^{(2)\to(1)} & \mathcal{A}^{(2)} & & \mathcal{B}^{(2)\to(Z)}\mathcal{C}^{(2)\to(Z)} \\ \vdots & & \ddots & \vdots \\ \mathcal{B}^{(Z)\to(1)}\mathcal{C}^{(Z)\to(1)} & & & \mathcal{A}^{(Z)} \end{bmatrix} . \tag{2.5}$$

The state, input and output operators, $\mathcal{A} : \mathbb{R}^N \to \mathbb{R}^N$, $\mathcal{B} : \mathbb{R}^M \to \mathbb{R}^N$ and $\mathcal{C} : \mathbb{R}^N \to \mathbb{R}^P$, govern the dynamics of, the input to and the output from the entire system $\mathcal{S}$ defined on the system volume $\Omega \subset \mathbb{R}^3$. The number of state functions, inputs and outputs are respectively given by N, M and P. The full

system model is hence complete and fully described if and only if the operators $\mathcal{A}$, $\mathcal{B}$ and $\mathcal{C}$ are defined. We call the set $(\mathcal{A},\mathcal{B},\mathcal{C})$ a continuous *model* that describes the dynamical behavior of the physical system $\mathcal{S}$.

The dynamics of the system $\mathcal{S}$ is measurable by a scalar metric, which is defined as the L_2-norm of the output. This so-called *output energy* $\mathcal{E}(t)$: $\mathbb{R}_0^+ \times \mathbb{R}^P \rightarrow \mathbb{R}_0^+$ thus corresponds to a weighted inner state product,

$$\begin{aligned}\mathcal{E} = \|y\|_2^2 &= \int_\Omega y^T y \,\mathrm{d}\Omega \\ &= \int_\Omega x^T \mathcal{C}^T \mathcal{C}\, x \,\mathrm{d}\Omega = \int_\Omega x^T \mathcal{W}\, x \,\mathrm{d}\Omega\,,\end{aligned} \tag{2.6}$$

with energy weighting operator $\mathcal{W} = \mathcal{C}^T\mathcal{C} : \mathbb{R}^N \rightarrow \mathbb{R}^N$. The term output energy does not necessarily allude to a physical energy measure with conservative properties, but merely originates from the fact that it is a square measure of the output y.

Upon discretization or modal expansion, the sets of partial differential state and output equations (2.3) reduce to ordinary differential equations (ODE),

$$\frac{\mathrm{d}\mathbf{x}}{\mathrm{d}t} = \mathbf{A}\mathbf{x} + \mathbf{B}\mathbf{u}\,, \tag{2.7a}$$

$$\mathbf{y} = \mathbf{C}\mathbf{x}\,, \tag{2.7b}$$

with discretized state, input and output vectors $\mathbf{x} \in \mathbb{R}^N$, $\mathbf{u} \in \mathbb{R}^M$, $\mathbf{y} \in \mathbb{R}^P$, respectively, and state, input and output matrices $\mathbf{A} \in \mathbb{R}^{N\times N}$, $\mathbf{B} \in \mathbb{R}^{N\times M}$, and $\mathbf{C} \in \mathbb{R}^{P\times N}$, respectively. M, N and P represent the respective number of discrete inputs, states and outputs. The state space model (SSM) defined by Eqs. (2.7) is graphically shown in Fig. 2.2. General introductions to state space analysis can be found in [54, 67].

In analogy to the output energy $\mathcal{E}$ of the continuous model $(\mathcal{A},\mathcal{B},\mathcal{C})$, the dynamics of the discrete model $(\mathbf{A},\mathbf{B},\mathbf{C})$ is measurable by the scalar output energy $E(t) : \mathbb{R}_0^+ \times \mathbb{R}^P \rightarrow \mathbb{R}_0^+$,

$$\begin{aligned}E = \|\mathbf{y}\|_2^2 &= \mathbf{y}^T\mathbf{y} \\ &= \mathbf{x}^T\mathbf{C}^T\mathbf{C}\mathbf{x} = \mathbf{x}^T\mathbf{W}\mathbf{x}\,,\end{aligned} \tag{2.8}$$

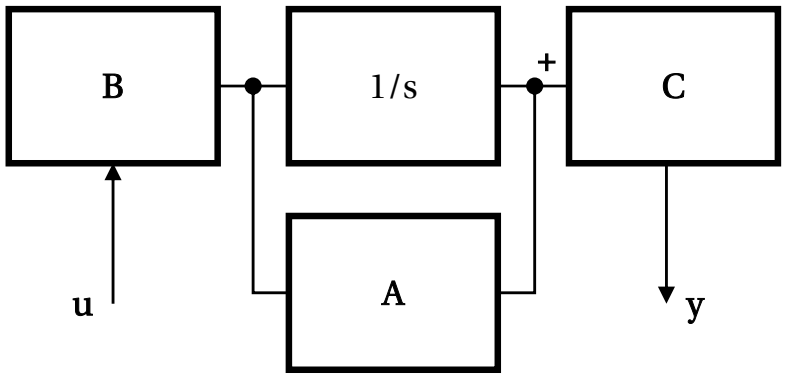

Figure 2.2: Scheme of the SSM $(\mathbf{A},\mathbf{B},\mathbf{C})$ describing $\mathcal{S}$.

with symmetric energy weighting matrix $\mathbf{W} = \mathbf{C}^T\mathbf{C} \in \mathbb{R}^{N\times N}$. As for $\mathcal{E}$, E does not necessarily correspond to a physical energy with conservative properties unless $\mathbf{C}$ (or $\mathbf{W}$) are defined accordingly.

The model definition in terms of $(\mathbf{A},\mathbf{B},\mathbf{C})$ is not unique. Consider a state transformation, $\tilde{\mathbf{x}} = \mathbf{T}^{-1}\mathbf{x}$ with full rank matrix $\mathbf{T} \in \mathbb{R}^{N\times N}$. Substitution into Eqs. (2.7) yields the transformed model,

$$\dot{\tilde{\mathbf{x}}} = \tilde{\mathbf{A}}\tilde{\mathbf{x}} + \tilde{\mathbf{B}}\mathbf{u}\,, \tag{2.9a}$$

$$\mathbf{y} = \tilde{\mathbf{C}}\tilde{\mathbf{x}}\,, \tag{2.9b}$$

where $\tilde{\mathbf{A}} = \mathbf{T}^{-1}\mathbf{A}\mathbf{T}$, $\tilde{\mathbf{B}} = \mathbf{T}^{-1}\mathbf{B}$ and $\tilde{\mathbf{C}} = \mathbf{C}\mathbf{T}$. The relation between input and output is state-transformation invariant. The action of $\mathbf{T}$ amounts to a mere change of basis and must therefore not affect the input and output. If $\mathbf{T}$ is the matrix of eigenvectors $\mathbf{V}$, this projection diagonalizes $\mathbf{A}$.

2.2 Definition of Stability

In the following, we introduce the definitions of stability used throughout the present work. For graphical illustration, see Fig. 2.3.

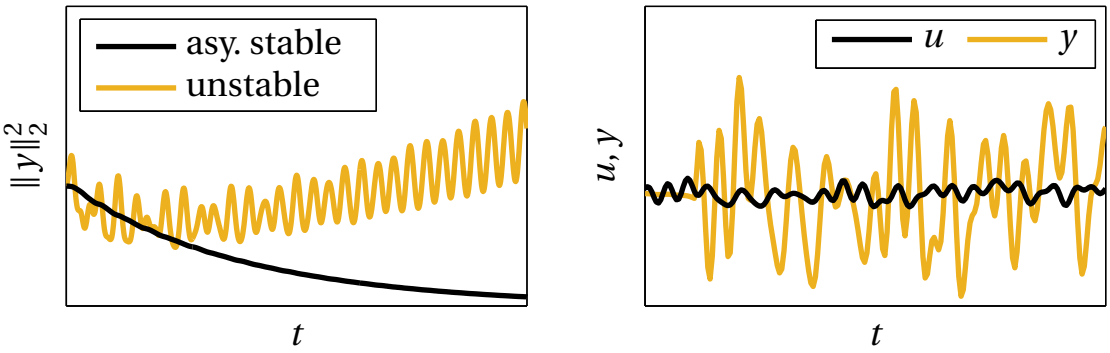

(a) Autonomous system. **(b)** Forced system.

Figure 2.3: Illustration of (a) an asymptotically stable (—) and unstable (—) autonomous system, and (b) a BIBO stable forced system with single input u (—) and single output y (—).

2.2.1 Stability of an Autonomous System

According to the Lyapunov stability approach [88, 102], the equilibrium state $\bar{\mathbf{x}}$ of the autonomous model given in Eqs. (2.7) with $\mathbf{u} = 0$ is

- *stable* if for any $\epsilon > 0$, there exists $\delta = \delta(\epsilon) > 0$ such that $\|\mathbf{x}(t_0) - \bar{\mathbf{x}}\|_2 < \delta \quad \Rightarrow \quad \|\mathbf{x}(t) - \bar{\mathbf{x}}\|_2 < \epsilon \quad \forall\ t \geq t_0$. That is, the system is stable if the L_2-norm of the state remains within a bound ϵ from the equilibrium for any initial difference in L_2-norm bounded by δ.
- *unstable* if it is not stable as defined above.
- *asymptotically stable* if it is stable as defined above and if for any $\epsilon > 0$, there exists $\delta = \delta(\epsilon) > 0$ such that $\|\mathbf{x}(t_0) - \bar{\mathbf{x}}\|_2 < \delta \quad \Rightarrow \quad \lim_{t \to \infty} \|\mathbf{x}(t) - \bar{\mathbf{x}}\|_2 = 0$, i.e., the state asymptotically converges towards the equilibrium.

The above definitions of stability can be restated as follows, known as the second method of Lyapunov [88, 102]: a system is *stable*, if there exists a positive definite function called Lyapunov function, $V(\mathbf{x}) \geq 0 : \mathbb{R}^N \rightarrow \mathbb{R}$, where $V = 0$ only for $\mathbf{x} = 0$, and of which the time derivative is negative semidefinite, $\mathrm{d}/\mathrm{d}t\big(V(\mathbf{x}(t))\big) \leq 0$, and *asymptotically stable* if its time derivative is negative definite, $\mathrm{d}/\mathrm{d}t\big(V(\mathbf{x}(t))\big) < 0$. That is, if a system is (asymptotically) stable, there

must exist a metric that is positive-valued for any $\mathbf{x} \neq 0$ and that (strictly) decreases in time (see Fig. 2.3(a)).

2.2.2 Stability of a Forced System

A forced model as given in Eqs. (2.7) with $\mathbf{u} \neq 0$ is *bounded input bounded output stable* (BIBO stable), if the output to a bounded input signal is also bounded, $\|\mathbf{u}\|_1 < \infty \Rightarrow \|\mathbf{y}\|_1 < \infty$. For a graphical illustration of BIBO stability, see Fig. 2.3(b).

In the past decades, Willems generalized the Lyapunov stability approach to an input-state-output setting in the behavioral framework [180, 181]. A system $\mathcal{S}$ is defined to be *dissipative*, if there exists a non-negative storage $V(\mathbf{x}) : \mathbb{R}^N \rightarrow \mathbb{R}$ and a supply rate $b(\mathbf{u},\mathbf{x},\mathbf{y}) : \mathbb{R}^{M\times N\times P} \rightarrow \mathbb{R}_0^+$, with $\mathbf{u} = 0 \Rightarrow b = 0$, such that

$$V\big(\mathbf{x}(t_2)\big) - V\big(\mathbf{x}(t_1)\big) \leq \int_{t_1}^{t_2} b\big(\mathbf{u}(t),\mathbf{x}(t),\mathbf{y}(t)\big)\,\mathrm{d}t\,. \tag{2.10}$$

This is analog to requiring $V(\mathbf{x})$ to be a positive semidefinite function with $\mathrm{d}/\mathrm{d}t\big(V(\mathbf{x}(t))\big) \leq b(\mathbf{u},\mathbf{x},\mathbf{y})$ (note the difference to autonomous systems for which $\mathrm{d}/\mathrm{d}t\big(V(\mathbf{x}(t))\big) \leq 0$). $\mathcal{S}$ must dissipate more than was supplied to it. If there exists any function $V(\mathbf{x})$ (not strictly positive semidefinite), $\mathcal{S}$ is defined to be *cyclo-dissipative*. The power of the concept of dissipative systems lies in its generality. A storage and supply rate can be found for any system, whether or not it interacts with its surroundings.

2.3 Solutions for the Model Output in Time and Frequency Domain

The present section deals with the output of the model describing $\mathcal{S}$. Section 2.3.1 links the above definitions of stability (see previous Sec. 2.2) to the analytical solutions of the output of linear time-invariant (LTI) systems. The solution in frequency domain is analyzed in Sec. 2.3.2.

2.3.1 Solution in Time Domain

The solution to the output of the SSM defined in Eqs. (2.7) reads

$$\mathbf{y}(t) = \mathbf{C}\, e^{\mathbf{A}t}\mathbf{x}_0 + \int_{t_0}^{t} \mathbf{C}\, e^{\mathbf{A}(t-\tau)}\mathbf{B}\,\mathbf{u}(\tau)\,\mathrm{d}\tau\,, \tag{2.11}$$

with initial condition $\mathbf{x}_0 = \mathbf{x}(t_0)$, and $t_0 = 0$ without loss of generality. The first and second term constitute the free and forced response, respectively, which will be analyzed in the following.

The Free Response

For $\mathbf{u} = 0$, the solution to the output is that of the autonomous system. If the real part of all eigenvalues of $\mathbf{A}$ are strictly located in the left half of the complex plane, $\mathrm{Re}(s_i) < 0\ \forall i \in \{1,2,\ldots,N\}$, the model is asymptotically stable [88], which is equivalent to the definition of asymptotic stability given in Sec. 2.2. This can easily be seen by substituting the eigenvalue decomposition $\mathbf{A} = \mathbf{V}^{-1}\Lambda\mathbf{V}$ into the first term in Eq. (2.11). The linear stability bound is thus found by inspection of the largest growth rate of the eigenvalues s_i, which arise as solutions of the characteristic equation

$$\det\Big[s\mathbf{I} - \mathbf{A}\Big] = 0\,. \tag{2.12}$$

Equation (2.12) is derived by transforming the autonomous part of the state equation (2.7a) into the complex-valued frequency space (see the definition of Laplace transform in Eq. (2.20) below). The spectral variable s thus represents a complex-valued frequency $s = \lambda + j\omega$, where λ and ω denote the growth rate and angular frequency of oscillation, respectively.

The Forced Response

For $\mathbf{x}_0 = 0$, the output $\mathbf{y}$ is given by a convolution integral (the second term in Eq. (2.11)). For an impulsive input of the form $\mathbf{u} = \mathbf{u}_0\,\delta(t)$, with Dirac delta function $\delta(\cdot)$, $\mathbf{y} = \mathbf{H}\,\mathbf{u}_0$ with impulse response matrix $\mathbf{H} : \mathbb{R}^+ \rightarrow \mathbb{R}^{P\times M}$,

$$\mathbf{H}(t) = \mathbf{C}\, e^{\mathbf{A}t}\,\mathbf{B}\,. \tag{2.13}$$

The impulse response matrix $\mathbf{H}$ is a full non-parametric description of a linear time-invariant (LTI) system. Note that $\mathbf{H}$ is a continuous function of time t. The term matrix refers to the discrete numbers of inputs and outputs in input and output space, respectively. The discrete time version of $\mathbf{H}$ is denoted by $\check{\mathbf{H}}$. With knowledge of $\mathbf{H}$, the system's outputs to arbitrary inputs can be computed.

Provided linearity and time-invariance [169], the convolution integral in Eq. (2.11) can be re-written as

$$\mathbf{y}(t) = \int_0^t \mathbf{H}(\tau)\,\mathbf{u}(t-\tau)\,\mathrm{d}\tau\,. \tag{2.14}$$

Equation (2.14) represents a so-called *impulse response model* of the input-output behavior of $\mathcal{S}$. However, any model possesses an impulse response matrix $\mathbf{H}$, independent of the particular model structure. It is thus important to distinguish between impulse response models (which are necessarily of input-output type), and the impulse response as inherent model property.

The impulse response matrix $\mathbf{H}$ gives a clear picture of how the output channels are affected by the different input channels. Every connection of input channel to output channel is given by a separate impulse response (IR) function $h(t) : \mathbb{R}^+ \rightarrow \mathbb{R}$. The impulse response matrix $\mathbf{H}$ thus consists of multiple impulse response functions h_i, where $i \in \{1, 2, \ldots, P \cdot M\}$. The upper time limit t_s for which $h(t \geq t_s) = 0$ corresponds to the settling time of the channel. If t_s is finite[1], h is a so-called finite impulse response (FIR) function [27]. IR functions are the time domain analogy of transfer/frequency response functions (see Sec. 2.3.2). They can be physically interpreted and yield characteristic time scales of response [12, 93, 163]. In the finite case, Eq. (2.14) represents a finite impulse response model.

The definition of BIBO stability given in Sec. 2.2 corresponds to the requirement that every channel of $\mathbf{H}(t)$ is integrable in time [139]. Using the eigenvalue decomposition $\mathbf{A} = \mathbf{V}^{-1}\Lambda\mathbf{V}$, Eq. (2.13) becomes $\mathbf{H}(t) = \mathbf{C}\mathbf{V}^{-1}\exp(\Lambda t)\mathbf{V}\mathbf{B}$. If the real parts of all eigenvalues of $\mathbf{A}$ contained on the diagonal of Λ are located in the left half of the complex plane, $\mathrm{Re}(s_i) \leq 0 \;\forall\, i \in \{1, 2, \ldots, N\}$, with

[1] Strictly speaking, t_s is only finite for discrete time models. In continuous time, Eq. (2.13) asymptotically converges towards zero. However, we speak of FIR models if the response drops below a small threshold $\epsilon > 0$.

rank deficiency of $\mathbf{A}$ equal to the number of algebraic multiplicities and the number of $\mathrm{Re}(s_i) = 0$, the model is BIBO stable [88].

The Coupled Response

In some cases, the input may depend on the state vector, $\mathbf{u} = \phi(\mathbf{x})$, which we refer to as *coupled input*. If $\phi(\mathbf{x})$ is a function of frequency, the relation between $\mathbf{u}$ and $\mathbf{x}$ can be expressed analog to Eq. (2.14) as

$$\mathbf{u} = \int_{t_0}^{t} \breve{\mathbf{H}}(\tau)\,\mathbf{x}(t-\tau)\,\mathrm{d}\tau\,. \tag{2.15}$$

Here, the impulse response matrix of the coupled input $\breve{\mathbf{H}}$ expresses the relation between inputs and states. Substitution of Eq. (2.15) into the state equation (2.7a) of the SSM yields a set of distributed delay differential equations (dDDE),

$$\dot{\mathbf{x}} = \mathbf{A}\mathbf{x} + \mathbf{B}\int_{t_0}^{t} \breve{\mathbf{H}}(\tau)\,\mathbf{x}(t-\tau)\,\mathrm{d}\tau\,. \tag{2.16}$$

As for the autonomous case, linear stability is assessed by inspection of the largest growth rate of the eigenvalues s_i, which arise as solutions of the modified characteristic equation [114, 163]

$$\det\Big[s\mathbf{I} - \mathbf{A} - \mathbf{B}\breve{\mathbf{F}}(s)\Big] = 0\,. \tag{2.17}$$

The above equation is an extension of the classical eigenvalue problem given in Eq. (2.12) by the term $\mathbf{B}\breve{\mathbf{F}}(s)$. This transcendental term causes Eq. (2.17) to have an infinite number of eigenvalues s_i. $\breve{\mathbf{F}}(s)$ corresponds to the transfer matrix of the coupled input (see Sec. 2.3.2 below).

2.3.2 Solution in Frequency Domain

The frequency domain solution to the output of the SSM defined in Eqs. (2.7) reads

$$\mathbf{Y}(s) = \mathbf{C}(s)\left(s\mathbf{I} - \mathbf{A}(s)\right)^{-1}\mathbf{B}(s)\,\mathbf{U}(s) = \mathbf{F}(s)\,\mathbf{U}(s)\,. \tag{2.18}$$

U and **Y** signify the corresponding time domain quantities in frequency domain. $\mathbf{F}(s) : \mathbb{C} \rightarrow \mathbb{C}^{P \times M}$ is the transfer matrix of the model. $\mathbf{F}(s)$ is the frequency domain analogy of the impulse response matrix $\mathbf{H}(t)$ in the time domain. Similar to $\mathbf{H}(t)$, $\mathbf{F}(s)$ is a continuous function of complex-valued frequency s. The term matrix refers to the discrete numbers of inputs and outputs in input and output space, respectively. The frequency-discrete version of **F** is denoted by $\check{F}$. For a single input single output (SISO) model, $P = M = 1$, and $\mathbf{F}(s)$ reduces to a transfer function $F(s) : \mathbb{C} \rightarrow \mathbb{C}$.

If the input is coupled as defined in Eq. (2.15), the solution to the output becomes

$$\mathbf{Y}(s) = \mathbf{C}(s) \left(s\mathbf{I} - \mathbf{A}(s) - \mathbf{B}(s) \check{\mathbf{F}}(s) \right)^{-1} \mathbf{X}(s) = \mathbf{F}(s) \mathbf{X}(s) \,. \tag{2.19}$$

Note the difference between $\check{\mathbf{F}}(s)$ and $\mathbf{F}(s)$, which are the transfer matrices of the coupled input and the full model, respectively. $\check{\mathbf{F}}(s)$ is the frequency domain analogy of the impulse response matrix $\check{\mathbf{H}}(t)$ of the coupled input.

Complex-valued frequency domain quantities are related to time domain quantities by Laplace transform,

$$\mathscr{L}\{\phi(t)\} = \Phi(s) = \int_0^\infty \phi(t)\, e^{-st} \, \mathrm{d}t \,. \tag{2.20}$$

This is why it has been assumed $\mathbf{x}_0 = 0$ in Eqs. (2.18) and (2.19) without loss of generality, as for stable systems the response to any $\mathbf{x}_0 \neq 0$ dies away in the time horizon of $t \rightarrow \infty$. Frequency domain analysis is thus not well-suited for transient analysis.

Real-valued frequency domain quantities are obtained from time domain quantities by one-sided Fourier transform,

$$\mathscr{F}\{\phi(t)\} = \Phi(\omega) = \int_0^\infty \phi(t)\, e^{-j\omega t} \, \mathrm{d}t \,. \tag{2.21}$$

In this case, the transfer matrix $\mathbf{F}(s)$ becomes the frequency response matrix $\mathbf{R}(\omega) : \mathbb{R}^+ \rightarrow \mathbb{C}^{P \times M}$, and for a SISO model the transfer function (TF) becomes the frequency response function (FRF) $R(\omega) : \mathbb{R}^+ \rightarrow \mathbb{C}$. It conveys the input-output behavior of the model as a function of real-valued angular frequencies

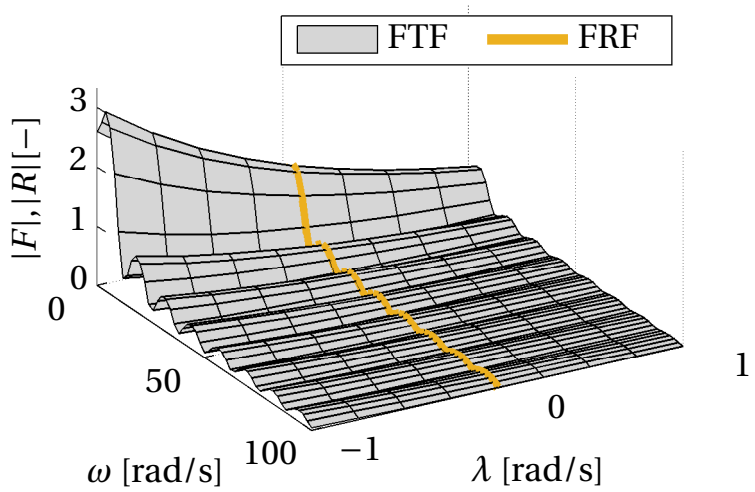

Figure 2.4: Gain of the transfer function $F(s)$ vs. gain of the frequency response function $R(\omega)$ of a SISO model in the complex-valued frequency space $s = \lambda + j\omega$. The FRF $R(\omega)$ corresponds to $F(s)$ at the cutting plane of $\lambda = 0$ (—).

of oscillation ω. This is usually visualized in terms of gain and phase, which gives insight into the physics of the response mechanisms [2, 27, 160].

In contrast to $\mathbf{F}(s)$, $\mathbf{R}(\omega)$ only exists for bounded input bounded output (BIBO) stable systems (see Sec. 2.2.2), as the Fourier transform of the input and output are only defined under these conditions. The FRF $\mathbf{R}(\omega)$ thus characterizes the response behavior in the complex-valued frequency space $s = \lambda + j\omega$ in the cutting plane of zero growth rate $\lambda = 0$ (see Fig. 2.4). Experimental data obtained at distinct harmonic frequencies of oscillation always represents FRF data, as one cannot measure the response to signals that grow or decay in time. To analyze the stability of a system, one must resort to transfer functions, which are defined in the entire complex-valued frequency space with growth rate $\lambda \neq 0$.

It is possible to construct $\mathbf{F}(s)$ from $\mathbf{R}(\omega)$ by arguments of analytic continuation [111, 159]. According to this concept, the gradients of a complex-valued function in both the real and imaginary direction are coupled in the absence of singularities. Hence, if the derivatives of a function with respect to the real direction are known to all orders, it is possible to extrapolate the function into

the imaginary direction and thereby to obtain the exact analytical function in the complex-valued space. If $\mathbf{R}(\omega)$ is thence given as a continuous analytic function, such that all derivatives with respect to ω are known, it is possible to extrapolate $\mathbf{R}(\omega)$ into the complex-valued s-space and thereby to obtain the exact expression for $\mathbf{F}(s)$. If FRF data is identified by an approximate function $\hat{\mathbf{R}}(\omega)$, the extrapolation to $\hat{\mathbf{F}}(s)$ is only valid in a limited region of confidence, which depends on the quality of fit and the frequency response behavior [146].

2.4 Non-Modal Analysis and Optimization

The present section introduces the key concepts related to the study of non-normal transient growth, which stands at the core of the present thesis. The temporal evolution of output energy is analyzed in Sec. 2.4.1. It is shown that transient growth unambiguously results from the formulation of the model describing the system $\mathcal{S}$, which is an important point made in the present work. We also link the concepts of Lyapunov stability introduced in Sec. 2.2 to non-normality. In Sec. 2.4.2, we define the optimization problem required to compute the optimal initial condition leading to maximum optimal non-normal transient growth. This is done for full and semi-norms, so as to retain a maximum degree of flexibility in choosing the output energy E. While the optimization procedure for full norms is well-known from literature, the proposed approach to deal with semi-norm optimization represents a contribution of the present thesis.

2.4.1 Evolution of Output Energy

The temporal variation of the output energy $\mathcal{E}$ of a continuous model $(\mathcal{A},\mathcal{B},\mathcal{C})$ can be expressed by a classical energy balance,

$$\frac{\partial}{\partial t}\mathcal{E} = \int_\Omega \left(\nabla f + s\right)\,\mathrm{d}\Omega + S_{\text{ext}} = \int_{\partial\Omega} f\cdot\mathbf{n}\,\mathrm{d}\Omega + S + S_{\text{ext}}\,, \tag{2.22}$$

with flux and source terms f and s, respectively, and normal vector $\mathbf{n}$. The flux and source terms unambiguously follow from the definition of the model

$(\mathcal{A},\mathcal{B},\mathcal{C})$, and can be derived analytically if the continuous model is available analytically. Depending on the definition of the output given by the output operator $\mathcal{C}$, the dynamics given by the state operator $\mathcal{A}$ shows up in Eq. (2.22) either as part of the output energy $\mathcal{E}$, or as flux or source terms f and S, respectively. The input, which is characterized by the input operator $\mathcal{B}$, is obviously contained in the external source term S_{ext}.

In accordance to the stability concept of dissipative systems given in Sec. 2.2.2, the right-hand side of Eq. (2.22) corresponds to a supply rate b that governs the temporal evolution of a storage function V. Here, the supply rate consists of a net flux $\int_{\partial\Omega} f\cdot\mathbf{n}\,\mathrm{d}\Omega$ over the domain boundaries $\partial\Omega$, a net source S within the domain volume Ω, and a net external source S_{ext}. The energy $\mathcal{E}$ may thus increase and decrease through a positive and negative supply rate, respectively.

We next turn towards the temporal evolution of the output energy E of a discrete model $(\mathbf{A},\mathbf{B},\mathbf{C})$. We thereby exclusively deal with autonomous models for ease of presentation. The discussion can nonetheless be extended to forced models in a straightforward manner. With Eq. (2.8), the temporal evolution of output energy E of an autonomous discrete model $(\mathbf{A},\mathbf{C})$ can be written as

$$\begin{aligned}\frac{\partial}{\partial t}E &= \frac{\partial}{\partial t}\left(\mathbf{y}^T\mathbf{y}\right)\\ &= \dot{\mathbf{x}}^T\mathbf{W}\mathbf{x}+\mathbf{x}^T\mathbf{W}\dot{\mathbf{x}}\\ &= \mathbf{x}^T\left(\mathbf{A}^T\mathbf{W}+\mathbf{W}\mathbf{A}\right)\mathbf{x}\,,\end{aligned} \tag{2.23}$$

with the symmetric energy weighting matrix $\mathbf{W}$ as introduced in Eq. (2.8). As for the continuous case, the flux and source terms driving the evolution of E are clearly fixed by the definition of the model $(\mathbf{A},\mathbf{C})$. If the dissipation matrix

$$\mathbf{Q}=\mathbf{A}^T\mathbf{W}+\mathbf{W}\mathbf{A}\,, \tag{2.24}$$

is positive semidefinite, the energy balance of flux and source terms given in Eq. (2.23) is not strictly negative, and there can be transient growth of output energy. Inspection of the eigenvalue $s_{\max}$ of $\mathbf{Q}$ with largest growth rate $\lambda_{\max}(\mathbf{Q})$ indicates an upper bound on the flux and source terms driving the time evolution of output energy E.

Equation (2.24) is the famous Lyapunov equation [102], which can be solved by numerical means [65, 128]. If the model is linear and asymptotically stable,

there exists a $\mathbf{W}$ such that $\mathbf{Q}$ is negative definite, and therefore E is a Lyapunov function (see Sec. 2.2.1). This $\mathbf{W}$ can be found by solving Eq. (2.24) for an arbitrary negative definite dissipation matrix $\mathbf{Q} < 0$. However, the resulting metric may not be physically meaningful or relevant to the problem (see Sec. 5.1).

It is now possible to relate the concepts of Lyapunov stability to non-normality[2]. An asymptotically stable system is non-normal if the dissipation matrix $\mathbf{Q}$ of the autonomous model ($\mathbf{A}, \mathbf{C} = \mathbf{I}$) is positive definite (with identity matrix $\mathbf{I}$). This is equivalent to stating that a system is non-normal if the L_2-norm of the state vector $\|\mathbf{x}\|_2$ modeling the system is not a Lyapunov function. Provided an asymptotically stable system is non-normal, non-normal transient growth is only observable if the definition of output energy is not a Lyapunov function.

For full output energy norms (i.e., non-singular $\mathbf{C}$), $\lambda_{\max}(\mathbf{Q})$ is very similar to the numerical abscissa [173], which indicates the maximum growth rate of output energy for $t = 0^+$. It is derived from a first-order Taylor series expansion of $\exp(\mathbf{A}t)$ around $t = 0$ [47, 148, 149, 173],

$$\begin{aligned}\max_{E_0} \frac{1}{E_0}\frac{\partial E}{\partial t} &= \max_{E_0} \frac{1}{E_0}\frac{\partial}{\partial t}\left\|\mathbf{C}\left(\mathbf{I}+\mathbf{A}t\right)\mathbf{x}_0\right\|_2^2 + \mathscr{O}(t^2) \\ &\approx s_{\max}\left(\frac{1}{2}\left(\mathbf{A}^T\mathbf{C}^T+\mathbf{C}\mathbf{A}\right)\right). \end{aligned} \tag{2.25}$$

The numerical abscissa is the maximum real part of the numerical range [69], which is the convex output space of an operator. For normal matrices, the numerical range is the hull of the eigenspectrum; for non-normal matrices, it reaches beyond.

2.4.2 Optimization of Output Energy

Despite asymptotic stability and $\|\mathbf{x}_0\|_2$ within the stability radius, the output energy can transiently increase if E is not a Lyapunov function. We define the

[2] Note that non-normality is *not* a stability property, but a characteristic of the linear(ized) system.

relative amplification of output energy of an autonomous model (i.e., $\mathbf{u} = 0$) as

$$\mathcal{G}(t, \mathbf{x}_0) = \frac{E(t)}{E_0} = \frac{\|\mathbf{C}\exp(\mathbf{A}t)\,\mathbf{x}_0\|_2^2}{\|\mathbf{C}\mathbf{x}_0\|_2^2}\,. \tag{2.26}$$

The output energy over time is thus measured with respect to the initial level of output energy at $t = 0$. To study non-normal transient growth, we are interested in finding the maximum $\mathcal{G}$ for all possible initial conditions $\mathbf{x}_0$. Applying such an optimization to Eq. (2.26) is mathematically sound if $\mathbf{C}$ is invertible. In this case, E defines a full norm of which the nullspace (kernel) is the trivial nullvector [52]. However, if $\mathbf{C}$ is singular, E does not include contributions from all states (of all subsystems). It thus defines a semi-norm, of which the kernel extends beyond the trivial nullvector. The optimization problem leading to the maximum of $\mathcal{G}$ is ill-posed if this nullspace is unbounded [52]. In this case, $\mathcal{G}$ can become unlimited, because the contributions from those states (of those subsystems) that are not mirrored in E are not constrained in magnitude within the optimization.

In order to deal with a well-posed optimization problem, it needs to be ensured that the optimization procedure leading to the maximum output energy is performed with respect to a full norm. To this end, we define the *total state energy*

$$E_N(t) = \mathbf{x}^T\mathbf{W}_N\mathbf{x} = \|\mathbf{C}_N\mathbf{x}\|_2^2 = \|\mathbf{y}_N\|_2^2\,, \tag{2.27}$$

with the total state energy weighting matrix $\mathbf{W}_N \in \mathbb{R}^{N\times N}$, the total state output matrix $\mathbf{C}_N \in \mathbb{R}^{N\times N}$ and the total state output vector $\mathbf{y}_N \in \mathbb{R}^N$. The total state energy weighting matrix $\mathbf{W}_N$ is purposefully defined as a positive definite matrix, which is thus also non-singular. The latter is achieved by including identity matrices $\mathbf{I}$ of appropriate sizes in the nullspaces of the output energy weighting matrix $\mathbf{W}$ (if any). These nullspaces can be found by diagonalization of $\mathbf{W}$. The total state output matrix $\mathbf{C}_N$ is subsequently computed as the Cholesky decomposition of $\mathbf{W}_N$, and is therefore invertible (regular) by definition. By construction, the total state energy E_N is thus a full norm.

It is then possible to define the optimization problem leading to the maximum *normalized* output energy amplification as

$$G(t) = \max_{\mathbf{y}_{N,0}} \frac{E(t)}{E_{N,0}}$$

$$
\begin{aligned}
&= \max_{\mathbf{y}_{N,0}} \frac{\|\mathbf{C}\exp(\mathbf{A}t)\,\mathbf{x}_0\|_2^2}{\|\mathbf{y}_{N,0}\|_2^2} \\
&= \max_{\mathbf{y}_{N,0}} \frac{\|\mathbf{C}\exp(\mathbf{A}t)\mathbf{C}_N^{-1}\|_2^2 \cdot \|\mathbf{y}_{N,0}\|_2^2}{\|\mathbf{y}_{N,0}\|_2^2} = \|\mathbf{C}\exp(\mathbf{A}t)\,\mathbf{C}_N^{-1}\|_2^2\,,
\end{aligned}
\tag{2.28}
$$

where the last equality is obtained at optimality $\mathbf{y}_{N,0}^* = (\mathbf{C}_N\mathbf{x}_0)^*$ as a consequence of the definition of the L_2 matrix norm. As defined above, the total state output matrix $\mathbf{C}_N$ is a fixed regular matrix describing a bijective linear map. It is therefore not part of the optimization problem leading to optimality, but merely weights the initial condition $\mathbf{x}_0$ over which the maximization in Eq. (2.28) is performed. The optimal initial condition is thus found by $\mathbf{x}_0^* = \mathbf{C}_N^{-1}\,\mathbf{y}_{N,0}^*$.

In contrast to the relative amplification of output energy $\mathcal{G}$, the maximum normalized amplification of output energy G is a measure of the output energy over time with respect to the initial level of total state energy E_N defined in Eq. (2.27). If $\mathbf{C}$ is invertible (and thus $\mathbf{W}$ does not contain any nullspaces), the total state energy equals the output energy, $E_N = E$, and thus $G = \max_{\mathbf{y}_0}\mathcal{G}$. Otherwise, E_N corresponds to a generic energy norm which is not necessarily a (physically) meaningful energy metric.

The difference between total state and output energy is expressed by the *kernel energy*,

$$
E^\dagger(t) = E_N(t) - E(t) = \mathbf{x}^T\mathbf{W}^\dagger\mathbf{x}\,,
\tag{2.29}
$$

with kernel energy weighting matrix $\mathbf{W}^\dagger = \mathbf{W}_N - \mathbf{W}$. Following Foures *et al.* [52], we define the ratio of kernel to output energy,

$$
\kappa(t) = \frac{E^\dagger(t)}{E(t)}\,, \quad 0 \le \kappa \le \infty\,.
\tag{2.30}
$$

If the output energy E defines a semi-norm, $E^\dagger > 0$, and thus $\kappa > 0$. For $\kappa = 0\ \forall\, t$, the total state energy E_N and the output energy E coincide, and E defines a full norm. The ratio of kernel to output energy κ is not an absolute measure, as it depends on the definition of the total state energy weighting matrix $\mathbf{W}_N$. The exact numeric values of κ are therefore of limited interest. However, κ serves as indication of how much energy is contained in the states (of those subsystems) that are not reflected in the output energy E.

The maximum possible (i.e., optimal) amplification of normalized output energy $G_{\max} = \max_t G(t)$ occurs at $t = t^*$, which is the time at optimality. Transient growth is possible if $G_{\max} > 1$. The optimal initial condition $\mathbf{x}_0^*$ (OIC) can be found from the singular value decomposition (SVD) of $\mathbf{C}\exp(\mathbf{A}t^*)\,\mathbf{C}_N^{-1} = \mathbf{DSP}^H$. $\mathbf{D} \in \mathbb{R}^{P\times P}$ and $\mathbf{P} \in \mathbb{R}^{N\times N}$ are unitary matrices of left- and right-singular vectors, respectively, and $\mathbf{S} \in \mathbb{R}^{P\times N}$ represents a diagonal matrix of singular values. The OIC $\mathbf{x}_0^*$ is the first right-singular vector multiplied by $\mathbf{C}_N^{-1}$ (see the discussion following Eq. (2.28)), which signifies the most amplified mode at $t = t^*$ by the action of $\mathbf{C}\exp(\mathbf{A}t)\,\mathbf{C}_N^{-1}$. The total state output vector at optimality $\mathbf{y}_N^*$ is given by the first left-singular vector. The optimal normalized energy growth $G_{\max}$ corresponds to the square of the first singular value on the diagonal of $\mathbf{S}$. The short-term dynamics of the output energy is thus not governed by the eigenvalues of $\mathbf{A}$, but by the singular values of $\mathbf{C}\exp(\mathbf{A}t)\,\mathbf{C}_N^{-1}$ [148].

In principle, the absolute values of the maximum normalized energy $G(t)$ and optimal energy growth $G_{\max}$ are state-transformation invariant, because they are a measure related to the output, which, in turn, does not depend on the definition of $\mathbf{x}$. The transformed maximum normalized energy growth $\tilde{G}$ of the state-transformed SSM defined in Eqs. (2.9) reads

$$\begin{aligned}\tilde{G}(t) &= \|\tilde{\mathbf{C}}\exp(\tilde{\mathbf{A}}t)\,\tilde{\mathbf{C}}_N^{-1}\|_2^2 \\ &= \|\mathbf{CTT}^{-1}\exp(\mathbf{A}t)\,\mathbf{TT}^{-1}\,\mathbf{C}_N^{-1}\|_2^2 = G(t)\,. \end{aligned} \tag{2.31}$$

The state-transformation invariance of G refutes the argument that non-normal transient growth follows from a wrong choice of basis space and can be eliminated by diagonalization of $\mathbf{A}$, in which case, $\tilde{\mathbf{A}} = \Lambda$, $\mathbf{T} = \mathbf{V}$, and $\tilde{\mathbf{C}} = \mathbf{CV}$.

However, the state-transformation invariance of G and $G_{\max}$ is only given if there exists a non-singular transformation matrix $\mathbf{T}$ linking two models of the same system. This condition is rarely met in practice, so the technical relevance of G being state-transformation invariant is limited. G and $G_{\max}$ hence serve as an indication for the occurrence of non-normal transient growth. While the order of magnitude is important, they should not be interpreted as absolute measure.

Using SVD, the procedure to find the OIC is computationally simple and fast. However, if the output energy E defines a semi-norm, the resulting optimal

normalized energy amplification given by $G_{\max}$ may not correspond to the maximum possible relative amplification of output energy $\mathcal{G}_{\max}$. This is because the optimization leading to $G_{\max}$ yields an optimal initial ratio of kernel to output energy κ_0^*, for which the *normalized* output energy is maximized. However, the optimization is not performed with respect to the optimal κ_0^* that would maximize the *relative* amplification of output energy $\mathcal{G}$. As highlighted in [52], this "true" maximization of relative amplification of output energy requires κ to be taken into account as additional optimization parameter. This can only be done using variational methods, such as constrained optimization with Lagrangian multipliers (Lagrangian optimization). Variational methods are very flexible and powerful (for example, one can optimize for an infinite number of constraints or cost functions), at the cost of increased complexity and effort in computation and implementation. A comprehensive review on optimization and control for flow systems is given by Kim & Bewley [90].

In the following, we propose an approach to avoid the above mentioned issues related to semi-norm optimization while still resorting to SVD. To this aim, it is necessary to extend the above concept of energy maximization to include forcing. In analogy to the relative amplification of output energy of an autonomous model $\mathcal{G}$, and using Eq. (2.11), we define the *relative* amplification of output energy of a forced model as

$$\mathcal{H}(t,\mathbf{x}_0,\mathbf{u}) = \frac{E(t)}{E_0} = \frac{\left\| \mathbf{C}\left(\exp(\mathbf{A}t)\,\mathbf{x}_0 + \int_0^t \exp\big(\mathbf{A}(t-\tau)\big)\,\mathbf{B}\,\mathbf{u}\,\mathrm{d}\tau\right)\right\|_2^2}{\left\| \mathbf{C}\left(\mathbf{x}_0 + \int_0^t \mathbf{u}\,\mathrm{d}\tau\right)\right\|_2^2}\,. \tag{2.32}$$

The definition of $\mathcal{H}$ represents a maximization problem that includes a penalization of the energy needed to produce the forcing action. As for $\mathcal{G}$, the maximization problem to find the maximum $\mathcal{H}$ is ill-posed if $\mathbf{C}$ is singular. We therefore define the maximum *normalized* output energy amplification of a

forced model as

$$H(t) = \max_{\mathbf{y}_{N,0}} \frac{E(t)}{E_{N,0}} = \max_{\mathbf{y}_{N,0}} \frac{\left\| \mathbf{C} \left(\exp(\mathbf{A}t)\,\mathbf{x}_0 + \int_0^t \exp\big(\mathbf{A}(t-\tau)\big)\,\mathbf{B}\,\mathbf{u}\,\mathrm{d}\tau \right) \right\|_2^2}{\left\| \mathbf{y}_{N,0} \right\|_2^2}, \tag{2.33}$$

where $\mathbf{y}_{N,0} = \mathbf{C}_N(\mathbf{x}_0 + \int_0^t \exp(\mathbf{A}(t-\tau))\,\mathbf{u}\,\mathrm{d}\tau)$. Depending on the applied input $\mathbf{u}$, solution of Eq. (2.33) may present a significant challenge.

An autonomous system can be represented as a forced system that is initially at rest and forced impulsively at $t = 0$ (i.e., $\mathbf{x}_0 = 0$ and $\mathbf{u} = \mathbf{u}_0\,\delta(t)$). The role of the initial condition $\mathbf{x}(0) = \mathbf{x}_0$ is then taken by $\mathbf{x}(0) = \mathbf{B}\,\mathbf{u}_0$, with input matrix $\mathbf{B}$ as introduced in Sec. 2.1. We define $\mathbf{B} \in \mathbb{R}^{N\times N}$ as diagonal matrix with $\|\mathbf{B}\|_2 = 1$, such that it is ensured that $\mathbf{x}(0)$ is representable, i.e., that $\mathbf{x}(0) \in \mathrm{span}(\mathbf{B})$. Substituting $\mathbf{x}_0 = 0$ and $\mathbf{u} = \mathbf{u}_0\,\delta(t)$ in Eq. (2.33), the initial total output vector becomes $\mathbf{y}_{N,0} = \mathbf{C}_N\,\mathbf{u}_0$, and Eq. (2.33) reduces to

$$\begin{aligned} H(t) &= \max_{\mathbf{y}_{N,0}} \frac{E(t)}{E_{N,0}} \\ &= \max_{\mathbf{y}_{N,0}} \frac{\left\| \mathbf{C}\exp(\mathbf{A}t)\,\mathbf{B}\,\mathbf{u}_0 \right\|_2^2}{\left\| \mathbf{y}_{N,0} \right\|_2^2} \\ &= \max_{\mathbf{y}_{N,0}} \frac{\left\| \mathbf{C}\exp(\mathbf{A}t)\,\mathbf{B}\,\mathbf{C}_N^{-1} \right\|_2^2 \cdot \left\| \mathbf{y}_{N,0} \right\|_2^2}{\left\| \mathbf{y}_{N,0} \right\|_2^2} = \left\| \underbrace{\mathbf{C}\exp(\mathbf{A}t)\,\mathbf{B}}_{\mathbf{H}(t)}\,\mathbf{C}_N^{-1} \right\|_2^2, \end{aligned} \tag{2.34}$$

where the last equality is obtained at optimality $\mathbf{y}_{N,0}^* = (\mathbf{C}_N\,\mathbf{u}_0)^*$ as a consequence of the definition of the L_2 matrix norm. As for the autonomous case, the total state output matrix $\mathbf{C}_N$ is not part of the optimization leading to optimality. The optimal initial forcing can thus be found by $\mathbf{u}_0^* = \mathbf{C}_N^{-1}\,\mathbf{y}_{N,0}^*$, and therefore $\mathbf{x}^*(0) = \mathbf{B}\,\mathbf{u}_0^* = \mathbf{B}\,\mathbf{C}_N^{-1}\,\mathbf{y}_{N,0}^*$. As for G, the optimal $H_{\max} = \max_t H(t)$ occurs at $t = t^*$. The optimal initial distribution $\mathbf{u}_0^*$ can be found from the SVD of $\mathbf{C}\exp(\mathbf{A}t^*)\,\mathbf{B}\,\mathbf{C}_N^{-1}$, where $\mathbf{u}_0^*$ corresponds to the first right-singular vector premultiplied by $\mathbf{C}_N^{-1}$.

In analogy to the definition of G in Eq. (2.28), H in Eq. (2.34) also describes an optimization problem of *normalized* output energy for autonomous systems.

However, the important advantage of H over G lies in the fact that it can be effectively used to compute the optimal *relative* amplification of energy $\mathcal{G}$ using SVD even if the output energy E defines a semi-norm. The procedure to find $\mathcal{G}_{\max}$ via optimization of H is explained in the following.

The definition of $\mathbf{B}$ as detailed above Eq. (2.34) allows to control the impact of the states of different subsystems onto the initial condition $\mathbf{x}(0) = \mathbf{B}\mathbf{u}_0$. This is done by varying the magnitude of the diagonal submatrices in $\mathbf{B}$ that relate to each subsystem. We thereby implicitly weight the contribution of each subsystem onto the initial levels of output and kernel energy, E_0 and $E_0^\dagger$, respectively (see Eq. (2.29)).

Consider as example a system consisting of two subsystems. The definition of

$$\mathbf{B} = \begin{bmatrix} k_1\mathbf{I} & \mathbf{0} \\ \mathbf{0} & k_2\mathbf{I} \end{bmatrix}, \quad \text{and} \quad \mathbf{C} = \begin{bmatrix} \mathbf{C}_1 & \mathbf{0} \\ \mathbf{0} & \mathbf{0} \end{bmatrix},$$

will lead to zero initial kernel energy $E_0^\dagger = 0$ for $k_1 = 1$ and $k_2 = 0$, and to zero initial output energy $E_0 = 0$ for $k_1 = 0$ and $k_2 = 1$. According to Eq. (2.30), the latter two limiting cases correspond to an initial ratio of kernel to output energy $\kappa_0 = 0$ and $\kappa_0 = \infty$, respectively. In the special case of $k_1 = k_2 = 1$, H is equivalent to G, and applying SVD to Eq. (2.34) yields the OIC $\mathbf{x}^*(0) = \mathbf{u}_0^*$, as well as the corresponding optimal initial ratio of kernel to output energy κ_0^* for which the normalized output energy is maximized.

The definition of H opens an interesting perspective on the study of non-normality. Analyzing the potential of a system to exhibit non-normal transient growth can be interpreted as analyzing the L_2-norm of the impulse response matrix of the system $\mathbf{H}$ scaled by $\mathbf{C}_N^{-1}$. In principle, and subject to the aforementioned practical limitations related to the absolute values of G, H is also state-transformation invariant.

In summary, variation of $\mathbf{B}$ amounts to optimizing for the maximum amplification of output energy as a function of the constrained kernel space. It is thus possible to compute $H_{\max}$ and the optimal evolution of output energy $E^*(t)$ over the entire range of κ_0. From there, it is straightforward to compute the corresponding maximum *relative* amplification of output energy $\mathcal{G}_{\max} = E^*(t = t^*)/E_0$. Although this approach requires multiple optimization

runs, it is easy to implement and for low-order models represents a computationally inexpensive alternative to variational methods.

2.5 Chapter Summary

The present chapter can be summarized as follows:

- A full coupled multi-physics system $\mathcal{S}$ consisting of Z interconnected subsystems is formulated in a systems engineering framework. Specification of the set of continuous partial differential operators $(\mathcal{A},\mathcal{B},\mathcal{C})$ defines a model that describes $\mathcal{S}$. The discrete counterpart is given by the discrete model defined by the set of matrices $(\mathbf{A},\mathbf{B},\mathbf{C})$.
- Stability is defined for autonomous and forced systems, and basic non-normal theory is laid out in the context of a systemic approach.
- Optimization approaches to maximize the output energy using SVD are presented for full and semi-norms.

3 The Heat Source Subsystem

The present chapter deals with the heat source, which represents the core element of a thermoacoustic system. In the context of a systemic approach, the aim is to formulate the heat source as a subsystem that can be inserted as generic block into the full thermoacoustic system $\mathcal{S}^{(T)}$ (see the schematic in Fig. 1.8). It is labeled as *heat source subsystem* $\mathcal{S}^{(F)}$.

In most practical applications, the heat source is given by a flame. Combustion dynamics is complex and presents a major field of research [22, 99, 120, 182]. Any attempt to resolve the detailed transport and chemical processes occurring in a combusting medium leads to a model with a large number of degrees of freedom. To study non-normal transient growth in thermoacoustics, the dominant combustion dynamics therefore needs to be condensed and incorporated into a low-order model. Due to their industrial relevance and low emission properties [95], we shall focus our analysis on premixed flames, although the systemic approach of modeling a heat source subsystem is, in principle, applicable to any other kind of heat source.

The structure of the chapter is schematically depicted in Fig. 3.1, and is organized as follows. In Sec. 3.1, we derive a nonlinear analytical low-order model describing the dynamics of laminar premixed flames, including the flame response to fluctuations in velocity and fuel mixture. The full model is referred to as *G-equation flame*. Section 3.2 deals with systems representations of the heat source subsystem $\mathcal{S}^{(F)}$: The G-equation flame is cast into a nonlinear state space form in Sec. 3.2.1, whereas Sec. 3.2.2 introduces a generic filter-based state space representation that is valid for any linear time-invariant (LTI) system. For the latter, the system dynamics is entirely given by an IR function. Different approaches to obtain such IR functions characterizing the linear dynamics of heat sources are presented in Sec. 3.3: In Sec. 3.3.1, we analytically derive the IR function of the linearized G-equation flame under fully

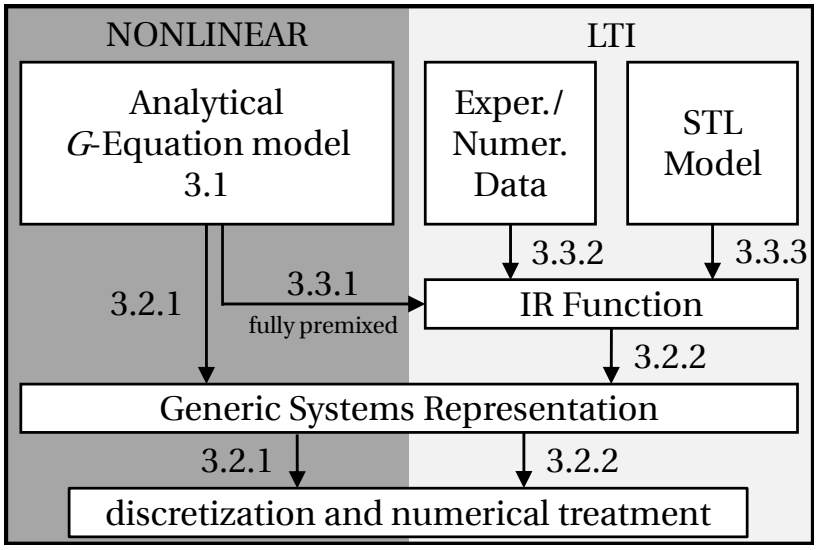

Figure 3.1: Overview of the structure of Chap. 3. The section numbers indicate which parts of the chapter cover the different topics.

premixed conditions (referred to as *linearized G-equation flame*). Sections 3.3.2 and 3.3.3 deal with IR functions stemming from experimental or numerical data, and from single time lag models (STL), respectively.

In contrast to common non-dimensionalized notation (for example, [12, 154, 163]), the heat source subsystem is treated in dimensional form throughout the present work. In the author's opinion, omitting non-dimensionalization, and especially normalization, is found to enhance consistency in presentation and to facilitate interpretation of results.

3.1 An Analytical Model of Laminar Premixed Flames

In the present section, we derive a nonlinear analytical model describing the response dynamics of laminar premixed flames to velocity and fuel mixture perturbations, a so-called *G*-equation flame. The model is motivated in Sec. 3.1.1, before deriving the equations of flame motion in Sec. 3.1.2. The equations governing the heat release rate of the flame are derived and linearized in Secs. 3.1.3 and 3.1.4, respectively.

3.1.1 Mechanisms of Heat Release

When perturbed, premixed flames produce changes in heat release rate $\dot{q}$, which in turn affect the acoustic field. Perturbations in $\dot{q}$ result from mixture inhomogeneities (fluctuations in equivalence ratio ϕ), and from fluctuations in the surrounding velocity and pressure fields, v and p, respectively. However, the sensitivity of premixed flames to pressure changes is small. This is especially true if the flame length is small compared to the wavelength of the perturbations (i.e., flame compactness). Changes in ϕ modify the burning velocity S_L at which the flame consumes the unburnt gaseous mixture, the heat of reaction q_R, and the flame surface area A. The velocity v modifies the balance between flame propagation and convection, thereby leading to flame displacement and wrinkling of the flame surface, and thus modifying A. Strong flame wrinkling and straining also leads to stretch and curvature effects that in turn modify S_L and affect the wrinkle structure. Confinement effects may also play a role [32]. An extensive review on premixed flame–acoustic interaction can be found in [98].

For laminar premixed flames in the absence of high-frequency velocity perturbations, strain, stretch and curvature effects are negligible [175], and setting aside confinement effects, the coarse-grained dynamics of $\dot{q}$ is governed by changes in S_L, q_R and A. An increase in S_L means higher specific fuel consumption, and an increase in q_R leads to more available heat per unit mass of gaseous fuel. Changes in A vary the amount of area that is able to release heat. All three effects thus directly modify $\dot{q}$.

The mechanism of flame wrinkling through velocity perturbations occurs directly (i.e., the flame moves subject to an increase in v), but much stronger so by an indirect effect. In this case, the perturbation in v is transformed to a perturbation in A at the flame base, which then convects downstream through the flame at convective velocity w. The effect of this transfer mechanism is observed in experiments [9, 18, 167] and captured in models [32, 138, 154]. However, the detailed physical mechanisms behind this acoustic-convective (mode) transfer are yet a matter of debate. One of the likely causes may be vorticity generation at the flame holder.

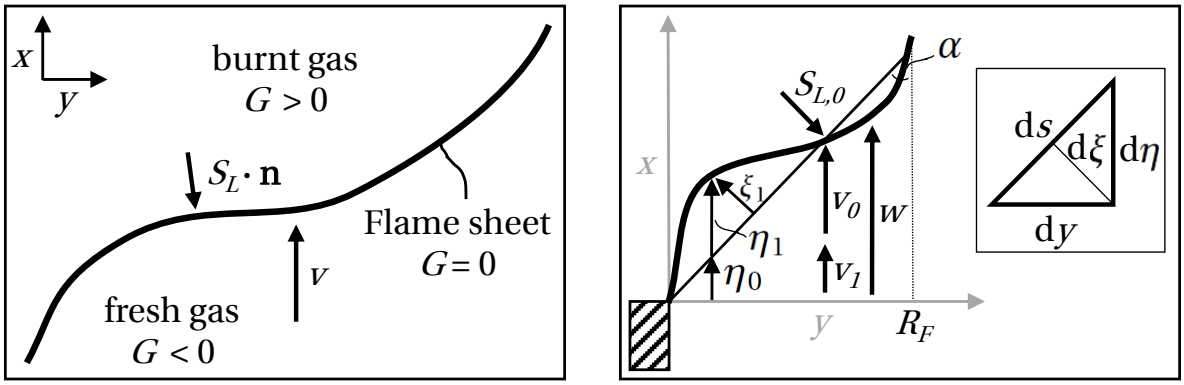

(a) Velocity components. **(b)** Mean and perturbed flame sheet.

Figure 3.2: G-equation model of a premixed flame: (a) The velocity components governing the position of the flame sheet at $G = 0$, which separates fresh fuel ($G < 0$) from burnt products ($G > 0$). (b) The mean and perturbed flame sheet and forcing velocity components. The full flame is obtained by rotation around $y = 0$ (wedge) or $y = R_F$ (conical).

In the following, an analytical model is derived that condenses the coarse-grained dynamics of laminar premixed flames into changes in S_L, q_R and A. Detailed chemistry and higher-order effects are not incorporated, which allows for a low-order model representation.

3.1.2 Flame Motion

A straightforward approach to modeling the flame dynamics is to treat the flame surface as a level-set function, known as the G-equation framework [87, 110]. The complex combustion processes occurring in a flame are lumped into an infinitesimally thin reacting flame sheet in which fresh gas is instantaneously transformed to burnt products. The state of the gas (fresh/burnt) is tracked by a scalar field G. We define the flame sheet to be located at the (in principle arbitrary) level-set value of $G = 0$, which separates fresh gas upstream ($G < 0$) from burnt gas downstream ($G > 0$), as depicted in Fig. 3.2(a). The material derivative of the scalar field $G(x, y, t)$ must remain constant over

time,

$$\frac{\mathrm{D}G}{\mathrm{D}t} = 0 \quad \Leftrightarrow \quad \frac{\partial G}{\partial t} + \mathbf{v}_{eff} \cdot \nabla G = 0 \,, \tag{3.1}$$

where $\mathbf{v}_{eff} = \mathbf{v} - S_L \mathbf{n}$ is the effective velocity acting on $G = 0$ and results from the balance of transport of fresh gas at rate $\mathbf{v}$ and burning velocity normal to the flame sheet $S_L \mathbf{n}$ (see Fig. 3.2(a)). With $\mathbf{n} = \nabla G / |\nabla G|$, Eq. (3.1) is rewritten as

$$\frac{\partial G}{\partial t} + \mathbf{v} \cdot \nabla G = S_L |\nabla G| \,. \tag{3.2}$$

In the present study, transport of fresh gas is strictly confined to the x-direction, $\mathbf{v} = [\, v \;,\; 0 \,]^T$. Also, the position of the flame sheet at $G = 0$ is expressed in terms of a flame displacement function η that only depends on the radial spatial component y, $G(x, y, t) = x - \eta(y, t) = 0$ (see Fig. 3.2(b)). With these two assumptions, the equation governing the flame sheet motion becomes

$$\frac{\partial \eta}{\partial t} + v = S_L \sqrt{1 + \left(\frac{\partial \eta}{\partial y} \right)^2} \,. \tag{3.3}$$

Unlike studies using the 2-D G-equation framework [66, 82, 153], such a nonlinear 1-D formulation cannot capture flame sheet overlap in the y-direction, which requires a parametric description of the flame surface in two dimensions. Phenomena such as cusp formation can therefore be identified as to the occurring locations, but the analysis breaks down as soon as the cusps form. It is nonetheless a widely used model and has been extensively studied in the literature [19, 34, 36, 49, 97, 98, 138, 154]. Although of low order, it has been shown to be a very good representation of real laminar premixed flames, both under linear[1] and nonlinear conditions. The G-equation framework is therefore well-suited for the purpose of the present study, which relies on an accurate low-order flame model in the linear[1] and nonlinear regime. Graphical comparisons exhibiting good agreement between flame shapes of laminar premixed conical flames determined from experiments and from a G-equation model are shown in Fig. 3 of [153].

Concerning the boundary conditions, the G-equation flame is able to swim upstream (flame flashback) provided the perturbed velocity field is sufficiently

[1] The linear framework of the G-equation flame is obtained by linearization as shown in Sec. 3.1.4.

strong in the negative x-direction. In this case, we prescribe a zero-gradient boundary condition at the flame base. The flame re-attaches when it again reaches the flame holder. This boundary condition was proposed and investigated in the G-equation framework by Dowling [34]. In the linear regime (i.e., for small perturbations), the linearized G-equation flame is assumed to remain attached to the flame holder at all times, $\eta_0(x=0) = \eta_1(x=0) = 0$.

3.1.3 Heat Release Rate

As mentioned in the introduction of this chapter, the heat release rate $\dot{q}$ is assumed a mere function of the mean density of the unburnt premixed fuel ρ_0, flame speed S_L, heat of reaction q_R and flame surface area A,

$$\mathrm{d}\dot{q} = \rho_0 \, S_L \, q_R \, \mathrm{d}A \,. \tag{3.4}$$

S_L and q_R are both functions of equivalence ratio ϕ. In the present study, we employ a methane-air premixture model developed by You *et al.* [183]. The corresponding graphs are shown in Fig. 3.3. It can be seen that for lean flames ($\phi < 1$), S_L and q_R are monotonically increasing functions of ϕ. It is also visible that the slope of q_R is steeper for lean than for rich flames. Slight perturbations in ϕ thus lead to large variations in $\dot{q}$ for lean flames, which may couple back to the acoustic field. This is one of the reasons why the lean regime is more susceptible to thermoacoustic instability with respect to mixture inhomogeneities than the rich regime.

For axisymmetric flames, the flame surface area A is computed by revolving a weighted infinitesimal portion of flame length $\mathrm{d}l$ around the axis of rotation, which is located at $y = 0$ (wedge flame) or $y = R_F$ (conical flame), with flame radius R_F (see Fig. 3.2(b)),

$$\mathrm{d}A = \int_0^{2\pi} k(y) \, \mathrm{d}\varphi \, \mathrm{d}l \,. \tag{3.5}$$

The weighting function $k(y)$ is a geometrical factor, which takes the form $k = y$ or $k = R_F - y$ for wedge or conical flames, respectively. The infinitesimal portion of flame length $\mathrm{d}l = \mathrm{d}y \sqrt{1 + (\partial\eta/\partial y)^2}$ can be expressed in terms of

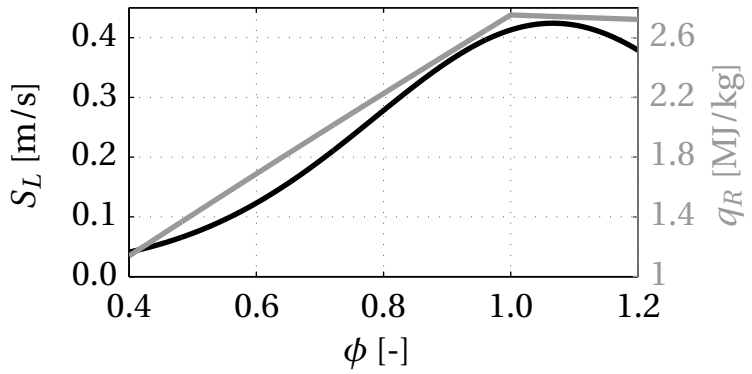

Figure 3.3: S_L and q_R as a function of fuel-to-air ratio ϕ for a methane-air premixture model by [183].

changes in flame displacement η, so that the overall heat release rate finally becomes

$$\dot{q} = 2\pi\,\rho_0 \int_0^{R_F} S_L\, q_R\, k(y) \sqrt{1+\left(\frac{\partial \eta}{\partial y}\right)^2}\,\mathrm{d}y\,. \tag{3.6}$$

3.1.4 Orders of Flame Dynamics

In the following, we investigate the mean and linearized expressions of the flame sheet and heat release rate dynamics given in Eqs. (3.3) and (3.6), respectively. To this aim, all relevant quantities are expanded in terms of powers of a small variable ϵ,

$$\phi = \sum_{i=0}^{\infty} \epsilon^i\, \phi_i \tag{3.7a}$$

$$= \epsilon^0\, \phi_0 + \epsilon^1\, \phi_1 + \mathscr{O}(\epsilon^2)\,, \tag{3.7b}$$

where index i expresses the i-th order field of quantity ϕ. $i = 0$ and $i = 1$ correspond to the mean field and first-order (linearized) perturbations to the mean field, respectively. It is assumed that the fields at every order of ϵ are of order 1, such that the solution converges to the mean field for $\epsilon \to 0$. This therefore also holds true for all partial derivatives of the respective fields.

The variables η, v, S_L, q_R and $\dot{q}$ are expanded to first order according to (3.7b), and substituted into the square of Eq. (3.3) and into the square of the differ-

ential version of Eq. (3.6). Grouping in orders of ϵ yields the solutions of the mean and linearized fields.

Mean Fields $\mathcal{O}(\epsilon^0)$

$$\frac{\partial \eta_0}{\partial t} = 0\,, \tag{3.8a}$$

$$\dot{q}_0 = \pi R_F^2 \rho_0 \, v_0 \, q_{R,0}\,. \tag{3.8b}$$

In the absence of perturbations, the flame speed balances the supply rate of fresh gas normal to the flame front, $S_{L,0} = v_0 \sin\alpha$. The mean flame position is thus stationary (see Eq. (3.8a)) and given by $\partial\eta_0/\partial y = const. = \arctan\alpha$. The mean flame shape is hence fully described by flame angle α (see Fig. 3.2(b)). Steeper flames are obtained by increasing the mean flow velocity v_0, or by decreasing S_L via ϕ. According to Eq. (3.8b), the mean heat release rate $\dot{q}_0$ is simply given as the mass flow of fresh premixed fuel through the circular base area of the flame times the heat of reaction.

Linearized Fields $\mathcal{O}(\epsilon^1)$

$$\frac{\partial \eta_1}{\partial t} = -v_0 \sin\alpha \cos\alpha \frac{\partial \eta_1}{\partial y} + v_1 - \frac{S_{L,1}}{\sin\alpha}\,, \tag{3.9a}$$

$$\dot{q}_1 = 2\pi \rho_0 \int_0^{R_F} k \left[v_0 \, q_{R,0} \sin\alpha \cos\alpha \frac{\partial \eta_1}{\partial y} + v_0 \, q_{R,1} + q_{R,0} \frac{S_{L,1}}{\sin\alpha} \right] \mathrm{d}y\,. \tag{3.9b}$$

The linearized flame motion given in Eq. (3.9a) represents an advection equation, where wrinkles induced by perturbations in v and $-S_L/\sin\alpha$ (i.e., both in positive x-direction) are convected along the length of the flame in y-direction at a rate of $v_{r,\perp} = v_0 \sin\alpha\cos\alpha$. This corresponds to $v_{r,\parallel} = v_0\cos\alpha$ along the flame front. The time it takes for wrinkles to advect from the base to the tip of the flame is termed *restorative* time scale $\tau_r = R_F/v_{r,\perp}$ in [12]. We will return to this point in Sec. 3.3.1.

As mentioned in Sec. 3.1.1, the forcing of η_1 by v_1 is a convective process. Flow perturbations generated by acoustics at the flame base are convected along

the length of the flame in the direction of the mean flow at convective velocity w,

$$\frac{\partial v_1}{\partial t} = -w\frac{\partial v_1}{\partial x} + v_1^B\,, \tag{3.10}$$

with the acoustic velocity at the flame base $v_1^B = v_1(x=0)$. The time it takes for perturbations to advect from the base to the tip of the flame is termed *convective* time scale $\tau_c = R_F/(w\tan\alpha)$ in [12] (see Sec. 3.3.1). The dynamics of $S_{L,1}$ is also governed by a forced advection equation of the form of Eq. (3.10), but substituting v_1 by $S_{L,1}$, and the convective velocity w by the mean flow velocity v_0. This is because mixture inhomogeneities are advected downstream with the mean flow.

The convective velocity w is determined by the physics of the specific problem of interest. Due to the variability of w, we treat the ratio of convective to mean flow velocity,

$$\mu = \frac{w}{v_0}\,, \tag{3.11}$$

as a free model parameter throughout the present work. It is observed that $\mu \sim \mathcal{O}(1)$ at low frequencies [18, 167]. At higher frequencies, μ may be much larger than one. Presumably, these fast waves emanate from aeroacoustic effects and are similar to those observed in free jets [9]. Kashinath *et al.* [83] confirm the frequency-dependency of μ. They also find that μ is critical for the variety of limit cycles that a coupled thermoacoustic system can reach. It is determined that subcritical bifurcation of a thermoacoustic system is only possible for $\mu < 1$, i.e., for $w < v_0$ [84].

The limiting case of $\mu \to \infty$ expresses a *uniform* velocity model [12, 154], where perturbations are homogeneously and instantaneously distributed in space. This velocity model is often used in the context of low-frequency acoustics, where the acoustic wave length is much larger than the flame length. However, the uniform velocity model does not capture the convective nature of flame response, and will not be treated in the present study. In real setups, it is nonetheless possible that premixed flames respond to both convective and uniform velocity perturbations in parallel. To represent this case, one would need to superimpose the response models of premixed flames subject to both types of forcing, which can be done in a straightforward manner. The convec-

tive response model is analytically derived in Sec. 3.3.1. The uniform model subsequently follows by substituting $\mu \rightarrow \infty$. A more detailed treatment of the response characteristics of premixed flames to uniform velocity models in the time domain can be found in [12].

There are various studies employing the G-equation framework which describe the flame motion in a flame-based reference in terms of flame displacement ξ_1, as indicated in Fig. 3.2(b) (see, for example, [1, 12, 19, 154]). In a linearized framework, the perturbations are small by definition (of the order of ϵ). In this case, it is valid to substitute $\eta_1 = \xi_1 \sin\alpha$ into the governing Eqs. (3.9). Subsequently rotating y to join the tilted flame axis leads to the same expressions as used in the above cited articles. In the linear regime, both representations are hence equal and do not possess any particular merits with respect to one another. However, the straightforward substitution of ξ for η is not possible for large perturbations, in which case Eqs. (3.3) and (3.6) need to be used. Large perturbations at the flame tip cannot be captured in the flame-based reference system, as ξ always extends orthogonally from the flame sheet. The displacement ξ at the flame tip hence misses out on flame wrinkles over a radial range of $\xi \sin\alpha$. This may lead to significant differences in the flame dynamics at large amplitudes, especially for wedge flames. This matter is further discussed in App. A.

In the following, the G-equation description of a premixed flame is cast into the systemic context of a heat source subsystem. We shall deal with fully premixed fuel supply in the remainder of this thesis, so $\phi_1 = 0$ and thus $S_{L,1} = q_{R,1} = 0$. For a detailed investigation of the effect of ϕ_1 on the linear response of premixed flames, the interested reader is referred to [1, 155].

3.2 Systems Representation of the Heat Source Subsystem

In the current section, we cast different models for the heat source subsystem $\mathcal{S}^{(F)}$ into the generic form of a continuous state space representation. Subsequently, the latter is discretized to yield a discrete state space model, which can be solved by numerical means. In Sec. 3.2.1, we do so for the nonlinear

G-equation flame derived in the previous Sec. 3.1. Section 3.2.2 introduces a generic filter-based state space representation of the heat source subsystem $\mathcal{S}^{(F)}$ that is, in principle, valid for any linear time-invariant system. For the latter, the system dynamics is entirely given by an IR function (see Sec. 2.3.1).

3.2.1 G-Equation Representation

The heat source subsystem $\mathcal{S}^{(F)}$ modeled by the G-equation framework introduced in the previous section consists itself of two subsystems, the linear velocity model subsystem $\mathcal{S}^{(F,v)}$ (see Eq. (3.10)) and the nonlinear G-equation flame subsystem $\mathcal{S}^{(F,G)}$ (see Eqs. (3.3) and (3.6)). The corresponding schematic is depicted in Fig. 3.4. The nonlinear continuous partial differential state space representation of $\mathcal{S}^{(F)}$ takes the form of Eqs. (2.3),

$$\dot{x}^{(F)} = \mathcal{A}^{(F)}\left(x^{(F)}\right) x^{(F)} + \mathcal{B}^{(F)}\, u^{(F)}\,, \tag{3.12a}$$

$$y^{(F)} = \mathcal{C}^{(F)}\left(x^{(F)}\right) x^{(F)}\,, \tag{3.12b}$$

with

$$u^{(F)} = u^{(F,v)}\,, \quad x^{(F)} = \left[\, x^{(F,v)}\,,\, x^{(F,G)} \,\right]^T, \quad y^{(F)} = y^{(F,G)}\,. \tag{3.13}$$

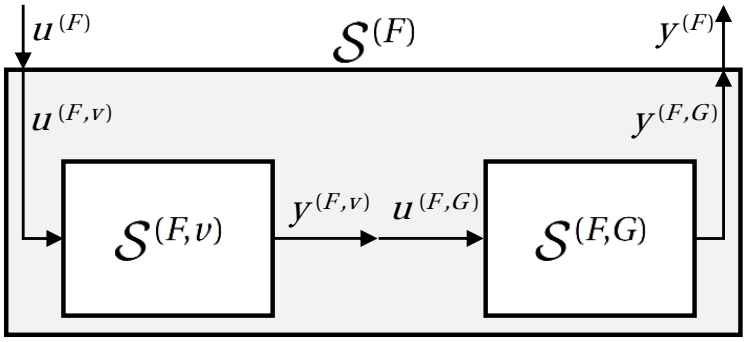

Figure 3.4: Scheme of the heat source subsystem $\mathcal{S}^{(F)}$, itself made up of a serial connection of two subsystems, the subsystem velocity model $\mathcal{S}^{(F,v)}$ and the subsystem G-equation flame $\mathcal{S}^{(F,G)}$.

The model $(\mathcal{A}^{(F)}, \mathcal{B}^{(F)}, \mathcal{C}^{(F)})$ is defined by

$$\mathcal{A}^{(F)} = \begin{bmatrix} \mathcal{A}^{(F,v)} & 0 \\ \mathcal{B}^{(F,G)}\mathcal{C}^{(F,v)}\left(x^{(F,v)}\right) & \mathcal{A}^{(F,G)}\left(x^{(F,G)}\right) \end{bmatrix}, \tag{3.14a}$$

$$\mathcal{B}^{(F)} = \begin{bmatrix} \mathcal{B}^{(F,v)} , 0 \end{bmatrix}^T, \tag{3.14b}$$

$$\mathcal{C}^{(F)} = \begin{bmatrix} 0 , \mathcal{C}^{(F,G)}\left(x^{(F,G)}\right) \end{bmatrix}. \tag{3.14c}$$

According to Eq. (3.10), the continuous input-state-output variables of $\mathcal{S}^{(F,v)}$ are velocity fluctuations at the flame base, velocity fluctuations in x-direction, and velocity fluctuations at the position of the flame sheet,

$$u^{(F,v)} = v_1^B , \quad x^{(F,v)} = v_1(x) , \quad y^{(F,v)} = v_1(\eta) . \tag{3.15}$$

Accordingly, the input operator $\mathcal{B}^{(F,v)}$ passes on v_1^B to the states, the state operator is the differential operator with respect to x, $\mathcal{A}^{(F,v)} = [-w\,\partial/\partial x]$, and the output operator $\mathcal{C}^{(F,v)}$ acts as time-varying interpolation operator according to the position of the flame sheet.

For $\mathcal{S}^{(F,G)}$, the continuous input-state-output variables are given as velocity fluctuations[2] at the position of the flame sheet, flame displacement, and heat release rate,

$$u^{(F,G)} = v_1(\eta) , \quad x^{(F,G)} = \eta(y) , \quad y^{(F,G)} = \dot{q} . \tag{3.16}$$

Accordingly, $\mathcal{B}^{(F,G)} = \mathcal{I}$, and $\mathcal{A}^{(F,G)}$ and $\mathcal{C}^{(F,G)}$ are nonlinear partial differential and integral operators performing the right-hand sides of Eqs. (3.3) and (3.6), respectively.

The state vectors of both subsystems in $\mathcal{S}^{(F)}$ are discretized uniformly to render the partial differential and integral operators amenable to numerical treatment,

$$\mathbf{x}^{(F,v)} = \begin{bmatrix} v_1(\Delta x) , v_1(2\Delta x) , \cdots , v_1(N_{F,v}\Delta x) \end{bmatrix}^T, \quad N_{F,v}\Delta x \geq \max_y \eta(y) , \tag{3.17a}$$

$$\mathbf{x}^{(F,G)} = \begin{bmatrix} \eta(0) , \eta(\Delta y) , \cdots , \eta(N_{F,G}\Delta y) \end{bmatrix}^T, \quad N_{F,G}\Delta y = R_F . \tag{3.17b}$$

[2]Note that η is forced by v and not only by v_1 in Eq. (3.3), so the input to $\mathcal{S}^{(F,G)}$ should be the full velocity field at the position of the flame sheet. However, as $v_0 = const.$, it is known everywhere in space, and only the dynamics of v_1 needs to be computed explicitly.

Since $\mathcal{S}^{(F,v)}$ and $\mathcal{S}^{(F,G)}$ are SISO, $\mathbf{u}^{(F,v)} = u^{(F,v)}$, $\mathbf{u}^{(F,G)} = u^{(F,G)}$, $\mathbf{y}^{(F,v)} = y^{(F,v)}$ and $\mathbf{y}^{(F,G)} = y^{(F,G)}$ as defined in Eqs. (3.15) and (3.16), respectively.

The state equation of the velocity model subsystem $\mathcal{S}^{(F,v)}$ may be approximated by finite elements (FE). This scheme is well-suited for solving advective processes, as it exhibits little dissipation and can handle steep gradients. The downstream boundary is modeled as zero gradient outflow condition. The corresponding set of discrete matrices $(\mathbf{A}^{(F,v)}, \mathbf{B}^{(F,v)}, \mathbf{C}^{(F,v)})$ is explicitly given in App. C.1.

The partial differentials in the state and output equation of the G-equation flame subsystem $\mathcal{S}^{(F,G)}$ are solved by a 5^{th} order WENO scheme [156, 157, 184], which is 3^{rd} order accurate in regions with steep gradients and 5^{th} order accurate otherwise. This WENO scheme is frequently used in the context of the G-equation flame (for example, [154, 165]). The boundary condition at the flame holder is implemented analog to Dowling [34]. The integral in the output equation of $\mathcal{S}^{(F,G)}$ is approximated by trapezoidal summation. Time marching is performed by a 3^{rd} order Runge-Kutta (RK) total variation diminishing (TVD) scheme [62].

3.2.2 IR-Based Representation of LTI Systems

As introduced in Sec. 2.3.1, a linear time-invariant (LTI) system is completely characterized by its impulse response matrix $\mathbf{H}(t)$ (or IR function $h(t)$ for a SISO system). The convolution equation given in Eq. (2.14) is a full description of the output dynamics subject to any input. In the following, we extend the input-output framework of an IR model to an input-state-output framework. We therefore define the lagged inputs appearing in the convolution integral given in Eq. (2.14) as states.

The continuous state space representation of any LTI system $\mathcal{S}^{(\text{LTI})}$ then reads

$$\frac{\partial \mathbf{u}(t-\tau)}{\partial t} = -a_{\text{IR}} \frac{\partial \mathbf{u}(t-\tau)}{\partial \tau} + \mathbf{u}(t)\,, \tag{3.18a}$$

$$\mathbf{y}(t) = \int_{t_0}^{t} \mathbf{H}(\tau)\, \mathbf{u}(t-\tau)\, \mathrm{d}\tau\,. \tag{3.18b}$$

The state equation (3.18a) takes the form of an advection equation (see, for example, Eq. (3.10)), where the current input $\mathbf{u}(t)$ is propagated through history τ at a rate of a_{IR}. It is thereby possible to track the history of inputs $\mathbf{u}(t-\tau)$, which in turn are defined as states. The output equation (3.18b) corresponds to the convolution equation between input and output as given in Eq. (2.14). However, as the states are lagged inputs, the output equation is a relation between states and output. This is conform to the definition of a state space model.

The input-state-output variables of $\mathcal{S}^{(\mathrm{LTI})}$ are hence given as current discrete inputs, lagged discrete inputs, and current discrete outputs,

$$u^{(\mathrm{IR})} = \mathbf{u}(t)\,, \quad x^{(\mathrm{IR})} = \mathbf{u}(t-\tau)\,, \quad y^{(\mathrm{IR})} = \mathbf{y}(t)\,. \tag{3.19}$$

Accordingly, the input operator $\mathcal{B}^{(\mathrm{IR})}$ passes the input to the states, the state operator is the differential operator with respect to τ, $\mathcal{A}^{(\mathrm{IR})} = [\,-a_{\mathrm{IR}}\,\partial/\partial\tau\,]$, and the output operator $\mathcal{C}^{(\mathrm{IR})}$ is a convolution operator weighted by $\mathbf{H}(t)$.

The filter-based state space representation defined in Eqs. (3.18) can be used to model any (sub-)system that is LTI. That is, different models differ in their impulse response matrix $\mathbf{H}(t)$, but not in terms of their SSM structure. Representing a system in terms of its IR characteristics is useful if the IR matrix is finite, i.e., if $\mathbf{H}$ possesses a finite settling time τ_s. In this case, the number of lagged states is also finite and suitable uniform discretization in the τ-direction yields,

$$\mathbf{x}^{(\mathrm{IR})} = \Big[\,\mathbf{u}(t-\Delta\tau)\,,\,\mathbf{u}(t-2\Delta\tau)\,,\,\cdots\,,\,\mathbf{u}(t-N_{\mathrm{IR}}\Delta\tau)\,\Big]^T\,, \quad N_{\mathrm{IR}}\Delta\tau = \tau_s\,. \tag{3.20}$$

Since $\mathcal{S}^{(\mathrm{IR})}$ is SISO, $\mathbf{u}^{(\mathrm{IR})} = u^{(\mathrm{IR})}$ and $\mathbf{y}^{(\mathrm{IR})} = y^{(\mathrm{IR})}$ as defined in Eq. (3.19). As in the previous section, the partial differential in the state equation is approximated by finite elements with a zero gradient outflow condition. The convolution integral in the output equation is solved by trapezoidal summation, and time marching is performed by an RK3 TVD scheme. The set of discrete matrices $(\mathbf{A}^{(\mathrm{IR})}, \mathbf{B}^{(\mathrm{IR})}, \mathbf{C}^{(\mathrm{IR})})$ is explicitly given in App. C.2.

3.3 Obtaining Impulse Reponse Functions

The present section deals with different approaches to obtain IR functions of the *linear time-invariant SISO* heat source subsystem $\mathcal{S}^{(F)}$ with finite settling time τ_s. The single input $u = v_1^B$ and single output $y = \dot{q}_1$ are velocity fluctuations at the base of the heat source and fluctuations in heat release rate, respectively. Once obtained, the IR functions can be substituted into the IR-based model structure defined in Eqs. (3.18) in the previous section to arrive at the continuous model $(\mathcal{A}^{(F)}, \mathcal{B}^{(F)}, \mathcal{C}^{(F)})$ of the *linear* heat source subsystem $\mathcal{S}^{(F)}$. IR functions also contain information on the response mechanisms and can be interpreted physically.

In Sec. 3.3.1, we analytically derive and analyze the IR function of the *linearized* G-equation model introduced in Sec. 3.1 under fully premixed conditions. In Sec. 3.3.2, we turn to flame models that emanate from experimentally or numerically determined frequency response data. Section 3.3.3 treats single time lag models well-known in thermoacoustics as n-τ models.

3.3.1 Linearized Analytical G-Equation Flame Model

Deriving the IR Function

In the present section, we derive the IR function of the heat source subsystem $\mathcal{S}^{(F)}$ consisting of the two subsystems convective velocity model $\mathcal{S}^{(F,v)}$ and linearized G-equation flame $\mathcal{S}^{(F,G_{\text{lin}})}$ as introduced in Sec. 3.1.4. The analysis is inspired by the derivation shown in [12]. However, in contrast to [12], the current analysis is carried out in the laboratory-fixed reference. Possible issues of the G-equation framework regarding the choice of reference frame are discussed in App. A.

The continuous model governing $\mathcal{S}^{(F,G_{\text{lin}})}$ is given in Eq. (3.9). In the absence of mixture inhomogeneities, it can be re-written as

$$\frac{\partial \eta_1}{\partial t} = -v_{r,\perp} \frac{\partial \eta_1}{\partial y} + v_1 \,, \tag{3.21a}$$

$$\dot{q}_1 = \frac{\dot{q}_0}{R_F^2}\sin(2\alpha)\begin{cases} \displaystyle\int_0^{R_F}\eta_1\,\mathrm{d}y & \text{conical flame} \\ \left\{R_F\,\eta_1(R_F) - \displaystyle\int_0^{R_F}\eta_1\,\mathrm{d}y\right\} & \text{wedge flame} \end{cases}, \tag{3.21b}$$

with restorative velocity $v_{r,\perp} = v_0 \sin\alpha\cos\alpha$, $\dot{q}_0$ as defined in Eq. (3.8b), and applying integration by parts to arrive at the output equation (3.21b). The analytical solution of the state equation (3.21a) represents a memory integral,

$$\eta_1(y,t) = \frac{1}{v_{r,\perp}}\int_0^y v_1\left(y', t - \frac{y-y'}{v_{r,\perp}}\right)\mathrm{d}y', \tag{3.22}$$

which substituted into Eq. (3.21b) leads to the solution of the output over time for both types of flames.

We excite $\mathcal{S}^{(F)}$ by an impulsive input $u^{(F)} = v_1^B = d\,\delta(t-t_0)$, with $t_0 = 0$ without loss of generality, and displacement magnitude d. With Eq. (3.18b), the IR function then becomes

$$h(t) = \frac{\dot{q}_1}{d}. \tag{3.23}$$

According to the flow depicted in Fig. 3.4, the output of $\mathcal{S}^{(F,v)}$ is fed as input into $\mathcal{S}^{(F,G_{\mathrm{lin}})}$,

$$y^{(F,v)} = u^{(F,G)} = d\,\delta\left(t - \frac{y}{w_\perp}\right), \tag{3.24}$$

with $w_\perp = w\tan\alpha$ the convective velocity component in y-direction. Substitution of Eq. (3.24) into Eq. (3.22) yields

$$\eta_1(y,t) = d\,\frac{\mu}{\mu - \cos^2\alpha}\left[\theta\left(t - \frac{y}{w_\perp}\right) - \theta\left(t - \frac{y}{v_{r,\perp}}\right)\right], \tag{3.25}$$

with Heaviside step function $\theta(\cdot)$, and $\mu = w/v_0$ as defined in Eq. (3.11).

The competition of the two convective processes given in Eq. (3.25) is illustrated graphically in Fig. 3.5. The flame is locally displaced by a distance $\eta_1 = d\,\mu/(\mu - \cos^2\alpha)$ convecting downstream in the mean flow direction at a rate of w (emanating from the action of the subsystem velocity model $\mathcal{S}^{(F,v)}$). The time scale of this process is given as *convective* time scale $\tau_c = R_F/w_\perp = R_F/(w\tan\alpha)$. In parallel, a second process emanating from the action of the subsystem linearized G-equation flame $\mathcal{S}^{(F,G_{\mathrm{lin}})}$ restores the initial flame

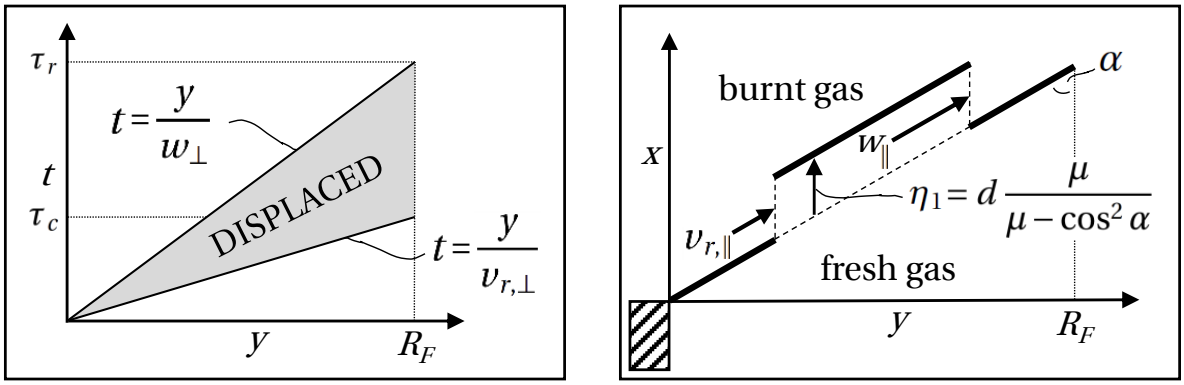

(a) $\eta_1 > 0$ in y-t-plane. **(b)** $\eta_1 > 0$ in y-x-plane.

Figure 3.5: (a) Graphical illustration of Eq. (3.25) in terms of displaced flame sheet in the y-t-plane. (b) Snapshot of the displaced flame sheet at some $t < \tau_c$ in the y-x-plane.

shape convecting downstream in the direction of the mean flow at a rate of $v_{r,\perp}/\tan\alpha = v_0\cos^2\alpha$. This happens because a new flame sheet develops from the flame holder as soon as the initial flame is displaced. The displaced flame sheet downstream is gradually deprived of fresh premixture and extinguishes, such that eventually the original flame sheet is re-established. The time scale of this process is given as *restorative* time scale $\tau_r = R_F/v_{r,\perp}$.[3] The competition between both processes is only defined if $\mu - \cos^2\alpha > 0$. For any $\mu \in \{0;1\}$, this yields a prescription for a permissible range of α. In terms of the ratio of time scales Π, this requirement can be stated as

$$\Pi = \frac{\tau_c}{\tau_r} = \frac{\cos^2\alpha}{\mu} < 1\,. \tag{3.26}$$

The IR functions of $\mathcal{S}^{(F)}$ are found by substituting Eq. (3.25) into the output equation (3.21b). With Eq. (3.23), they read for conical and wedge flames (indices C and W, respectively),

$$h_C(t) = \frac{\dot{q}_0}{R_F^2}\sin(2\alpha)\begin{cases} w_\perp\, t & 0 \le t \le \tau_c \\ \dfrac{1}{1-\Pi}\left(R_F - v_{r,\perp}\, t\right) & \tau_c < t \le \tau_r \\ 0 & \text{otherwise} \end{cases} \tag{3.27a}$$

[3] See App. A for a commentary on this matter.

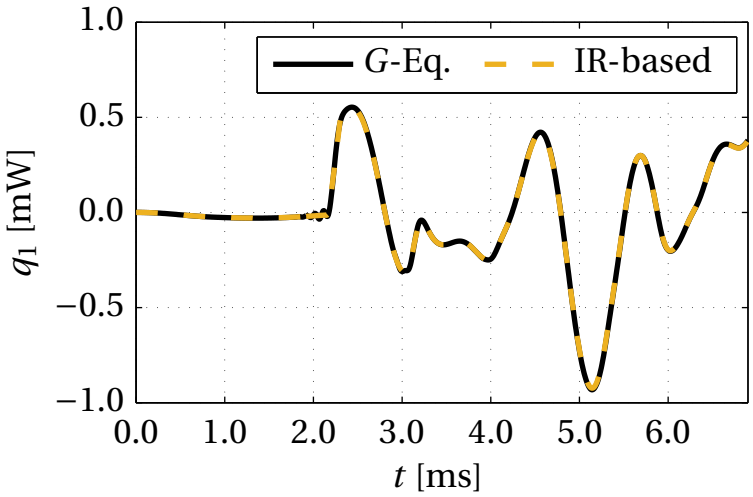

Figure 3.6: Comparison of the linear output of $\mathcal{S}^{(F)}$ modeled by the G-equation (—) and the IR-based representation (– – –) subject to the same arbitrary input signal.

$$h_W(t) = \frac{\dot{q}_0}{R_F^2}\sin(2\alpha)\begin{cases} -w_\perp\, t & 0 \le t \le \tau_c \\ \dfrac{1}{1-\Pi}\, v_{r,\perp}\, t & \tau_c < t \le \tau_r \\ 0 & \text{otherwise} \end{cases} \tag{3.27b}$$

With Eq. (3.27), we have obtained a full non-parametric description of $\mathcal{S}^{(F)}$, which substituted into Eqs. (3.18), yields an IR-based representation of $\mathcal{S}^{(F)}$. For validation, it remains to be ensured that the IR-based (see Sec. 3.2.2) and the G-equation representation (see Sec. 3.2.1) of $\mathcal{S}^{(F)}$ exhibit the same output behavior in the linear regime. This must be the case as both discrete representations are uniquely linked by a state-transformation matrix $\mathbf{T}$ (see Sec. 2.1). As plotted in Fig. 3.6, the output of the IR-based is identical to the G-equation representation for small amplitudes. It is thereby also warranted that the transition from the linear to the nonlinear regime is smooth, which is crucial for the purpose of the present study. We will return to this point in Chap. 7.

Interpreting the IR Function

The IR functions h_C and h_W are depicted in Figs. 3.7(a) and 3.7(b), respectively, for different ratios of time scales Π. The IR functions are normalized by

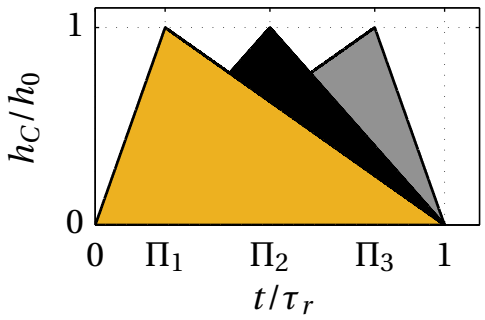

(a) IR function of conical flame.

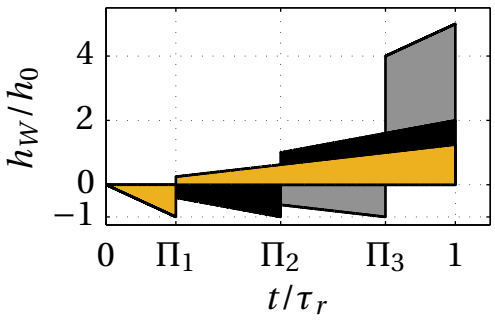

(b) IR function of wedge flame.

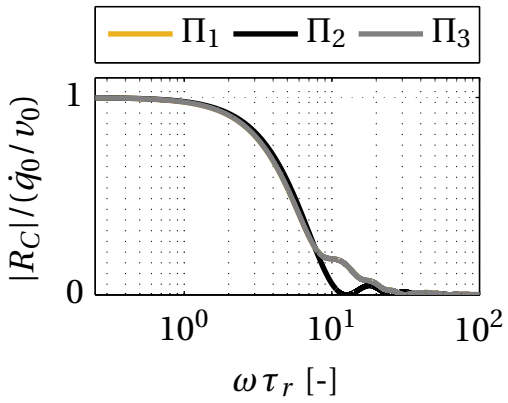

(c) Gain of FRF of conical flame.

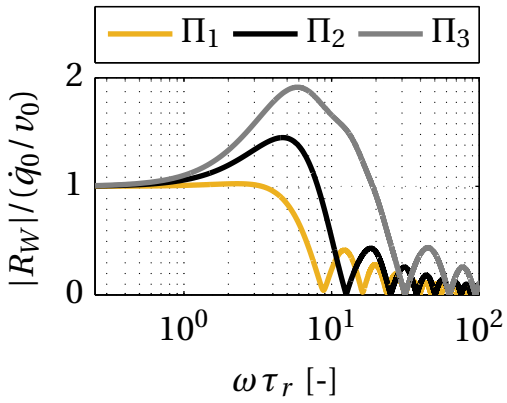

(d) Gain of FRF of wedge flame.

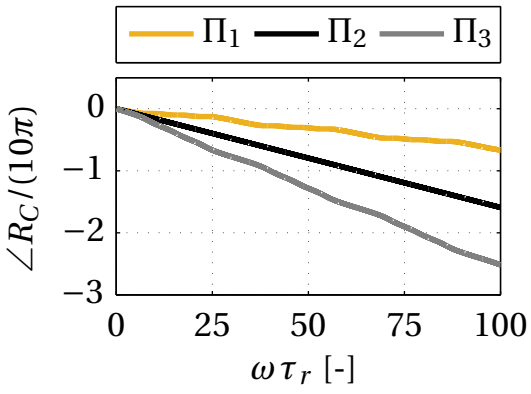

(e) Phase of FRF of conical flame.

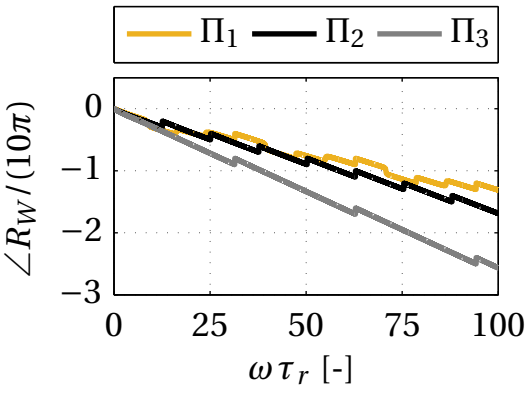

(f) Phase of FRF of wedge flame.

Figure 3.7: IR function h normalized by $h_0 = \dot{q}_0 \sin(2\alpha)/R_F$ (top row) and gain and phase of the corresponding FRF (middle and bottom row, respectively) of the linearized G-equation flame describing $\mathcal{S}^{(F)}$ for different ratios of time scales Π. The left and right column represent a conical and a wedge flame, respectively.

$h_0 = \dot{q}_0 \sin(2\alpha)/R_F$. Their shape yields a straightforward view on the physical response mechanisms. In the linear regime, $\dot{q}_1$ is determined by the amount of displaced flame front for both flames, see Eq. (3.21b). For a conical flame, the response in $\dot{q}_1$ builds up linearly, as an increasing amount of flame front is displaced while the perturbation resulting from the convective process moves downstream faster than the restoration process. Once the convective perturbation leaves the flame front, the initial flame shape is gradually restored, leading to a linear decrease in $\dot{q}_1$. For the wedge flame, the displaced amount of the flame front is subtracted from the displacement at the flame tip. This explains why the response first decreases linearly. Once the convective perturbation leaves the flame and thereby displaces the flame tip, the response in $\dot{q}_1$ shoots up and then increases linearly until the restorative process has regained the steady-state flame front. The jump from $h < 0$ to $h > 0$ is more pronounced for larger Π.

The IR functions given in Eq. (3.27) can be transformed to the frequency domain by Fourier transform defined in Eq. (2.21) to yield the FRF $R(\omega)$ of $\mathcal{S}^{(F)}$. The analytical expressions obtained match those given in [138, 154], and are therefore not explicitly shown. Gain and phase of $R(\omega)$ are plotted in Figs. 3.7(c)–3.7(f) for selected values of Π. Knowledge of the characteristic time scales of response may be used to explain certain phenomena visible in the gain and phase of $R(\omega)$. In the following, we summarize some findings to this regard, which are presented more elaborately in [12].

As is visible from Figs. 3.7(e) and 3.7(f), the phase of both FRFs are (nearly) linearly decreasing functions of ω. This indicates a convective dominance of flame response, which, as discussed above, is due to the dynamics of the subsystem velocity model $\mathcal{S}^{(F,v)}$. Non-dimensionalizing the frequency ω by the corresponding characteristic time scale of this process τ_c leads to a collapsing of the phase evolutions into a single curve (see Fig. 3.8(a) for a conical flame). The phase of the flame response is thus self-similar with respect to the non-dimensional group $\omega\tau_c$ over a wide range of Π.

Other interesting phenomena are the alternating periodic cutoff and local maxima of the gain of a wedge flame visible in Fig. 3.7(d). The maxima for low frequencies may even exceed unity (so-called excess gain behavior). Both

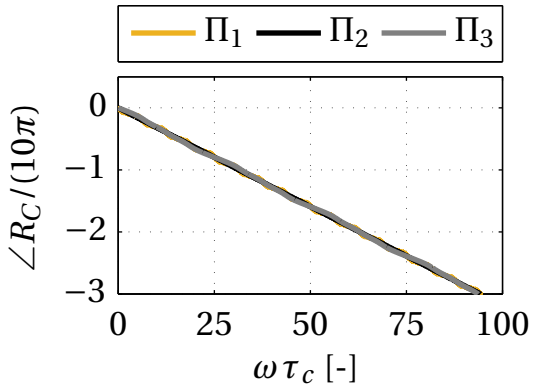

(a) Phase of FRF of conical flame.

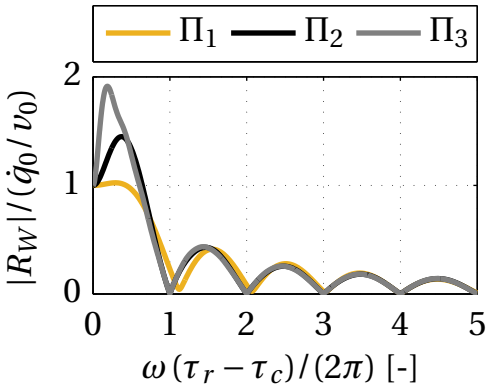

(b) Gain of FRF of wedge flame.

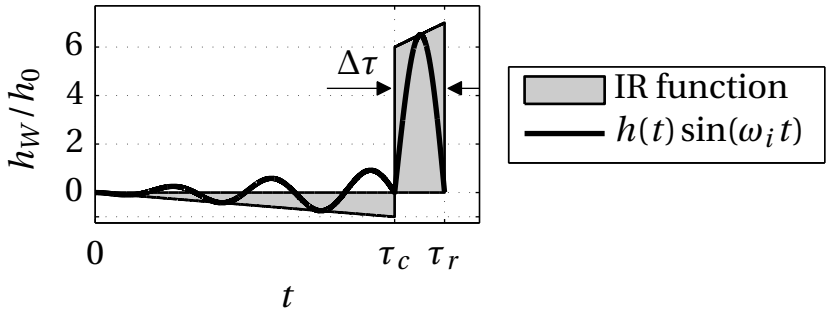

(c) IR function of wedge flame.

Figure 3.8: (a) Self-similar phase with respect to the non-dimensional frequency $\omega\tau_c$. (b) Self-similar gain with respect to the non-dimensional frequency $\omega\Delta\tau$. (c) IR function of a sharp wedge flame (shaded gray) and weighted response to harmonic forcing at first cutoff frequency ω_i (—).

phenomena can be explained by the shape of h_W. As can be seen from Fig. 3.7(b), the dominant portion of flame response occurs for $\tau_c < t \leq \tau_r$, i.e., after the jump from $h < 0$ to $h > 0$. If the wavelength of a given frequency of forcing ω_i is such that it spans this dominant region of flame response (see Fig. 3.8(c)), it is effectively damped and a significant drop in response is observed at ω_i. The opposite is true if half of the wavelength corresponding to ω_i spans the region $\tau_c < t \leq \tau_r$. In this case, the response at ω_i is significantly amplified. Non-dimensionalization of ω by the characteristic time scale of this

process $\Delta\tau = \tau_r - \tau_c$ leads to self-similar behavior of the gain with respect to the non-dimensional group $\omega\Delta\tau$. In this reference, cutoff lies at multiples of 2π, whereas all maxima lie at multiples of $(2\pi - 1)$ over a wide range of Π (see Fig. 3.8(b)). Self-similarity is only broken for small values of Π, as the jump in h_W at $t = \tau_c$ decreases for decreasing Π, and one cannot speak of a dominant region of flame response anymore.

3.3.2 IR-Based Models from Measurements

The IR function can also be obtained from experimentally measured or numerically computed data. The overall goal consists in building a parametric model that captures the dynamics of the system under investigation. The approaches used differ in whether the data is available in time or frequency domain.

In time domain, system identification methods provide a sound basis to estimating the parameters of a fixed generic model structure [101, 169]. In the most general case, the parameters of a so-called Box-Jenkins (BJ) model—a combination of different plant and noise models— are estimated in an optimal sense [101]. FIR, ARX (autoregressive with exogeneous input), ARMA (autoregressive moving average) and OE (output error) models are special cases of BJ models. The IR function results from any of these models as an inherent property. In general, the IR function is a *distributed* function of time (as, for example, in case of the linearized analytical G-equation flame model, see Figs. 3.7(a)–3.7(b)).

In the frequency domain, it is possible to estimate a complex-valued function $\hat{R}(\omega)$ that captures the response behavior $R(\omega_i)$, where $R(\omega_i)$ is usually given in terms of gain and phase (or equivalently in terms of real and imaginary part) at discrete frequencies of oscillation ω_i. If $\hat{R}(\omega)$ is an analytic function, the transfer function $\hat{F}(s)$ can be constructed by arguments of analytical continuation (see Sec. 2.3.2). This is imperative when performing quantitative stability analysis in frequency domain [146]. The estimated FRF and FTF, $\hat{R}(\omega)$ and $\hat{F}(s)$, respectively, are valid in the band of discrete frequencies in which $R(\omega_i)$ is known. Subsequent inverse Fourier transform of $\hat{R}(\omega)$ yields the approxi-

mate IR function $\hat{h}(t)$ in time domain. In analogy to the frequency domain, $\hat{h}(t)$ is valid in the signal spectrum of known frequencies ω_i.

Estimating the IR Function from FRF Data

An elegant approach to estimating $\hat{R}(\omega)$ is by rational function approximations, where $R(\omega_i)$ is expressed as a sum of rational functions [64],

$$\hat{R}(\omega) = \sum_{n=1}^{N_n} \frac{b_n}{j\omega - a_n} + d\,. \tag{3.28}$$

The zeros b_n, poles a_n and delay d are estimated in terms of a nonlinear least squares problem. Besides the low number of parameters to be estimated, the main advantage using rational functions lies in the ease of computing the inverse Fourier transform to arrive at the IR function,

$$\hat{h}(t) = \mathscr{F}^{-1}\left\{\hat{R}(\omega)\right\} = \left(\sum_{n=1}^{N_n} b_n e^{-a_n t}\right) + d\,\delta(t)\,. \tag{3.29}$$

As the approximated FRF data is BIBO stable by definition, $d = 0$ and $a_n > 0\ \forall\ n$. The IR function $\hat{h}(t)$ is hence a linear combination of decaying exponential functions.

As shown in detail in [163], the rational function approximation (3.28) is applied to experimentally determined FRF data of a turbulent premixed swirl flame with $\dot{q}_0 = 30\,\mathrm{kW}$ and $v_0 = 11.3\,\mathrm{m/s}$ studied in [93, 170] and supplemented with the condition that the FRF should approach a value of $\dot{q}_0/v_0 = 2.65\,\mathrm{kN}$ (gain) and zero (phase) in the limit of zero frequency [135]. It is visible from Fig. 3.9(a)–3.9(b) that the rational fit of order $N_n = 12$ fits the measured data accurately. Figure 3.9(c) depicts the corresponding IR function obtained from Eq. (3.29). As $h(t)$ is expressed as a sum of decaying exponential functions, it is an infinite IR function and its response to an impulse is infinitely long in theory. However, the response is negligible for $t > 11.5\,\mathrm{ms}$ (not shown). The IR function has therefore been trimmed to a finite IR function with non-zero values for $0 \le t \le 11.5\,\mathrm{ms}$.

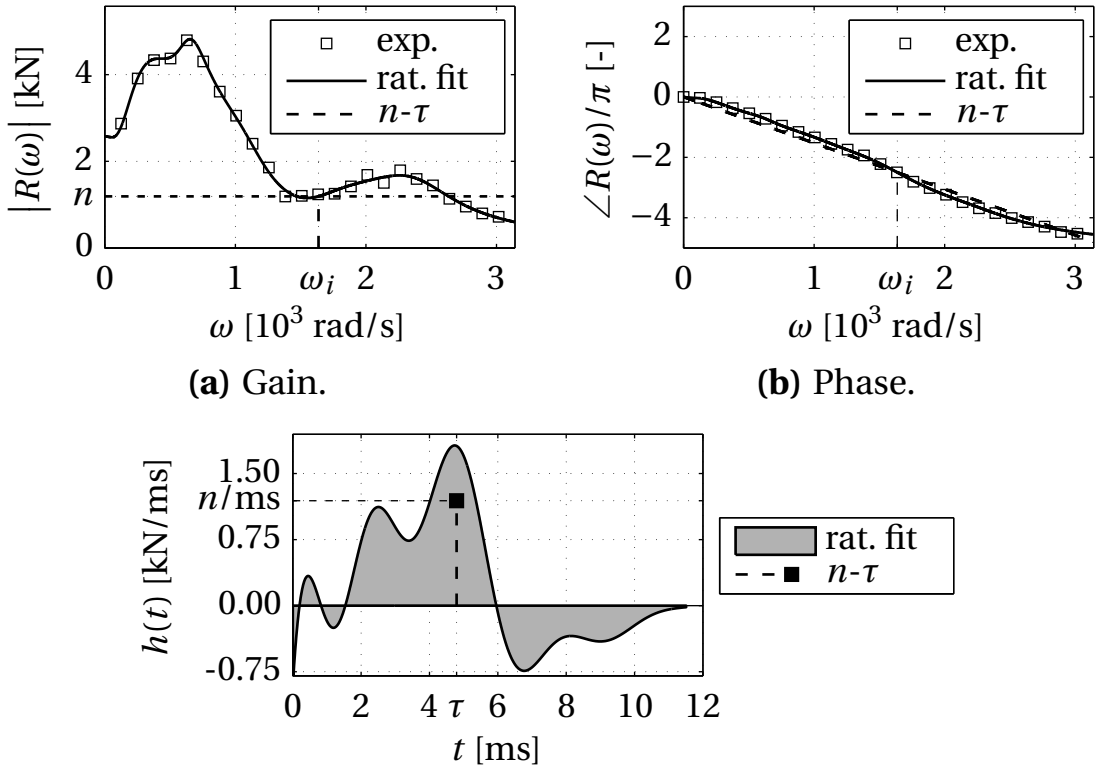

(a) Gain.

(b) Phase.

(c) IR function.

Figure 3.9: (a) Gain and (b) phase of experimentally measured FRF data of a turbulent premixed swirl flame (□), corresponding rational fit function (—), and n-τ model (− − −). (c) Corresponding IR functions of rational fit (gray-shaded) and n-τ model (■).

Interpreting the IR Function

As for the linearized G-equation flame model, the shape of h can be interpreted physically. In this experimental case, the number of processes occurring in parallel, and thus the number of characteristic time scales, is more than only two as in the analytical case. It is hence more difficult to isolate individual response mechanisms. Still, the shape of h can be explained by the superposition of two main response mechanisms that have been studied in [93].

The first is the response to axial acoustic waves, which induce flame wrinkles at the flame base. The latter convect downstream at a phase velocity w in

analogy to the convective response mechanism detailed for the linearized G-equation flame in Sec. 3.3.1. The dominant hump of the IR function at $t = \tau \approx 4.8\,\text{ms}$ and the almost linearly decaying slope of the phase (see Fig. 3.9(b)) can be attributed to this response mechanism. With average flame height $\approx 4\,\text{cm}$ [170], this leads to $w \approx 8.33\,\text{m/s}$ and $\mu \approx 0.74$. The second mechanism is the response to a convective perturbation in circulation, which is created when an axial acoustic wave passes the swirler unit. A temporary variation in the swirl number leads to an alternating positive and negative response in $\dot{q}$ (see Fig. 9 of [93]), which can be attributed to flame roll-up and to a temporal variation of the flame angle α [125]. For details on the response mechanisms of turbulent premixed swirl flames, the interested reader is referred to [93, 124, 125].

Both main response mechanisms are convectively driven. This explains why, in a good approximation, the IR function of the turbulent premixed swirl flame is finite. The fluctuations in $\dot{q}$ cease once the wrinkles and perturbations in swirl have convected out of the flame. In combination with the discussion on laminar premixed flames given in Sec. 3.3.1, it is concluded that since premixed flames are dominated by convective processes, their response dynamics is nicely approximated by finite IR function-based models.

3.3.3 Single Time Lag Model

As seen above, the response dynamics of premixed flames is convectively driven. A very simple low-order modeling approach consists in expressing all convective processes by a single dominant time constant τ, and in defining a so-called interaction index n that determines an output-to-input ratio. This single time lag (STL) model is well-known in the thermoacoustic community as n-τ model, and builds on pioneering work by Crocco [28]. The corresponding IR function is simply a weighted delayed impulse, $h(t) = n\,\delta(t-\tau)$. In frequency domain, this leads to an FRF $R(\omega) = n\exp(-j\omega\tau)$. The gain takes the constant value n over all frequencies, and the phase linearly decreases with constant slope τ.

Given experimentally or numerically determined FRF data, an STL model can be sought to capture the response behavior at a single frequency ω_i if the

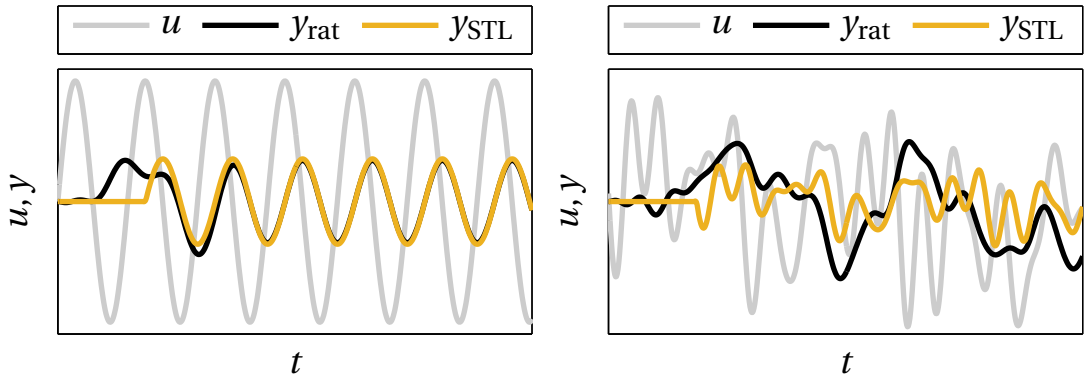

(a) Monofrequent excitation. **(b)** Arbitrary excitation.

Figure 3.10: Output y of the turbulent premixed swirl flame represented by an STL model (—) and an IR-based model obtained from a rational function approximation (—). (a) The input is given as the monofrequent input signal at which the STL model is fitted. Both models produce the same stationary output. (b) For an arbitrary input signal, the STL model does not capture the full dynamics.

response behavior is indeed dominated by a single convective process. In this case, the coarse-grained slope of the phase can be approximated by the time constant τ, and n is chosen such that it matches the gain at ω_i. This is done for the turbulent premixed swirl flame introduced in the previous section at $\omega_i \approx 1640\,\mathrm{rad/s}$. The interaction index is determined as $n \approx 1.19\,\mathrm{kN}$ and $\tau \approx 4.8\,\mathrm{ms}$ corresponds to the characteristic time scale of the axial convective response mechanism discussed above. The gain, phase and the IR function of the STL model are overlaid in Fig. 3.9.

The shortcomings of an STL model are evident. A model with constant gain over all frequencies and a single time constant (i.e., a single physical process) is a poor representation of most processes. These limitations become apparent when comparing the output y of the STL model to that of the IR-based model found from the rational fit approximation in Sec. 3.3.2. The latter contains *all* time constants of the system. It is visible from Fig. 3.10(a) that both models asymptotically produce the same output when forced at the single frequency of oscillation ω_i of the STL model. However, when probing the STL

model with an arbitrary signal that contains multiple frequencies, the output differs significantly from that of the IR-based model (see Fig. 3.10(b)).

More comprehensive studies on the limited use of STL models, especially with respect to linear stability analysis, are given in [146, 163]. Altogether, physical interpretation of STL models is limited, and they cannot be used for transient analysis. For these reasons, STL models are ill-suited for the purpose of the present study, and are not further considered.

3.4 Chapter Summary

The present chapter can be summarized as follows:

- Different methods are presented to obtain a model $(\mathbf{A}^{(F)}, \mathbf{B}^{(F)}, \mathbf{C}^{(F)})$ describing the heat source subsystem $\mathcal{S}^{(F)}$. For all linear representations, the response behavior is fully characterized by an IR function.
- The relevance of IR functions is highlighted. They yield insight into the time scales of dominant response mechanisms and provide physical insight.
- The response behavior of premixed flames is dominated by convective processes. It is therefore a good approximation to express the response dynamics by finite IR function-based models.

4 The Acoustics Subsystem

The present chapter deals with the acoustic field, the second element of a thermoacoustic system. The aim is to formulate the acoustic field as a subsystem that can be inserted as generic block into the full thermoacoustic system $\mathcal{S}^{(T)}$ (see the schematic in Fig. 1.8). It is labeled as *acoustics subsystem* $\mathcal{S}^{(A)}$.

The chapter is organized as follows. The governing acoustic equations are presented and a brief introduction to acoustic theory is given in Sec. 4.1. In Sec. 4.2, we define the model describing the acoustic reference system that forms the basis of further investigation, and relevant model parameters are introduced. The acoustic model is brought to input-state-output form in Sec. 4.3, where we also summarize a selection of existing systemic approaches in the field. Section 4.4 is dedicated to different methods of numerically approximating the model describing $\mathcal{S}^{(A)}$. Finally, the effect of non-zero mean flow and temperature gradients on the acoustic field are discussed in Sec. 4.5.

4.1 Deriving the Equations for the Acoustic Field

The dynamics of an isentropic perfect gas is governed by the conservation equations of mass, momentum and energy, and an equation for the transport of entropy σ. They can be combined as [131, 142]:

MOMENTUM:
$$\frac{\mathrm{D}\mathbf{v}}{\mathrm{D}t} = -\frac{1}{\rho}\nabla p + \frac{1}{\rho}\nabla\cdot\tau + \mathbf{s}_f\,, \tag{4.1a}$$

MASS+ENERGY:
$$\frac{\mathrm{D}p}{\mathrm{D}t} = -\gamma p\nabla\cdot\mathbf{v} + \left(\gamma-1\right)\dot{q}\,\psi + s_m + \left(\gamma-1\right)\left[\nabla\cdot\left(\lambda\nabla T\right) + \tau : \nabla\mathbf{v}\right], \tag{4.1b}$$

ENTROPY:
$$\frac{\mathrm{D}\sigma}{\mathrm{D}t} = 0\,. \tag{4.1c}$$

$\mathrm{D}\phi/\mathrm{D}t = \partial\phi/\partial t + \mathbf{v}\cdot\nabla\phi$ denotes the material derivative (of dummy variable ϕ) with respect to time, with velocity vector $\mathbf{v} = \left[v_1, v_2, v_3\right]^T$ in all three spatial directions (ξ_1, ξ_2, ξ_3), and differential operator $\nabla = \left[\partial/\partial\xi_1, \partial/\partial\xi_2, \partial/\partial\xi_3\right]^T$. It is assumed that all species involved possess equal heat capacities and molar weights, such that $\gamma = c_p/c_v$ is the ratio of heat capacities at constant pressure and volume, respectively, and λ the thermal conductivity of the entire system. The stress tensor is denoted by τ. For an incompressible Newtonian fluid, it is possible to write $\nabla\cdot\tau = \mu\nabla^2\mathbf{v}$, with constant dynamic viscosity μ. Equation (4.1b) expressed in terms of pressure is obtained from the conservation of sensible energy for a perfect gas combined with mass conservation [121, 131]. $\mathbf{s}_f$ and s_m represent source terms in body forces and mass, respectively. The variation in p is driven by s_m and by the heat added to the system via the heat release rate per unit volume $\dot{q}\,\psi$, where ψ governs the profile of heat addition over the system volume. The mass and energy balance is damped by molecular diffusion of heat and momentum (see the second row in Eq. (4.1b)).

The acoustic field is assumed to consist of perturbations to a *steady* mean flow field (i.e., $\partial\phi_0/\partial t = 0$). This splitting assumption is the same as commonly applied to linearized laminar fluid dynamic problems. Using the decomposition introduced in Eq. (3.7), the splitting assumption amounts to decoupling the zero-th and first-order fields (of orders ϵ^0 and ϵ^1, respectively), and to assuming that any changes to the full fields are entirely accounted for by changes in first-order quantities. The resulting set of linearized equations can be obtained by substituting the expansion (3.7b) into the set of governing equations (4.1). Combining all powers of ϵ^1 yields the governing acoustic equations,

$$\text{MOMENTUM:} \qquad \frac{\mathrm{D}\mathbf{v}_1}{\mathrm{D}t} = -\mathbf{v}_1\cdot\nabla\mathbf{v}_0 - \frac{1}{\rho_0}\nabla p_1 + \frac{1}{\rho_0}\nabla\cdot\tau_1 + \mathbf{s}_{f,1}\,, \tag{4.2a}$$

$$\text{MASS+ENERGY:} \qquad \frac{\mathrm{D}p_1}{\mathrm{D}t} = -\gamma p_0\nabla\cdot\mathbf{v}_1 - \gamma p_1\nabla\cdot\mathbf{v}_0 + \left(\gamma-1\right)\dot{q}_1\psi + s_{m,1} + \left(\gamma-1\right)\left[\nabla\cdot\left(\lambda\nabla T_1\right) + \tau_0 : \nabla\mathbf{v}_1\right], \tag{4.2b}$$

$$\text{ENTROPY:} \qquad \frac{\mathrm{D}\sigma_1}{\mathrm{D}t} = -\mathbf{v}_1\cdot\nabla\sigma_0\,. \tag{4.2c}$$

It is implicitly assumed that $\nabla p_0 = 0$ and $\mathbf{v}_0\cdot\nabla\mathbf{v}_0 = 0$. These are both fair assumptions in the low Mach number regime. Equations (4.2a)–(4.2b) form a

parabolic problem formally known as the linearized Navier-Stokes equations (LNSE) of an isentropic perfect gas. If viscous and heat diffusivity are neglected, Eqs. (4.2a)–(4.2b) become hyperbolic and are known as linearized Euler equations (LEE).

Under uniform flow conditions, $\nabla \mathbf{v}_0 = 0$ and $\nabla \cdot \mathbf{v}_0 = 0$, Eqs. (4.2a)–(4.2b) can be combined to yield a wave equation for p_1, from which the basic mechanisms of sound production become directly apparent. With the speed of sound $c_0 = \gamma\,(p_0/\rho_0)$, the resulting wave equation reads

$$\frac{\mathrm{D}^2 p_1}{\mathrm{D}t^2} - \nabla \cdot \left(c_0^2 \nabla p_1 \right) = \underbrace{-\gamma p_0 \nabla \cdot \mathbf{s}_{f,1} + \frac{\mathrm{D}}{\mathrm{D}t}\left[\left(\gamma - 1\right) \dot{q}_1 \psi + s_{m,1} \right]}_{\text{driving}}$$
$$\underbrace{-\nabla \cdot \left(c_0^2 \nabla \cdot \tau_1 \right) + \left(\gamma - 1\right) \frac{\mathrm{D}}{\mathrm{D}t}\left[\nabla \cdot \left(\lambda \nabla T_1 \right) + \tau_0 : \nabla \mathbf{v}_1 \right]}_{\text{damping}} . \quad (4.3)$$

The above equation resembles a forced harmonic oscillator, where viscosity and heat diffusion dissipate sound. On the other hand, in a quiescent or uniformly flowing medium, sound is produced by spatially varying body force fields ($\propto \nabla \cdot s_{f,1}$), and by temporal variations in heat release rate ($\propto \mathrm{D}\dot{q}_1/\mathrm{D}t$) or in mass source intensity ($\propto \mathrm{D}s_{m,1}/\mathrm{D}t$). As illustrative examples for these three sources, consider a rotating lasso, a flickering candle and an open car window through which bulks of air periodically enter and leave the interior. By imposing uniform mean flow conditions, other sources of sound such as vortices (for example, in turbulent flow) cannot be captured. For a more detailed overview on acoustic theory, the interested reader is referred to standard literature (for example, [39, 92, 116, 130, 142]).

Reducing the analysis to one spatial dimension ξ, and provided a uniform medium without source terms, Eq. (4.3) can be re-written as

$$\left(\frac{\partial}{\partial t} + \left(c_0 + v_0 \right) \frac{\partial}{\partial \xi} \right) \left(\frac{\partial}{\partial t} - \left(c_0 - v_0 \right) \frac{\partial}{\partial \xi} \right) p_1 = 0 . \quad (4.4)$$

The left-hand side is given as the product of two advection equations with advection velocities $c_0 \pm v_0$, respectively. This suggests a solution of p_1 in terms of rightward and leftward traveling waves f and g, that are conserved along their

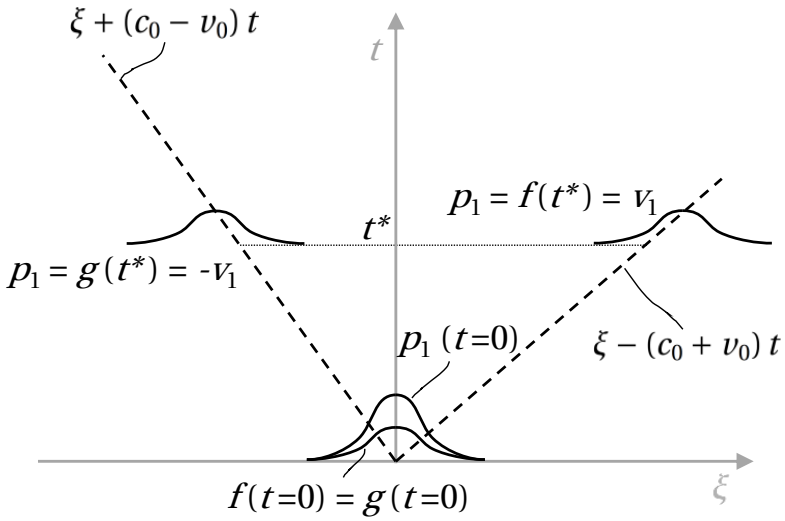

Figure 4.1: Planar acoustic wave propagation in the ξ-t-plane. The primitive acoustic variables v_1 and p_1 are equivalently represented in terms of the characteristic waves f and g. The latter advect along the respective characteristics $\xi \mp (c_0 \pm v_0)\,t$.

respective characteristics, $f = f\big(\xi - (c_0 + v_0)\,t\big)$ and $g = g\big(\xi + (c_0 - v_0)\,t\big)$. It can easily be verified that a solution to Eq. (4.4) is given by $p_1 = \rho_0 c_0\,(f + g)$. By use of Eq. (4.2a) in the absence of sources, we find an equivalent representation of planar acoustic wave propagation in terms of the so-called characteristic waves,

$$\begin{bmatrix} v_1 \\ p_1 \end{bmatrix} = \begin{bmatrix} 1 & -1 \\ \rho_0 c_0 & \rho_0 c_0 \end{bmatrix} \begin{bmatrix} f \\ g \end{bmatrix}. \tag{4.5}$$

In contrast to the primitive variables v_1 and p_1, f and g are directed waves. At times, this may facilitate physical interpretation and prove beneficial to distinguishing cause from effect, or signal from response. Still, whichever representation best suits the problem at hand needs to be determined on a case-to-case basis. The propagation of 1-D acoustic waves in both representations is depicted in the ξ-t-plane in Fig. 4.1 for illustration.

4.2 A Simple Acoustic System

The present study is intended to investigate the basic origins and mechanisms of non-normal transient growth in thermoacoustic systems. The analysis is therefore intentionally reduced to a minimum degree of complexity, so as to isolate the interaction of a heat source and an acoustic field. This is conveniently done by studying the most basic of all thermoacoustic systems, a configuration inspired by the classical Rijke tube [143]. In the following, we will derive the corresponding governing equations, for which the set of equations (4.2) serves as starting point.

The setup is illustrated in Fig. 4.2. It consists of a straight duct of length L_A and constant cross-sectional area A_A. The spatial domain of the duct is defined by the 1-D set $X = \{\xi : \xi \in [0,1]\}$. A heat source is located at $\xi = \xi_F$. The spatial extent of the flame is assumed to be much smaller than an acoustic wave length. The flame is therefore treated as acoustically compact. All other source terms to the acoustic field appearing in Eq. (4.3) are zero. The dissipative effects of heat and viscous diffusivity are modeled by negative semidefinite damping terms for velocity and pressure, ζ_v and ζ_p, respectively. We consider planar wave propagation in one spatial dimension ξ. The volume function ψ can thus be expressed by a 1-D function ψ_q, $\psi = \psi_q / A_A$, as the heat source affects the acoustic field over a constant cross-sectional area A_A. We further assume homentropic conditions, $\sigma_1 = 0$. Equation (4.2c) therefore does not need to be taken into account. Both duct ends are treated as acous-

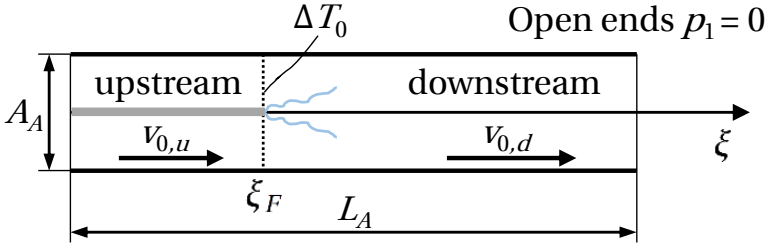

Figure 4.2: 1-D duct configuration with non-zero mean flow v_0 and non-zero mean temperature jump ΔT_0 resulting from the heat source located at ξ_F. The open duct ends are acoustically fully reflective.

tically open, which corresponds to perfectly reflective ends with $p_1 = 0$ resulting from an area jump to the outside of infinity. The zero-th order quantities are assumed constant up- and downstream of the heat source. That is, T_0, ρ_0 and c_0 may only vary if $\psi_q \neq 0$. As mentioned above, $p_0 = const.$ everywhere, because the Mach number is small. Finally, in order to bring pressure and velocity perturbations to the same order of magnitude, all acoustic variables are non-dimensionalized by the reference scales,

$$\begin{aligned} v_{\mathrm{ref}} &= c_0\,, \quad \xi_{\mathrm{ref}} = L_A\,, \quad p_{\mathrm{ref}} = \rho_0\, c_0^2\,, \quad \dot{q}_{\mathrm{ref}} = \dot{q}_0\,, \\ t_{\mathrm{ref}} &= \frac{\xi_{\mathrm{ref}}}{v_{\mathrm{ref}}} = \frac{L_A}{c_0}\,, \quad \zeta_{\mathrm{ref}} = \frac{1}{t_{\mathrm{ref}}} = \frac{c_0}{L_A}\,, \quad \psi_{\xi,\mathrm{ref}} = \frac{1}{L_A}\,. \end{aligned} \tag{4.6}$$

Applying the assumptions introduced in the previous paragraph to Eqs. (4.2a)–(4.2b) and using the reference scales (4.6) yields the following set of non-dimensional governing equations[1]:

$$\frac{\partial v_1}{\partial t} = -M\frac{\partial v_1}{\partial \xi} - \left(3\frac{\partial M}{\partial \xi} - \zeta_v\right) v_1 - \frac{\partial p_1}{\partial \xi}\,, \tag{4.7a}$$

$$\frac{\partial p_1}{\partial t} = -\frac{\partial v_1}{\partial \xi} - \frac{1}{\beta}\frac{\partial \beta}{\partial \xi}\, v_1 - M\frac{\partial p_1}{\partial \xi} - \left(2\gamma\frac{\partial M}{\partial \xi} - \zeta_p\right) p_1 + K\,\dot{q}_1\,\psi_q\,. \tag{4.7b}$$

The steps of non-dimensionalization are presented in App. B. The term $\beta = \beta(\xi)$ in Eq. (4.7b), which expresses the spatial profile of the speed of sound normalized by its mean value upstream of the heat source, is a function of the spatial temperature profile along the duct,

$$\beta(\xi) = \frac{c_0(\xi)}{c_{0,u}} = 1 + \Delta_\beta \int_0^\xi \psi_q(\tilde{\xi})\,\mathrm{d}\tilde{\xi}\,, \tag{4.8}$$

with the 1-D function of heat addition ψ_q, the temperature incremental factor $\Delta_\beta = \sqrt{T_{0,d}\,/\,T_{0,u}} - 1$, and where $T_{0,d}\,/\,T_{0,u}$ represents the ratio of mean temperatures down- (index d) and upstream (index u) of the heat source. Equivalently, $\Delta_\beta = c_{0,d}\,/\,c_{0,u} - 1$ is related to the ratio of speeds of sound. The Mach number is defined as $M = v_0\,/\,c_0$. As the bulk mean flow must obey continuity

[1] In the following, unless otherwise mentioned, all acoustic variables are given in dimensionless form. A formal symbolic distinction to dimensional quantities is omitted in the interest of readability.

$\rho_0 v_0 = const.$, the local Mach number varies as $M_d = (\Delta_\beta + 1)\, M_u$, and thus

$$M(\xi) = \frac{v_0(\xi)}{c_0(\xi)} = M_u \left(1 + \Delta_\beta \int_0^\xi \psi_q(\tilde{\xi})\, \mathrm{d}\tilde{\xi} \right). \tag{4.9}$$

Finally, the strength of the heat source is regulated by the scalar

$$K = K_0 \left(\gamma - 1\right) \frac{\dot{q}_0}{\rho_0\, c_0^3\, A_A}, \tag{4.10}$$

which normalizes the mean heat release rate per duct area with an equivalent acoustic power per unit area. The parameter K_0 has been introduced to adjust the strength of the fluctuating heat source.

In reality, the parameter $K_0 = 1$, such that mean flow, damping, the temperature jump and the strength of the heat source are not independent from each other. Whatever heat is produced by the heat source spreads by convection and molecular diffusion; if it is a reacting heat source, fresh combustibles are transported to the flame by the mean flow; and so on. However, the simple model given in terms of Eqs. (4.7) contains M_u, Δ_β, K_0 and ζ_i as independent parameters. This provides a basis for investigating different effects separately: the effect of mean flow (controlled by M_u), the effect of a fluctuating heat source (controlled by Δ_β, K, ψ_q), and the effect of damping terms (regulated by ζ_v, ζ_p). In the present study, K is effectively used as bifurcation parameter (see Sec. 6.2). An overview of parameters encountered in previous studies of laminar thermoacoustic systems is shown in Tab. 1.1.

In the present study, the heat source is assumed acoustically compact. The heat is thus locally added to the flow field at the position of the compact heat source ξ_F, and the 0-th order quantities remain constant up- and downstream of the heat source, respectively. That is, the mean temperature T_0, density ρ_0 and speed of sound c_0 exhibit a jump at ξ_F. We therefore define the 1-D spatial profile ψ_q appearing in Eqs. (4.8) and (4.9) as a Dirac measure δ_{ξ_F} for any subset $X_A \subseteq X$,

$$\psi_q = \delta_{\xi_F}(X_A) = \begin{cases} 1 & \text{if } \xi_F \in X_A \\ 0 & \text{if } \xi_F \notin X_A\,. \end{cases} \tag{4.11}$$

Consequently, the identity

$$\int_{X_A} \phi(\tilde{\xi})\, \delta_{\xi_F}(\tilde{\xi})\, \mathrm{d}\tilde{\xi} = \begin{cases} \phi(\xi_F) & \text{if } \xi_F \in X_A \\ 0 & \text{if } \xi_F \notin X_A\,, \end{cases} \tag{4.12}$$

holds for any given function $\phi(\xi)$.

With this definition for ψ_q, Eqs. (4.8)–(4.9) become

$$\beta(\xi) = \begin{cases} 1 & \text{for } 0 \le \xi < \xi_F \\ 1+\Delta_\beta & \text{for } \xi_F \le \xi \le 1\,, \end{cases}$$

$$M(\xi) = \begin{cases} M_u & \text{for } 0 \le \xi < \xi_F \\ M_u\,(1+\Delta_\beta) & \text{for } \xi_F \le \xi \le 1\,, \end{cases}$$

and the terms $1/\beta\,\partial\beta/\partial\xi$ and $\partial M/\partial\xi$ in Eqs. (4.7) read

$$\frac{1}{\beta}\frac{\partial\beta}{\partial\xi} = \begin{cases} \dfrac{\Delta_\beta}{1+\Delta_\beta} & \text{for } \xi = \xi_F \\ 0 & \text{for } 0 \le \xi < \xi_F \wedge \xi_F < \xi \le 1\,, \end{cases}$$

$$\frac{\partial M}{\partial\xi} = \begin{cases} M_u\,\Delta_\beta & \text{for } \xi = \xi_F \\ 0 & \text{for } 0 \le \xi < \xi_F \wedge \xi_F < \xi \le 1\,, \end{cases}$$

For non-compact heat sources, other functions expressing the spatial profile of heat addition are conceivable (e.g., a Gaussian or a polynomial function).

In the following, the above description of a simple acoustic field is put into the systemic context of an acoustics subsystem.

4.3 Systems Representation of the Acoustics Subsystem

In analogy to the procedure followed for the heat source subsystem $\mathcal{S}^{(F)}$ in Sec. 3.2, the present section deals with putting the model of the simple acoustic system defined in the previous Sec. 4.2 into the generic form of an input-state-output model structure (see Sec. 4.3.1). In Sec. 4.3.2, we discuss existing system theory-based approaches in the field of thermoacoustics.

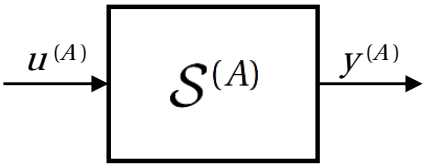

Figure 4.3: Scheme of the acoustics subsystem $\mathcal{S}^{(A)}$.

4.3.1 A Simple Acoustic Model

The acoustics subsystem $\mathcal{S}^{(A)}$ as introduced in the previous section is schematically depicted in Fig. 4.3. The continuous partial differential state space representation of $\mathcal{S}^{(A)}$ takes the form of Eq. (2.3), where the input-state-output variables of $\mathcal{S}^{(A)}$ are directly apparent from Eq. (4.7). They are fluctuations in heat release rate, the acoustic variables in ξ, and velocity fluctuations at the position of the heat source (which, in turn, serve as input to the heat source subsystem $\mathcal{S}^{(F)}$),

$$u^{(A)} = \dot{q}_1\,, \quad x^{(A)} = \left[\, v_1(\xi)\,,\; p_1(\xi) \,\right]^T, \quad y^{(A)} = v_1(\xi_F)\,. \tag{4.13}$$

Accordingly, the model $(\mathcal{A}^{(A)}, \mathcal{B}^{(A)}, \mathcal{C}^{(A)})$ is defined by the differential operators,

$$\mathcal{A}^{(A)} = \begin{bmatrix} -M\dfrac{\partial}{\partial\xi} - \left(3\dfrac{\partial M}{\partial\xi} - \zeta_v\right) & -\dfrac{\partial}{\partial\xi} \\ -\dfrac{\partial}{\partial\xi} - \dfrac{1}{\beta}\dfrac{\partial\beta}{\partial\xi} & -M\dfrac{\partial}{\partial\xi} - \left(2\gamma\dfrac{\partial M}{\partial\xi} - \zeta_p\right) \end{bmatrix}, \tag{4.14a}$$

$$\mathcal{B}^{(A)} = \left[\, 0\,,\; K\psi_q \,\right]^T, \tag{4.14b}$$

$$\mathcal{C}^{(A)} = \left[\, \psi_q\,,\; 0 \,\right]. \tag{4.14c}$$

An equivalent representation of the model describing $\mathcal{S}^{(A)}$ in terms of characteristic waves is obtained by state transformation with the non-dimensionalized version of the state transformation given in Eq. (4.5). This leads to a continuous partial differential state space representation of the form

of Eq. (2.3) with the transformed states given as characteristic waves in space,

$$\tilde{x}^{(A)} = \Big[\, f(\xi)\,,\; g(\xi) \,\Big]^T . \tag{4.15}$$

The transformed model $(\tilde{\mathcal{A}}^{(A)}, \tilde{\mathcal{B}}^{(A)}, \tilde{\mathcal{C}}^{(A)})$ is defined by

$$\tilde{\mathcal{A}}^{(A)} = \begin{bmatrix} -\big(1+M\big)\dfrac{\partial}{\partial\xi} - D_\beta - D_M^+ + \dfrac{\big(\zeta_p+\zeta_v\big)}{2} & D_\beta + D_M^- + \dfrac{\big(\zeta_p-\zeta_v\big)}{2} \\ -D_\beta + D_M^- + \dfrac{\big(\zeta_p-\zeta_v\big)}{2} & \big(1-M\big)\dfrac{\partial}{\partial\xi} + D_\beta - D_M^+ + \dfrac{\big(\zeta_p+\zeta_v\big)}{2} \end{bmatrix}, \tag{4.16a}$$

$$\tilde{\mathcal{B}}^{(A)} = \frac{1}{2}\Big[\, K\psi_q\,,\; K\psi_q \,\Big]^T , \tag{4.16b}$$

$$\tilde{\mathcal{C}}^{(A)} = \Big[\, \psi_q\,,\; -\psi_q \,\Big] , \tag{4.16c}$$

with the abbreviated terms

$$D_\beta = \frac{1}{2\beta}\frac{\partial\beta}{\partial\xi} , \quad \text{and} \quad D_M^\pm = \frac{\big(3\pm 2\gamma\big)}{2}\frac{\partial M}{\partial\xi} .$$

For the conditions under which the characteristic waves were derived following Eq. (4.4) (i.e., $\Delta_\beta = 0$ and $\zeta_p = \zeta_v = 0$, so $D_\beta = D_M^\pm = 0$), it is apparent that $\tilde{\mathcal{A}}^{(A)}$ reduces to a diagonal partial differential operator, in which the non-zero entries govern the propagation of f and g waves to the right and left at phase velocities $(1 \pm M)$, respectively.

The model of the acoustics subsystem $\mathcal{S}^{(A)}$ represented by Eqs. (4.14) or (4.16) is not amenable to an analytical solution. It needs to be solved by numerical means, which will be addressed in Sec. 4.4.

4.3.2 Other Representations

Naturally, there exist other approaches to representing an acoustic system $\mathcal{S}^{(A)}$ in state space form. Among others, two merit special attention, since—to the author's knowledge—they have been the first in the field of thermoacoustics to adopt a systemic perspective.

Schuermans *et al.* adopt a hybrid analytical/numerical approach [150–152]. They bring an analytical solution of the simple wave equation Eq. (4.4) without mean flow and one generic source term to state space form. The analytical solution, which is detailed in [29], depends on the eigenfunctions and -frequencies of the system. This provides for a considerable amount of flexibility, as the eigenmodes can be obtained numerically for various geometries, or even analytically for very simple configurations.

Paschereit and co-workers follow a similar approach as that detailed in Sec. 3.3.2 for the heat source subsystem $\mathcal{S}^{(F)}$ [16, 126]. Starting from measured or computed frequency response data of an acoustic element of interest, they compute a SSM with corresponding input-output behavior. The resulting SSM is mostly of very low order ($N \sim \mathcal{O}(10^1)$). As the only constraints to the model are with respect to input and output, the states are arbitrary and do not necessarily correspond to physically identifiable quantities.

In the present work, we resort to numerically solving the partial differential state space representation of $\mathcal{S}^{(A)}$ defined in Sec. 4.3.1. Despite limiting our analysis to very simple duct configurations, there are strong reasons in doing so with regards to the aim of the present study. As mentioned in Sec. 1.3, we wish to retain a maximum degree of flexibility in studying different output metrics. This excludes the approach taken by Paschereit and co-workers, since it would require significant effort to obtain a variety of corresponding output data, to which a low-order SSM could be fitted. The other approach mentioned above relies on very complicated analytical models, which strictly speaking only exist for a rather constrictive set of assumptions (for example, no temperature jump, no mean flow, etc.). Flexibility in determining the eigenmodes does not outweigh these drawbacks.

4.4 Numerical Implementation

In the present section, the model describing $\mathcal{S}^{(A)}$ introduced in Sec. 4.3.1 is rendered amenable to numerical treatment by discretization in space (see Sec. 4.4.1) and alternatively by projection onto basis functions (see Sec. 4.4.2).

4.4.1 Direct Solution by Finite Differences

Primitive Variables-Based Representation

The continuous state vector $x^{(A)}$ is uniformly discretized in space as

$$\mathbf{x}^{(A)} = \Big[v_1(0)\,,\; v_1(\Delta\xi)\,,\; v_1(2\Delta\xi)\,,\; \cdots\,,\; v_1(N_{A,\mathrm{FD}}\Delta\xi)\,, \\ p_1(\Delta\xi)\,,\; p_1(2\Delta\xi)\,,\; \cdots\,,\; p_1((N_{A,\mathrm{FD}}-1)\Delta\xi) \Big]^T\,, \quad N_{A,\mathrm{FD}}\Delta\xi = 1\,, \tag{4.17}$$

and the partial differentials in $\mathcal{A}^{(A)}$ are approximated by 2$^{\mathrm{nd}}$ order central finite differences (FD). The discrete input and output matrices are trivial. As for the model describing the heat source subsystem $\mathcal{S}^{(F)}$, time marching is performed by an RK3 TVD scheme. Since $\mathcal{S}^{(A)}$ is SISO, $\mathbf{u}^{(A)} = u^{(A)}$ and $\mathbf{y}^{(A)} = y^{(A)}$ as defined in Eq. (4.13). The set of discrete matrices $(\mathbf{A}^{(A)}, \mathbf{B}^{(A)}, \mathbf{C}^{(A)})$ are explicitly given in App. C.3.1. Sufficient grid independence on the computed results is achieved for $N_{A,\mathrm{FD}} = 100$ (see Tab. 4.1).

The pressure nodes at the boundaries are not contained in $\mathbf{x}^{(A)}$, as the duct ends are acoustically fully reflective, $p_1(\xi = 0) = p_1(\xi = 1) = 0$. The non-reflecting boundary conditions for v_1 are implemented by so-called local one-dimensional inviscid (LODI) relations [131]. They are derived by transforming the left-hand side of the state equation to a characteristics-based representation, which leads to an evolution equation for the characteristic waves in terms of primitive variables. The unknown incoming wave is then computed as a function of the known outgoing wave. For full reflection, they must be equal. Assuming $\psi_q = 0$ at the boundaries, this yields the following equations for v_1:

$$\frac{\partial v_1}{\partial t} = \begin{cases} \big(1 - M_u\big)\dfrac{\partial v_1}{\partial \xi} + \zeta_v\, v_1 - \big(1 - M_u\big)\dfrac{\partial p_1}{\partial \xi} & \text{at } \xi = 0\,, \\ -\big(1 + M_d\big)\dfrac{\partial v_1}{\partial \xi} + \zeta_v\, v_1 - \big(1 + M_d\big)\dfrac{\partial p_1}{\partial \xi} & \text{at } \xi = 1\,, \end{cases} \tag{4.18}$$

which are solved by 2$^{\mathrm{nd}}$ order one-sided finite differences.

As mentioned in Sec. 3.2.1, FD methods are ill-suited for numerically resolving steep gradients. The function of the spatial profile of heat release rate ψ_q

	rel. deviation of λ | ω of eigenfrequency # [%]				
$N_{A,\mathrm{FD}}$	1	2	3	4	5
10	-13.2 | 12.1	-0.82 | -3.98	6.78 | -16.84	0.76 | -38.0	0.72 | -43.37
50	6.20 | -0.67	0.81 | -0.30	-0.10 | -0.72	-0.48 | -1.13	0.15 | -0.17
100	0.86 | -0.13	0.03 | -0.04	-0.02 | -0.07	0.07 | -0.10	0.39 | -0.14
200	0.00 | 0.07	0.00 | -0.00	-0.00 | -0.03	-0.00 | -0.06	-0.00 | -0.08
500	–	–	–	–	–

Table 4.1: Grid study of the primitive variables-based FD method: relative deviation in the values of growth rate λ and angular frequency of oscillation ω with respect to the absolute values of the first five complex-valued eigenfrequencies of $\mathbf{A}^{(A)}$ as a function of the number of discrete points $N_{A,\mathrm{FD}}$. The deviation is computed with respect to the finer grid resolution. Sufficient grid resolution is achieved for $N_{A,\mathrm{FD}} = 100$, because a finer resolution does not improve the results by more than 1 %. Other parameters: $\xi_F = 0.2$, $\zeta_v = -0.08$, $\zeta_p = -0.025$, $\Delta_\beta = 2$, $M_u = 0.01$.

therefore takes the shape of a discrete Gaussian distribution function of width $0.05\,N_{A,\mathrm{FD}}\Delta\xi$ centered at the node at ξ_F. In this manner, the heat addition to the acoustic field is smoothened around ξ_F, and is flawlessly captured by the 2^{nd} order central FD scheme. This is reflected in $\mathbf{B}^{(A)}$ (see Eq. (C.11)).

Characteristic Waves-Based Representation

In analogy to the primitive variables representation, it is possible to directly solve the transformed model describing $\mathcal{S}^{(A)}$ in terms of characteristic waves by FD or FE schemes. However, as f and g are governed by advection equations, an elegant alternative is to make use of a time-space solution technique, which is described in the following.

As shown in Fig. 4.4, the continuous state vector $\tilde{x}^{(A)}$ is discretized in space as

$$\tilde{\mathbf{x}}^{(A)} = \Big[f(\Delta_f\xi\,,\, f(2\Delta_f\xi\,,\,\cdots\,,\, f(N_{\tilde{A},f}\Delta_f\xi\,, \\ g(0\,,\, g(\Delta_g\xi\,,\, g(2\Delta_g\xi\,,\,\cdots\,,\, g((N_{\tilde{A},g}-1)\Delta_g\xi\Big]^T\,, \\ \text{where } N_{\tilde{A},f}\Delta_f\xi = N_{\tilde{A},g}\Delta_g\xi = 1\,. \tag{4.19}$$

The spatial step width is chosen such that information propagates by one node per numerical time step Δt, which is equivalent to a Courant number of CFL = 1,

$$\frac{(1+M)\,\Delta t}{\Delta_f\xi} = \frac{(1-M)\,\Delta t}{\Delta_g\xi} = 1\,. \tag{4.20}$$

Approximating the partial differentials in $\tilde{\mathcal{A}}^{(A)}$ given in Eq. (4.16a) by 1st order backward and forward FD schemes for rightward-traveling f and leftward-traveling g waves, respectively, in combination with a 1st order forward FD scheme in time, leads to a simple, yet numerically absolutely stable and non-dissipative discrete time-space scheme,

$$f_i^{n+1} = f_{i-1}^n - \Delta t\left(D_\beta + D_M^+ - \frac{\zeta_p+\zeta_v}{2}\right) f_i^n + \Delta t\left(D_\beta + D_M^- + \frac{\zeta_p-\zeta_v}{2}\right) g_i^n\,, \tag{4.21a}$$

$$g_i^{n+1} = g_{i+1}^n - \Delta t\left(D_\beta - D_M^- - \frac{\zeta_p-\zeta_v}{2}\right) f_i^n + \Delta t\left(D_\beta - D_M^+ + \frac{\zeta_p+\zeta_v}{2}\right) g_i^n\,, \tag{4.21b}$$

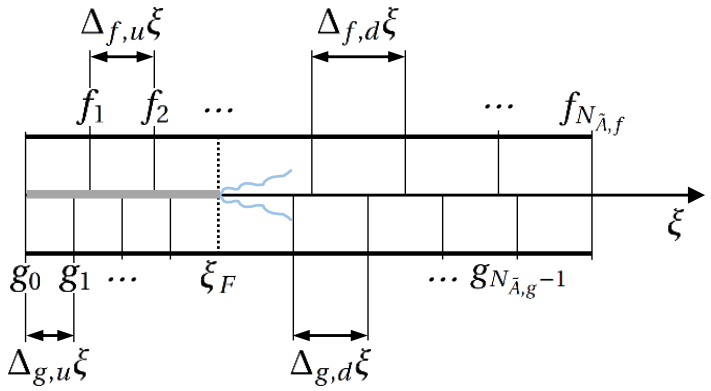

Figure 4.4: Discretization of the characteristic waves-based model of $\mathcal{S}^{(A)}$. The step widths $\Delta_f\xi$ and $\Delta_g\xi$ depend on the spatially varying Mach number $M(\xi)$.

with the abbreviated terms D_β and $D_M^\pm$ as detailed in the following paragraph. The index i and superscript n denote respective discrete steps in space and time. $i \in [2; N_{\tilde{A},f}]$ and $i \in [0, N_{\tilde{A},g} - 2]$ for f and g, respectively. The first term in each of the Eqs. (4.21) is called *history update* by Mangesius & Polifke ("tomorrow's yesterday is today") [105]. They were the first to use this scheme in the thermoacoustic context.

The abbreviated terms in Eqs. (4.21) read

$$D_\beta = \frac{\Delta_\beta}{2\left(1+\Delta_\beta\right)}\psi_q\,, \quad \text{and} \quad D_M^\pm = \frac{\left(3 \pm 2\gamma\right)}{2} M_u \Delta_\beta \psi_q\,. \tag{4.22}$$

For an acoustically compact heat source, the spatial temperature profile is the Dirac delta function measure as defined in Eq. (4.11). The effect of a non-zero compact temperature jump hence causes a scaling operation of the acoustic waves at the node at ξ_F. This amounts to scattering the acoustic waves at the impedance jump, where the incoming waves are transmitted and reflected.

Fully reflective boundary conditions are achieved by referencing the history update of the (unknown) incoming waves f_1 and $g_{N_{\tilde{A},g}-1}$ to the (known) outgoing waves g_0 and $f_{N_{\tilde{A},f}}$,

$$\begin{aligned} f_1^{n+1} &= g_0^n - \Delta t \left(D_\beta + D_M^+ - \frac{\zeta_p + \zeta_v}{2} \right) f_1^n\,, \\ g_{N_{\tilde{A},g}-1}^{n+1} &= f_{N_{\tilde{A},f}}^n + \Delta t \left(D_\beta - D_M^+ + \frac{\zeta_p + \zeta_v}{2} \right) g_{N_{\tilde{A},g}-1}^n\,, \end{aligned} \tag{4.23}$$

which is analog to the LODI relations introduced in the previous section.

Despite its elegance and apparent simplicity, the challenge involved with the present time-space scheme lies in finding a suitable discretization of f and g. From Eq. (4.20), it follows that one needs to find *integer* numbers of steps $N_{\tilde{A},f}$ and $N_{\tilde{A},g}$, that fulfill $N_{\tilde{A},g}/N_{\tilde{A},f} = (1-M)/(1+M)$. Without mean flow $M_d = 0$, or without a temperature jump $\Delta_\beta = 0$, this is straightforward. However, in the more practical case of $M_d \neq 0$ and $\Delta_\beta \neq 0$, M is a function of space (see Eq. (4.9)). The step width thus varies from up- to downstream side of the heat source. Under these circumstances, finding suitable $N_{\tilde{A},f}$ and $N_{\tilde{A},g}$ is all but trivial. This is also challenging from an implementation point of view.

As the present study is intended to study the effects of M_u and Δ_β on non-normal transient growth in thermoacoustics, the characteristic waves-based representation is not further considered in the present work. It is nonetheless a viable and elegant modeling option.

4.4.2 Method of Weighted Residuals

In the following, we introduce a method that uses a variational formulation to approximate the governing set of partial differential equations (PDE) (4.7). It is very similar to FE methods and well known under the name of Galerkin method (to name but a few examples in the thermoacoustic literature, [77, 107, 165]). However, in recent historical overviews of the method [30, 31], Culick argues that the full breadth and universal character of the method reaches far beyond Galerkin's intentions. We follow Culick's line of arguments, and refer to the method as *method of weighted residuals* (MWR).

The variational formulation of the MWR starts from the partial differential state equation governing $\mathcal{S}^{(A)}$,

$$\int_0^1 \left(\dot{x}^{(A)} - \mathcal{A}^{(A)}\, x^{(A)} - \mathcal{B}^{(A)}\, u^{(A)} \right) \mathrm{d}\xi = 0\,, \tag{4.24}$$

The state variables are projected onto spatial basis functions $T_{M,j}(\xi)$,

$$x^{(A)} = \sum_{j=1}^{N_{A,M}} x_{M,j}^{(A)}(t)\, T_{M,j}(\xi) = \mathcal{T}_M \mathbf{x}_M^{(A)}\,, \tag{4.25}$$

which amounts to a time-space decoupling state transformation of the continuous acoustic state vector $x^{(A)}(\xi, t)$ to the discrete state vector of the MWR $\mathbf{x}_M^{(A)}(t)$. The columns of $\mathcal{T}_M$ contain the spatial basis functions $T_{M,j}$. Substituting Eq. (4.25) into Eq. (4.24) and multiplying by test functions $T_{M,k}(\xi)$—which are chosen as the same as the basis functions[2]—, leads to an ordinary differ-

[2] This step is sometimes referred to as the *Galerkin choice*.

ential state equation for $\mathbf{x}_M^{(A)}$:

$$\left(\int_0^1 \mathcal{T}_M \mathcal{T}_M \,\mathrm{d}\xi\right) \dot{\mathbf{x}}_M^{(A)} = \left(\int_0^1 \left(\mathcal{A}^{(A)} \mathcal{T}_M\right) \mathcal{T}_M \,\mathrm{d}\xi\right) \mathbf{x}_M^{(A)} + \left(\int_0^1 \left(\mathcal{B}^{(A)} \mathcal{T}_M\right) \mathrm{d}\xi\right) u^{(A)} \,. \tag{4.26}$$

The partial differential operators $\mathcal{A}^{(A)}$ and $\mathcal{B}^{(A)}$ hence operate on known spatial expansion functions $T_{M,j}$. Equation (4.26) can then be brought to the form of a discrete SSM

$$\dot{\mathbf{x}}_M^{(A)} = \mathbf{A}_M^{(A)} \mathbf{x}_M^{(A)} + \mathbf{B}_M^{(A)} \mathbf{u}_M^{(A)} \,, \tag{4.27a}$$

$$\mathbf{y}_M^{(A)} = \mathbf{C}_M^{(A)} \mathbf{x}_M^{(A)} \,. \tag{4.27b}$$

Since $\mathcal{S}^{(A)}$ is SISO, $\mathbf{u}_M^{(A)} = u^{(A)}$ and $\mathbf{y}_M^{(A)} = y^{(A)}$ as defined in Eq. (4.13).

The crucial step consists in selecting adequate expansion functions, so as to minimize the residual of the approximation Eq. (4.26) (hence the name of the method). Although not mandatory in principle, it is useful to base the choice on physical considerations of the problem at hand.

For the primitive acoustic variables v_1 and p_1, it is convenient to use the mode shapes of the fundamental acoustic duct problem without mean flow, temperature jump and heat source as expansion functions,

$$v_1(\xi, t) = \sum_{j=1}^{N_{A,M}} \cos(j\pi\xi)\, v_{M,j}(t) \,, \tag{4.28a}$$

$$p_1(\xi, t) = \sum_{j=1}^{N_{A,M}} \sin(j\pi\xi)\, p_{M,j}(t) \,, \tag{4.28b}$$

so

$$\begin{aligned} \mathbf{x}_M^{(A)} = \Big[& v_{M,1}(t) \,,\, v_{M,2}(t) \,,\, \cdots \,,\, v_{M,N_{A,M}}(t) \\ & p_{M,1}(t) \,,\, p_{M,2}(t) \,,\, \cdots \,,\, p_{M,N_{A,M}}(t) \Big]^T \,, \end{aligned} \tag{4.29}$$

and

$$\mathcal{T}_M = \begin{bmatrix} \cos(\pi\xi) & \cos(2\pi\xi) & \cdots & \cos(N_{A,M}\pi\xi) \\ \sin(\pi\xi) & \sin(2\pi\xi) & \cdots & \sin(N_{A,M}\pi\xi) \end{bmatrix} \,. \tag{4.30}$$

	rel. deviation of λ | ω of eigenfrequency # [%]				
$N_{A,M}$	1	2	3	4	5
1	0.47 | -0.18	-0.21 | -54.1	-0.52 | -70.7	-0.81 | -78.2	-1.27 | -82.1
5	-0.08 | 0.17	-0.02 | 0.04	0.02 | -0.03	0.00 | -0.10	0.25 | 0.19
10	-0.01 | 0.14	-0.01 | 0.03	0.00 | -0.02	-0.00 | -0.03	-0.01 | 0.00
50	-0.00 | 0.02	-0.00 | 0.00	0.00 | -0.00	0.00 | -0.00	0.00 | 0.00
100	–	–	–	–	–

Table 4.2: Grid study of the MWR: relative deviation in the values of growth rate λ and frequency of oscillation ω with respect to the absolute values of the first five complex-valued eigenfrequencies of $\mathbf{A}_M^{(A)}$ as a function of the number of expansion functions $N_{A,M}$. The deviation is computed with respect to the finer resolution. Sufficient resolution is achieved for $N_{A,M} = 5$, because an increase in $N_{A,M}$ does not improve the results by more than 1 %. Other parameters: $\xi_F = 0.2$, $\zeta_1 = -0.08$, $\zeta_2 = -0.025$, $\Delta_\beta = 2$, $M_u = 0.01$.

The main benefit is that these expansion functions implicitly fulfill the boundary conditions at the duct ends, $p_1 = 0$ and $\partial v_1/\partial\xi \approx 0$ at $\xi = 0$ and $\xi = 1$.[3] Additional flux terms at the boundaries are thus not needed.

Analog to the characteristic waves-based representation, the MWR can account for a compact heat source with impulsive 1-D temperature profiles ψ_q as defined in Eq. (4.11). Also, since the acoustic field is modally expanded, the MWR provides for a unique possibility to implement frequency-dependent damping in time domain. This stands in contrast to the solution by FD, where the damping terms can only assume constant values. We use a damping correlation by Matveev & Culick [113], where damping increases with frequency,

$$\zeta_v = 0\,, \quad \text{and} \quad \zeta_p = \zeta_{p,j} = \zeta_1\, j + \zeta_2 \sqrt{\frac{1}{j}}\,. \tag{4.31}$$

This *modal damping model* and variants thereof are widely used in the thermoacoustic community (for example, [77, 82, 108, 165]). The damping co-

[3] The boundary condition for v_1 is a good approximation for low Mach numbers, as $\partial v_1/\partial\xi = -M\,\partial p_1/\partial\xi$, see Eq. (4.7b).

efficients ζ_1 and ζ_2 model the effects of dissipation at the duct ends and in the boundary layer, respectively. According to [81], typical values for laboratory-scale Rijke tubes are $\zeta_1 \approx -0.01 \ldots -0.13$ and $\zeta_2 \approx -0.005 \ldots -0.03$.

The corresponding set of discrete matrices $(\mathbf{A}_M^{(A)}, \mathbf{B}_M^{(A)}, \mathbf{C}_M^{(A)})$ is given in App. C.3.2. It is visible from Tab. 4.2 that sufficient independence upon the number of expansion functions is achieved for $N_{A,M} = 5$. However, to ensure numerical independence in the presence of a fluctuating heat source (see the study on numerical resolution in Fig. 7.5), we decide to use $N_{A,M} \leq 30$ in the remainder of the present work. As for all other methods introduced in Chaps. 3 and 4, integration in time is realized by an RK3 TVD scheme.

Unless otherwise mentioned, the acoustics subsystem $\mathcal{S}^{(A)}$ is approximated by the MWR in the remainder of this thesis. The first reason is the reduced computational cost as compared to the FD scheme due to the lower number of degrees of freedom necessary for numerical convergence, while still being able to incorporate non-zero mean flow and temperature jump. Secondly, the possibility of making use of a modal damping method is appealing, because it is a better approximation of experimentally observed damping characteristics than a constant damping model. Thirdly, the discrete matrices of the MWR possess a better condition number as compared to the FD scheme, which is important for non-normal analysis. We will return to this point in Sec. 7.1.

4.5 The Effect of a Base Flow and Temperature Jump

The present section intends to investigate the effect of a non-zero base flow and temperature jump at the position of the heat source onto the acoustic field in the simple thermoacoustic system as introduced in Sec. 4.2. Nicoud & Wieczorek [122] have found mean flow to change the growth rate and frequency of oscillation of acoustic modes significantly even for very small Mach numbers. In the following, we analyze the change in acoustic eigenmodes and eigenvalues subject to the range of upstream Mach numbers and temperature incremental factors, $M_u \in [0, 0.01]$ and $\Delta_\beta \in [0, 2]$, respectively.

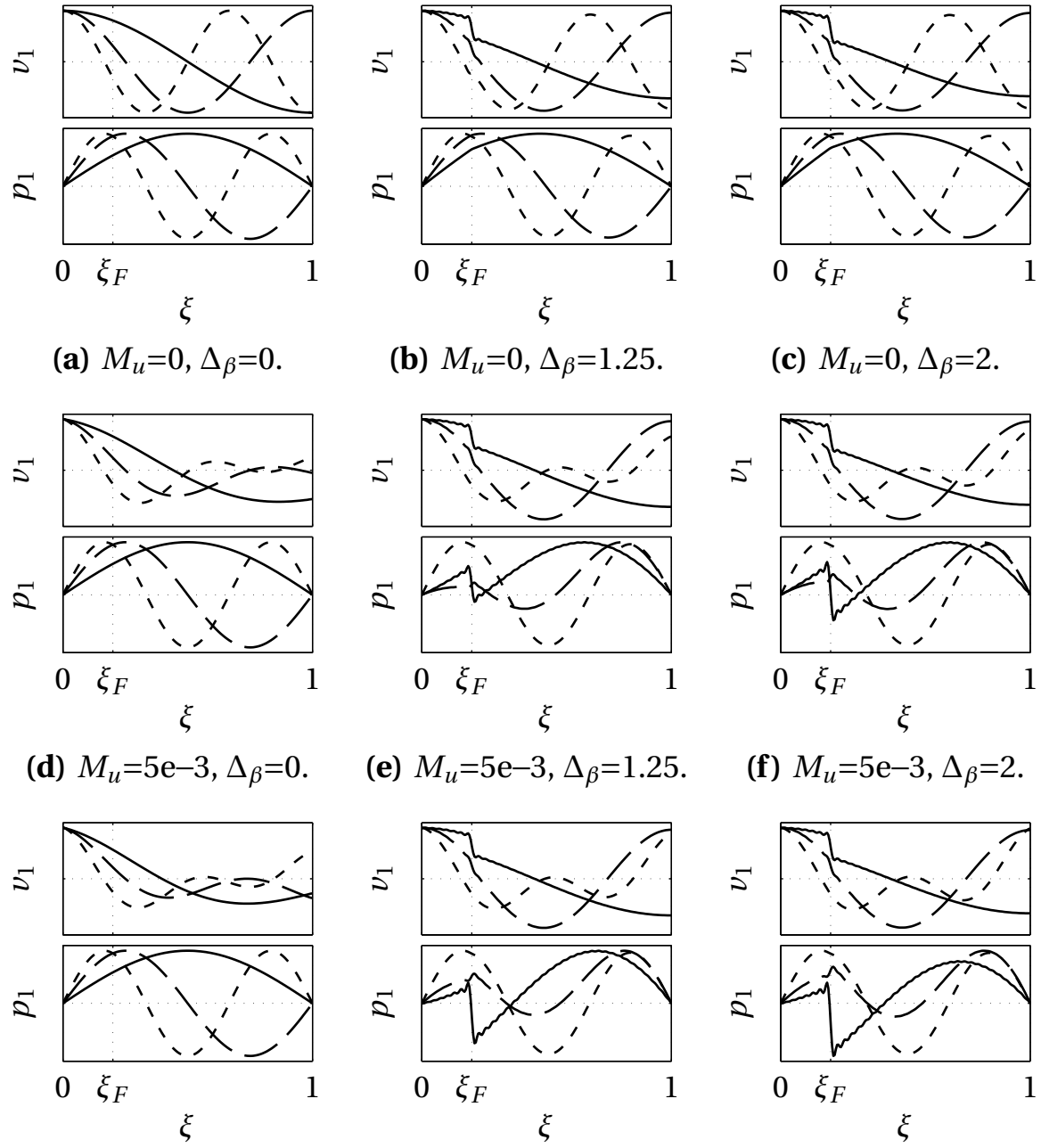

(a) M_u=0, Δ_β=0. **(b)** M_u=0, Δ_β=1.25. **(c)** M_u=0, Δ_β=2.

(d) M_u=5e–3, Δ_β=0. **(e)** M_u=5e–3, Δ_β=1.25. **(f)** M_u=5e–3, Δ_β=2.

(g) M_u=1e–2, Δ_β=0. **(h)** M_u=1e–2, Δ_β=1.25. **(i)** M_u=1e–2, Δ_β=2.

Figure 4.5: First (—), second (− − −) and third (···) eigenmodes of $\mathcal{S}^{(A)}$ in terms of $v_1(\xi)$ and $p_1(\xi)$ as a function of increasing M_u (from top to bottom) and Δ_β (from left to right). Note that all quantities are non-dimensionalized by the scales given in Eq. (4.6). Results are obtained by spectral analysis of the system matrix $\mathbf{A}_M^{(A)}$ of the MWR with $N_{A,M} = 70$. Other parameters: $\xi_F = 0.2$, $\zeta_1 = -0.08$, $\zeta_2 = -0.025$.

The effects of mean flow and temperature jump on the shapes of the first three acoustic eigenmodes given in terms of $v_1(\xi)$ and $p_1(\xi)$ are shown in Fig. 4.5. The eigenmodes are computed by the MWR with $N_{A,M} = 70$. Note that $v_1(\xi)$ is non-dimensionalized by the local mean speed of sound $c_0(\xi)$ (see the reference scales in Eq. (4.6)), which explains the jump in v_1 at ξ_F for $\Delta_\beta > 0$.

Figure 4.5(a) depicts the well-known acoustic eigenmodes in the absence of mean flow and temperature jump. Increasing M_u for $\Delta_\beta = 0$ leads to a stretching of the profiles of acoustic velocity (see the first column of Fig. 4.5), whereas the profiles of acoustic pressure are nearly unaffected. Increasing Δ_β for $M_u = 0$ changes the wave number of the velocity profiles on the hot side of the duct for $\xi > \xi_F = 0.2$ (see the first row of Fig. 4.5). The pressure profiles are nearly unaffected. The latter case is of theoretical nature, because the induced mean temperature jump at ξ_F would not spread into the downstream part of the duct without mean flow. The combined effect of $M_u > 0$ with $\Delta_\beta > 0$ noticeably modifies the profiles of velocity and pressure. It is clear that the eigenmodes differ significantly with respect to the pure acoustic duct modes.

Slight oscillatory phenomena are visible for mode shapes with steep jumps at the position of the heat source ξ_F. This effect is inherent to the MWR, since the mode shapes are expanded as a linear combination of sines and cosines. These oscillations are significantly larger when using a constant damping model (as for the FD model) rather than the modal damping model introduced in Eq. (4.31). For the latter, damping increases with the number of modes, and unphysical high-frequency oscillatory phenomena are inhibited more effectively. The FD model and the MWR thus work best for different damping models. Also, the FD model requires a smoothening of the temperature jump, whereas the MWR does not. A direct quantitative comparison is therefore not instructive and has been omitted.

In Fig. 4.6, we visualize the shift in eigenvalues caused by non-zero mean flow and a non-zero temperature jump. It is visible that the theoretical case of increasing the temperature jump in the absence of mean flow ($M_u = 0$ with $\Delta_\beta \in [0,2]$) leads to a change in the complex-valued eigenfrequency, especially with respect to the angular frequency of oscillation ω (see the green paths in Fig. 4.6). On the other hand, increasing the mean flow in the absence of a

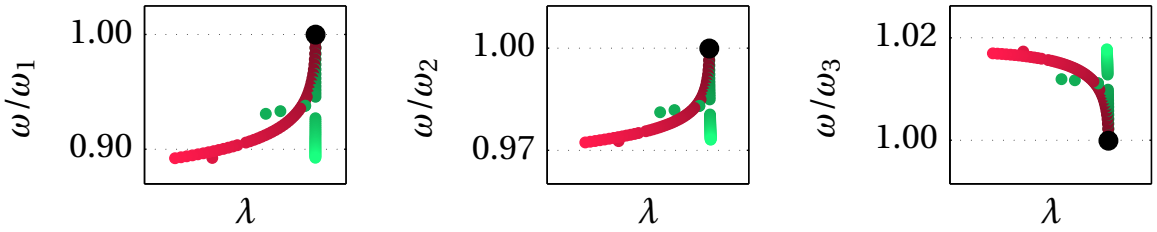

(a) First eigenvalue. **(b)** Second eigenvalue. **(c)** Third eigenvalue.

Figure 4.6: First three acoustic eigenvalues plotted as a function of growth rate λ and frequency of oscillation ω for the cases $M_u = 0$ with $\Delta_\beta \in [0,2]$ (from black to green), $M_u \in [0,0.01]$ with $\Delta_\beta = 0$ (from black to blue—not visible), and $M_u \in [0,0.01]$ with $\Delta_\beta \in [0,2]$ (from black to red) computed by the MWR with $N_{A,M} = 70$. Starting point are the acoustic eigenfrequencies for $M_u = \Delta_\beta = 0$ indicated by thick black dots. Other parameters: $\xi_F = 0.2$, $\zeta_1 = -0.08$, $\zeta_2 = -0.025$.

temperature jump ($M_u \in [0,0.01]$ with $\Delta_\beta = 0$) does not result in a noticeable shift in the complex-valued eigenfrequencies of $\mathcal{S}^{(A)}$. However, once both parameters are increased in parallel, we observe a significant shift in angular frequency ω and growth rate λ (see the red paths in Fig. 4.6). This corroborates the above observation that mean flow and a temperature jump have a significant effect on the acoustic field.

4.6 Chapter Summary

The present chapter can be summarized as follows:

- The governing equations for the acoustics subsystem $\mathcal{S}^{(A)}$ are derived and brought to input-state-output form.
- Different numerical approaches are presented to efficiently solve the acoustics subsystem $\mathcal{S}^{(A)}$.
- The effects of mean flow and of inhomogeneous spatial temperature profiles on the 1-D acoustic field are illustrated and shown to be significant.

5 The Output Energy

As introduced in Sec. 1.3, one major issue when investigating transient growth is the question of appropriate metric to describe the system dynamics. We have seen in Sec. 2.3.1 that the definition of output affects the magnitude of observable transient growth. What is thus the proper output energy of a thermoacoustic system? Should it incorporate the dynamics of the acoustic subsystem $\mathcal{S}^{(A)}$, or also of the heat source subsystem $\mathcal{S}^{(F)}$, or both? If both, how should the proportions be weighted with respect to one another?

Since the definition of output is, in principle, a matter of choice, we highlight in Sec. 5.1 that the output merely defines the perspective that one adopts on the problem. The line of arguments is similar to that followed in [14]. We then turn towards physically motivated outputs of thermoacoustic systems in Sec. 5.2. Unless otherwise mentioned, the present chapter deals with dimensional quantities.

5.1 The Output Defines the Perspective

To address the question of metric, we first recall some facts from Chap. 2. The output equation of the continuous model defined in Eq. (2.3b) shows that an output is a function of states, $y = \mathcal{C}\,x$. The output is therefore entirely defined by the output operator $\mathcal{C}$, which weights the impact of the individual states onto the output. It is further defined in Eq. (2.6) that the energy of the model $\mathcal{E}$ corresponds to the L_2-norm of the output y, and that it varies subject to flux and source terms, f and S, respectively. The latter unambiguously result from the definition of the autonomous model $(\mathcal{A},\mathcal{C})$, as this defines how much energy is produced or dissipated. The output matrix $\mathcal{C}$ is hence needed to close the model definition. Since $\mathcal{C}$ does not affect the dynamics as such, which

is entirely given by $\mathcal{A}$, the definition of $\mathcal{C}$ is a matter of choice. The output thus merely defines the perspective that the investigator chooses to have on the problem, and how the dynamics evolves from the chosen viewpoint. The question of appropriate energy norm should thus be restated as a question of appropriate *perspective* ("you get what you ask for").

The choice of output may be motivated by physical or mathematical arguments, practical reasons, modeling constraints or simply by personal preference. As examples for these categories, the output energy may be chosen to correspond to a physical energy or to a Lyapunov function; it may be chosen such that it represents a quantity that is accessible in an experiment; it may be chosen to penalize an unwanted effect that results from a given numerical scheme; or it may be chosen to represent a measure that can be used to support or to reject a certain hypothesis. However, as the output defines the perspective in which the results need to be interpreted, some outputs may be more apt to analyze a given situation than others. That is, some outputs may suggest a misleading conclusion or an incomplete picture, which other outputs may not. We will elaborate on these points in the following using three examples. The first example uses dimensional quantities, the second and third refer to the simple acoustic system as defined in Sec. 4.2.

The first example is taken from literature, where Wieczorek *et al.* [179] analyze the non-normal transient growth of a non-isentropic thermoacoustic system with a non-zero steady heat source (i.e., $\dot{q}_1 = 0$, but $\dot{q}_0 \neq 0$). The system is described by two autonomous models that only differ in the definition of output, $(\mathcal{A},\mathcal{C}_1)$ and $(\mathcal{A},\mathcal{C}_2)$. The system dynamics contained in $\mathcal{A}$ is given by the dimensional Eqs. (4.2) without source terms (the exact set of governing equations treated by Wieczorek *et al.* is given in Eqs. (2.5)–(2.7) in [122]; for further details, see [179]). The output operator of the first model $\mathcal{C}_1$ is chosen such that the output energy $\mathcal{E}_1$ corresponds to the acoustic energy as derived by Cantrell & Hart [23], which measures the kinetic and potential perturbation energy of the acoustic field with mean flow (see the first, second and last term in Eq. (5.3) below). The output operator of the second model $\mathcal{C}_2$ is chosen such that $\mathcal{E}_2$ additionally takes into account fluctuations in entropy (see Eq. (5.3)). This perturbation energy was first rigorously derived by Myers [117].

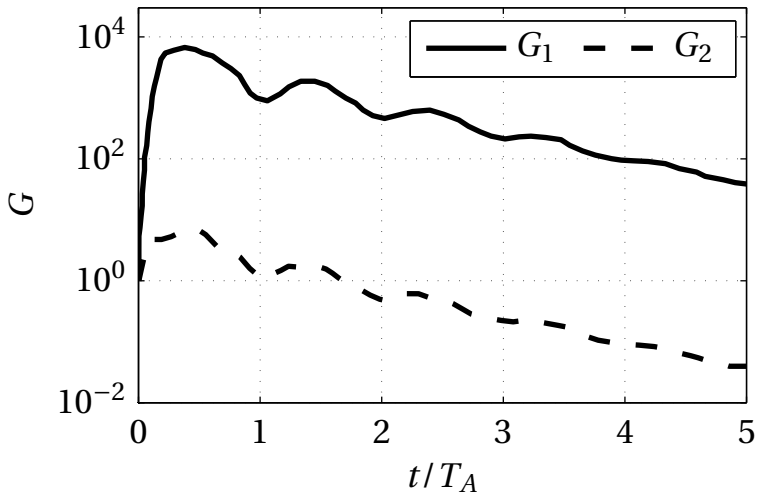

Figure 5.1: $G(t)$ of $(\mathcal{A},\mathcal{C}_1)$ (—) and of $(\mathcal{A},\mathcal{C}_2)$ (− − −). $G_{\max,1} = 6.7 \times 10^3$ and $G_{\max,2} = 6.5$. Figure redrawn from Fig. 4(a) in [179].

Wieczorek *et al.* report a significant difference in maximum transient growth between the models, $G_{\max,1} = \mathcal{O}(10^3)$ and $G_{\max,2} = \mathcal{O}(10^0)$ (see Fig. 5.1). This difference is explained by the fact that the optimal initial state can contain non-zero entries in σ_1, which are not accounted for in $\mathcal{E}_1$. The output energy of the first model $\mathcal{E}_1$ subsequently increases significantly when these entropy perturbations are converted to acoustics.

This finding can also be explained by comparing the flux and source terms of both models, which are responsible for driving or dissipating the respective output energies $\mathcal{E}_i(t)$ over time. As introduced in the discussion following Eq. (2.22), the temporal evolution of $\mathcal{E}$ is governed by the flux and source terms resulting from the model formulation. That is, depending on the definition of output energy, the dynamics of the model is balanced as part of the output energy, or alternatively as flux or source terms. For the case of Wieczorek *et al.*, the differences in flux and source terms, which lead to the difference in temporal evolution of energies $\partial\mathcal{E}_1/\partial t - \partial\mathcal{E}_2/\partial t$, are derived analytically as

$$f_1 = f_2 + \frac{\rho_0 v_0}{2}\sigma_0 \frac{\sigma_0 T_0}{c_p}\left(\frac{\sigma_1}{\sigma_0}\right)^2 , \tag{5.1a}$$

$$S_1 = S_2 + \int_{L_A} \rho_0 v_0 \frac{\sigma_0 T_0}{c_p}\left(\frac{\sigma_1}{\sigma_0}\right)\left(\frac{v_1}{v_0}\right)\frac{\partial \sigma_0}{\partial \xi}\,\mathrm{d}\xi\,. \tag{5.1b}$$

The additional flux term in Eq. (5.1a) is strictly positive and expresses the fact that regions of fluctuating entropy (so-called hot spots) exit the domain downstream. This process is not contained in the definition of $\mathcal{E}_1$ and thus shows up as flux term (unphysically) generating $\mathcal{E}_1$ at the downstream boundary. The entropy perturbations are created by the interaction of the acoustic field with a mean entropy gradient, as indicated by the additional source term in Eq. (5.1b). As before, $\mathcal{E}_1$ does not contain a measure for this transfer of kinetic to internal energy. This leads to an additional (unphysical) source term.

The order of magnitude of the additional flux and source terms can be estimated using the parameters given in [179]. With $\rho_0 v_0 \approx \mathcal{O}(10^1)$, $\sigma_0 T_0/c_p \approx \mathcal{O}(10^3)$, $\sigma_0 \approx \mathcal{O}(10^3)$ downstream of the heat source, $\partial\sigma_0 \approx \Delta\sigma_0 = c_v \ln(\Delta T_0) \approx \mathcal{O}(10^3)$, $v_1/v_0 \approx \mathcal{O}(10^{-2})$ and $\sigma_1/\sigma_0 \approx \mathcal{O}(10^{-2})$, both additional terms are of the order of 10^3, which corresponds to the observed difference in $G_{\max}$. The difference in non-normal transient growth can hence be fully explained by the difference in the order of magnitude of f and S driving the energies of the models $(\mathcal{A},\mathcal{C}_1)$ and $(\mathcal{A},\mathcal{C}_2)$.

This example shows that the system dynamics may exhibit itself very differently subject to a different output. Choosing $\mathcal{E}_2$ seems straightforward from a physical point of view. However, the change of perspective does not alter the dynamics as such (which is the same for both models), but requires the result to be interpreted accordingly. Choosing $\mathcal{E}_1$ will lead to the same conclusion if the altered perspective is taken into account in the interpretation of results.

Consider as a second example the simple acoustic system introduced in Sec. 4.2 with fully reflective ends and a non-zero temperature jump at the center of the duct. We exclude fluctuations in heat release rate (i.e., $K = 0$), and neglect damping and mean flow (i.e., $\zeta_i = 0$ and $M_u = 0$). Since the state vector of the corresponding model reads $x = [v_1(\xi), p_1(\xi)]^T$, it is straightforward to use the kinetic and potential energy of the system as output (i.e., acoustic energy, see the first, second and last term in Eq. (5.3) below). This choice fixes $\mathcal{C}$ and closes the model $(\mathcal{A},\mathcal{C})$. For this academic test case, physical arguments suggest that the fluctuating energy content of the system remains constant over time, as there are no physical sources or sinks of energy. However, with

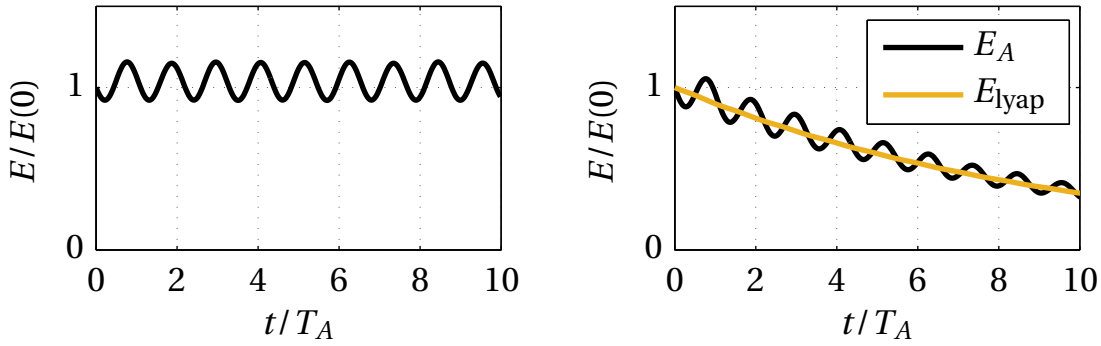

(a) Stable (no damping). **(b)** Asymptotically stable.

Figure 5.2: Time traces of output energy of autonomous models describing the simple acoustic system defined in Sec. 4.2 (a) without damping and E representing the acoustic energy E_A, and (b) with modal damping ($\zeta_1 = -0.08$, $\zeta_2 = -0.025$) and E as the acoustic energy E_A (—) and as a Lyapunov function E_{lyap} (—). Other parameters: $\xi_F = 0.2$, $M_u = 0$, $\Delta_\beta = 1.25$, $K = 0$.

the choice of $\mathcal{C}$, the temporal evolution of energy is derived analytically as

$$\frac{\partial \mathcal{E}}{\partial t} = -v_1 \, p_1 \frac{1}{\beta} \frac{\partial \beta}{\partial \xi} \, . \tag{5.2}$$

That is, the analysis identifies a source term in the region of the non-zero temperature gradient. The acoustic energy thus does not remain constant over time, which is visible from Fig. 5.2(a). The output energy E of the corresponding discrete model oscillates around the initial value $E(0)$.

This seemingly unphysical behavior with spurious energy growth and decay can be explained as follows. The heat source defines a flame at rest located at $\xi = \xi_F$. The flame is thus not able to move in response to an acoustic wave. Instead, a local increase in velocity leads to a larger volume of fresh gas being pushed into and consumed by the flame, and thus to more heat produced, because the downstream temperature is assumed constant. A local decrease in velocity due to $v_1 < 0$ causes the opposite effect. We are thus left with the relation $\dot{q}_1 \propto v_1$, which substituted into Eq. (5.2) yields a source term analog to the classical Rayleigh source term $\partial \mathcal{E} / \partial t \propto \dot{q}_1 \, p_1$ [14]. The phenomenon of a flame at rest producing fluctuations in energy is referred to as “the classical

paradox of thermoacoustics" by Bauerheim *et al.* [8] and is also explained by Strobio Chen *et al.* [162].

The above described mechanism of creating fluctuations in heat release rate is fundamentally different from the fluctuations in heat release rate resulting from an active flame as described in Chap. 3 (these fluctuations are excluded in the present example by definition). The active flame mechanism stems from the convectively driven response of premixed flames to acoustic perturbations, which are transformed to flame wrinkles at the flame base and advect along the flame with the mean flow. In contrast, the above mechanism with a flame at rest happens at an acoustic time scale. It results from simplistic modeling assumptions, because the model does not allow for movement of the center of heat release. The identified source term in Eq. (5.2) is thus physical, but, strictly speaking, the assumption as such of a flame at rest is not (although it is widespread in thermoacoustics). Both mechanisms have in common that they alter the acoustic energy via the Rayleigh and a Rayleigh-like source term, which only differ in the pre-factors K and $-1/\beta\,\partial\beta/\partial\xi$, respectively.

For this second example, the adopted perspective prescribed by the choice of output highlights the implicit assumptions and limitations of the model. A different output may have accounted for the inability of the heat source to move with flow perturbations, and yielded results that better match physical intuition (e.g., constant energy over time). However, this argument does not render one or another choice of output more or less appropriate.

The third example builds on the previous one. Consider the same academic test case as before, but including non-zero damping. The system is now asymptotically stable. To use the output energy to prove stability, we may design the discrete model $(\mathbf{A},\mathbf{C})$ such that E is a Lyapunov function V (see Sec. 2.2.1). In this case, we can find the output matrix $\mathbf{C}$ via the Lyapunov equation (2.24), if we require the dissipation matrix to be an arbitrary negative definite matrix (for example, $\mathbf{Q} = -\mathbf{I}$). As can be seen from Fig. 5.2(b), $E(t)$ is indeed strictly decaying. The evolution of output energy of a model where E represents acoustic energy is overlaid for illustration. The mathematically motivated choice of $\mathbf{C}$ being a Lyapunov function comes at the expense of E not being physically interpretable. The corresponding energy weighting ma-

trix $\mathbf{W} = \mathbf{C}^T\mathbf{C}$ is a dense symmetric matrix, which means that E contains mixed terms of spatially coupled velocity and pressure fluctuations.

5.2 Physically Motivated Energies for Thermoacoustics

The question of appropriate output energy is an ongoing matter of debate in thermoacoustics [13, 20, 56, 57, 121]. The discussion is strongly motivated by the aim to find a metric that is both physically meaningful and allows to reliably assess the stability of a thermoacoustic system [37, 58]. For example, the concept of instability potentiality relies on using the acoustic energy as metric to identify stable/unstable configurations of thermoacoustic systems [3, 133, 171]. We have seen in Secs. 2.2 and 5.1 that an output energy is only apt to determine stability if it is a Lyapunov function. In most cases, this goes hand in hand with loss of physical insight. We thus back down with respect to the Lyapunov function and rather seek an output energy that generates insight into the physics of thermoacoustic interaction. This will facilitate interpretation of the origins of non-normal transient growth in thermoacoustic systems.

To comply to a certain formalism, Giauque *et al.* [59] and George & Sujith [56] argue that the output energy should fulfill three requirements so as to qualify as a mathematically consistent energy norm and as a "faithful measure of the disturbance amplitude" [56]. These are:

1. $\mathcal{E}$ should be a quadratic function of only the first-order (fluctuating) terms of the primitive variables.
2. $\mathcal{E}$ should be positive definite and non-zero unless all primitive variables are zero.
3. $\mathcal{E}$ should not grow or decay in the absence of physical sources or sinks.

Over the decades, various authors have derived disturbance energies from first principles, each valid under certain conditions (for example, [23, 26, 115, 130]). In 1991, Myers published a profound paper, in which he derives the

	$\mathcal{S}^{(A)}$	$\mathcal{S}^{(F)}$
$\mathcal{S}^{(A)}$	$\frac{1}{2}\int_{\Omega_A}\left[\rho_0\mathbf{v}_1^2+2\rho_1\mathbf{v}_0\cdot\mathbf{v}_1+\frac{\rho_0 T_0\sigma_1^2}{c_p}+\frac{p_1^2}{\rho_0 c_0^2}\right]\mathrm{d}\Omega$	$\frac{1}{2}\int_{\Omega_A}\left[\rho_0\left(\frac{T_{0,d}}{T_{0,u}}-1\right)^2\left(\frac{v_{0,u}}{\dot{q}_0}\right)^2\dot{q}_1^2\right]\mathrm{d}\Omega$
$\mathcal{S}^{(F)}$	$\frac{1}{2}\int_{\Omega_F}\left[\rho_0\mathbf{v}_1^2+\rho_1\mathbf{v}_0\cdot\mathbf{v}_1\right]\mathrm{d}\Omega$	see Eq. (B3) in [20]

Table 5.1: Selection of second-order physical energy expressions for thermoacoustic systems consisting of the interacting subsystems acoustics and heat source, $\mathcal{S}^{(A)}$ and $\mathcal{S}^{(F)}$.

most general form of disturbance energy [117]. It is shown that his energy expression is able to unify the derivations cited above and to relax the assumptions made therein. His approach consists in expanding the governing equations *and* the total energy balance in orders of ϵ (see the expansion defined in Eq. (3.7)). By comparing equal orders of ϵ^n of governing equations and energy balance, it is possible to establish relations governing total energy conservation at n-th order. It is found that total energy conservation at orders $n=0$ and $n=1$ is implicitly fulfilled by the corresponding sets of governing equations. For $n\geq 2$, it is shown that the total energy balance at n-th order is fulfilled by an equation of the form of Eq. (2.22), $\partial\mathcal{E}_n/\partial t = f_n + S_n$, where $\mathcal{E}_n$ only depends on quadratic quantities of order $n-1$. Myers' approach was recently extended to gaseous combustion and to a time-averaged stationary base flow [20].

Myers' result is astonishing for two reasons. First, the above mentioned requirement 1. to a mathematically consistent energy norm is shown to be inherently fulfilled by disturbance energies that are derived from first principles.[1] And second, the perturbation energy related to first-order quantities governs total energy conservation at order 2. For small disturbances (i.e., in the linear regime), disturbance energies derived from first principles are thus an exact reflection of the principle of total energy conservation up to 2$^{\text{nd}}$ order.

Large parts of the present study are conducted in the linear regime (except for the synthesis in Sec. 7.4), and non-normal transient growth is a linear phe-

[1] Whether an energy norm complies with requirements 2. and 3. needs to be found out on a case-to-case basis. According to [56] for the case of uniform mean flow in 1-D, Myers' 2$^{\text{nd}}$ order energy is positive definite and does not exhibit unphysical growth/decay in the absence of physical sources/sinks if $M<1/\sqrt{\gamma}$.

nomenon. Second-order energies are therefore sufficiently well-suited metrics for the purpose of the present analysis. In the following, we put selected physically meaningful second-order disturbance energy expressions into the systemic context of a thermoacoustic system $\mathcal{S}^{(T)}$ consisting of the two subsystems in feedback, $\mathcal{S}^{(A)}$ and $\mathcal{S}^{(F)}$. The motivating question is how to measure the energy stored in and/or the work done by each of the subsystems and in the interaction between them. A summarizing overview is given in Tab. 5.1.

$\mathcal{S}^{(A)} \rightarrow \mathcal{S}^{(A)}$. The energy measure of $\mathcal{S}^{(A)}$ may reflect the kinetic ($\sim \mathbf{v}_1^2$) and internal ($\sim \sigma_1^2$) energies stored in the first-order fields, in addition to the work done by elastic compression ($\sim p_1^2$) and by the mean flow advecting perturbations in mass flux downstream. All these contributions are contained in Myers' 2nd order disturbance energy,

$$\mathcal{E}_2^{(AA)} = \frac{1}{2}\int_{\Omega_A} \left[\underbrace{\rho_0 \mathbf{v}_1^2}_{\text{kinetic}} + \underbrace{2\rho_1 \mathbf{v}_0 \cdot \mathbf{v}_1}_{\text{advection}} + \underbrace{\frac{\rho_0 T_0 \sigma_1^2}{c_p}}_{\text{internal}} + \underbrace{\frac{p_1^2}{\rho_0 c_0^2}}_{\text{el. comp.}} \right] \mathrm{d}\Omega \,. \tag{5.3}$$

$\mathcal{S}^{(F)} \rightarrow \mathcal{S}^{(A)}$. For an acoustically compact heat source, the effect of $\mathcal{S}^{(F)}$ onto $\mathcal{S}^{(A)}$ can be viewed as an acoustic monopole creating a difference in acoustic velocity $\delta \mathbf{v}_1$ up- and downstream of the heat source. From the linearized Rankine-Hugoniot equations governing the jump conditions of planar acoustic waves at the acoustically compact heat source [86, 136], we obtain

$$\delta v_1 = \left(\frac{T_{0,d}}{T_{0,u}} - 1 \right) \frac{v_{0,u}}{\dot{q}_0} \dot{q}_1 \,, \tag{5.4}$$

which is accurate to first order in Mach number, and where $p_1/p_{0,u}$ is neglected. The energy density of the acoustic monopole should then be given as $\rho_0(\delta \mathbf{v}_1)^2/2$ [116, 130], and thus

$$\begin{aligned} \mathcal{E}_2^{(AF)} &= \frac{1}{2}\int_{\Omega_A} \left[\rho_0 \left(\frac{T_{0,d}}{T_{0,u}} - 1 \right)^2 \left(\frac{v_{0,u}}{\dot{q}_0} \right)^2 \dot{q}_1^2 \right] \mathrm{d}\Omega \\ &= \frac{1}{2} \Omega_F \rho_0 \left(\frac{T_{0,d}}{T_{0,u}} - 1 \right)^2 \left(\frac{v_{0,u}}{\dot{q}_0} \right)^2 \dot{q}_1^2 \,, \end{aligned} \tag{5.5}$$

because $\dot{q}_1 \neq 0$ only within the heat source volume Ω_F. For acoustically compact heat sources, $\Omega_F \ll \Omega_A$. Further, if mean flow effects are small, $v_{0,u} \ll c_{0,u}$, it can be expected that $\mathcal{E}_2^{(AF)}$ is negligible in magnitude.

$\mathcal{S}^{(A)} \rightarrow \mathcal{S}^{(F)}$. The effect of $\mathcal{S}^{(A)}$ onto $\mathcal{S}^{(F)}$ may be measured by the kinetic energy stored in the volumetric portion of the first-order fields that perturb the heat source, in addition to the work done by the mean flow to advect the perturbed mass flux through the flame volume Ω_F,

$$\mathcal{E}_2^{(FA)} = \frac{1}{2} \int_{\Omega_F} \left[\rho_0 \mathbf{v}_1^2 + \rho_1 \mathbf{v}_0 \cdot \mathbf{v}_1 \right] \mathrm{d}\Omega \,. \tag{5.6}$$

Note that from the perspective of $\mathcal{S}^{(F)}$, Ω_F is finite. However, as Ω_F is contained in Ω_A, $\mathcal{E}_2^{(FA)}$ is already accounted for in $\mathcal{E}_2^{(AA)}$ (see the first two terms in Eq. (5.3)).

$\mathcal{S}^{(F)} \rightarrow \mathcal{S}^{(F)}$. An energy measure of $\mathcal{S}^{(F)}$ is proposed by Brear *et al.* in [20] for the case of gaseous combustion. The full energy is given by

$$\mathcal{E}^{(FF)} = \int_{\Omega_F} \rho \sum_{k=0}^{n-1} g_{0,k} \, Y_k \, \mathrm{d}\Omega \,, \tag{5.7}$$

with $g_{0,k}$ and Y_k the Gibbs' free energy and mass fraction of the k-th species. $g_{0,k}$ corresponds to the chemical potential of the k-th species for isobaric combustion. The second-order energy $\mathcal{E}_2^{(FF)}$ is obtained by expanding Eq. (5.7) to second order and making use of equilibrium and non-equilibrium thermodynamic differentials. The details of the derivation are given in App. B of [20]. The exact expression for $\mathcal{E}_2^{(FF)}$ is not written here but can be found in Eq. (B3) of [20].

The above selection of second-order energy norms is to a certain extent arbitrary, and other choices are conceivable. However, as seen in the previous Sec. 5.1, the choice of output merely defines the perspective the investigator wishes to have on the dynamics. Here, we choose to have a perspective on the matter that is motivated by a physical energy (i.e., a scalar measure of the entire spatially distributed dynamics of the system). This stands in contrast to physically motivated measures that are spatially confined to a certain monitoring plane of Ω_A, such as, for example, pressure or velocity fluctuations at

the position of the heat source, or at the inlets and outlets. Whether the above selection of energies can be used to define the output of a model describing the thermoacoustic system $\mathcal{S}^{(T)}$ is subject to the fineness of the model.

5.3 Chapter Summary

The present chapter can be summarized as follows:

- It is highlighted that the definition of output is, in principle, a matter of choice that is critically tied to the dynamics described by the system model. The output merely defines the perspective of how the system dynamics exhibits itself, but it does not alter the system dynamics as such. The output therefore prescribes the way in which results should be interpreted.
- A selection of physical disturbance energies for thermoacoustic systems are put into the systemic context of interacting subsystems acoustics and heat source, respectively.

6 Linear System Analysis of the Full Thermoacoustic Model

The present chapter is dedicated to a linear system analysis of the full autonomous low-order model $(\mathcal{A}^{(T)}, \mathcal{C}^{(T)})$ describing $\mathcal{S}^{(T)}$. In Sec. 6.1, the thermoacoustic model is assembled by combining the heat source subsystem $\mathcal{S}^{(F)}$, the acoustics subsystem $\mathcal{S}^{(A)}$, and the definition of output (i.e., the outcomes of Chaps. 3, 4 and 5, respectively). We further analyze the evolution of output energy from an analytical perspective, and discuss the effect of a fluctuating heat source on the acoustic field. The impact of different model parameters on linear stability is studied in Sec. 6.2.

6.1 The Full Low-Order Thermoacoustic Model

The present section begins by assembling the autonomous thermoacoustic model in Sec. 6.1.1. The output energy is analyzed from an analytical perspective in Sec. 6.1.2, before investigating the effect of a fluctuating heat source on the acoustic field in Sec. 6.1.3.

6.1.1 Model Assembly

The full thermoacoustic system $\mathcal{S}^{(T)}$ consists of the subsystems heat source $\mathcal{S}^{(F)}$ and acoustics $\mathcal{S}^{(A)}$, which are assembled as an autonomous system of $Z = 2$ interconnected subsystems as defined in Sec. 2.1. The thermoacoustic system $\mathcal{S}^{(T)}$ is then described by a continuous input-state-output model of the form of Eq. (2.3) with

$$x^{(T)} = \left[x^{(A)\,T} \,,\, x^{(F)\,T} \right]^T , \tag{6.1}$$

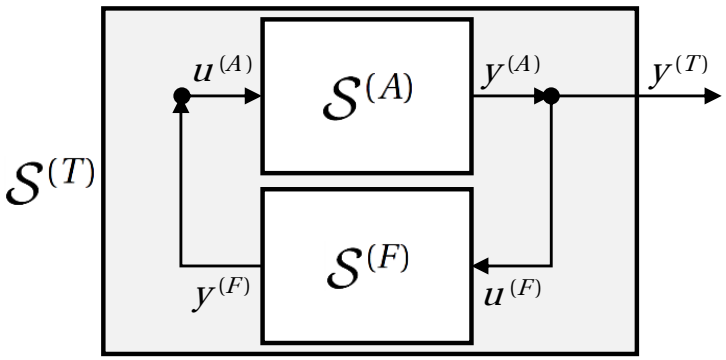

Figure 6.1: Scheme of the autonomous thermoacoustic system $\mathcal{S}^{(T)}$ consisting of the interacting subsystems acoustics $\mathcal{S}^{(A)}$ and heat source $\mathcal{S}^{(F)}$.

and

$$\mathcal{A}^{(T)} = \begin{bmatrix} \mathcal{A}^{(A)} & \mathcal{B}^{(A)}\mathcal{C}^{(F)} \\ \mathcal{B}^{(F)}\mathcal{C}^{(A)} & \mathcal{A}^{(F)} \end{bmatrix} . \tag{6.2}$$

A graphical illustration of $\mathcal{S}^{(T)}$ is shown in Fig. 6.1.

The model $(\mathcal{A}^{(A)},\mathcal{B}^{(A)},\mathcal{C}^{(A)})$ representing $\mathcal{S}^{(A)}$ is given by the simple 1-D homentropic model defined in Eqs. (4.14) with an acoustically compact heat source and fully reflective duct ends. In the nonlinear regime, the model $(\mathcal{A}^{(F)},\mathcal{B}^{(F)},\mathcal{C}^{(F)})$ describing $\mathcal{S}^{(F)}$ is defined by the G-equation flame model given in Eq. (3.14). Provided linearity, we use the IR-based representation defined in Sec. 3.2.2 with the analytically derived IR functions of a linearized G-equation flame given in Eqs. (3.27).

Although the heat source is acoustically compact (i.e., there is a disparity in characteristic length scales between the subsystems acoustics $\mathcal{S}^{(A)}$ and heat source $\mathcal{S}^{(F)}$, $L_F \ll L_A$), it is not convectively compact, since the time scales of the heat source subsystem $\mathcal{S}^{(F)}$ result from convective processes. The heat source is therefore distributed in time (as can be seen from the IR function of the linearized G-equation flame), but nevertheless compact in space. The point-wise coupling with the acoustic field, as done in the present work, is therefore a good approximation in this situation.

Following the discussion of the previous Chap. 5, we decide to choose the output such that the output energy $\mathcal{E}$ corresponds to a physical energy. The low-

order models used to describe $\mathcal{S}^{(T)}$ cannot represent all physical energies that are introduced in Sec. 5.2 (see Tab. 5.1). For instance, the second-order flame energy $\mathcal{E}_2^{(FF)}$ is not resolvable because we do not model detailed combustion processes. The same holds for fluctuations in internal energy present in $\mathcal{E}_2^{(AA)}$, since $\sigma_1 = 0$ in the homentropic case. Further, the heat source is assumed acoustically compact, so $\mathcal{E}_2^{(AF)} = 0$. We are thus left with the pure acoustic energy with non-zero mean flow (i.e., $\mathcal{E}_2^{(AA)}$ as defined in Eq. (5.3) with $\sigma_1 = 0$), which is sometimes referred to as Cantrell & Hart energy [23, 56, 117]. This is the only form of perturbation energy that is resolvable by the present low-order model describing $\mathcal{S}^{(T)}$.

Using the reference scales given in Eq. (4.6) in addition to $\Omega_{A,\mathrm{ref}} = A_A L_A$, the non-dimensionalized output energy $\mathcal{E}^{(T)}$ reads

$$\mathcal{E}^{(T)} = \frac{1}{2} \int_0^1 \left[v_1^2 + 2M\, v_1 p_1 + p_1^2 \right] \mathrm{d}\xi \,. \tag{6.3}$$

The autonomous thermoacoustic model $(\mathcal{A}^{(T)}, \mathcal{C}^{(T)})$ describing $\mathcal{S}^{(T)}$ is thus closed by defining

$$\mathcal{C}^{(T)} = \left[\mathcal{C}^{(T,A)} \,,\, 0 \right], \tag{6.4}$$

where

$$\mathcal{C}^{(T,A)} = \frac{\sqrt{2}}{2} \begin{bmatrix} 1 & M \\ 0 & \sqrt{1-M^2} \end{bmatrix} . \tag{6.5}$$

The output energy $\mathcal{E}^{(T)}$ defines a semi-norm, because the definition of output does not include the states $x^{(F)}$ of the subsystem $\mathcal{S}^{(F)}$. This will become important in Chap. 7 when investigating non-normal transient growth by means of SVD (see also the discussion in Sec. 2.4.2).

The set of discrete matrices $(\mathbf{A}^{(T)}, \mathbf{C}^{(T)})$ and $(\mathbf{A}_M^{(T)}, \mathbf{C}_M^{(T)})$—depending on whether the acoustic model of $\mathcal{S}^{(A)}$ is solved by finite differences or the MWR—are given in App. C.4. As stated in Sec. 4.4.2, we use the MWR unless otherwise mentioned. By default, the discrete thermoacoustic model is thus given by $(\mathbf{A}_M^{(T)}, \mathbf{C}_M^{(T)})$.

Each of the two subsystems $\mathcal{S}^{(A)}$ and $\mathcal{S}^{(F)}$ possesses a characteristic time scale. For $\mathcal{S}^{(A)}$, $T_A = L_A / c_0$ corresponds to the travel time of an acoustic wave

			acoustic			mixed		flame		
	ξ_F	ζ_1	ζ_2	Δ_β	M_u	Sr	ϕ	α	μ	type
default	0.2	−0.08	−0.025	1.25	0.005	1	0.85	23°	0.9	wedge

Table 6.1: Default parameter values of the low-order thermoacoustic model as used in the present study: flame position ξ_F, damping coefficients ζ_1 and ζ_2, temperature incremental factor Δ_β, upstream Mach number M_u, Strouhal number Sr, equivalence ratio ϕ, flame angle α, ratio of convective to mean flow velocity μ, and the type of the laminar premixed flame.

through the duct (see t_{ref} defined in Eq. (4.6)). For $\mathcal{S}^{(F)}$, T_F represents the settling time of the flame, which for the G-equation flame is given by the restorative time scale $\tau_r = 2R_F/(v_0 \sin(2\alpha))$ (see Sec. 3.3.1) [12]. Combining both subsystems thus yields an additional parameter, which is the Strouhal number,

$$\begin{aligned} \mathrm{Sr} &= \frac{T_F}{T_A} \\ &= \frac{2\,R_F\,c_0}{L_A\,v_0\sin(2\alpha)} = \frac{\mathrm{He}}{M}\,\frac{2}{\sin(2\alpha)}\,. \end{aligned} \tag{6.6}$$

Sr corresponds to a ratio of non-dimensional groups that are representative of the geometry and flow, the Helmholtz number $\mathrm{He} = L_F/L_A$ and the Mach number M. The additional factor $2/\sin(\alpha)$ in Eq. (6.6) stems from the specific definitions of the characteristic length and velocity scales of the G-equation flame. Obviously, Sr results from the configuration under investigation. However, in the present low-order model of $\mathcal{S}^{(T)}$, Sr can be specified as independent parameter. A different Strouhal number frequently used in thermoacoustic literature is defined as $\widetilde{\mathrm{Sr}} = T_F\,\omega$, where ω represents the angular frequency of oscillation of the input to the heat source [12, 138, 153, 154].

Values of Strouhal numbers typically found in laminar thermoacoustic systems are shown in Tab. 1.1. Configurations with premixed flames have much larger Strouhal numbers than configurations using a heated wire as heat source, $\mathrm{Sr} = \mathcal{O}(10^0 \ldots 10^1)$ vs. $\mathrm{Sr} = \mathcal{O}(10^{-2})$. This highlights the convective nature of premixed flames.

The default parameters of the thermoacoustic model used in the present study are summarized in Tab. 6.2. They originate from the parameters of the subsystems acoustics and heat source, $\mathcal{S}^{(A)}$ and $\mathcal{S}^{(F)}$, respectively, as well as the mixed parameter Sr. The parameter values are inspired by values encountered in a typical configuration of a laminar thermoacoustic system (cf. Tab. 1.1). As mentioned above, it is a special feature of the low-order model that all parameters can be treated as independent.

6.1.2 Analysis of Output Energy

For the thermoacoustic model $(\mathcal{A}^{(T)}, \mathcal{C}^{(T)})$, the flux and net source terms due to which $\mathcal{E}^{(T)}$ varies in time are derived analytically as

$$f^{(T)} = -\left(M\, v_1^2 + \left(1+M^2\right) v_1\, p_1 + M\, p_1^2\right), \tag{6.7a}$$

$$\begin{aligned} S^{(T)} = \quad & \underbrace{K\, \dot{q}_1 \int_{L_A} \Big[p_1 + M\, v_1\Big]\, \psi_q \,\mathrm{d}\xi}_{\text{(extended) Rayleigh source term}} \\ & \underbrace{- \int_{L_A} \left[\frac{\partial M}{\partial \xi}\left[4\, v_1^2 + M\left(3+\gamma\right) v_1\, p_1 + 2\,\gamma\, p_1^2\right] + \frac{1}{\beta}\frac{\partial \beta}{\partial \xi}\, p_1\, v_1\right] \mathrm{d}\xi}_{\text{source term related to gradients in mean flow and temperature}} \\ & \underbrace{+ \int_{L_A} \Big[\zeta_v\, v_1^2 + M\left(\zeta_v + \zeta_p\right) v_1\, p_1 + \zeta_p\, p_1^2\Big] \,\mathrm{d}\xi}_{\text{damping term}} . \end{aligned} \tag{6.7b}$$

In the absence of mean flow, the flux term $f^{(T)}$ reduces to the well-known acoustic flux $(v_1\, p_1)$ over the boundaries. However, in the present model, $p_1 = 0$ at the boundaries, so $f^{(T)} = -M\, v_1^2$. $\mathcal{E}^{(T)}$ thus increases (decreases) if a higher (lower) convective flux $M\, v_1^2$ enters the domain upstream than leaves the domain downstream.

The source term $S^{(T)}$ given in Eq. (6.7b) consists of a term resulting from the interaction of the fluctuating heat source with the acoustic field (see the first line of Eq. (6.7b)), a source term related to the gradients in mean flow and temperature, $\partial M/\partial \xi$ and $\partial \beta/\partial \xi$, respectively (see the second line of Eq. (6.7b)), and

a damping term (see the third line of Eq. (6.7b)). For small mean flow (i.e., $M_u \ll 1$), the source terms in Eq. (6.7b) that depend on M and $\partial M/\partial\xi$ are negligible in magnitude. The main sources to $\mathcal{E}^{(T)}$ are thus the classical Rayleigh term $K\dot{q}_1 \int_{L_A} p_1 \psi_q \, \mathrm{d}\xi$, the Rayleigh-like source term due to the assumption of a flame at rest (see the last term in the second line of Eq. (6.7b)), and two strictly dissipative damping terms (see the first and last terms in third line of Eq. (6.7b)). As discussed in the second example of Sec. 5.1, the Rayleigh-like source term results from the assumption of a flame at rest, which is inherent to the model. We therefore refer to this source term as *inherent source term* in the remainder of the present work.

Since the net flux and source terms are not strictly dissipative, it obviously follows that the thermoacoustic model $(\mathcal{A},\mathcal{C})$ admits transient growth, and that $\mathcal{E}^{(T)}$ is not a Lyapunov function. The main sources to $\mathcal{E}^{(T)}$ are the Rayleigh source term and the Rayleigh-like inherent source term, which scale with the strength of the heat source and the mean temperature jump, respectively. We therefore expect the strength of the heat source regulated by K and the magnitude of the temperature jump regulated by the temperature incremental factor Δ_β to dominate transient energy growth. This matter will be discussed in Sec. 7.2.2.

6.1.3 The Effect of a Fluctuating Heat Source

The present section investigates the effect of a fluctuating heat source on the eigenmodes and eigenfrequencies of $\mathcal{S}^{(T)}$. In structure, the present section is similar to Sec. 4.5.

The effect of a heat source on the shapes of the eigenmodes of $\mathcal{S}^{(T)}$ can be seen in Fig. 6.2. In the absence of a heat source (i.e., $K = 0$), the velocity and pressure profiles are those of the uncoupled acoustic subsystem (cf. Figs. 6.2(a) and 6.2(b) to Figs. 4.5(a) and 4.5(e), respectively). For $K > 0$, the velocity profiles exhibit an increasingly strong jump δv_1 at $\xi = \xi_F$. This is due to the heat source acting as an acoustic monopole source. The pressure profiles also change, but less prominently than the velocity profiles. A compact heat source

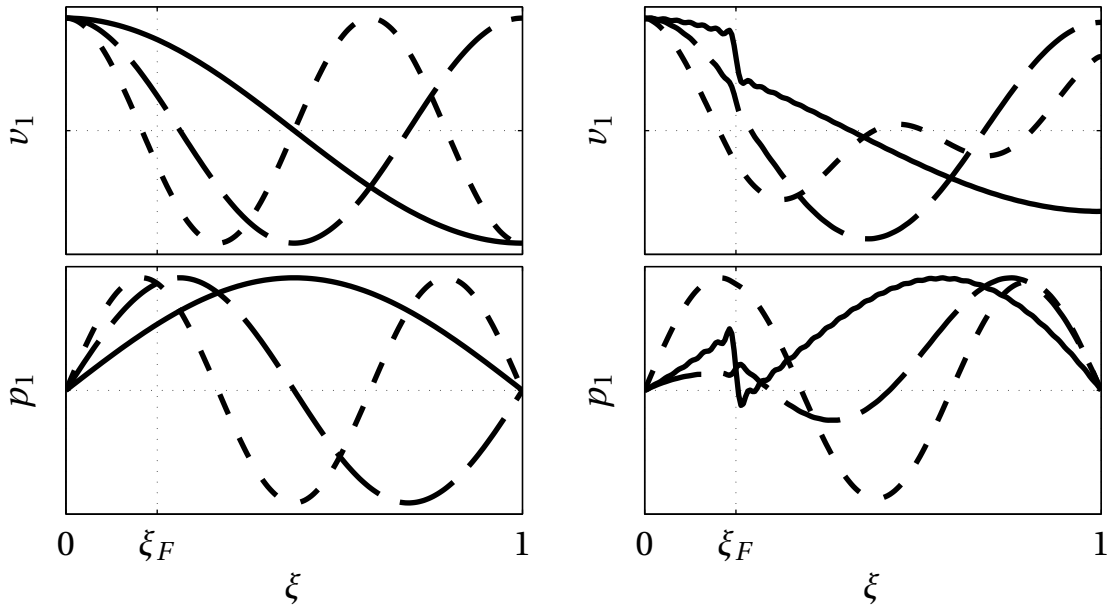

(a) M_u=0, Δ_β=0, K=0.

(b) M_u=5e–3, Δ_β=1.25, K=0.

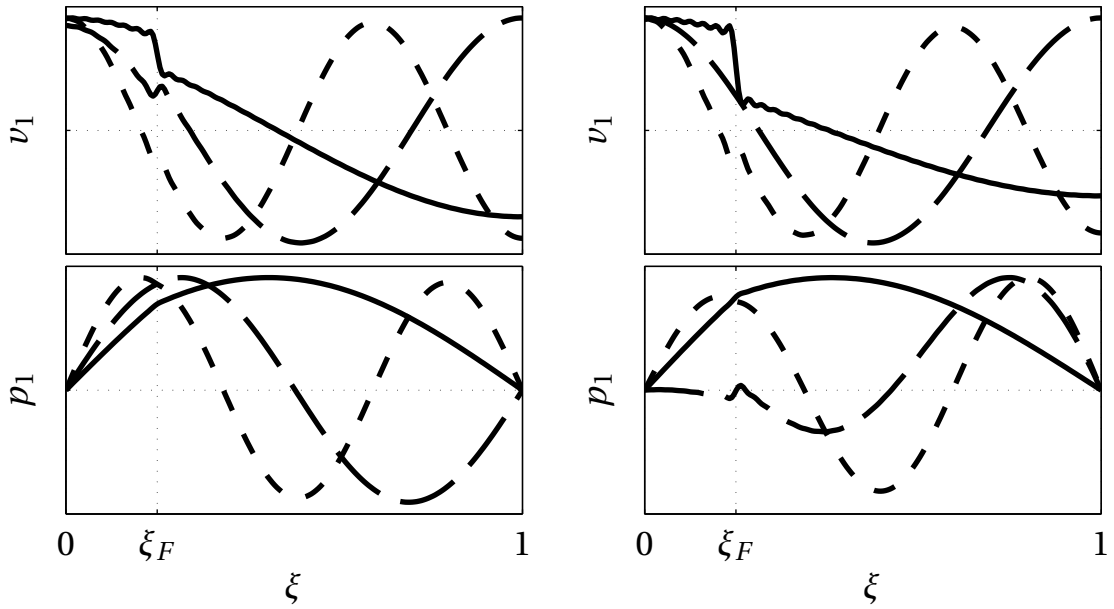

(c) M_u=0, Δ_β=0, K=5.9e–4.

(d) M_u=5e–3, Δ_β=1.25, K=5.9e–4.

Figure 6.2: First (—), second (− − −) and third (···) eigenmodes of $\mathcal{S}^{(T)}$ in terms of $v_1(\xi)$ and $p_1(\xi)$ as a function of K, M_u and Δ_β. Results are obtained by spectral analysis of $\mathbf{A}_M^{(T)}$ with otherwise default parameter values.

thus changes the acoustic mode shapes significantly. The change would even be more pronounced for heat sources that are distributed in space.

The complete eigenspectrum of $\mathcal{S}^{(T)}$ is plotted in Fig. 6.3. For the uncoupled case (i.e., $K = 0$), the eigenvalues associated to $\mathcal{S}^{(A)}$ and $\mathcal{S}^{(F)}$ are clearly separated (see Fig. 6.3(a)). Once coupled (i.e., $K > 0$), the eigenspectra move together to form a *thermoacoustic* eigenspectrum (see Fig. 6.3(b)). The coupled and uncoupled eigenspectrum differ significantly, and a net distinction between the eigenvalues associated to the individual subsystems is not possible.

In Fig. 6.4, we plot the paths of the first three (initially acoustic) eigenvalues for a range of increasing strength of the fluctuating heat source $K = [0, 7.4 \times 10^{-4}]$. The paths of the eigenvalues of three thermoacoustic configurations are compared, which differ only in the Strouhal number Sr: a fast heat source with $\mathrm{Sr} = 10^{-2}$, such as a heated wire (indicated by the blue path in Fig. 6.4), and two slower heat sources with $\mathrm{Sr} = 1$ and $\mathrm{Sr} = 3$, respectively, indicative of a premixed flame (see the green and red paths in Fig. 6.4, respectively).

For all Sr, the eigenvalues change in growth rate λ and angular frequency of os-

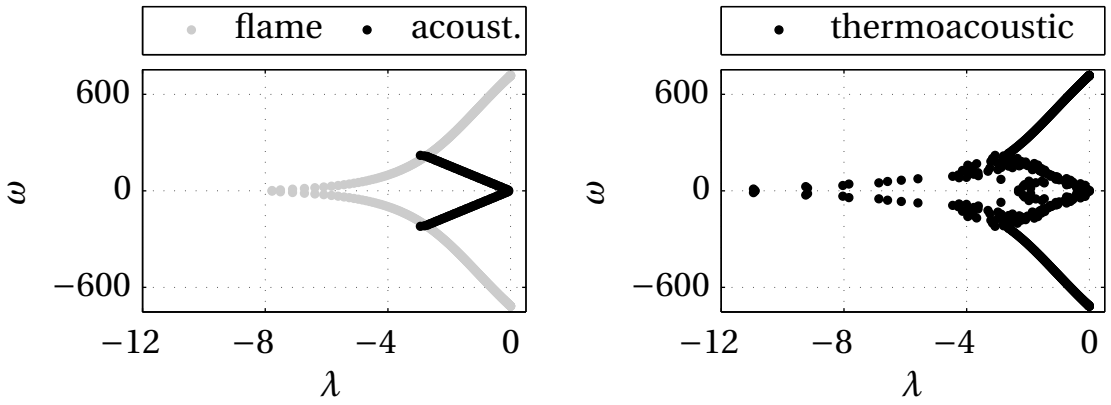

(a) Uncoupled: $K = 0$. **(b)** Coupled: $K = 7.4 \times 10^{-4}$.

Figure 6.3: Eigenspectra of $\mathcal{S}^{(T)}$ for (a) uncoupled and (b) coupled subsystems $\mathcal{S}^{(A)}$ and $\mathcal{S}^{(F)}$. For $K > 0$, the eigenvalues of both subsystems merge to form a *thermoacoustic* eigenspectrum. Results are obtained by spectral analysis of $\mathbf{A}_M^{(T)}$ with otherwise default parameter values.

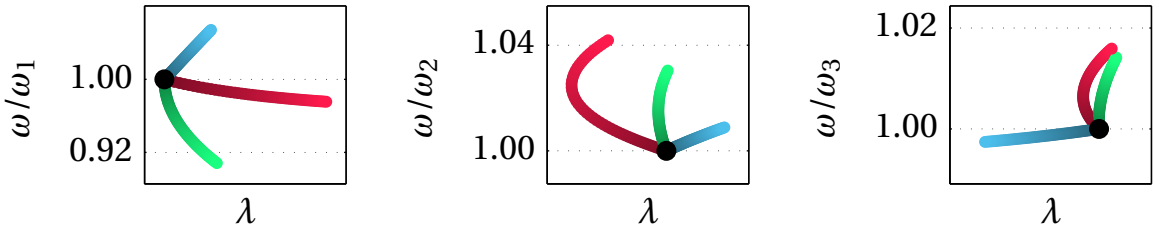

(a) First eigenvalue. **(b)** Second eigenvalue. **(c)** Third eigenvalue.

Figure 6.4: First three eigenvalues of $\mathcal{S}^{(T)}$ plotted as a function of growth rate λ and frequency of oscillation ω subject to the increasing strength of the heat source $K = [0, 7.4 \times 10^{-4}]$ for Sr = 0.1 (from black to blue), Sr = 1 (from black to green), and Sr = 3 (from black to red) computed from spectral analysis of $\mathbf{A}_M^{(T)}$ with otherwise default parameter values. Starting point are the acoustic eigenfrequencies for the uncoupled case $K = 0$ indicated by the thick black dots.

cillation ω subject to an increase in the strength of the fluctuating heat source K. For the fast heat source with Sr = 0.1, the eigenvalues move in the same direction over the entire range of increasing K. That is, the eigenvalues either become more stable (as the first two eigenvalues shown in Figs. 6.4(a) and 6.4(b)), or more unstable (as the third eigenvalue shown in Figs. 6.4(c)). This stands in contrast to the slow heat sources with Sr = 1 and Sr = 3. Here the direction of the path may change while K is increased. That is, while increasing the strength of the fluctuating heat source, an eigenvalue may first become more stable and then move back towards higher growth rates, or vice versa. This behavior seems to become more pronounced for increasing Strouhal number Sr (see the second and third eigenvalues in Figs. 6.4(b) and 6.4(c)).

A similar finding of thermoacoustic eigenvalues changing direction while the strength of the fluctuating heat source is increased is reported by Emmert *et al.* [41]. Strictly speaking, this behavior makes K less apt to be used as linear stability parameter. It cannot be excluded that the system returns to the linearly stable regime when increasing K beyond a critical threshold at which the system becomes unstable. However, for the present low-order model of $\mathcal{S}^{(T)}$ with the investigated configuration, the turning behavior is stronger for eigenvalues with higher than with lower frequency of oscillation (see Fig. 6.4).

	acoustic				mixed		flame			
	ξ_F	ζ_1	ζ_2	Δ_β	M_u	Sr	ϕ	α	μ	type
min.	0.025	−0.13	−0.03	0	0	10^{-3}	0.5	20°	0.86	wedge
max.	0.475	−0.01	−0.005	2	0.05	5	1	25°	1	wedge

Table 6.2: Parameter ranges for the linear stability analysis of $\mathcal{S}^{(T)}$.

Due to the employed modal damping model, these higher modes are damped more strongly. The first eigenmode is thus most likely to govern the overall linear stability behavior of $\mathcal{S}^{(T)}$. In this case, K represents a reliable linear stability parameter, and will be used as such in the following Sec. 6.2.

Altogether, a spectral analysis of $\mathcal{S}^{(T)}$ highlights that thermoacoustic systems should be seen as a whole. This stands in contrast to the traditional approach of viewing thermoacoustics as an acoustic system that is slightly perturbed by a fluctuating heat source (see the discussion in the introductory Sec. 1.2). As $\mathcal{S}^{(A)}$ and $\mathcal{S}^{(F)}$ are inherently coupled, it makes sense to speak of *thermoacoustic* behavior, rather than seeking to separate cause and effect of two subsystems that are in direct feedback.

6.2 Linear Stability Analysis

The present section deals with the linear stability behavior of $\mathcal{S}^{(T)}$. The stability bounds are obtained in two ways, which are detailed in the following.

6.2.1 Classical Eigenvalue Analysis of the System Operator

In the first approach, linear stability is determined by finding the critical strength of the heat source $K = K_{\text{crit}}$ at which the system is marginally stable. Marginal stability is reached when the largest growth rate of the eigenvalues of the discrete system matrix $\mathbf{A}_M^{(T)}$ is zero. The resulting stability maps are presented in a 2-parameter space. Larger (smaller) values of K_{crit} indicate more (less) stable regions. The theoretical limiting case of $K_{\text{crit}} = 0$ would mean that

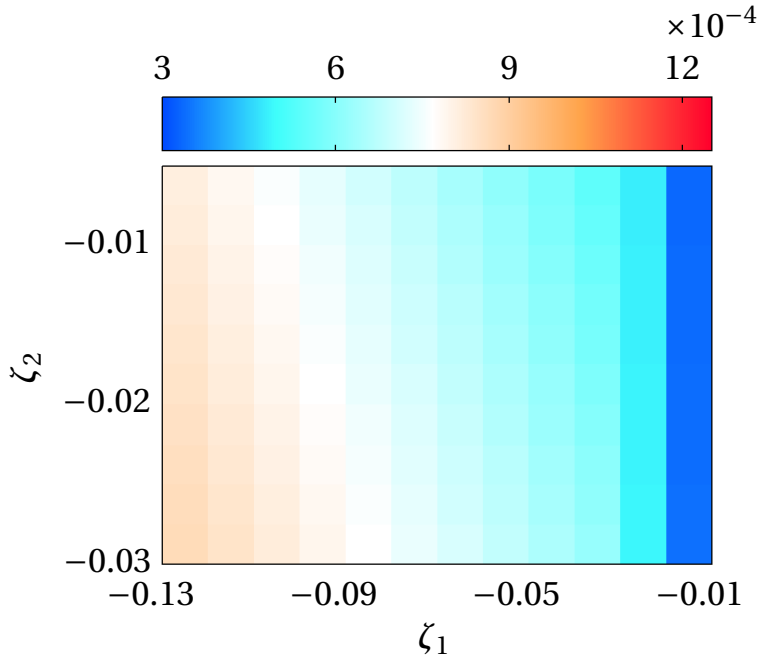

Figure 6.5: Linear stability map of $\mathcal{S}^{(T)}$ in terms of K_{crit} in the (ζ_1,ζ_2)-parameter space with otherwise default parameter values. More (less) stable regions are indicated by larger (smaller) values of K_{crit}.

the system is linearly unstable even in the absence of thermoacoustic coupling.

The parameter ranges over which linear stability of the thermoacoustic model is investigated are summarized in Tab. 6.2. As for the default parameter values given in Tab. 6.1, the parameter ranges are inspired by values encountered in typical configurations of laminar thermoacoustic systems (cf. Tab. 1.1).

Consider as example the linear stability map of ζ_1 vs. ζ_2 given in Fig. 6.5. The critical strength of the heat source K_{crit} increases for increasing values of ζ_i. As anticipated, linear stability is thus enhanced for larger damping. Due to the definition of the modal damping model in Eq. (4.31), ζ_1 is more influential than ζ_2.

The linear stability maps of $\mathcal{S}^{(T)}$ in different 2-parameter spaces are shown in Fig. 6.6. To ease comparison, the first parameter is always given by the temperature incremental factor Δ_β. The first column represents the effect on linear

stability of the acoustic and mixed parameters ξ_F, M_u and Sr, whereas the second column shows the effect of the flame parameters ϕ, α and μ. The results are summarized in the following:

- Flame position ξ_F (Fig. 6.6(a)). The spatial location at which the fluctuating heat source feeds into the acoustic field is an important factor for the linear stability of $\mathcal{S}^{(T)}$. The acoustic field is least receptive for $\dot{q}_1$ (i.e., most stable) in the region of $\xi_F = 0.28 \ldots 0.38$. The downstream half of the duct for $0.5 < \xi_F < 1$ is not shown, because it does not yield additional relevant information as compared to the upstream half depicted in Fig. 6.6(a).

- Upstream Mach number M_u (Fig. 6.6(c)). The effect of non-zero mean flow on linear stability is small in the range of upstream Mach numbers considered. For the temperature incremental factor $\Delta_\beta < 0.5$, increasing mean flow has a slightly destabilizing effect on $\mathcal{S}^{(T)}$. For $\Delta_\beta > 0.5$, this trend is inverted. It is difficult to give a physical explanation of the observed stability map, because the variation of K_{crit} is marginal in the range of M_u and Δ_β considered. However, both the mean flow and the temperature jump affect the thermoacoustic eigenmodes (see Figs. 4.5 and 6.2), and thereby also alter the linear stability behavior.

- Strouhal number Sr (Fig. 6.6(e)). The ratio of time scales between the subsystems $\mathcal{S}^{(F)}$ and $\mathcal{S}^{(A)}$ has a destabilizing effect on $\mathcal{S}^{(T)}$. That is, heat sources with large characteristic time scales tend to be detrimental for the stability of the thermoacoustic system. It is well-known from control theory that systems with large delays are more difficult to control [169], because a change in the delayed part of the system shows its effect only after some time lag. This is also the case for the thermoacoustic interaction present in $\mathcal{S}^{(T)}$. Conversely, fast heat sources have a stabilizing effect on $\mathcal{S}^{(T)}$. For small values of Sr, K_{crit} is of the order of four times larger than the maximum K_{crit} associated to the red color shading.

- Fuel-to-air ratio ϕ (Fig. 6.6(b)). Lean combustion clearly has a destabilizing effect on $\mathcal{S}^{(T)}$. In the present study, the reason for this stability behavior is linked to the specific model of the premixed flame. From Fig. 3.3, it is visible that decreasing ϕ entrains a decrease in flame speed S_L and in

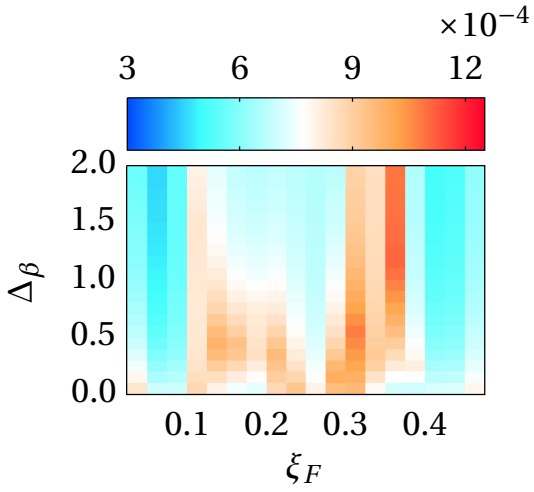

(a) K_{crit} for Δ_β vs. ξ_F.

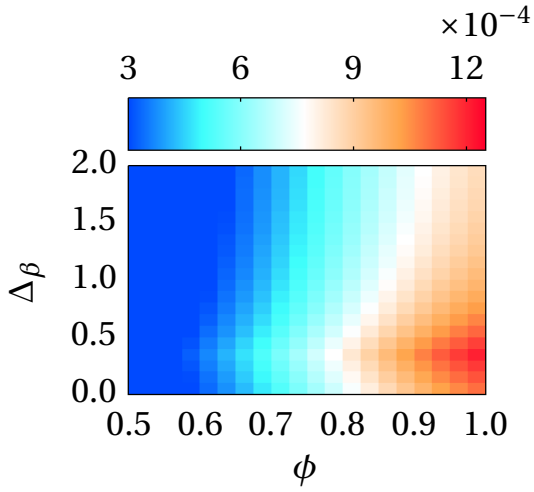

(b) K_{crit} for Δ_β vs. ϕ.

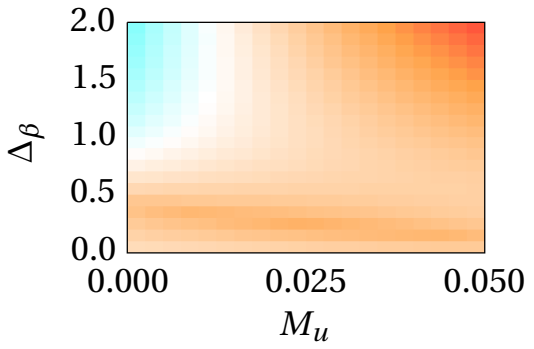

(c) K_{crit} for Δ_β vs. M_u.

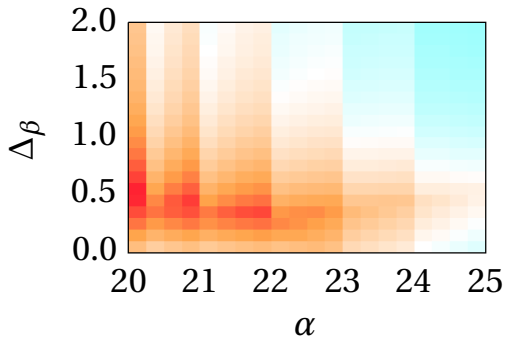

(d) K_{crit} for Δ_β vs. α.

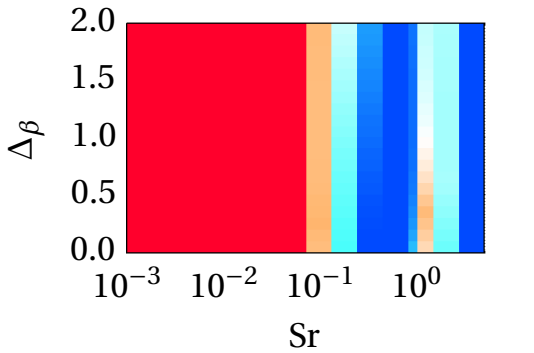

(e) K_{crit} for Δ_β vs. Sr.

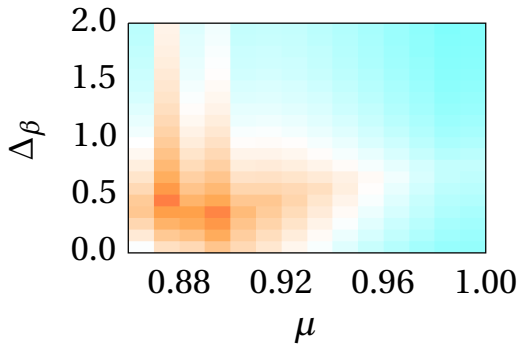

(f) K_{crit} for Δ_β vs. μ.

Figure 6.6: Linear stability maps of $\mathcal{S}^{(T)}$ given in terms of K_{crit} in different 2-parameter spaces with otherwise default parameter values. More (less) stable regions are indicated by larger (smaller) values of K_{crit}.

heat of reaction q_R. Both directly affect the mean heat release rate $\dot{q}_0$ (i.e., the mean power of the flame), which thus reduces with ϕ (see Eq. (3.8b)). In addition, since we require the Strouhal number to remain constant at the default parameter value of Sr = 1, a decrease in S_L requires an equivalent decrease in the flame radius R_F (see the definition of Sr in Eq. (6.6)). Finally, the prefactor appearing in the definition of the IR function of the premixed wedge flame in Eq. (3.27b) contains the term $\dot{q}_0/R_F^2$. The latter IR function governs the strength of the fluctuations in heat release rate $\dot{q}_1$. In reducing $\dot{q}_0$ and R_F with ϕ, the fluctuating heat source thus gains strength, and leads to a destabilization of $\mathcal{S}^{(T)}$.

- Flame angle α (Fig. 6.6(d)). In a general fashion, increasing the flame angle α has a destabilizing effect on $\mathcal{S}^{(F)}$. That is, short flames, where the ratio of convective to restorative times scales Π is small, are less stable. It thus seems that the configuration is less stable the more the process of convection and restoration are decoupled. However, this trend is not homogeneous. As can be seen from the corresponding stability map, the stabilizing impact of α is largest for $\Delta_\beta < 0.5$.

- Ratio of convective to mean flow velocities μ (Fig. 6.6(f)). In a general fashion, increasing μ has a destabilizing effect on $\mathcal{S}^{(T)}$. That is, the system becomes more stable for small convective velocities, which—as for the flame angle α—amounts to large ratios of convective to restorative time scales Π. This is why the corresponding stability map is very similar to that of α vs. Δ_β given in Fig. 6.6(d). Both parameters affect the shape of the IR function of the flame (see Fig. 3.7 in Sec. 3.3.1).

- Temperature incremental factor Δ_β (all plots in Fig. 6.6). The effect of a temperature jump on the linear stability behavior of $\mathcal{S}^{(T)}$ is strong. However, depending on the operating point, the effect may be stabilizing or destabilizing. A general trend cannot be stated.

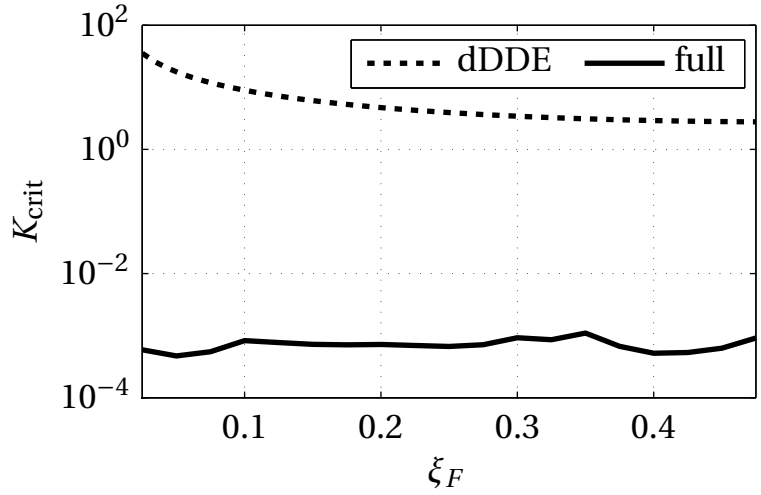

Figure 6.7: Linear stability bound of $\mathcal{S}^{(T)}$ given in terms of K_{crit} as a function of ξ_F computed from the analytical solution of Eq. (6.8) (– – –) with $N_{A,M} = 1$ and by spectral analysis of $\mathbf{A}_M^{(T)}$ (—) with $N_{A,M} = 70$. Configuration: $M_u = 0$, $\Delta_\beta = 0$, and otherwise default parameters.

6.2.2 Eigenvalue Analysis of Delay Differential Equations

The second approach to determine linear stability makes use of the definition of a coupled input given in Sec. 2.3.1. As $\mathcal{S}^{(F)}$ is modeled by an IR-based representation, its state vector is given as lagged acoustic velocity fluctuations at the flame base, $x^{(F)} = v_1^B(t-\tau)$ (see Sec. 3.2.2). In this special case, $\mathcal{S}^{(F)}$ acts as coupled input to $\mathcal{S}^{(A)}$. Upon discretization, the linear stability can therefore alternatively be determined by solving for the roots of the characteristic equation (2.17) of a set of distributed delay differential equations (dDDE). For the present low-order model, the characteristic equation reads [114, 163]

$$\det\left[s\mathbf{I} - \mathbf{A}_M^{(A)} - \mathrm{diag}\left(\mathbf{B}_M^{(A)}\right) F^{(F)}(s)\right] = 0\,, \tag{6.8}$$

where $F^{(F)}(s)$ represents the transfer function of the linearized G-equation flame, which is obtained by Laplace transform of the IR functions given in Eqs. (3.27).

As mentioned in Sec. 2.3.1, the characteristic equation (6.8) possesses an infinite number of eigenvalues s_i. It can be solved using software packages designed for the numerical treatment of delay differential equations, such as

DDE-BIFTOOL [42] or TRACE-DDE [21]. In a single-mode approximation of the MWR (i.e., $N_{A,M} = 1$), the linear stability bound of Eq. (6.8) can be determined analytically by setting $s = \pm j\omega$ [166].

Although the current approach describes an elegant analytical solution and a quick estimate of the linear stability bound [163], the latter may not be very accurate. This is shown in Fig. 6.7, where K_{crit} of $\mathcal{S}^{(T)}$ is plotted as a function of ξ_F. The analytical estimates of the stability bounds do not match at all, neither in trend nor in order of magnitude, to those computed by spectral analysis of the full operator $\mathbf{A}_M^{(T)}$ with $N_{A,M} = 70$. This mismatch is due to the inability of a single mode to resolve the thermoacoustic mode shapes.

6.3 Chapter Summary

The present chapter can be summarized as follows:

- The low-order thermoacoustic model is assembled and studied as to its linear system behavior. This includes the effect of different parameters on the linear stability bounds of $\mathcal{S}^{(T)}$, as well as analyzing the flux and source terms in charge of driving and damping the output energy.
- We highlight the benefit of adopting a holistic view on thermoacoustic systems, rather than treating it as an acoustic problem that is slightly perturbed by a heat source.

7 Non-Normal Transient Growth in Thermoacoustics

The present chapter stands at the core of the present thesis. The low-order thermoacoustic model formulated in the previous chapters is employed to investigate non-normal transient growth of a simple thermoacoustic system around a stable fix point. The overall aim is to gain a deeper understanding on the basic dynamics of non-normal transient growth and to indicate whether it could be a threat for triggering $\mathcal{S}^{(T)}$ to an oscillating state.

The chapter is organized as follows. In Sec. 7.1, we contrast spurious to physical non-normal transient growth, which is strongly related to the numerical schemes used to resolve the model of $\mathcal{S}^{(T)}$. Physical non-normal transient growth is analyzed in detail as to its dynamics and to the relevant parameters influencing transient growth in Sec. 7.2. In Sec. 7.3, we determine the probability of observing any (optimal or suboptimal) level of transient growth in $\mathcal{S}^{(T)}$. The concept is exemplified for a toy model of $\mathcal{S}^{(T)}$ with two degrees of freedom, before being applied to the full low-order model of $\mathcal{S}^{(T)}$. The relevance of non-normal transient growth for triggering is discussed in Sec. 7.4.

7.1 Spurious Non-Normal Transient Growth

As discussed in the introductory Sec. 1.1.1, the study of non-normality first arose in the field of numerical computation to determine the condition of operators [60, 94, 174]. If an operator is ill-conditioned due to the underlying numerical scheme, this may cause non-normality that cannot be attributed to the physical problem at hand. In this case, the operator exhibits *spurious* non-normality, which may lead to spurious non-normal transient growth.

The majority of discretized numerical operators possesses a certain amount of spurious non-normality, which is inevitable due to the necessary inclusion of boundary conditions, field inhomogeneities or meshing constraints. This does not alter the ability of these operators to represent the dynamics of the problem, so as to generate reliable stability maps or to correctly forward the problem in time. However, if one is interested in studying non-normal transient growth, the amount of spurious non-normality should not dominate the total amount of non-normality.

In general, it is difficult to distinguish between spurious and physical non-normality, because both are present in parallel. One approach is to analyze a normal system that by definition lacks any sources of physical non-normality. Such a normal system is given by the isolated and undamped simple acoustic subsystem $\mathcal{S}^{(A)}$ defined in Sec. 4.2 without mean flow and temperature jump, $K = 0$, $M_u = 0$, $\zeta_i = 0$ and $\Delta_\beta = 0$. As the boundary conditions are acoustically fully reflective, the acoustic energy of any acoustic field initialized inside the duct remains constant over time. Growth or decay of acoustic energy are thus not possible in this theoretical configuration, and the problem is free of physical non-normality.

The time traces of the maximum normalized output energy $G(t)$ and the evolution of optimal relative amplification of output energy $\mathcal{G}^*(t)$ of the normal configuration of $\mathcal{S}^{(A)}$ are shown in Fig. 7.1 using the FD scheme and the method of weighted residuals (MWR) defined in Secs. 4.4.1 and 4.4.2, respectively. It is evident that the MWR predicts the anticipated result of $G(t) = \mathcal{G}^*(t) = const. = 1$. In contrast, the FD scheme predicts $G_{\max} \approx 2$, and $\mathcal{G}^*(t)$ distinctly increases twice before remaining constant for $t > 1$ acoustic time scale. The FD system matrix $\mathbf{A}^{(A)}$ thus exhibits spurious non-normality.

The origins of spurious non-normality of the FD scheme can be explained with the help of Fig. 7.2, where the optimal initial mode shapes given in terms of $v_1(\xi)$ and $p_1(\xi)$ and their evolutions in time are plotted at different snapshots corresponding to those indicated in Fig. 7.1. The optimal initial mode shape $\mathbf{x}_0^{*(A)}$ at $t = 0$ depicted in Fig. 7.2(a) contains wrinkles with steep gradients near the boundaries. At $t = t_1$, these wrinkles have been reflected at the boundaries, which is visible from the phase change of the acoustic pressure in

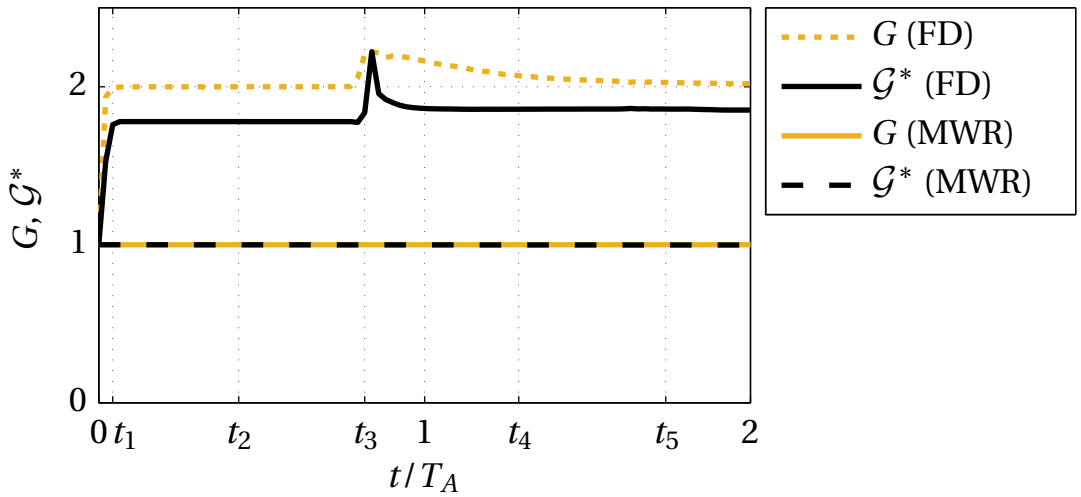

Figure 7.1: The maximum normalized output energy G and the optimal relative amplification of output energy $\mathcal{G}^*$ from the OIC $\mathbf{x}_0^{*(A)}$ of the normal configuration of $\mathcal{S}^{(A)}$ (without damping, mean flow, heat source and temperature jump) using the FD scheme and the method of weighted residuals (MWR) defined in Secs. 4.4.1 and 4.4.2, respectively. The FD scheme exhibits spurious non-normal transient growth, whereas the MWR does not.

Fig. 7.2(b). This goes hand in hand with a significant increase in the optimal relative amplification of output energy $\mathcal{G}^*$ (see Fig. 7.1). The latter remains constant while the wrinkles are propagated through the duct (see Fig. 7.2(c)), and again increases when the wrinkles are once more reflected at the boundary (see Fig. 7.2(d)). As the FD method used is not apt to handle oscillations with steep gradients, the wrinkles are dissipated, which can be seen from the smoothened shape of the wrinkles at $t = t_4$ in Fig. 7.2(e). From this point onwards, the wrinkles do not contain strong gradients anymore, and the optimal relative amplification of output energy $\mathcal{G}^*$ remains constant over time as it should be, even when the acoustic waves are reflected at the boundaries (cf. Figs. 7.2(f) and 7.1).

For the FD scheme, the implemented boundary conditions thus render the discrete state matrix ill-conditioned (see also the structure of $\mathbf{A}^{(A)}$ given in App. C.3.1). The optimization algorithm, which optimizes over the *entire*

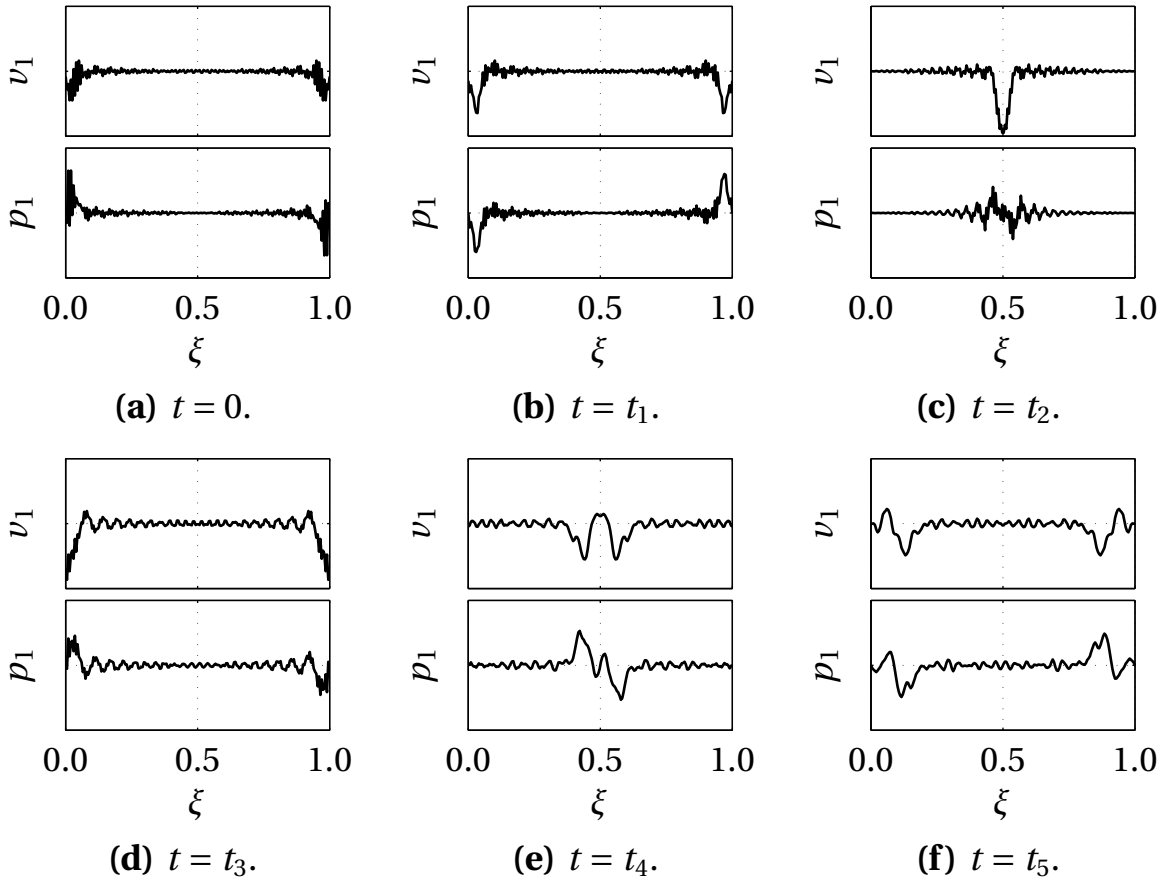

(a) $t = 0$. **(b)** $t = t_1$. **(c)** $t = t_2$.

(d) $t = t_3$. **(e)** $t = t_4$. **(f)** $t = t_5$.

Figure 7.2: OIC $\mathbf{x}_0^{*(A)}$ and its evolution in time of the normal configuration of $\mathcal{S}^{(A)}$ using the FD scheme defined in Sec. 4.4.1. The snapshots in time are indicated in the corresponding time traces of $G(t)$ and $\mathcal{G}^*(t)$ in Fig. 7.1. $\mathbf{x}_0^{*(A)}$ is visualized in terms of $v_1^*(\xi)$ and $p_1^*(\xi)$.

space of initial conditions, thus generates oscillations in $\mathbf{x}_0^{*(A)}$ that are not consistent with the imposed boundary conditions, and that the underlying numerical scheme cannot handle. Thereby, spurious energy is generated. Avoidance of these unphysical oscillations in $\mathbf{x}_0^{*(A)}$ would require an additional constraint to limit the space of permissible initial conditions. This is only possible using variational optimization methods (see the discussion in Sec. 2.4.2). In contrast, the MWR does not exhibit spurious non-normal transient growth, because the entire space of initial conditions implicitly fulfills the boundary conditions. The latter hence do not alter the condition of the discretized numerical operator $\mathbf{A}_M^{(A)}$.

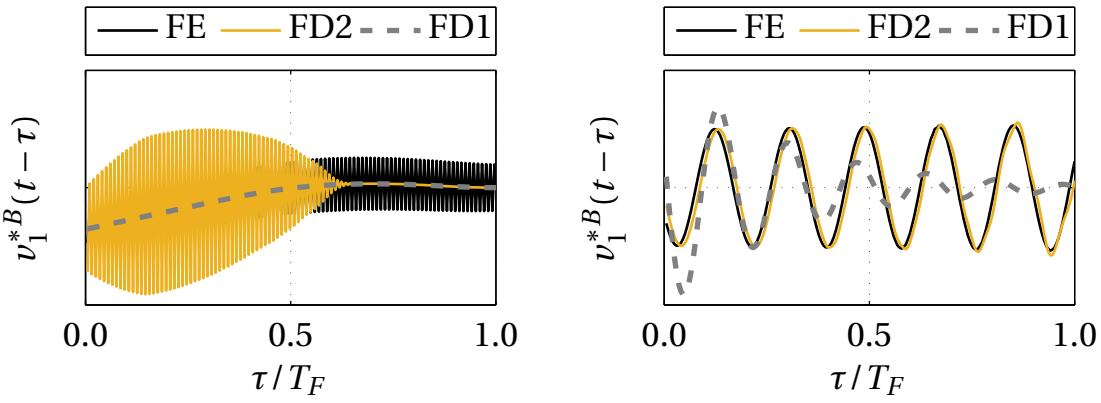

(a) Optimal initial condition $\mathbf{x}_0^{*(F)}$. **(b)** Stationary harmonic forcing.

Figure 7.3: (a) Optimal initial condition $\mathbf{x}_0^{*(F)}$ given in terms of $v_1^{*B}(t-\tau)$ at $t=0$ plotted over the history variable τ of a generic test case using an FE (—), FD2 central (—), and FD1 backward scheme (– – –). The boundary conditions of the FE and FD2 schemes render the underlying operators ill-conditioned, leading to unphysical oscillations in $\mathbf{x}_0^{*(F)}$. (b) Profiles of $v_1^B(t-\tau)$ subject to mono-frequent harmonic forcing. Unlike the FD schemes, the FE scheme is nearly free of dissipation and dispersion.

The same phenomenon of unphysical oscillations in the optimal initial condition is also observable for different numerical schemes modeling the heat source subsystem $\mathcal{S}^{(F)}$. In Fig. 7.3(a), we compare $\mathbf{x}_0^{*(F)}$ given in terms of the optimal initial profiles of lagged acoustic velocity at the flame base $v_1^{*B}(t-\tau)$ plotted over the history variable τ of a generic test case obtained by an FE scheme (the default scheme used), a 2$^{\text{nd}}$ order central FD scheme (FD2), and a 1$^{\text{st}}$ order backward FD scheme (FD1). The latter scheme was used by Subramanian & Sujith in a similar context [165]. The discretized numerical operators of the FE and FD2 schemes are ill-conditioned due to the implemented boundary conditions, and the corresponding $\mathbf{x}_0^{*(F)}$ exhibit unphysical oscillations. This is not the case for the FD1 scheme, where the boundary condition does not alter the condition of the matrix (not shown, see for example Eq. (B6) in [165]). However, the coarse-grained shape of $\mathbf{x}_0^{*(F)}$ is the same for all three schemes.

The picture changes when comparing the performance of the different numerical schemes with respect to profiles that are not computed from an optimization routine. Figure 7.3(b) displays the profiles of $v_1^B(t-\tau)$ subject to mono-frequent harmonic excitation. The FE scheme is the only scheme nearly free of dissipation and dispersion. Despite producing the best results with respect to the OIC, the FD1 scheme is highly dispersive and dissipative.

As mentioned in the beginning of the present section, spurious non-normality is troublesome if its effect on transient growth is of the same order of magnitude as that resulting from physical non-normality. In Fig. 7.4, we plot the growth rate $\lambda_{\max}$ of the most unstable eigenvalue $s_{\max}$ of the dissipation matrix $\mathbf{Q}^{(T)}$ of the low-order thermoacoustic model describing $\mathcal{S}^{(T)}$ over the strength of the fluctuating heat source K. The acoustics subsystem $\mathcal{S}^{(A)}$ is modeled using the FD scheme and the MWR, respectively, and the heat source subsystem $\mathcal{S}^{(F)}$ is modeled using the FE scheme. According to the discussion given in Sec. 2.4.1, the largest growth rate $\lambda_{\max}(\mathbf{Q}^{(T)})$ indicates an upper bound on the supply rate to the temporal change in output energy. For $K = 0$ ($K > 0$), the subsystems $\mathcal{S}^{(A)}$ and $\mathcal{S}^{(F)}$ are uncoupled (coupled). Increasing K to the linear stability bound at $K = K_{\text{crit}}$ thus introduces physical non-normality to $\mathcal{S}^{(T)}$.

The dashed lines in Fig. 7.4 depict the case without mean flow and temperature jump. For $K = 0$, only damping affects the output energy (see the flux and source terms in Eqs. (6.7)). The output energy E then represents a strictly decaying Lyapunov function, and $\lambda_{\max}(\mathbf{Q}) < 0$. For $K > 0$, the output energy E may transiently grow due to the first source term in Eq. (6.7b), and $\lambda_{\max}(\mathbf{Q}) > 0$. Using the MWR to model $\mathcal{S}^{(A)}$, $\lambda_{\max}(\mathbf{Q})$ follows the anticipated trend and monotonically increases with K. Using the FD scheme, $\lambda_{\max}(\mathbf{Q}) = const.$ for all K. This shows that for this configuration spurious non-normality is stronger than or at least of the same order of magnitude as physical non-normality.

The full lines in Fig. 7.4 signify the case where $\mathcal{S}^{(T)}$ is configured using the default parameter values given in Tab. 6.1. In this case, all source terms given in Eq. (6.7b) are present, and transient growth is possible even for $K = 0$. We therefore expect $\lambda_{\max}(\mathbf{Q}) > 0$ for all K. This is confirmed by both methods describing $\mathcal{S}^{(A)}$. For the FD scheme, $\lambda_{\max}(\mathbf{Q}) = const.$ takes nearly the

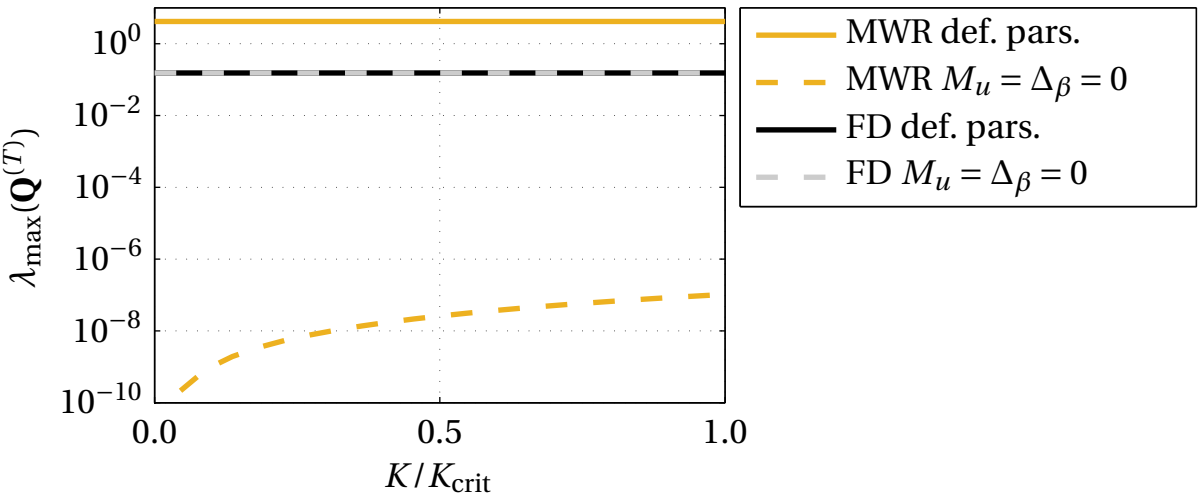

Figure 7.4: Growth rate $\lambda_{\max}$ of the most unstable eigenvalue $s_{\max}$ of $\mathbf{Q}^{(T)}$ over K/K_{crit}. $\mathcal{S}^{(A)}$ is modeled using the FD scheme or the MWR. For $M_u = 0$ and $\Delta_\beta = 0$ $(---)$, $\lambda_{\max}(\mathbf{Q})^{(T)}$ should increase with K, as is the case for the MWR, but not for the FD scheme. For default parameter values, it is expected that $\lambda_{\max}(\mathbf{Q})^{(T)} > 0$, because non-zero source terms can cause non-normal transient growth of energy even for $K = 0$. This trend is confirmed by both methods.

same value as without mean flow and temperature jump. For the MWR, $\lambda_{\max}(\mathbf{Q}) = const.$ is much larger than without mean flow and temperature jump. As the condition of the operator is now also affected by the presence of mean flow and temperature jump, it is not possible to distinguish the effects of spurious and physical non-normality. However, since the presence of mean flow and temperature jump shows an effect on $\lambda_{\max}(\mathbf{Q})$, and since $\lambda_{\max}(\mathbf{Q})$ follows the anticipated trend, it is concluded that the MWR is nonetheless better suited to study non-normal transient growth than the FD scheme.

In summary, the FD scheme is not suited for the study of non-normal transient growth. Corroborating the arguments in favor of the MWR made in the end of Sec. 4.4.2, all results produced in the remainder of this chapter thus make use of the MWR to model the acoustics subsystem $\mathcal{S}_A$. Concerning the performance of the schemes modeling $\mathcal{S}^{(F)}$, we decide to use the FE scheme for transient simulations (as defined by default in Sec. 3.2.2), and to use the FD1 scheme to compute the OIC $\mathbf{x}_0^{*(F)}$.

7.2 Analysis of Physical Non-Normal Transient Growth

The current section deals with the analysis of the physical non-normal transient growth observed in the simple thermoacoustic system $\mathcal{S}^{(T)}$. Since the output energy defines a semi-norm, we investigate the influence on transient growth of those initial states that are not contained in the output energy, and how the optimal normalized energy amplification $H_{\max}$ and the optimal mode shapes evolve in time (see Sec. 7.2.1). The influence of different model parameters on transient growth is addressed in Sec. 7.2.2. By default and unless otherwise mentioned, the strength of the fluctuating heat source K is set to approximately 99 % of the critical value K_{crit} at the linear stability bound.

Before proceeding, it is necessary to ensure that the results presented in the following are independent of the resolution of the numerical schemes used. In Fig. 7.5(a), we investigate the value of $H_{\max}$ obtained when varying the number of basis functions $N_{A,M}$ used in the numerical model of $\mathcal{S}^{(A)}$. Since N_{IR}

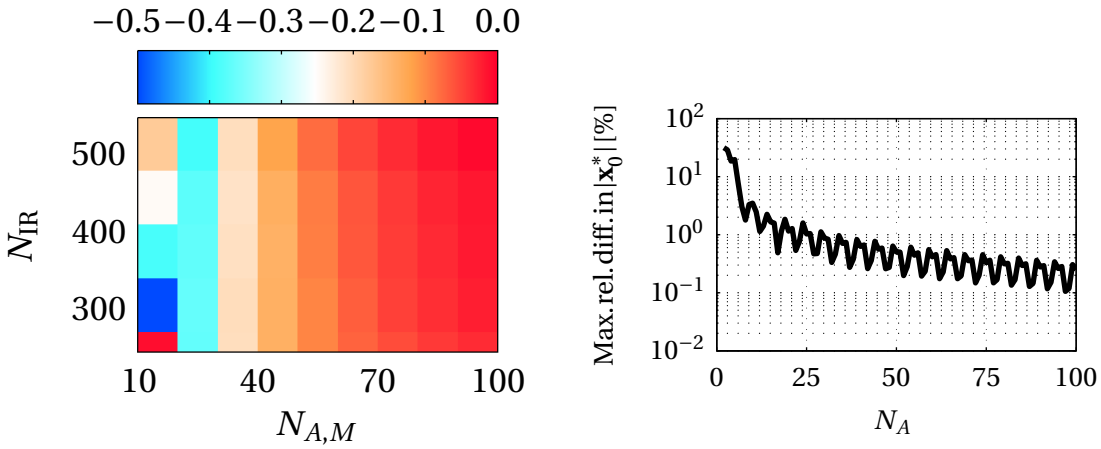

(a) Relative difference of $H_{\max}$ (%). **(b)** Max. of rel. diff. in $|\mathbf{x}_0^{*(T)}|$ (%).

Figure 7.5: (a) Relative difference of $H_{\max}$ (%) as a function of the number of basis functions $N_{A,M}$ (and thus N_{IR}). The reference value of $H_{\max} \approx 1.6$ is taken at the finest grid resolution $N_{A,M} = 100$ (corresponding to $N_{\text{IR}} = 550$). (b) Maximum of the relative difference (%) between $|\mathbf{x}_0^{*(T)}|$ with $N_{A,M}$ and $N_{A,M}-1$ as a function of $N_{A,M}$. Configuration: $\kappa_0 = 0$, $K = 7.3 \times 10^{-4}$, default parameter values.

used in the numerical model of $\mathcal{S}^{(F)}$ is linked to $N_{A,M}$ by a condition ensuring numerical stability, $N_{\mathrm{IR}} \propto (N_{A,M}, \mathrm{Sr}, \Delta_\beta, M_u)$, variation of $N_{A,M}$ accordingly changes N_{IR}. The color shading indicates the difference in $H_{\max}$ relative to the finest resolution in the top right corner of the plot. It is visible that $H_{\max} \approx 1.6$ changes by less than 0.1 % for $N_{A,M} > 50$.

The maximum of the relative difference between $|\mathbf{x}_0^{*(T)}|$ with $N_{A,M}$ and $N_{A,M}-1$ basis functions is plotted in Fig. 7.5(b) over $N_{A,M}$. For $N_{A,M} > 30$, the coarse-grained slope of this error measure is below 1 %. To ensure independence from the numerical resolution, all following results are produced with $N_{A,M} = 70$ unless otherwise mentioned. For default parameter values, this corresponds to $N_{\mathrm{IR}} = 414$.

7.2.1 The Dynamics of Non-Normal Transient Growth

The Effect of Kernel Energy

Since the output energy E of the discrete model $(\mathbf{A}^{(T)}, \mathbf{C}^{(T)})$ of $\mathcal{S}^{(T)}$ defines a semi-norm (see Sec. 6.1.1), the initial ratio of kernel to output energy κ_0 should be taken into account as an additional optimization parameter to find the optimal relative amplification of output energy $\mathcal{G}_{\max} = E_{\max}/E_0$ (see also the discussion in Sec. 2.4.2).

The first limiting case is that of $\kappa_0 = 0$, where the initial condition does not contain fluctuations in the heat source subsystem $\mathcal{S}^{(F)}$. The corresponding time traces of the maximum normalized energy amplification H (defined in Eq. (2.34)) and optimal relative energy amplification $\mathcal{G}^*$ (defined in Eq. (2.26)) are plotted in Fig. 7.6(a) and 7.6(c) for default and minimum values of damping, respectively. For default damping values, $H_{\max} \approx 1.6$ is reached at $t^* = 1.69$ acoustic time scales. For low damping, $H_{\max} \approx 1.7$ occurs very quickly at $t^* = 0.34$ acoustic time scales.

The other limiting case is obtained for $\kappa_0 = \infty$, where the initial output energy $E_0 = 0$ and thus $\mathcal{G}_{\max} = \infty$. In this case, the optimal initial condition $\mathbf{x}_0^{*(T)}$ contains non-zero entries only in $\mathbf{x}_0^{(F)}$, which subsequently affect the acoustic field

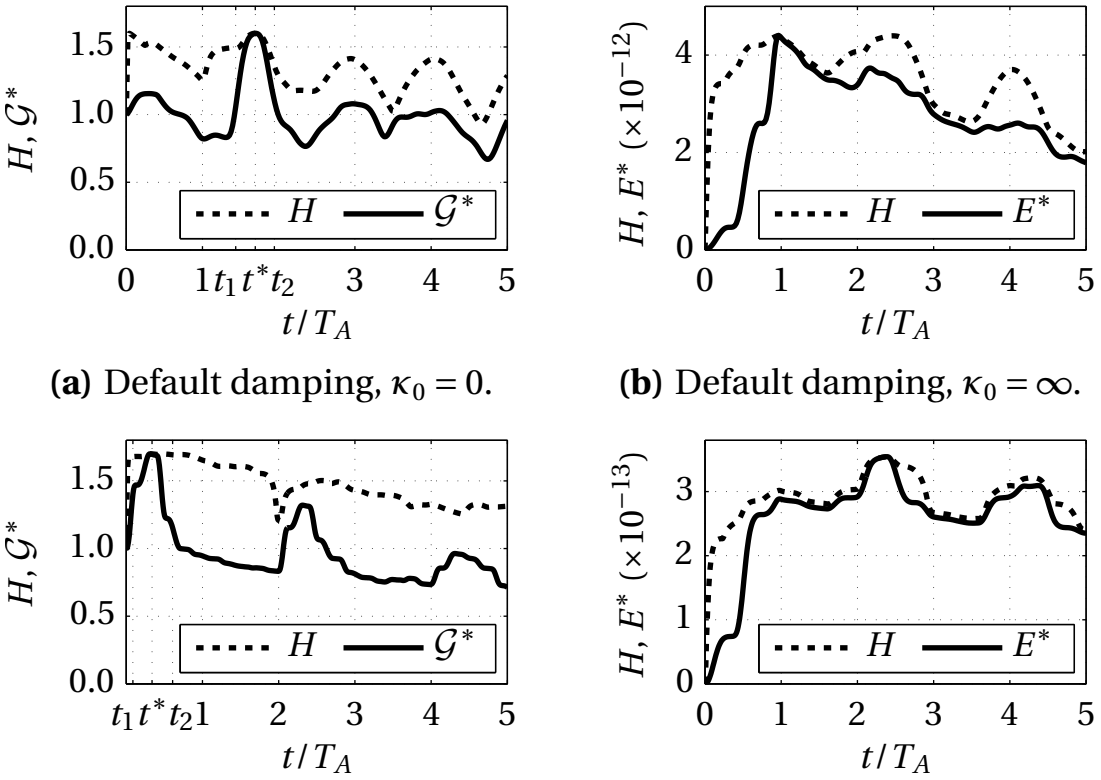

(a) Default damping, $\kappa_0 = 0$.

(b) Default damping, $\kappa_0 = \infty$.

(c) Low damping, $\kappa_0 = 0$.

(d) Low damping, $\kappa_0 = \infty$.

Figure 7.6: Left column: Time traces of the maximum normalized output energy H defined in Eq. (2.34) (− − −) and optimal relative energy amplification $\mathcal{G}^*$ defined in Eq. (2.26) (—) in the limiting case of $\kappa_0 = 0$ (i.e., no kernel energy at $t = 0$). Right column: Same as left column, but for $\kappa_0 = \infty$. In this case $E_0 = 0$, and we plot the optimal amplification of output energy E^* (—). Damping is given by the default (top row) and the minimum parameter values (bottom row) shown in Tabs. 6.1 and 6.2, respectively. Configuration: $K = 7.3 \times 10^{-4}$ and $K = 1.8 \times 10^{-4}$ for default and low damping values, respectively, otherwise default parameter values.

(and thus the output energy E) for $t > 0$. This corresponds to an initial condition where the heat source is perturbed in a quiescent acoustic environment (for example, by oscillating the flame holder without this action generating noise). The time traces of the maximum normalized output energy H and the optimal output energy E^* corresponding to this limiting case are plotted

in Fig. 7.6(b) and 7.6(d) for default and minimum values of damping, respectively. It can be seen that $E_0 = 0$ increases up to $E_{\max} = H_{\max}$ at optimality for $t = t^*$.

In practice, it is not possible to generate initial conditions that are exclusively affecting only one of the subsystems. It is therefore interesting to investigate how the initial ratio of kernel to output energy κ_0 affects the maximum levels of non-normal transient growth. Using the optimization procedure laid out in Sec. 2.4.2, we compute the maximum relative and normalized amplification of output energy $\mathcal{G}_{\max}$ and $H_{\max}$, respectively, over a range of κ_0. As κ_0 is reduced, the initial level of output energy E_0 increases. This decreases the available amount of kernel energy that could potentially be converted to output energy through the coupling between both subsystems. One might therefore expect that the maximum relative energy amplification $\mathcal{G}_{\max}$ increases monotonically with κ_0, as shown by Foures *et al.* [52] for a model of a viscous turbulent flow. For the present model describing $\mathcal{S}^{(T)}$, however, $\mathcal{G}_{\max}$ is not a monotone function of κ_0. As can be seen from Fig. 7.7, $\mathcal{G}_{\max} \approx H_{\max} \approx 1.6$ for $0 \leq \kappa_0 < 10^3$. For $\kappa_0 > 10^3$, $H_{\max}$ tends to infinity, whereas $\mathcal{G}_{\max}$ decreases to values slightly above unity, before finally tending to the anticipated maximum of infinity for $\kappa_0 > 10^{10}$.

Although the initial output energy E_0 indeed decreases for increasing κ_0, the effect of $\mathcal{S}^{(F)}$ onto $\mathcal{S}^{(A)}$ is not sufficiently strong so as to convert large parts of the kernel energy to output energy. This is due to the Rayleigh source term given in the first row of Eq. (6.7b), which dictates that the conversion from kernel to output energy can only take place if the acoustic field is receptive to fluctuations in heat release rate. Otherwise, the interaction of both subsystems does not modify or even decreases E, and kernel energy is not converted to output energy. This effect is fundamentally different from flow systems, where the entire kernel energy eventually transfers to output energy [52].

The behavior of $\mathcal{G}_{\max}$ with respect to κ_0 indicates that the OICs with non-zero initial output energy E_0 are dominated by non-zero values in the state vector $\mathbf{x}_0^{(A)}$ of the acoustics subsystem $\mathcal{S}^{(A)}$. Since the Rayleigh term inhibits conservative transfer of kernel to output energy, initial perturbations in the heat source subsystem $\mathcal{S}^{(F)}$ are not very effective at maximizing the acoustic en-

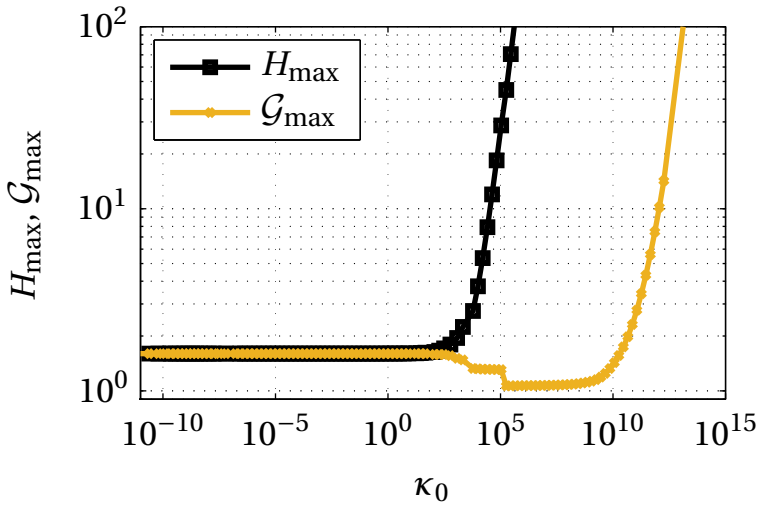

Figure 7.7: Maximum normalized and relative amplification of output energy, $H_{\max}$ and $\mathcal{G}_{\max}$, respectively, as a function of the initial ratio of kernel to output energy κ_0. For $\kappa_0 < 10^3$, $\mathcal{G}_{\max} \approx H_{\max} \approx 1.6$. For $\kappa_0 > 10^3$, $H_{\max}$ tends to infinity, whereas $\mathcal{G}_{\max}$ decreases and only tends to infinity for $\kappa_0 > 10^{10}$. Configuration: $K = 7.3 \times 10^{-4}$, default parameter values.

ergy. As mentioned above, for all practical setups the initial output energy $E_0 > 0$, and thus $\kappa_0 \ll \infty$. In addition, $\mathcal{G}_{\max} \approx H_{\max} \approx 1.6$ is unaffected by the magnitude of the initial kernel energy over a wide range of κ_0. This translates to small perturbations in the heat source subsystem $\mathcal{S}^{(F)}$ not causing a significant change in the dynamics of non-normal transient growth of $\mathcal{S}^{(T)}$. We therefore focus further analysis onto the limiting case of $\kappa_0 = 0$ (i.e., the initial condition does not contain any fluctuations in the heat source subsystem $\mathcal{S}^{(F)}$). This also facilitates interpretation of results, as the relative equals the normalized amplification of output energy, $\mathcal{G}(t) = H(t) = G(t)$.

The Process of Non-Normal Transient Growth

The evolution of the acoustic states $x^{(A)} = [v_1(\xi), p_1(\xi)]^T$ and the flame states $x^{(F)} = v_1^B(t-\tau)$ during the occurrence of non-normal transient growth is visualized in Fig. 7.8 for the default and low damping values specified in Tabs. 6.1 and 6.2. Four snapshots in time are depicted, each corresponding to the op-

timal evolution of relative amplification of output energy $\mathcal{G}^*$ shown in the left column of Fig. 7.6: the OIC at $t = 0$, the phase of dominant transient growth at $t = t_1$, optimality at $t = t^*$, and the phase of decay following $H_{\max}$ at $t = t_2$.

The OIC at $t = 0$ is not instructive as such, but it sets the stage for the phase of growth leading to the optimal energy amplification. This process is analyzed in the following in the context of the flux and source terms driving the temporal evolution of output energy. Since $M = 0.05$ is very small, we neglect the corresponding flux and source terms in Eqs. (6.7). With this simplification, and as discussed in Sec. 6.1.2, transient growth can be explained by two driving source terms, the (physical) Rayleigh source term resulting from the interaction of the acoustic field with the heat source, and the inherent source term resulting from the assumption of a flame at rest. In order to lead to an increase in output energy, driving needs to overcome the strictly dissipative damping term.

For low damping values, the optimal energy amplification $H_{\max}$ occurs at $t^* = 0.34$ acoustic time scales. By this time, the fluctuations in velocity at the flame base have not yet been advected to the tip of the flame, where the dominant flame response in $\dot{q}_1$ is generated. For reference, the shape of the IR function of the premixed wedge flame derived and discussed in Sec. 3.3.1 is overlaid onto the lagged values of velocity fluctuations at the flame base $v_1^B(t-\tau)$ in the right column of Fig. 7.8. Non-zero $v_1^B(t-\tau)$ (indicated by the yellow lines) does not encounter the region of strong flame response in any of the snapshots. Thus no significant fluctuations in heat release rate $\dot{q}_1$ are generated (see also the convolution equation (3.18b) governing the output of the heat source subsystem), and the Rayleigh source term is negligible. On the other hand, the inherent source term is positive if $v_1(\xi_F)$ and $p_1(\xi_F)$ are of opposite sign. This is the case during the driving phase at $t = t_1$. At optimality, $\mathrm{d}E/\mathrm{d}t = 0$, and the net source terms are zero. During the phase of decay at $t = t_2$, $v_1(\xi_F)$ and $p_1(\xi_F)$ are of same sign and thus the output energy E decreases more strongly than solely by the action of dissipative damping.

For default damping values, the optimal energy amplification $H_{\max}$ occurs at $t^* = 1.69$ acoustic time scales. In contrast to the case with low damping, the phase of dominant transient growth is due to both source terms driving the

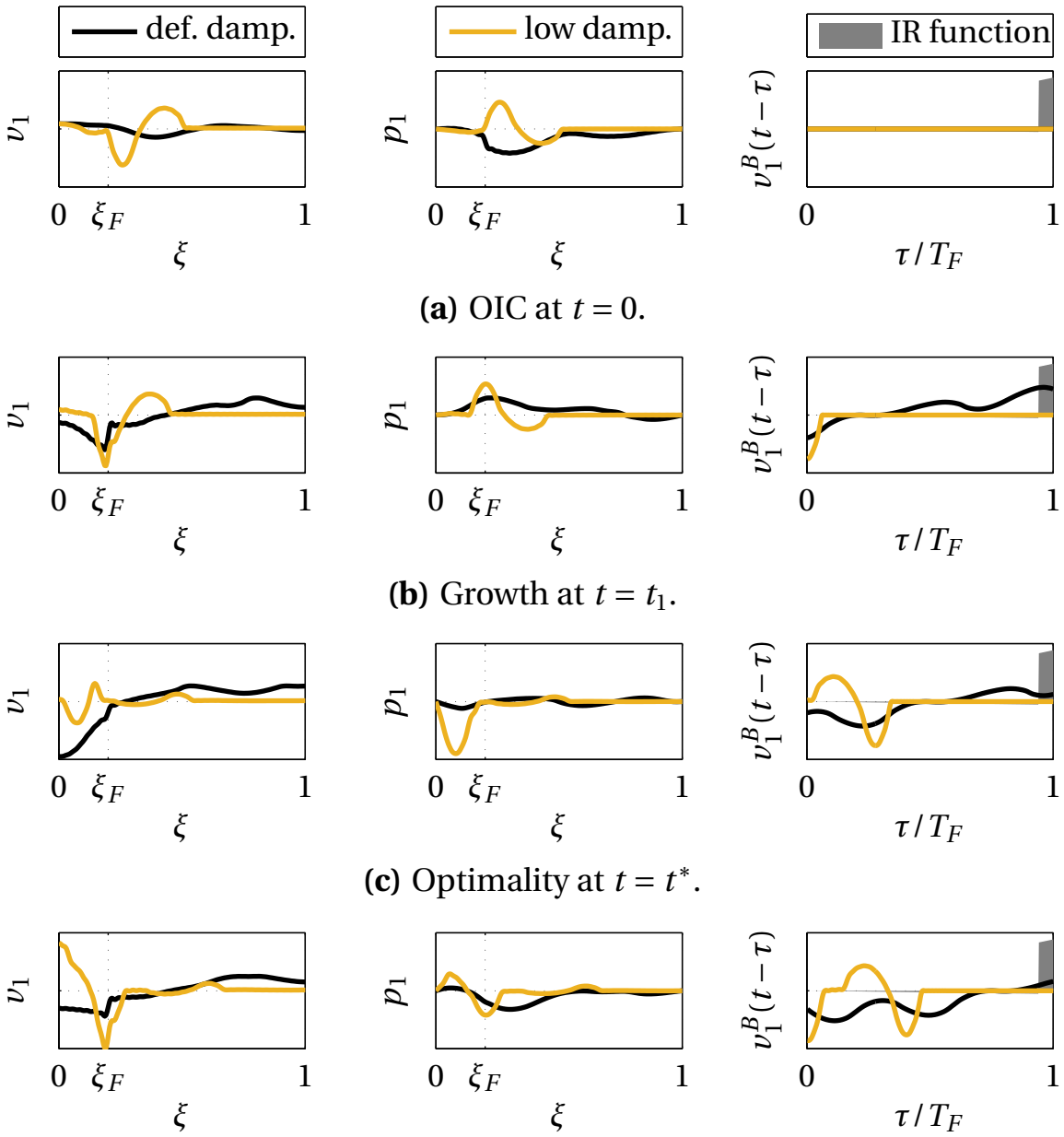

(a) OIC at $t = 0$.

(b) Growth at $t = t_1$.

(c) Optimality at $t = t^*$.

(d) Decay at $t = t_2$.

Figure 7.8: Profiles of $v_1(\xi)$, $p_1(\xi)$ and $v_1^B(t-\tau)$ (left, center and right columns, respectively) during non-normal transient growth for default (—) and low damping (—): (a) The OIC at $t = 0$, (b) the phase of dominant transient growth at $t = t_1$, (c) optimality at $t = t^*$, (d) the phase of decay at $t = t_2$ (all snapshots are indicated in Fig. 7.6). The IR function is overlaid in the right column. Configuration: $\kappa_0 = 0$, $K = 7.3 \times 10^{-4}$ and $K = 1.8 \times 10^{-4}$ for default and low damping, respectively, otherwise default parameter values.

output energy in parallel, as can be seen from the black lines in the second row of Fig. 7.8. At $t = t_1$, $v_1(\xi_F)$ and $p_1(\xi_F)$ are of opposite sign. Also, dominant non-zero values of the lagged acoustic velocity at the flame base $v_1^B(t-\tau)$ meets the dominant zone of the IR function, thus generating significant $\dot{q}_1$, that in turn is of the same sign as $p_1(\xi_F)$. The Rayleigh source term is hence positive. At optimality, the net source terms are zero as before. During the phase of decay at $t = t_2$, $v_1(\xi_F)$ and $p_1(\xi_F)$ are of same sign, whereas $\dot{q}_1$ and $p_1(\xi_F)$ are of opposite sign. In addition to damping mechanisms, both source terms thus contribute to a decay in output energy.

In summary, the OIC is such that the source terms driving the output energy are maximized during a short period of time. We can distinguish two scenarios of *optimal* non-normal transient growth, which are discussed in the following.

If optimality is reached at time scales much shorter than the characteristic time scales of the heat source subsystem $\mathcal{S}^{(F)}$, that is, at an acoustic time scale, non-normal transient growth is due to the inherent modeling assumption of a flame at rest. In the present low-order model, this scenario is observed for low damping values. As mentioned in Sec. 6.1.2, the inherent scenario of non-normal transient growth is physical as such. However, the modeling assumption of a flame at rest, strictly speaking, is not physical.

If optimality is reached at time scales of the order of or larger than the characteristic time scales of the heat source subsystem $\mathcal{S}^{(F)}$, optimal non-normal transient growth is due to the interaction of the heat source with the acoustic field. This second scenario represents a physical event of non-normal transient growth in thermoacoustic systems. It is observed in the present low-order model for default damping conditions.

Despite the physical nature of the second scenario of non-normal transient growth, transient growth originating from the temperature gradient as in the first scenario is also present. As is visible from Fig. 7.6(a), transient growth can already occur for very small times (i.e., $H > 1$ for $t > 0^+$). This indicates that both scenarios of non-normal transient growth occur in parallel. For this configuration, however, largest (i.e., optimal) transient growth is due to the physical coupling of the heat source with the acoustic field.

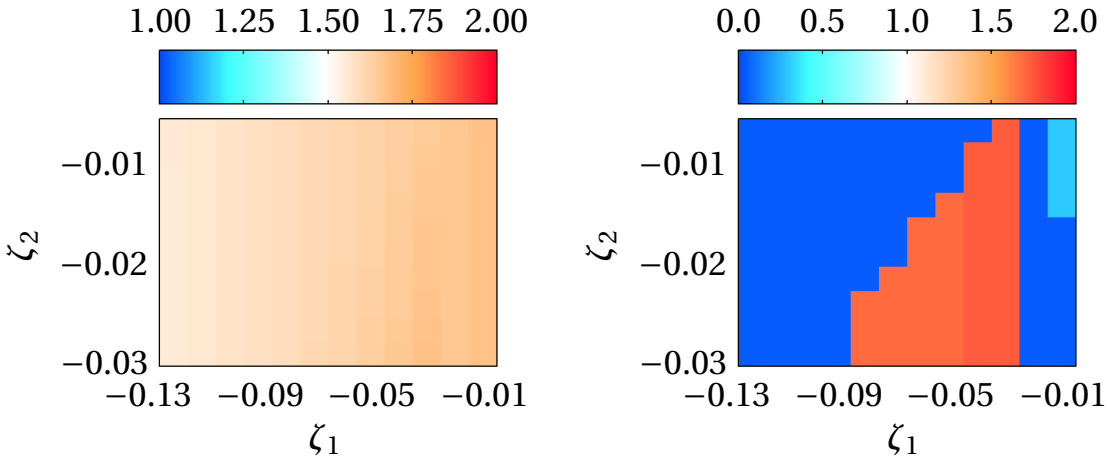

(a) $H_{\max}$ for ζ_1 vs. ζ_2. **(b)** t^*/T_A for ζ_1 vs. ζ_2.

Figure 7.9: (a) The optimal energy amplification $H_{\max}$ and (b) the time at optimality t^*/T_A of $\mathcal{S}^{(T)}$ in the (ζ_1,ζ_2)-parameter space with $\kappa_0 = 0$, $K \approx 0.99\,K_{\text{crit}}$, and otherwise default parameter values.

7.2.2 Parameters Influencing Transient Growth

In the following, we analyze the influence of the parameters of the low-order model describing $\mathcal{S}^{(T)}$ on non-normal transient growth. In particular, the optimal normalized energy amplification $H_{\max}$ and the time at optimality t^* are displayed in a 2-parameter space in analogy to the linear stability maps in Sec. 6.2.1.

As a first illustrating example, consider $H_{\max}$ and t^* as a function of the damping coefficients (ζ_1,ζ_2) shown in Fig. 7.9. Whereas damping does not have a large impact on the magnitude of non-normal transient growth (see Fig. 7.9(a)), it does on the time at which optimality occurs (see Fig. 7.9(b)). For very low and very high values of ζ_1, $H_{\max}$ is reached very quickly, indicative of the inherent first scenario of non-normal transient growth. At intermediate values of ζ_1, $H_{\max}$ occurs at around two acoustic time scales, which matches the second scenario of non-normal transient growth discussed in the previous section.

The maps of the optimal normalized energy amplification $H_{\max}$ and the time at optimality t^* in different 2-parameter spaces are shown in Figs. 7.10–7.11. To ease comparison, the first parameter is always given by the temperature incremental factor Δ_β. In analogy to the linear stability maps in Sec. 6.2.1, Fig. 7.10 represents the acoustic and mixed parameters ξ_F, M_u and Sr, whereas Fig. 7.11 depicts the flame parameters ϕ, α and μ. The results are summarized in the following:

- Flame position ξ_F (Figs. 7.10(a)–7.10(b)). The optimal energy growth $H_{\max}$ is more pronounced in the surroundings of $\xi_F \approx 0.1$ and $\xi_F \approx 0.35$. In these regions, t^* is also large, indicative of the physical second scenario of transient growth via the Rayleigh term. By inspection of the linear stability map shown in Fig. 6.6(a), it is noticeable that regions of large $H_{\max}$ align well with regions of enhanced linear stability, where K_{crit} is large. This also hints at the second scenario, because enhanced linear stability goes hand in hand with the system being able to bear a stronger fluctuating heat source before becoming linearly unstable, and thus a stronger Rayleigh term.

- Upstream Mach number M_u (Figs. 7.10(c)–7.10(d)). The effect of mean flow on $H_{\max}$ and on t^* is barely noticeable in the range of upstream Mach numbers considered. The simplifying assumption of neglecting the flux and source terms that depend on M_u, and thus to explain non-normal transient growth with only two dominant source terms, is therefore valid.

- Strouhal number Sr (Figs. 7.10(e)–7.10(f)). The ratio of time scales between the subsystems $\mathcal{S}^{(F)}$ and $\mathcal{S}^{(A)}$ plays a crucial role for non-normal transient growth. In general, $H_{\max}$ decreases with Sr. For large Strouhal numbers (except for Sr = 1), which are those encountered in many thermoacoustic systems, $H_{\max}$ and t^* are small. This behavior is indicative of the inherent first scenario of transient growth, where the interaction of the heat source and the acoustic field is negligible. By the time the effect of a slow heat source is noticeable in a thermoacoustic configuration, damping mechanisms have already significantly diminished the amplitude levels of the acoustic field. On the other hand, transient

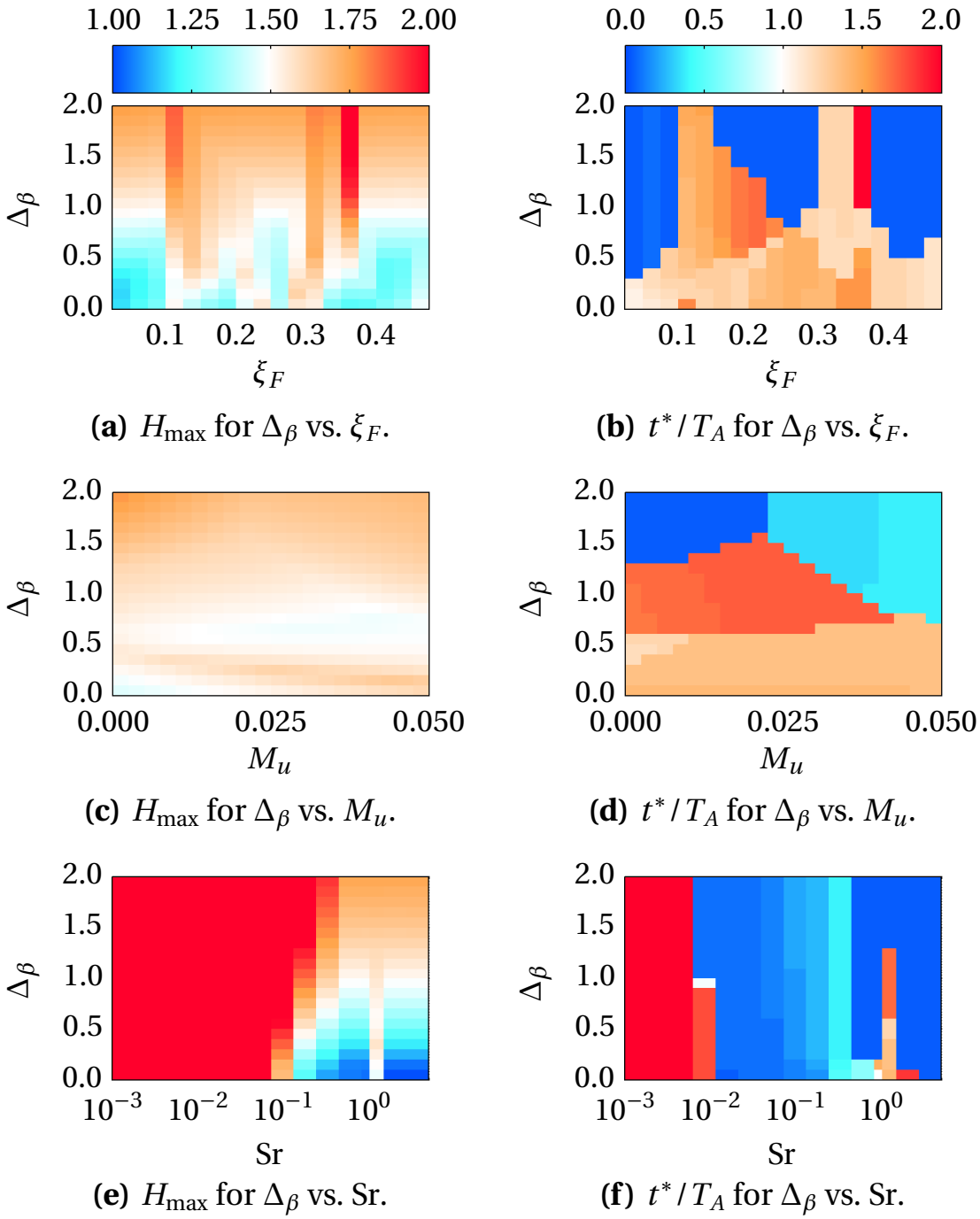

(a) $H_{\max}$ for Δ_β vs. ξ_F.

(b) t^*/T_A for Δ_β vs. ξ_F.

(c) $H_{\max}$ for Δ_β vs. M_u.

(d) t^*/T_A for Δ_β vs. M_u.

(e) $H_{\max}$ for Δ_β vs. Sr.

(f) t^*/T_A for Δ_β vs. Sr.

Figure 7.10: The optimal energy amplification $H_{\max}$ (first column) and the time at optimality t^* (second column) of $\mathcal{S}^{(T)}$ in different 2-parameter spaces with $\kappa_0 = 0$, $K \approx 0.99\,K_{\text{crit}}$, and otherwise default parameter values: (a)–(b) Δ_β vs. ξ_F, (c)–(d) Δ_β vs. M_u, (e)–(f) Δ_β vs. Sr.

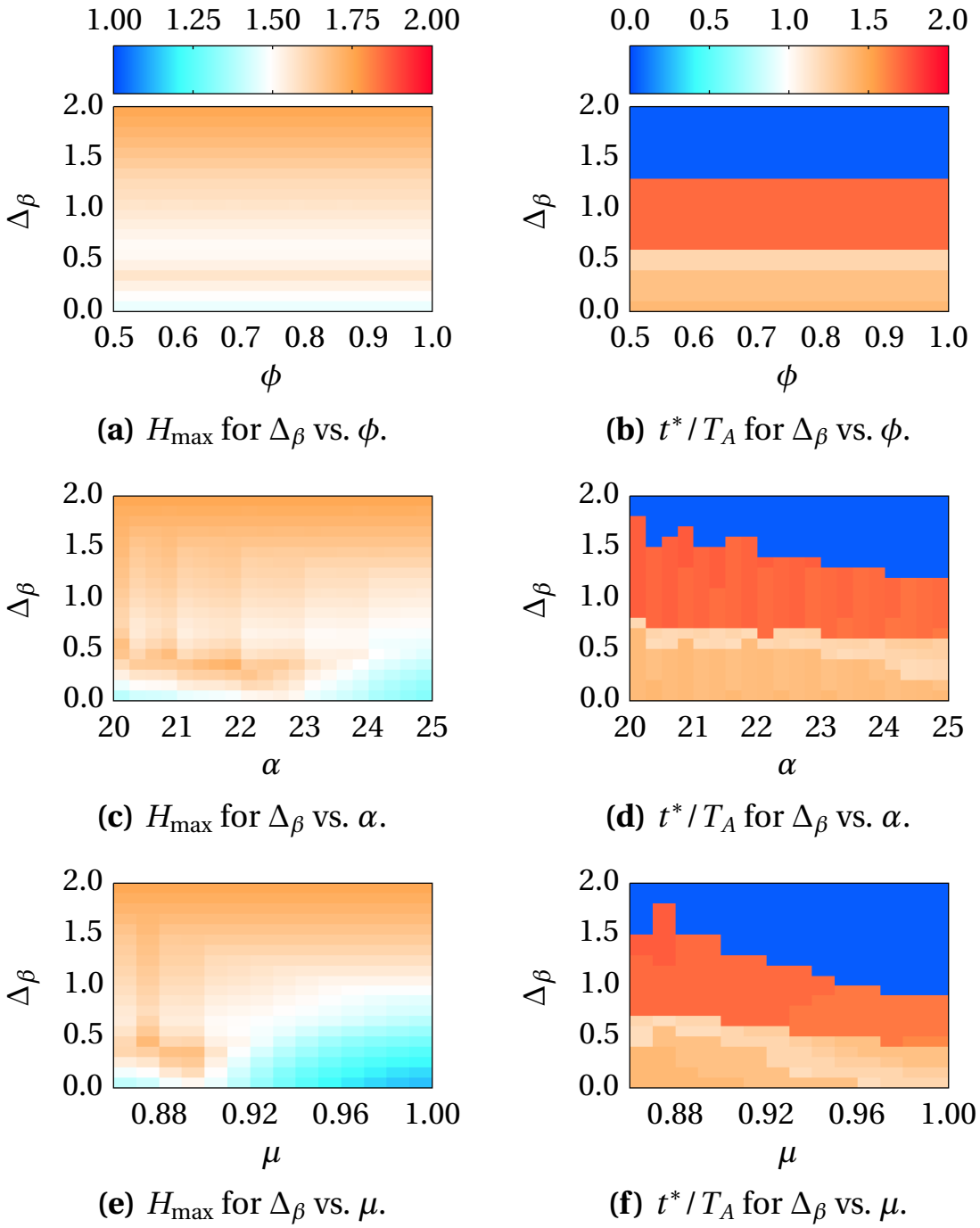

(a) $H_{\max}$ for Δ_β vs. ϕ.

(b) t^* / T_A for Δ_β vs. ϕ.

(c) $H_{\max}$ for Δ_β vs. α.

(d) t^* / T_A for Δ_β vs. α.

(e) $H_{\max}$ for Δ_β vs. μ.

(f) t^* / T_A for Δ_β vs. μ.

Figure 7.11: The optimal energy amplification $H_{\max}$ (first column) and the time at optimality t^* (second column) of $\mathcal{S}^{(T)}$ in different 2-parameter spaces with $\kappa_0 = 0$, $K \approx 0.99\,K_{\text{crit}}$, and otherwise default parameter values: (a)–(b) Δ_β vs. ϕ, (c)–(d) Δ_β vs. α, (e)–(f) Δ_β vs. μ.

growth through the physical second scenario via the Rayleigh term is extremely pronounced for very low Strouhal numbers. For example, at $\mathrm{Sr} = 10^{-3}$, $H_{\max} \approx 20$, which exceeds the maximum color shading by an order of magnitude. Optimality is reached at the order of two acoustic time scales. As observed for ξ_F, these regions align well with regions of enhanced linear stability (see Fig. 6.6(e)). Since the system can bear a stronger heat source before becoming linearly unstable, the Rayleigh term leading to non-normal transient growth is also stronger.

- Fuel-to-air ratio ϕ (Figs. 7.11(a)–7.11(b)). The equivalence ratio does not have a noticeable effect on non-normal transient growth. This is because ϕ only alters the mean heat release rate $\dot{q}_0$. However, the strength of the heat source K is regulated by the adjustable parameter K_0, $K \propto K_0 \dot{q}_0$ (see Eq. (4.10)). If $\dot{q}_0$ increases due to an increase in ϕ, K_0 decreases accordingly, such that the critical strength of the heat source at the linear stability bound K_{crit} remains unaffected by ϕ.

- Flame angle α (Figs. 7.11(c)–7.11(d)) and ratio of convective to mean flow velocities μ (Figs. 7.11(e)–7.11(f)). As seen for the linear stability maps depicted in Figs. 6.6(d) and 6.6(f), α and μ have a similar effect on $H_{\max}$ and on t^*, as both alter the shape of the IR function. Transient growth is marginally enhanced for small values of α and μ, which corresponds to the convective and restorative processes of flame response occurring at increasingly similar time scales (i.e., large ratios of convective to restorative time scales Π). Regions of increased $H_{\max}$ also align with regions of enhanced stability, indicative of the physical second scenario of non-normal transient growth.

- Temperature incremental factor Δ_β (all plots in Figs. 7.10–7.11). The effect of a temperature jump on $H_{\max}$ and especially on t^* is strong, which is in agreement with the study of Li & Zhao [96]. In general, low and intermediate values of Δ_β favor the physical second scenario of transient growth via the Rayleigh term. For high Δ_β, transient growth more likely occurs through the inherent first scenario, as the source term resulting from the gradient in temperature at ξ_F are increased. These observations are especially well visible from Figs. 7.11(a)–7.11(b), where the second

parameter ϕ does not exhibit any effect on $H_{\max}$ and t^*. However, the temperature jump does not alter the order of magnitude of maximum non-normal transient growth.

In summary, optimal non-normal transient growth thus results from a maximization of the source and flux terms associated with the formulation of the model describing $\mathcal{S}^{(T)}$. This observation was anticipated by analytical arguments in Sec. 6.1.2. For the present model, the transient maximization of source terms either leads to the advent of inherent transient growth (due to the assumption of a flame at rest), or to the advent of physical transient growth with a transiently maximized Rayleigh term. Thermoacoustic configurations that can bear a stronger heat source (i.e., more stable configurations) can thus exhibit larger levels of non-normal transient growth. This is especially well visible in the present model for certain values of the position of the heat source ξ_F, and for extremely low values of Strouhal number Sr.

7.3 Probability of Transient Growth

From the previous section, it is clear that physical non-normal transient growth can occur in simple thermoacoustic systems $\mathcal{S}^{(T)}$. Similar to most studies in this area, the analysis so far dealt with worst case scenarios (i.e., optimal mode shapes leading to largest growth). Other mode shapes resulting in suboptimal transient energy amplification were not considered. To obtain a more in-depth picture of the phenomenon, we therefore shift the focus on the likelihood of encountering transient growth in general. That is, how large is the subset of all possible initial conditions $\mathbf{x}_0$ resulting in (any non-zero) level of transient growth, and how probable is it to encounter such an initial condition? The latter question seems important to determine the relevance of non-normal transient growth with respect to triggering, and bridges theoretical and practical aspects of non-normal transient growth.

For models of very low order (i.e., with number of states $N = \mathcal{O}(10^0)$), it is possible to determine the probability distribution of the output energy subject to a given initial state distribution by analytical means. This will be ad-

dressed in Sec. 7.3.1. For larger models and for a more sophisticated analysis, it is necessary to resort to random sampling, so-called Monte Carlo methods (see Sec. 7.3.2).

7.3.1 Analytically Determined Probability

Consider a low-order model in state space form of the type of Eq. (2.7) with $N = 2$ states, of which the output evolves from the initial condition in time,

$$\begin{bmatrix} y_1 \\ y_2 \end{bmatrix}(t) = \mathbf{L}(t) \begin{bmatrix} x_{0,1} \\ x_{0,2} \end{bmatrix}, \tag{7.1}$$

with output energy $E = y_1^2 + y_2^2$. The propagator $\mathbf{L}$ is defined as

$$\mathbf{L}(t) = \begin{bmatrix} l_{11}(t) & l_{12}(t) \\ l_{21}(t) & l_{22}(t) \end{bmatrix} = \underbrace{\begin{bmatrix} c_{11} & c_{12} \\ c_{21} & c_{22} \end{bmatrix}}_{\mathbf{C}} \exp\left(t \underbrace{\begin{bmatrix} a_{11} & a_{12} \\ a_{21} & a_{22} \end{bmatrix}}_{\mathbf{A}} \right), \tag{7.2}$$

such that E can be computed from the initial state values $x_{0,1}$ and $x_{0,2}$ at any instant in time using the mathematical operations of multiplication by a scalar, summation and squaring.

Suppose both initial values $x_{0,i}$ are given as independent random variables that can take values on the support (outcome space) z_i. The corresponding probabilities P_i of falling into a given interval $[z_1, z_2]$ are then defined by the respective probability distribution functions (pdf) $\varphi_{x_{0,i}} : x_{0,i} \rightarrow \mathbb{R}_0^+$,

$$P_i(z_1 \leq x_{0,i} \leq z_2) = \int_{z_1}^{z_2} \varphi_{x_{0,i}}(\tilde{z}_i)\, \mathrm{d}\tilde{z}_i \,. \tag{7.3}$$

In this case, the operations of scalar multiplication, summation and squaring given in Eq. (7.2) cannot be applied in the same manner as in the deterministic

case. For independent random variables, the latter operations are defined by

$$\text{SCALAR MULT.:} \qquad \varphi(a\,z) = \varphi(z)\,\frac{1}{a}\,, \tag{7.4a}$$

$$\text{SUMMATION:} \qquad \varphi_1(z_1) + \varphi_2(z_2) = \int_{-\infty}^{\infty} \varphi_1(z_1)\,\varphi_2(z_1 - z_2)\,\mathrm{d}z_2\,, \tag{7.4b}$$

$$\text{SQUARING:} \qquad \Big[\varphi(z)\Big]^2 = \frac{1}{2\sqrt{2}}\Big(\varphi(\sqrt{z}) + \varphi(-\sqrt{z})\Big)\,, \tag{7.4c}$$

with scalar $a \neq 0$. In the stochastic case, multiplication by a scalar thus amounts to scaling, summation becomes a convolution, and squaring is a nonlinear operation of the initial pdf. The supports z change accordingly. Equations (7.4) are derived from principles of random variable transform [33].

With Eqs. (7.4), it is possible to compute the pdf of output energy φ_E over time subject to given initial state probability distribution functions $\varphi_{x_{0,1}}$ and $\varphi_{x_{0,2}}$. We do so in the following for an extremely low-order model describing the simple thermoacoustic system $\mathcal{S}^{(T)}$, which in the following is referred to as the *toy model* of $\mathcal{S}^{(T)}$. Although such a model is a very coarse approximation of the dynamics of $\mathcal{S}^{(T)}$, it can be used as a rough estimate of the probability of transient growth. More importantly, this simple example serves to convey the basic approach of investigating the probability of transient growth.

The toy model describing $\mathcal{S}^{(T)}$ is given by the acoustics subsystem $\mathcal{S}^{(A)}$ without mean flow and temperature jump, $M_u = \Delta_\beta = 0$. It is modeled by the MWR with $N_{A,M} = 1$. The fields of $v_1(\xi)$ and $p_1(\xi)$ are thus each described by one mode, and the entire model consists of only $N = 2$ degrees of freedom. Fluctuations in heat release rate occurring through the heat source subsystem $\mathcal{S}^{(F)}$ are computed by a single time lag model $\dot{q}_1 = K\,v_1^B(t-\tau)$, which for small time lags $\tau \ll 1$ (corresponding to $\mathrm{Sr} \ll 1$) can be approximated by a first-order Taylor series as $\dot{q}_1 \approx K\,(v_1^B(t) - \tau\,\partial v_1^B(t)/\partial t + \mathscr{O}(\tau^2))$. With this approximation, the model describing $\mathcal{S}^{(F)}$ does not require separate states and can be directly incorporated into $\mathcal{S}^{(T)}$. The same approximation has been employed by different authors to investigate non-normal transient growth [5, 77]. The employed model parameters are summarized in the caption of Fig. 7.12.

For the presently investigated configuration, the time traces of the maximum normalized output energy H and the optimal relative amplification of output

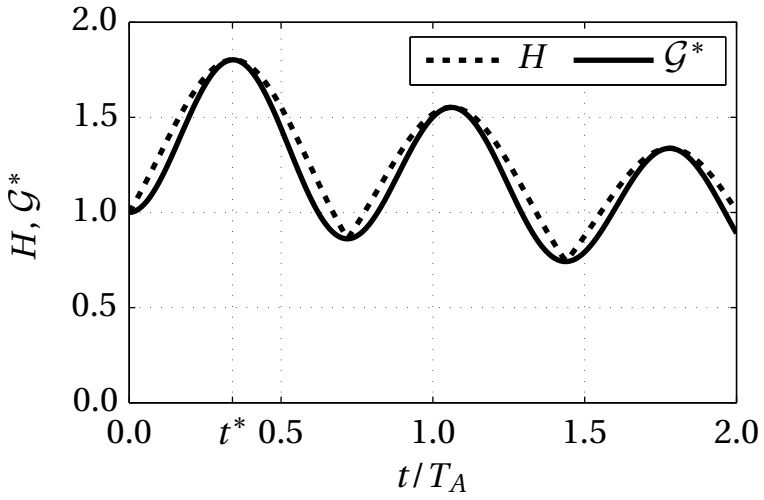

Figure 7.12: Time traces of the maximum normalized amplification of output energy H (− − −) and the optimal relative amplification of output energy $\mathcal{G}^*$ (—) of the thermoacoustic toy model describing $\mathcal{S}^{(T)}$ with two degrees of freedom ($N_{A,M} = 1$). The OIC $\mathbf{x}_0^{*(T)} = [-1; -5.1 \times 10^{-3}]^T$ is reached at $t^*/T_A = 0.34$. Configuration: $K = 10$, $\xi_F = 0.4$, $\zeta_p = -0.3$, $\Delta_\beta = 0$, $M_u = 0$, $\mathrm{Sr} = 10^{-2}$, flame modeled as STL model.

energy $\mathcal{G}^*$ are depicted in Fig. 7.12. In a coarse-grained manner, the traces are similar to those obtained from a finer model describing $\mathcal{S}^{(T)}$ (cf. Fig. 7.6(a)). Transient growth is due to the physical second scenario discussed at the end of Sec. 7.2.1, because the Rayleigh term $K\,p_1\,\dot{q}_1$ is the only source driving the output energy.

We define the pdfs of both initial states as independent uniform distributions $\varphi_{x_{0,i}} \sim \mathcal{U}([-1,1])$ (see Fig. 7.13(a)). Any possible initial condition $\mathbf{x}_0^{(T)}$, including the OIC $\mathbf{x}_0^{*(T)} = [-1; -5.1\times10^{-3}]^T$, is thus reachable with the same probability. The resulting pdf of the initial output energy φ_{E_0} is defined on the support $[0, 0.5]$, because the output energy as defined in Eq. (6.5) can take values in the interval $[0, 0.5]$ for the present configuration of $\mathcal{S}^{(T)}$. It can be seen from Fig. 7.13(a) that φ_{E_0} is not uniformly distributed, but that it is more likely to start from low initial output energies. The probability distributions of energy $\varphi(E(t))$ are computed by evolving the model equations (7.1) in time starting from the above defined uniform pdfs for the initial values. We therefore make

use of the random variable operations defined in Eqs. (7.4).

Figure 7.13(b) depicts the probability P of exceeding $\max E_0 = 0.5$ over time, which reaches its peak $P_{\max} \approx 5\%$ at $t \approx 0.2$ acoustic time scales. It is interesting to note a significant drop in P at the time of optimality $t^*/T_A = 0.34$. This might indicate that it is more likely to obtain a moderate amount of transient growth from non-optimal initial conditions than from the optimal initial condition $\mathbf{x}_0^{*(T)}$.

However, Fig. 7.13(b) only serves as indication but not as sufficient quantification of non-normal transient growth. This is because φ_E is not normalized by φ_{E_0}. Since φ_E and φ_{E_0} are not independent random distributions, an analytical random variable transform yielding the pdf of relative output energy $\mathcal{G} = E/E_0$ does not exist. It is thus not possible to identify and to quantify the probability of relative amplification of output energy $\mathcal{G}$ by analytical means. We therefore resort to an analysis of random sampling in the following section.

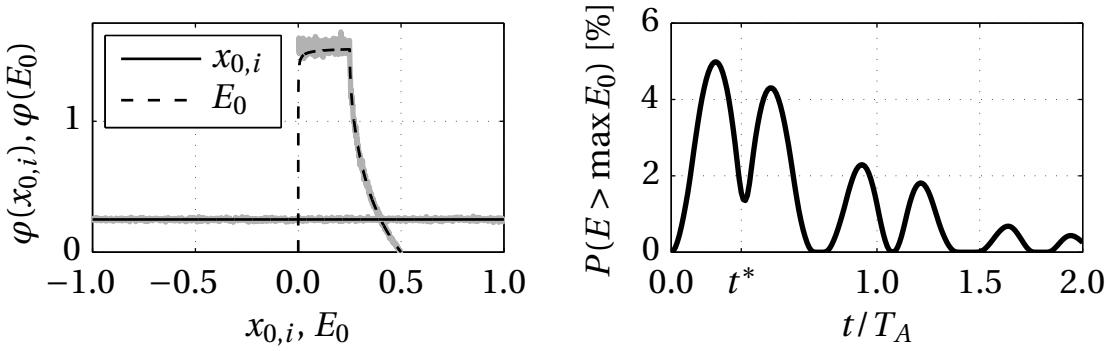

(a) Initial pdfs. **(b)** Probability over time.

Figure 7.13: (a) Initial analytical pdfs $\varphi(x_{0,i}) \sim \mathcal{U}([-1,1])$ (—) and $\varphi(E_0)$ (− − −). The corresponding pdfs obtained from 10^6 random samples are indicated in gray. (b) Analytically determined probability P of exceeding the maximum initial level of output energy $\max E_0$.

7.3.2 Random Sampling

In the present section, we determine the probability of non-normal transient growth by random sampling. This is first done for the toy model of $\mathcal{S}^{(T)}$ with $N = 2$ degrees of freedom introduced in the previous section. Subsequently, the same analysis is carried out for the default thermoacoustic model used throughout the present work.

The Toy Model of $\mathcal{S}^{(T)}$

The toy model of $\mathcal{S}^{(T)}$ is initialized and evolved in time from $N_p = 10^6$ randomly sampled initial conditions. The resulting normalized energy levels are recorded in time and saved in a histogram, from which the probability of reaching a given energy level can be examined. As for the analytical case, the pdfs of the individual initial states $\varphi_{x_{0,1}}$ and $\varphi_{x_{0,2}}$ are uniformly distributed, which leads to a given pdf of the initial output energy φ_{E_0}. To validate the agreement between the analytical and the sampled initial pdfs, the sampled distributions are overlaid in Fig. 7.13(a).

The resulting probability of exceeding a given relative level of output energy $\mathcal{G} = E/E_0$ is plotted over time in Fig. 7.14(a). It can be seen that the probability of exceeding $H(t)$ is zero, which confirms the theoretically determined maximum of the normalized output energy. It is also visible that the relative energy level is bounded from below, indicated by the probability of $P = 100\,\%$ of exceeding a lower level of $\mathcal{G}$. At multiples of $t/T_A = n\,T/2$, where $T \approx 1.44$ corresponds to the only period of oscillation of the model, the upper and lower bounds coincide. That is, all time traces of $\mathcal{G}$ meet every half a period of oscillation.

The probability of observing non-normal transient growth over time—which corresponds to the probability of exceeding $\mathcal{G} = 1$ in Fig. 7.14(a)—is shown in Fig. 7.14(b). In a general manner, the probability to observe transient growth follows the trend of $H(t)$. With $P_{\max} \approx 61\,\%$ at $t = t^*$, it is most probable to observe transient growth at the time of optimality.

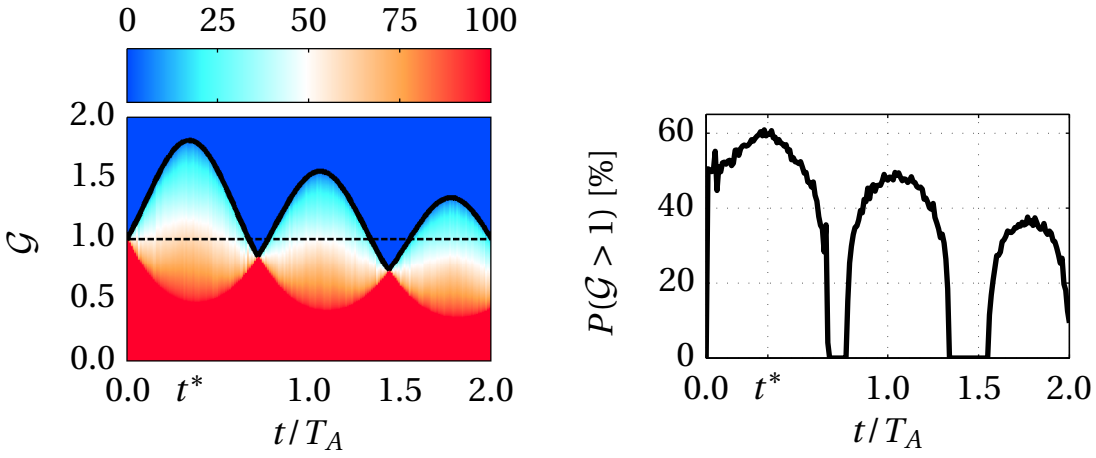

(a) Probability of energy level (%). **(b)** Probability of growth (%).

Figure 7.14: (a) Probability P of exceeding a given relative energy level $\mathcal{G} = E/E_0$ over time of the toy model of $\mathcal{S}^{(T)}$ recorded from $N_p = 10^6$ sampled runs. The maximum achievable level above which $P = 0$ corresponds to $H(t)$ (—). (b) Probability of non-normal transient growth $P(\mathcal{G} > 1)$, which corresponds to the contour plot in (a) sliced at $\mathcal{G} = 1$.

The overall probability of reaching transient energy amplification at at least one point in time can be deduced from the histogram of the maximum relative amplification of output energy $\mathcal{G}_{\max} = \max_t \mathcal{G}$ depicted in Fig. 7.15. Only 15 % of all runs exhibit $\mathcal{G}_{\max} \leq 1.02$. In fact, 11.2 % of all runs do not exhibit transient growth at all. It is interesting to see that the surrounding of $H_{\max}$ is reached more frequently than intermediate values of maximum transient growth. This might be due to the fact that the present toy model of $\mathcal{S}^{(T)}$ behaves very much like a damped harmonic oscillator.

Non-normal transient growth for the present toy model of $\mathcal{S}^{(T)}$ with $N = 2$ degrees of freedom is thus very likely. In the following section, we apply the same approach of random sampling to the low-order model employed throughout the present work. The factors limiting the interpretability and generality of the results obtained from the toy model of $\mathcal{S}^{(T)}$ are thereby relaxed (for example, no temperature jump and mean flow, a single time lag model for the heat source, very low Strouhal number, insufficient resolution of mode shapes).

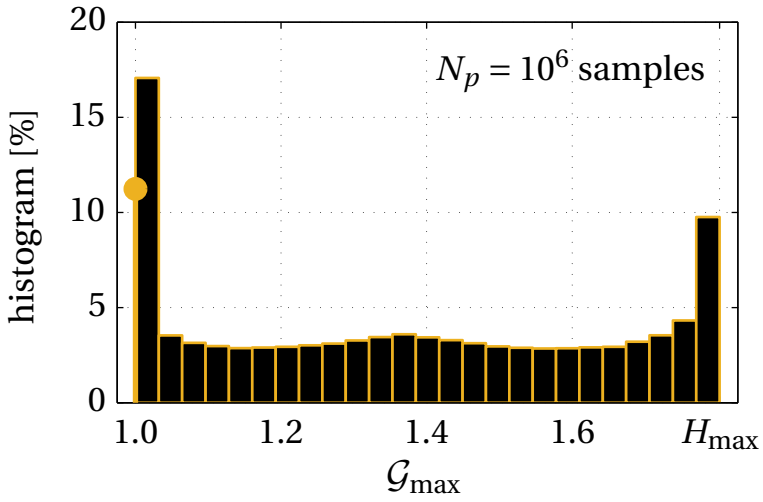

Figure 7.15: Normalized histogram of the maximum relative amplification of output energy $\mathcal{G}_{\max}$ of the toy model of $\mathcal{S}^{(T)}$ recorded from $N_p = 10^6$ sampled runs. 11.2 % of all runs do not exhibit transient growth at all (indicated by the thick dot at $\mathcal{G}_{\max} = 1$).

The Full Low-Order Model of $\mathcal{S}^{(T)}$

With $N = \mathcal{O}(10^2)$ states, performing a probability analysis of the full low-order model of $\mathcal{S}^{(T)}$ requires significantly more computational effort than for the toy model of $\mathcal{S}^{(T)}$. This is the case for the analytical approach as well as for the random sampling method. The analytical approach is not pursued at all, because the number of required random transform operations scales with N^2. In view of the limited insight, we directly focus on random sampling.

The full low-order model of $\mathcal{S}^{(T)}$ with default parameter values as given in Tab. 6.1 and $K = 7.3 \times 10^{-4}$ is evolved in time from randomly sampled initial conditions. For reasons discussed in Sec. 7.2.1, the initial ratio of kernel to output energy $\kappa_0 = 0$, such that the initial condition only contains non-zero acoustic states $\mathbf{x}_0^{(A)}$. The initial conditions are created as random linear combinations of thermoacoustic eigenmodes (cf. Fig. 6.2(d)),

$$\mathbf{x}_0^{(A)} = \sum_{i=1}^{N_x} \left[a_i \mathbf{V}_{v,i}^T \, , \, b_i \mathbf{V}_{p,i}^T \right]^T \, , \tag{7.5}$$

where $\mathbf{V}_{v,i}$ and $\mathbf{V}_{p,i}$ represent the vectors of discretized eigenmodes in terms of

acoustic velocity and pressure, respectively, and a_i and b_i are the corresponding random coefficients of velocity and pressure, respectively, each uniformly distributed $a_i \sim \mathcal{U}([-1,1])$ and $b_i \sim \mathcal{U}([-1,1])$ $\forall\, i \in \{1,2,\ldots,N_x\}$.

By creating the initial conditions according to Eq. (7.5), it is ensured that the model is initialized from reachable and physically meaningful initial conditions. The initial conditions can be designed to contain contributions from up to $N_x = N_{A,M}$ resolvable eigenmodes of the model. Choosing different coefficients for the velocity and pressure distributions amounts to controlling the initial phase between acoustic velocity and pressure. The number of random variables is thus given as $2N_x$.

If we assume the random coefficients a_i and b_i to take N_i discrete values within the interval $[-1,1]$, we require at least N_i to the power of $2N_x$ randomly initialized runs in order for the probability analysis to produce substantiated and reliable results. With $N_i = 10$ and default $N_x = N_{A,M} = 70$, the number of runs would surpass numerical feasibility despite the low-order nature of the thermoacoustic model. In the following, we therefore limit the analysis to the first three eigenmodes, $N_x = 3$ and thus $2N_x = 6$ random variables. The chosen number of eigenmodes is also of interest from a practical point of view, because it corresponds to the number of eigenmodes that can be initialized in an experimental setup. Beyond $N_x = 3$, it is very hard to excite a mode in practice, as the damping encountered by the higher modes is quite high.

With the above definitions, the low-order model of $\mathcal{S}^{(T)}$ is thus initialized and evolved in time from $N_p = 8.27 \times 10^6$ randomly sampled initial conditions consisting of the first three eigenmodes of the model as defined in Eq. (7.5). The resulting normalized energy levels are recorded in time and saved in a histogram. To save computational time, we reduce the number of modes of the MWR to $N_{A,M} = 30$, which according to Fig. 7.5 still yields accurate results. Also, we limit the time horizon over which the evolution of energy is traced to slightly beyond the time at optimality $t = t^*$, which amounts to $t_{\max} = 2$ acoustic time scales (cf. 7.6(a)).

The probability of exceeding a given level of $\mathcal{G} = E/E_0$ is shown in Fig. 7.16(a). As for the toy model of $\mathcal{S}^{(T)}$, the relative energy level is bounded from below.

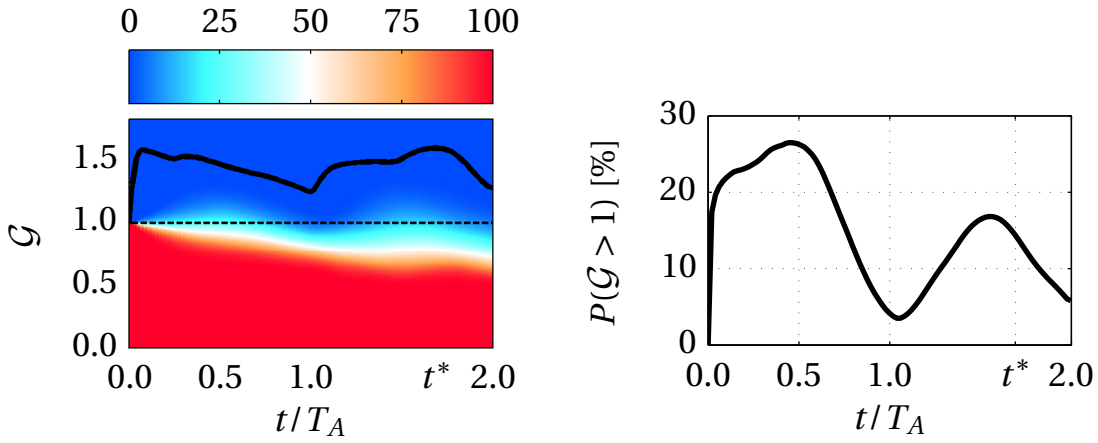

(a) Probability of energy level (%). **(b)** Probability of growth (%).

Figure 7.16: (a) Probability P of exceeding a given relative energy level $\mathcal{G} = E/E_0$ over time of the full low-order model of $\mathcal{S}^{(T)}$ recorded from $N_p = 8.27 \times 10^6$ sampled runs. The theoretical maximum given by $H(t)$ (—) is never reached. (b) Probability of non-normal transient growth $P(\mathcal{G} > 1)$, which corresponds to the contour plot in (a) sliced at $\mathcal{G} = 1$. The initial conditions consist of random linear combinations of the first three eigenmodes. Configuration: $\kappa_0 = 0$, $K = 7.3 \times 10^{-4}$, default parameters values.

It is also visible that there is a certain non-zero probability of transient energy amplification. However, the upper threshold of zero probability lies far below the theoretical maximum given by $H(t)$. This indicates that optimal non-normal transient growth cannot occur from initial conditions consisting of contributions from only three eigenmodes.

The probability of exceeding $\mathcal{G} = 1$, that is the probability of obtaining any non-zero level of relative amplification of output energy, is plotted in Fig. 7.16(b). It is confirmed that transient growth can happen over the entire investigated time horizon. The highest probability of exceeding $\mathcal{G} = 1$ occurs for small times, peaking with $P_{\max} = 26.5\,\%$ at $t \approx 0.5$ acoustic time scales. This hints at the inherent first scenario of transient growth defined in the end of Sec. 7.2.1. The probability $P(\mathcal{G} > 1)$ then exhibits a minimum at $t = 1$ acoustic time scales, before increasing to a smaller second peak of $P \approx 17\,\%$ at $t \approx 1.5$

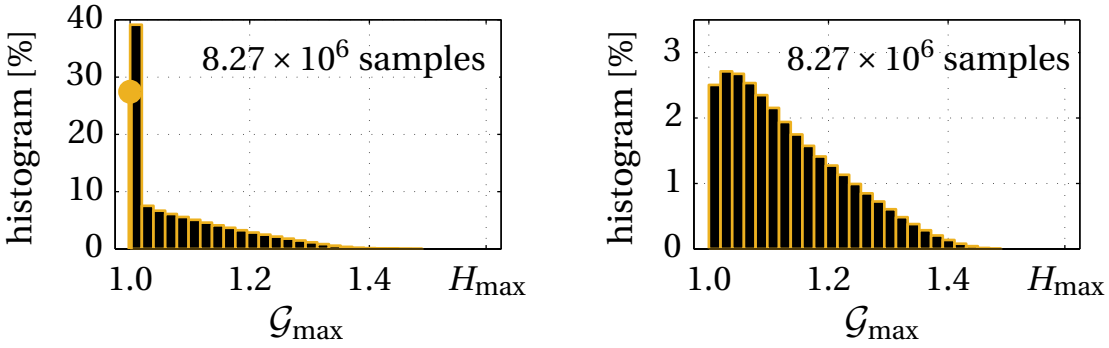

(a) $\mathcal{G}_{\max}$ of all runs. **(b)** $\mathcal{G}_{\max}$ only if $t_{\max}/T_A > 0.9$.

Figure 7.17: Normalized histograms of $\mathcal{G}_{\max}$ of the full low-order model of $\mathcal{S}^{(T)}$ recorded from $N_p = 8.27 \times 10^6$ sampled runs: (a) all runs, (b) only runs where $\mathcal{G}_{\max}$ occurs at $t > 0.9$ acoustic time scales to exclude the inherent first scenario of transient growth. 27.4 % of all runs do not exhibit transient growth at all (indicated by the thick dot at $\mathcal{G}_{\max} = 1$ in (a)). The initial conditions consist of random linear combinations of the first three eigenmodes.

acoustic time scales. Since the ratio of flame to acoustic time scales Sr = 1, this time range is of the order of the characteristic time scale of flame response. The observed energy amplification therefore results from the second scenario of non-normal transient growth discussed at the end of Sec. 7.2.1.

The histogram of $\mathcal{G}_{\max} = \max_t \mathcal{G}$ is depicted in Fig. 7.17(a). Approximately 40 % of all runs exhibit transient growth of $\mathcal{G}_{\max} \leq 1.02$, and 27.4 % of all runs do not result in transient energy growth at all. The largest level of relative energy amplification is $\max \mathcal{G}_{\max} = 1.48$, which happens in the marginal event of 2.6×10^{-3} % of all runs. The surroundings of the theoretically determined optimal energy amplification $H_{\max}$ are not reached by initial conditions consisting of three eigenmodes. This shows that optimal (i.e., largest) energy amplification requires very specific initial conditions (see the optimal initial mode shapes depicted in the first row of Fig. 7.8).

As discussed above, the largest probability of observing transient energy amplification occurs at small times through the inherent first scenario of transient growth. To filter out this effect, we plot in Fig. 7.17(b) the histogram of

$\mathcal{G}_{\max}$ exclusively taking into account those runs where the maximum energy is reached for $t > 0.9$ acoustic time scales. This applies to 28.8 % of all runs. That is, transient growth through the second scenario of transient growth is observed in less than one third of all runs, whereas inherent transient growth happens in 43.8 % of all runs. However, it is visible that the events of larger relative energy amplification $\mathcal{G}_{\max} > 1.2$ are all due to the scenario of the fluctuating heat source coupling with the acoustic field.

In summary, the present probability analysis of $\mathcal{S}^{(T)}$ shows that suboptimal non-normal transient growth is a possible event. Approximately one third of all random initial conditions containing contributions from the first three thermoacoustic eigenmodes exhibit physical non-normal transient energy amplification. However, approximately 87 % of these physical events of non-normal transient growth exhibit relative energy amplification of less than 1.25. That is, only 3.8 % of all runs lead to a physical relative energy growth of $\mathcal{G}_{\max} > 1.25$, which still lies far below the theoretically determined optimal non-normal energy amplification of $H_{\max} \approx 1.6$. Non-normal transient growth around a stable fix point in simple thermoacoustic systems thus seems unlikely, and, if occurring, is of small magnitude. Given the measurement noise present in any practical setup, it is thus unlikely to find substantiated experimental evidence of transient growth in simple thermoacoustic systems. This conclusion is in agreement with the thesis of Mariappan [106]. The question of classifying probabilities as low or even fully insignificant is yet an open matter of debate, and will need to be addressed in future studies.

7.4 Discussion

The current section serves as brief synthesis of the present chapter, with the aim of indicating the impact of non-normal transient growth around a stable fix point onto triggering.

There are at least two requirements that need to be fulfilled in order to trigger a linearly stable system away from its stable fix point. First, the operating point needs to lie in a bistable region of the operating map (subcritical bifurcation,

see Fig. 1.1). Second, linear growth mechanisms need to be sufficiently strong so as to initiate nonlinearities. Otherwise it is not possible for the dynamics of the system to be attracted towards an unstable limit cycle, which, in turn, propels the solution towards a stable oscillating limit cycle (see the scenario of triggering from low-amplitude perturbations in Chap. 1).

The first point is not discussed here, as it exceeds the scope of the present study without generating any novel insights. It has been shown by Kashinath *et al.* [81–84] that a G-equation flame coupled to a 1-D acoustic field is capable of reproducing subcritical bifurcation behavior, and also of attaining limit cycles in analogy to those observed in experiments [79].

The second point is addressed in the following, where we compare the orders of magnitude of the optimal relative amplification of output energy $\mathcal{G}^*$ of the same configuration of $\mathcal{S}^{(T)}$ in the linear and nonlinear regime. The aim is to investigate whether, in principle, non-normal transient growth is sufficiently pronounced so as to initiate the nonlinear terms that are present in the heat source subsystem $\mathcal{S}^{(F)}$. The time traces of $\mathcal{G}^*$ are therefore plotted in Fig. 7.18(a) for different amplitude levels of velocity fluctuations $\max_{\xi,t}|v_1^*(\xi,t)|/v_0$. The plots are obtained from the nonlinear thermoacoustic model describing $\mathcal{S}^{(T)}$, where the heat source subsystem $\mathcal{S}^{(F)}$ is given by the nonlinear G-equation model defined in Eqs. (3.14).

For amplitude levels $\max_{\xi,t}|v_1^*(\xi,t)|/v_0 < 5\,\%$, the time traces of $\mathcal{G}^*$ follow that of the linearized model (indicated by the dashed black line), where $H_{\max} \approx 1.6$ is reached at $t^* = 1.69$ (cf. Fig. 7.6(a)). For amplitude levels $\max_{\xi,t}|v_1^*(\xi,t)|/v_0 > 5\,\%$, the time traces of the optimal relative amplification of output energy $\mathcal{G}^*$ visibly differ from the linear evolution, and the nonlinear regime is reached. For the present configuration, increasing the amplitude levels leads to a decrease in the maximum relative amplification of output energy $\mathcal{G}_{\max}$. The same is reported by Juniper in [76].

The same time traces as for the optimal relative amplification of output energy $\mathcal{G}^*$, but in absolute values of optimal output energy E^*, are plotted in Fig. 7.18(b). The resulting evolutions of E^* with linear character (i.e., amplitude levels $\max_{\xi,t}|v_1^*(\xi,t)|/v_0 < 5\,\%$) are orders of magnitude smaller than

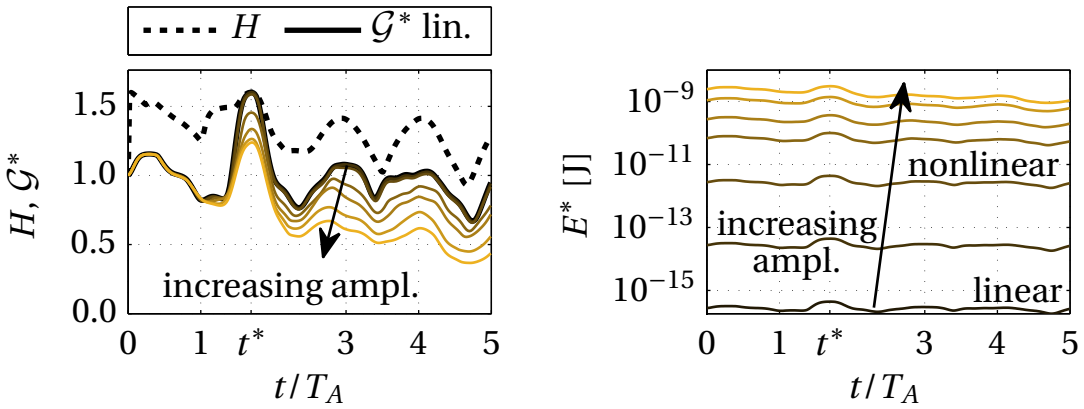

(a) Relative amplification. **(b)** Absolute values.

Figure 7.18: Time traces of optimal output energy obtained from the nonlinear model of $\mathcal{S}^{(T)}$ in (a) relative values given by the optimal relative amplification of output energy $\mathcal{G}^*$ and (b) in absolute values of optimal output energy E^*. The amplitude levels of velocity $\max_{\xi,t}|v_1^*(\xi,t)|/v_0 \in \{0.05, 0.47, 4.67, 23.37, 46.73, 93.46, 140.19\}\,\%$ (from black to yellow). The maximum normalized output energy H (– – –) and $\mathcal{G}^*$ (—) obtained from the linearized model of $\mathcal{S}^{(T)}$ are indicated in (a). Nonlinear effects are visible for amplitude levels exceeding 5 %. Configuration: $\kappa_0 = 0$, $K = 7.3 \times 10^{-4}$ and default parameter values.

those with nonlinear character (i.e., $\max_{\xi,t}|v_1^*(\xi,t)|/v_0 > 5\,\%$). Since non-normal transient growth is of the order of unity, it is not strong enough to increase the amplitude level by a sufficient amount so as to trigger nonlinearities. Also, the peak in transient growth occurs over less than one acoustic time scale. Thus, even if the initial level of energy is near the border of linear to nonlinear behavior, it seems unlikely that non-normal transient growth will initiate nonlinearities in a substantial and long-lasting manner.

In combination with the low probability of obtaining larger values of transient growth in the first place (see Sec. 7.3), results indicate that triggering through transient growth around a stable fix point may be an insignificant event for simple thermoacoustic systems. Although theoretically possible, its occurrence seems of academic nature.

The latter conclusion applies for realistic, but simple thermoacoustic systems, such as a Rijke tube. The situation may be very different for thermoacoustic systems in the presence of noise, with turbulent flow, multiple burners and/or complex geometries. Also, the above conclusion may not apply to triggering away from an unstable or stable oscillating attractor, which corresponds to the operating condition of a "humming" thermoacoustic system, such as a turbulent combustion chamber.

7.5 Chapter Summary

The present chapter can be summarized as follows:

- Care must be taken in distinguishing physical from spurious non-normal transient growth, especially if they are of the same order of magnitude. Spurious non-normality results from ill-conditioned discretized numerical operators.
- Non-normal transient growth *always* results from a transient maximization of the net flux and source terms driving the output energy. For the present model of $\mathcal{S}^{(T)}$, there are two main driving source terms. Their transient maximization leads to two different scenarios of transient growth, of which one is due to thermoacoustic coupling and the other is related to the modeling assumption of a flame at rest.
- For the present simple thermoacoustic system, physical optimal non-normal transient growth is of the order of unity ($H_{\max} \approx 1.6$ for a configuration using default parameter values). It is dominated by non-zero acoustic state values.
- For the present simple thermoacoustic system, it is quite likely to encounter physical suboptimal non-normal transient growth (with probability of approximately one third). However, the event of reaching optimal non-normal transient growth, as identified theoretically by mathematical tools, tends to zero for the present setup in the absence of noise.

- Results indicate that non-normal transient growth around a stable fix point might not be a frequently encountered cause for triggering simple thermoacoustic systems to a nonlinear oscillating state.

8 Summary and Outlook

In the present work, a thermoacoustic system is formulated as a generic multi-physics system consisting of two subsystems in feedback (acoustics and heat source). Different models based on analytical (e.g. the acoustics subsystem in terms of LEE), semi-analytical (e.g. the heat source subsystem in terms of G-equation flame) and data-driven frameworks (e.g. the heat source subsystem in terms of distributed time lag models) describing each of the subsystems are investigated in isolation as to their dynamical behavior, before subsequently performing a system analysis of the entire thermoacoustic system. The overall system analysis involves the study of output energy, linear stability bounds, spurious transient growth and the dynamics and probability of physical and model-inherent non-normal transient growth around a stable fix point and its impact on triggering.

The essential novelty of the present work consists in the study of non-normal transient growth including energy metrics that are semi-norms and taking into account optimal and suboptimal energy amplification. To the author's knowledge, a probability-based investigation of non-normal transient growth is unique in the thermoacoustic literature. Also, the low-order thermoacoustic model includes a mean temperature jump, a trivial, but non-zero mean flow, and a heat source with time-distributed response characteristics, of which the time lags need not be small with respect to the acoustic time scales.

The key finding of the present study indicates that non-normal transient growth around a stable fix point—although possible and theoretically sound—does not seem to be a likely cause for triggering in thermoacoustic systems in the absence of noise, with simple 1D geometries, where mean flow effects are trivial and the acoustic field is dominated by planar waves. For these simple systems, optimal non-normal transient growth is highly unlikely. Although energy amplification resulting from suboptimal non-normal tran-

sient growth is frequently encountered, its magnitude is small and will likely not suffice to trigger nonlinearities. Also, it occurs over short periods of time.

The above observations hold true independent of the energy norm used to quantify non-normal transient growth. It is highlighted that the energy metric merely prescribes the perspective from which non-normal transient growth needs to be interpreted. To this regard, the energy metric is a crucial factor to investigate non-normal transient growth. However, it does not alter the degree of non-normality as such.

The other main outcome of the present study is that adopting a systems framework to describe thermoacoustics is a promising approach. The systems approach is a robust and rigorous platform, where insights from different fields of research, such as acoustics, hydrodynamics and combustion dynamics, can be consistently combined using a common language. Owing to the flexible framework laid out above, the present study could be redone for different (perhaps more sophisticated) models of existing subsystems, simply by adding or replacing subsystems in the described framework.

Combining the key finding with the lessons learned from the systemic approach indicates research directions which may seem worthwhile taking. Although non-normal transient growth around a stable fix point might not seem a relevant issue for such simple thermoacoustic systems, the situation may be very different for sophisticated thermoacoustic systems of practical relevance. For such setups with noise, complex geometries and non-trivial flow fields, the challenge consists in obtaining low-order model descriptions of the subsystem flow or flow/acoustics (it has been outlined in Chap. 3 how to do extract low-order models of the heat source subsystem). Data-based model order reduction techniques may offer a starting point in this direction. If successful, the low-order descriptions of the different subsystems could be substituted into the framework outlined in the present thesis to study the effect of non-normal transient growth. Care should be taken in identifying and using numerical schemes that exhibit little spurious non-normality. Also, further effort needs to be aimed at studying the probability of non-normal transient growth, and of defining the threshold below which non-normal transient growth may be classified as an insignificant factor towards triggering.

Most industrial thermoacoustic systems operate under highly turbulent conditions around stable oscillating attractors (so-called *humming*). These systems are thus situated in the nonlinear regime even before becoming unstable. It might therefore be of greater interest to investigate the impact of non-normal transient growth around such an oscillating nonlinear state than around a linearly stable fix point. Data-driven approaches which include the effect of stochasticities may shed light on whether or not non-normal transient growth plays a determining role in destabilizing such setups. This knowledge would be of great benefit in understanding triggering beyond the framework of academic setups.

References

[1] A. Albayrak, A. Ulhaq, R. S. Blumenthal, and W. Polifke. Analytical derivation of laminar premixed flame impulse response to equivalence ratio perturbations. In *21st International Congress on Sound and Vibration (ICSV21)*, Beijing, China, 13-17 July 2014.

[2] K. J. Aström and R. M. Murray. *Feedback systems: an introduction for scientists and engineers*. Princeton University Press, 2010.

[3] Y. Aurégan and R. Starobinski. Determination of Acoustical Energy Dissipation/Production Potentiality from the Acoustical Transfer Functions of a Multiport. *Acta Acustica united with Acustica*, 85(6):5–5, 1999.

[4] K. Balasubramanian and R. I. Sujith. Non-normality and nonlinearity in combustion acoustic interaction in diffusion flames. *Journal of Fluid Mechanics*, 594:29–57, 2008.

[5] K. Balasubramanian and R. I. Sujith. Thermoacoustic instability in a Rijke tube: Non-normality and nonlinearity. *Physics of Fluids*, 20(4):044103, 2008.

[6] K. Balasubramanian and R. I. Sujith. Non-normality and nonlinearity in combustionâ€“acoustic interaction in diffusion flames â€“ CORRIGENDUM. *Journal of Fluid Mechanics*, 733:680–680, 2013.

[7] B. Bamieh and M. Dahleh. Disturbance energy amplification in three-dimensional channel flows. In *Proceedings of the American Control Conference 1999*, volume 6, pages 4532–4537. IEEE, 1999.

[8] M. Bauerheim, F. Nicoud, and T. Poinsot. Theoretical analysis of the

mass balance equation through a flame at zero and non-zero Mach numbers. *Combustion and Flame*, 162:60–67, 2014.

[9] D. Bechert and E. Pfizenmaier. On wavelike perturbations in a free jet travelling faster than the mean flow in the jet. *Journal of Fluid Mechanics*, 72(02):341–352, 1975.

[10] R. S. Blumenthal, P. Subramanian, R. I. Sujith, and W. Polifke. New Perspectives on Laminar Premixed Flame Dynamics derived from Time Domain Response Functions. In *ERCOFTAC Technologietag*, Stuttgart, Germany, October 2012.

[11] R. S. Blumenthal, P. Subramanian, R. I. Sujith, and W. Polifke. A Time Domain Perspective on the Response of Premixed Flames to Flow Perturbations. In *Euromech Colloquium 546 – Combustion Dynamics and Combustion Noise*, Menaggio, Italy, May 2013.

[12] R. S. Blumenthal, P. Subramanian, R. I. Sujith, and W. Polifke. Novel Perspectives on the Dynamics of Premixed Flames. *Combustion and Flame*, 160(7):1215–1224, 2013.

[13] R. S. Blumenthal, A. K. Tangirala, R. I. Sujith, and W. Polifke. A Contribution to the Discussion on Thermoacoustic Energy from a Systemic Perspective. In *n3l Workshop on Non-Normal and Nonlinear Effects in Aero- and Thermoacoustics*, Munich, Germany, June 2013.

[14] R. S. Blumenthal, A. K. Tangirala, R. I. Sujith, and W. Polifke. A Systems Perspective on Non-Normality in Low-Order Thermoacoustic Models: Full Norms, Semi-Norms and Transient Growth. accepted for publication in *International Journal of Spray and Combustion Dynamics*, 2016.

[15] S. Bomberg, T. Emmert, and W. Polifke. Thermal versus acoustic response of velocity sensitive premixed flames. *Proceedings of the Combustion Institute*, 35(3):3185 – 3192, 2015.

[16] M. R. Bothien, J. P. Moeck, A. Lacarelle, and C. O. Paschereit. Time domain modelling and stability analysis of complex thermoacoustic systems. *Proceedings of the Institution of Mechanical Engineers, Part A: Journal of Power and Energy*, 221(5):657–668, 2007.

[17] F. Boudy, D. Durox, T. Schuller, and S. Candel. Nonlinear mode triggering in a multiple flame combustor. *Proceedings of the Combustion Institute*, 33(1):1121–1128, 2011.

[18] A. Bourehla and F. Baillot. Appearance and stability of a laminar conical premixed flame subjected to an acoustic perturbation. *Combustion and Flame*, 114(3-4):303–318, 1998.

[19] L. Boyer and J. Quinard. On the dynamics of anchored flames. *Combustion and Flame*, 82(1):51–65, 1990.

[20] M. J. Brear, F. Nicoud, M. Talei, A. Giauque, and E. R. Hawkes. Disturbance energy transport and sound production in gaseous combustion. *Journal of Fluid Mechanics*, 707:53–73, 8 2012.

[21] D. Breda, S. Maset, and R. Vermiglio. TRACE-DDE: a Tool for Robust Analysis and Characteristic Equations for Delay Differential Equations. In Jean Jacques Loiseau, Wim Michiels, Silviu-Iulian Niculescu, and Rifat Sipahi, editors, *Topics in Time Delay Systems*, volume 388 of *Lecture Notes in Control and Information Sciences*, pages 145–155. Springer Berlin Heidelberg, 2009.

[22] J. Buckmaster, P. Clavin, A. Liñàn, M. Matalon, N. Peters, G. Sivashinsky, and F. A. Williams. Combustion theory and modeling. *Proceedings of the Combustion Institute*, 30(1):1–19, 2005.

[23] R. H. Cantrell and R. W. Hart. Interaction between sound and flow in acoustic cavities: Mass, momentum, and energy considerations. *The Journal of the Acoustical Society of America*, 36:697, 1964.

[24] G. Chagelishvili, R. Chanishvili, and D. Lominadze. Physics of the amplification of vortex disturbances in shear flows. *JETP Letters*, 63:543–549, 1996. 10.1134/1.567072.

[25] L. Tay Wo Chong, T. Komarek, R. Kaess, S. Föller, and W. Polifke. Identification of Flame Transfer Functions From LES of a Premixed Swirl Burner. *ASME Conference Proceedings*, 2010(43970):623–635, 2010.

[26] B.-T. Chu. On the energy transfer to small disturbances in fluid flow (Part I). *Acta Mechanica*, 1:215–234, 1965.

[27] D. R. Coughanowr. *Process systems analysis and control*. McGraw-Hill, New York, 1991.

[28] L. Crocco. Aspects of Combustion Stability in Liquid Propellant Rocket Motors Part 1: Fundamentals. Low frequency instability with monopropellants. *Journal of American Rocket Society*, pages 163–178, 1951.

[29] F. E. C. Culick. Dynamics of combustion systems: fundamentals, acoustics and control. *Active control of engine dynamics, RTO-EN-020*, pages 89–206, 2001.

[30] F. E. C. Culick. *Unsteady Motions in Combustion Chambers for Propulsion Systems*. Number AC/323(AVT-039)TP/103 in RTO AGARDograph. 2006.

[31] F. E. C. Culick. Spatial averaging combined with a perturbation/iteration procedure. *International Journal of spray and combustion dynamics*, 4(3):185–216, 2012.

[32] A. Cuquel. *Dynamics and nonlinear thermo-acoustic stability analysis of premixed conical flames*. PhD thesis, Ecole Centrale Paris, 2013.

[33] J. Devore. *Probability and Statistics for Engineering and the Sciences*. Cengage Learning, 2011.

[34] A. P. Dowling. A kinematic model of a ducted flame. *Journal of Fluid Mechanics*, 394:51–72, 1999.

[35] F. Duchaine, F. Boudy, D. Durox, and T. Poinsot. Sensitivity analysis of transfer functions of laminar flames. *Combustion and Flame*, 158(12):2384–2394, 2011.

[36] S. Ducruix, D. Durox, and S. Candel. Theoretical and experimental determinations of the flame transfer function of a laminar premixed flame. *Symposium (International) on Combustion*, 28:765–773, 2000.

[37] D. Durox, T. Schuller, N. Noiray, A. L. Birbaud, and S. Candel. Rayleigh criterion and acoustic energy balance in unconfined self-sustained oscillating flames. *Combustion and Flame*, 156(1):106–119, 2009.

[38] D. Durox, T. Schuller, N. Noiray, and S. Candel. Experimental analysis of nonlinear flame transfer functions for different flame geometries. *Proceedings of the Combustion Institute*, 32(1):1391–1398, 2009.

[39] Klaus Ehrenfried. Skript zur Vorlesung Strömungsakustik I. 2003.

[40] T. Emmert, S. Bomberg, and W. Polifke. Intrinsic thermoacoustic instability of premixed flames. *Combustion and Flame*, 162(1):75–85.

[41] T. Emmert, S. Bomberg, and W. Polifke. Intrinsic Thermoacoustic Eigenmodes of Premixed Flames. In *European Fluid Mechanics Conference EFMC10*, Copenhagen, Denmark, September 2014.

[42] K. Engelborghs, T. Luzyanina, and D. Roose. Numerical bifurcation analysis of delay differential equations using DDE-BIFTOOL. *ACM Transactions on Mathematical Software*, 28(1):1–21, 2002.

[43] B. Farrell. Modal and non-modal baroclinic waves. *Journal of the Atmospheric Sciences*, 41(4):668–673, 1984.

[44] B. F. Farrell. Optimal excitation of perturbations in viscous shear flow. *Physics of Fluids*, 31(8):2093, 1988.

[45] B. F. Farrell and P. J. Ioannou. Stochastic forcing of the linearized navier–stokes equations. *Physics of Fluids A: Fluid Dynamics*, 5:2600, 1993.

[46] B. F. Farrell and P. J. Ioannou. Variance maintained by stochastic forcing of non-normal dynamical systems associated with linearly stable shear flows. *Physical Review Letters*, 72:1188–1191, 1994.

[47] B. F. Farrell and P. J. Ioannou. Generalized Stability Theory. Part I: Autonomous Operators. *Journal of Atmospheric Sciences*, 53:2025–2040, July 1996.

[48] B. F. Farrell and P. J. Ioannou. Generalized Stability Theory. Part II: Nonautonomous Operators. *Journal of Atmospheric Sciences*, 53:2041–2053, July 1996.

[49] M. Fleifil, A. M. Annaswamy, Z. A. Ghoneim, and A. F. Ghoniem. Response of a laminar premixed flame to flow oscillations: A kinematic model and thermoacoustic instability results. *Combustion and Flame*, 106(4):487–510, 1996.

[50] S. Föller, F. Selimefendigil, and W. Polifke. Linear identification of the unsteady heat transfer of a cylinder in pulsating crossflow. In *Int. Conf. on Jets, Wakes and Separated Flows*, Berlin, Germany, September 16-19 2008. Technical University Berlin.

[51] S. Föller, F. Selimefendigil, and W. Polifke. The linear response of heat transfer from a cylinder in cross flow to velocity fluctuations. submitted to *Heat and Mass Transfer*, 2013.

[52] D. P. G. Foures, C. P. Caulfield, and P. J. Schmid. Variational framework for flow optimization using seminorm constraints. *Physical Review E*, 86:026306, 2012.

[53] B. A. Francis and K. Glover. Bounded peaking in the optimal linear regulator with cheap control. *Automatic Control, IEEE Transactions on*, 23(4):608–617, 1978.

[54] Bernard Friedland. *Control system design: an introduction to state-space methods*. Courier Corporation, 2012.

[55] T. Gebhardt and S. Grossmann. Chaos transition despite linear stability. *Physical Review E*, 50(5):3705–3711, 1994.

[56] K. J. George and R. I. Sujith. Disturbance energy norms: A critical analysis. *Journal of Sound and Vibration*, 331(7):1552 – 1566, 2012.

[57] K. J. George and R.I. Sujith. On Chu's disturbance energy. *Journal of Sound and Vibration*, 330(22):5280–5291, 2011.

[58] A. Giauque, F. Nicoud, and M. Brear. Numerical assessment of stability criteria from disturbance energies in gaseous combustion. In *13th AIAA/CEAS Aeroacoustics Conference (28th AIAA Aeroacoustics Conference)*, Rome, Italy, 2007.

[59] A. Giauque, T. Poinsot, M. Brear, and F. Nicoud. Budget of disturbance energy in gaseous reacting flows. Proceedings of the Summer Program 2006. Center for Turbulence Research, 2006.

[60] S. K. Godunov and V. S. Ryabenki. Theory of difference schemes-an introduction. *Amsterdam: North Holland, 1964*, 1, 1964.

[61] M. E. Goldstein. Aeroacoustics. *New York, McGraw-Hill International Book Co.*, 1, 1976.

[62] S. Gottlieb and C. W. Shu. Total variation diminishing Runge-Kutta schemes. *Mathematics of Computation*, 67:73–85, 1998.

[63] S. Grossmann. The onset of shear flow turbulence. *Review of Modern Physics*, 72:603–618, 2000.

[64] B. Gustavsen and A. Semlyen. Rational approximation of frequency domain responses by vector fitting. *Power Delivery, IEEE Transactions on*, 14(3):1052–1061, 1999.

[65] S. J. Hammarling. Numerical solution of the stable, non-negative definite Lyapunov equation. *IMA Journal of Numerical Analysis*, 2(3):303–323, 1982.

[66] S. Hemchandra. *Dynamics of turbulent premixed flames in acoustic fields*. PhD thesis, Georgia Institute of Technology, 2009.

[67] D. Hinrichsen and A. J. Pritchard. *Mathematical systems theory I: modelling, state space analysis, stability and robustness*, volume 1. Springer Science & Business Media, 2005.

[68] P. G. M. Hoeijmakers. *Flame–acoustic coupling in combustion instabilities*. PhD thesis, Technische Universiteit Eindhoven, Eindhoven, The Netherlands, 2014.

[69] R. A. Horn and C. R. Johnson. *Matrix analysis*. Cambridge university press, 2012.

[70] A. Huber and W. Polifke. Dynamics of Practical Premix Flames, Part I: Model Structure and Identification. *International Journal of Spray and Combustion Dynamics*, 1(2):199–229, 2009.

[71] A. Huber and W. Polifke. Dynamics of Practical Premix Flames, Part II: Identification and Interpretation of CFD Data. *International Journal of Spray and Combustion Dynamics*, 1(2):229–250, 2009.

[72] S. Jaensch, T. Emmert, C. F. Silva, and W. Polifke. A grey-box identification approach for thermoacoustic network models. In *Proceedings of ASME Turbo Expo 2014*, Düsseldorf, Germany, 2014. GT2014-27034.

[73] J. Jiménez. Localized amplification of energy in turbulent channels. *Center for Turbulence Research, Annual Research Briefs*, 2009.

[74] M. R. Jovanovic and B. Bamieh. Unstable modes versus non-normal modes in supercritical channel flows. In *American Control Conference, 2004. Proceedings of the 2004*, volume 3, pages 2245–2250. IEEE, 2004.

[75] M. R. Jovanovic, J. M. Fowler, B. Bamieh, and R. D'Andrea. On the peaking phenomenon in the control of vehicular platoons. *Systems & Control Letters*, 57(7):528–537, 2008.

[76] M. P. Juniper. Transient growth and triggering in the horizontal Rijke tube. *International Journal of Spray and Combustion Dynamics*, 3(3):209–224, 2011.

[77] M. P. Juniper. Triggering in the horizontal Rijke tube: non-normality, transient growth and bypass transition. *Journal of Fluid Mechanics*, 667:272–308, 2011.

[78] M. P. Juniper. Triggering in thermoacoustics. *International Journal of Spray and Combustion Dynamics*, 4(3):217–238, 2012.

[79] L. Kabiraj and R. I. Sujith. Nonlinear self-excited thermoacoustic oscillations: intermittency and flame blowout. *Journal of Fluid Mechanics*, 713:376–397, 2012.

[80] R. Kaess, A. Huber, and W. Polifke. A Time-Domain Impedance Boundary Condition for Compressible Turbulent Flow. In *14th AIAA/CEAS Aeroacoustics Conference (29th AIAA Aeroacoustics Conference)*, number AIAA-2008-2921, Vancouver, Canada, May 2008. AIAA/CEAS.

[81] K. Kashinath. *Nonlinear Thermoacoustic Oscillations of a Ducted Laminar Premixed Flame*. PhD thesis, University of Cambridge, 2013.

[82] K. Kashinath, S. Hemchandra, and M. P. Juniper. Nonlinear phenomena in thermoacoustic systems with premixed flames. *Journal of Engineering for Gas Turbines and Power*, 135(6):061502, 2013.

[83] K. Kashinath, S. Hemchandra, and M. P. Juniper. Nonlinear thermoacoustics of ducted premixed flames: the influence of perturbation convection speed. *Combustion and Flame*, 160(12):2856–2865, 2013.

[84] K. Kashinath, I. C. Waugh, and M. P. Juniper. Nonlinear self-excited thermoacoustic oscillations of a ducted premixed flame: bifurcations and routes to chaos. *Journal of Fluid Mechanics*, 761:399–430, 2014.

[85] K. S. Kedia, S. B. Nagaraja, and R. I. Sujith. Impact of linear coupling on thermoacoustic instabilities. *Combustion Science and Technology*, 180(9):1588–1612, 2008.

[86] J. J. Keller. Thermoacoustic oscillations in combustion chambers of gas turbines. *AIAA Journal*, volume 33, number 12:2280–2287, 1995.

[87] A. R. Kerstein, W. T. Ashurst, and F. A. Williams. Field equation for interface propagation in an unsteady homogeneous flow field. *Physical Review A*, 37:2728–2731, 1988.

[88] H. K. Khalil and J. W. Grizzle. *Nonlinear systems*, volume 3. Prentice hall Upper Saddle River, 2002.

[89] D. Kim and S. W. Park. Forced and self-excited oscillations in a natural gas fired lean premixed combustor. *Fuel Processing Technology*, 91(11):1670–1677, 2010.

[90] J. Kim and T. R. Bewley. A linear systems approach to flow control. *Annual Review of Fluid Mechanics*, 39:383–417, 2007.

[91] L. Kim and J. Moehlis. Characterizing the edge of chaos for a shear flow model. *Physical Review E*, 78:036315, 2008.

[92] L. E. Kinsler, A. R. Frey, A. B. Coppens, and J. V. Sanders. *Fundamentals of Acoustics, 4th Edition*. 1999.

[93] T. Komarek and W. Polifke. Impact of swirl fluctuations on the flame response of a perfectly premixed swirl burner. *Journal of Engineering for Gas Turbines and Power*, 132:061503, 2010.

[94] H. J. Landau. On Szegö's eigenvalue distribution theorem and non-Hermitian kernels. *Journal d'Analyse Mathématique*, 28(1):335–357, 1975.

[95] A. H. Lefebvre. The role of fuel preparation in low-emission combustion. *Journal of engineering for gas turbines and power*, 117(4):617–654, 1995.

[96] X. Li and D. Zhao. Mean Temperature Effect on a Thermoacoustic System Stability and Non-normality. *Low Frequency Noise, Vibration and Active Control*, 34(2):185–200, 2015.

[97] T. Lieuwen. Nonlinear kinematic response of premixed flames to harmonic velocity disturbances. *Symposium (International) on Combustion*, 30(2):1725–1732, 2005.

[98] T. C. Lieuwen. Modeling premixed combustion acoustic wave interactions: A review. *Journal of Propulsion and Power*, 19(5):765–781, 2003.

[99] T. C. Lieuwen. *Unsteady combustor physics*. Cambridge University Press, 2012.

[100] M. J. Lighthill. On sound generated aerodynamically. ii. turbulence as a source of sound. *Proceedings of the Royal Society of London. Series A. Mathematical and Physical Sciences*, 222(1148):1–32, 1954.

[101] L. Ljung. System identification: theory for the user. 1987.

[102] A. M. Lyapunov. The general problem of motion stability. *Kharkovskoye Matematicheskoe Obshchestvo*, 11, 1892.

[103] L. Magri. *Adjoint methods in thermo-acoustic and combustion instability*. PhD thesis, Cambridge University, 2015.

[104] L. Magri, K. Balasubramanian, R. I. Sujith, and M. P. Juniper. Non-normality in combustion-acoustic interaction in diffusion flames: a critical revision. *Journal of Fluid Mechanics*, 733:681–683, 2013.

[105] H. Mangesius and W. Polifke. A discrete-time, state-space approach for modelling non-normal effects in thermoacoustic systems. *International Journal of Spray and Combustion Dynamics*, 3(4):331–350, Dec 2011.

[106] S. Mariappan. *Theoretical and Experimental Investigation of the Non-Normal Nature of Thermoacoustic Interaction*. PhD thesis, Indian Institute of Technology Madras, 2012.

[107] S. Mariappan and R. I. Sujith. Thermoacoustic instability in a solid rocket motor: non-normality and nonlinear instabilities. *Journal of Fluid Mechanics*, 653:1–33, 2010.

[108] S. Mariappan and R. I. Sujith. Modelling nonlinear thermoacoustic instability in an electrically heated rijke tube. *Journal of Fluid Mechanics*, 680:511–533, 2011.

[109] S. Mariappan, R. I. Sujith, and P. Schmid. Non-normality of thermoacoustic interactions: an experimental investigation. *AIAA Paper*, 5555:2011, 2011.

[110] G. H. Markstein. *Nonsteady flame propagation*. Pergamon Press, New York, 1964.

[111] A. I. Markushevich and R. A. Silverman. *Theory of functions of a Complex Variable*. New York: American Mathematical Society, 2nd edition, 1977.

[112] P. Martínez-Lera, C. Schram, S. Föller, R. Kaess, and W. Polifke. Identification of the aeroacoustic response of a low Mach number flow through a T-joint. *The Journal of the Acoustical Society of America*, 126(2):582–586, 2009.

[113] K. I. Matveev and F. E. C. Culick. A model for combustion instability involving vortex shedding. *Combustion Science and Technology*, 175:1059–1083, 2003.

[114] W. Michiels and S.-I. Niculescu. *Stability and Stabilization of Time-delay Systems: An Eigenvalue-based Approach*, volume 12. SIAM, 2007.

[115] C. L. Morfey. Acoustic energy in non-uniform flows. *Journal of Sound and Vibration*, 14(2):159–170, 1971.

[116] P. M. Morse and K. Ingard. *Uno: Theoretical Acoustics*. McGraw-Hill Book Co., Inc., 1968.

[117] M. K. Myers. Transport of energy by disturbances in arbitrary steady flows. *Journal of Fluid Mechanics*, 226:383–400, 1991.

[118] S. Nagaraja, K. Kedia, and R. I. Sujith. Characterizing energy growth during combustion instabilities: Singularvalues or eigenvalues? *Proceedings of the Combustion Institute*, 32(2):2933–2940, 2009.

[119] V. Nair and R. I. Sujith. Multifractality in combustion noise: predicting an impending combustion instability. *Journal of Fluid Mechanics*, 747:635–655, 2014.

[120] M. S. Natanzon. *Combustion Instability*. American Institute of Aeronautics and Astronautics, 1996.

[121] F. Nicoud and T. Poinsot. Thermoacoustic instabilities: should the rayleigh criterion be extended to include entropy changes? *Combustion and Flame*, 142:153–159, 2005.

[122] F. Nicoud and K. Wieczorek. About the zero Mach number assumption in the calculation of thermoacoustic instabilities. *International Journal of Spray and Combustion Dynamics*, 1(1):67–111, 2008.

[123] N. Noiray, D. Durox, T. Schuller, and S. Candel. A unified framework for nonlinear combustion instability analysis based on the flame describing function. *Journal of Fluid Mechanics*, 615:139–167, 2008.

[124] P. Palies, D. Durox, T. Schuller, and S. Candel. The combined dynamics of swirler and turbulent premixed swirling flames. *Combustion and Flame*, 157(9):1698–1717, 2010.

[125] P. Palies, T. Schuller, D. Durox, L. Y. M. Gicquel, and S. Candel. Acoustically perturbed turbulent premixed swirling flames. *Physics of Fluids*, 23(3), 2011.

[126] C. O. Paschereit, J. P. Moeck, and M. R. Bothien. State-space modeling of thermoacoustic systems for stability analysis and time domain simulation. In *Proceedings of the 13th International Congress on Sound and Vibration, Vienna, Austria*, 2006.

[127] C. O. Paschereit, B. Schuermans, W. Polifke, and O. Mattson. Measurement of transfer matrices and source terms of premixed flames. *Journal of Engineering for Gas Turbines and Power*, 124(2):239–247, 2002.

[128] T. Penzl. Numerical solution of generalized Lyapunov equations. *Advances in Computational Mathematics*, 8(1-2):33–48, 1998.

[129] C. Pera and J. Reveillon. Direct numerical simulation of spray flame/acoustic interactions. *Proceedings of the Combustion Institute*, 31(2):2283–2290, 2007.

[130] A. D. Pierce. *Acoustics: an introduction to its physical principles and applications*. Acoustical Soc of America, 1989.

[131] T. Poinsot and D. Veynante. *Theoretical and Numerical Combustion*. R T Edwards Inc, 2nd edition, 2005.

[132] W. Polifke. Low-order analysis tools for aero- and thermo-acoustic instabilities. In C. Schram, editor, *Advances in Aero-Acoustics and Thermo-Acoustics*, number ISBN-13 978-2-87516-012-6 in VKI LS 2011-01. Von Karman Institute, Rhode-St-Genèse, BE, 2011.

[133] W. Polifke. Thermo-acoustic instability potentiality of a premix burner. In *European Combustion Meeting*, British Section of the Combustion Institute, Cardiff, UK, 2011.

[134] W. Polifke and A. Gentemann. Order and Realisability of Impulse Response Filters for Accurate Identification of Acoustical Multi-Ports from Transient CFD. *International Journal of Acoustics and Vibration*, 9(3):139–148, 2004.

[135] W. Polifke and C. Lawn. On the low-frequency limit of flame transfer functions. *Combustion and Flame*, 151(3):437–451, 2007.

[136] W. Polifke, C. O. Paschereit, and K. Döbbeling. Constructive and Destructive Interference of Acoustic and Entropy Waves in a Premixed Combustor with a Choked Exit. *International Journal of Acoustics and Vibration*, 6(3):135–146, 2001.

[137] Preetham and T. Lieuwen. Nonlinear flame-flow transfer function calculations: Flow disturbance celerity effects. In *40 th AIAA/ASME/SAE/ASEE Joint Propulsion Conference & Exhibit*, number AIAA 2004-4035, Fort Lauderdale, Florida, July 11-14 2004.

[138] Preetham, H. Santosh, and T. Lieuwen. Dynamics of laminar premixed flames forced by harmonic velocity disturbances. *Journal of Propulsion and Power*, 24(6):1390–1402, 2008.

[139] J. G. Proakis and D. G. Manolakis. *Digital signal processing: principles, algorithms, and applications*. Macmillan Publishing Co., Inc., Indianapolis, IN, USA, 1996.

[140] J. W. S. Rayleigh. The explanation of certain acoustical phenomena. *Nature*, 18(455):319–321, 1878.

[141] S. C. Reddy, P. J. Schmid, and D. S. Henningson. Pseudospectra of the Orr-Sommerfeld operator. *SIAM Journal on Applied Mathematics*, 53:15–47, 1993.

[142] S. W. Rienstra and A. Hirschberg. *An Introduction to Acoustics*. Einhoven University of Technology, 2014.

[143] P. L. Rijke. LXXI. Notice of a new method of causing a vibration of the air contained in a tube open at both ends. *The London, Edinburgh, and*

Dublin Philosophical Magazine and Journal of Science, 17(116):419–422, 1859.

[144] T. Sattelmayer and W. Polifke. Assessments of Methods for the Computation of the Linear Stability of Combustors. *Combustion Science and Technology*, 175(3):453–476, 2003.

[145] T. Sattelmayer and W. Polifke. A novel method for the computation of the linear stability of combustors. *Combustion Science and Technology*, 175:477–497, 2003.

[146] M. Schmid, R. S. Blumenthal, M. Schulze, W. Polifke, and T. Sattelmayer. Quantitative Stability Analysis Using Real Frequency Response Data. *Journal of Engineering for Gas Turbines and Power*, 135(1):121601, 2013.

[147] M. Schmid, R. S. Blumenthal, M. Schulze, W. Polifke, and T. Sattelmayer. Quantitative Stability Analysis Using Real-Valued Frequency Response Data. In *ASME Turbo Expo*, number GT2013-95459, San Antonio, Texas, USA, 2013.

[148] P. J. Schmid. Nonmodal Stability Theory. *Annual Review of Fluid Mechanics*, 39:129–162, 2007.

[149] P. J. Schmid and D. S. Henningson. *Stability and transition in shear flows*. Springer Verlag, New York, NY, USA, 2001.

[150] B. Schuermans. *Modelling and Control of Thermoacoustic Instabilities*. PhD thesis, Ecole Polytechnique Federale De Lausanne, 2003.

[151] B. Schuermans, V. Bellucci, D. Nowak, and C. O. Paschereit. Modeling of complex thermoacoustic systems: a state-space approach. 9th Int. Congress on Sound and Vibration, May 2002.

[152] B. Schuermans, V. Bellucci, and C. O. Paschereit. Thermoacoustic modeling and control of multi burner combustion systems. Number GT2003-38688 in Proc. of ASME Turbo Expo 2003 Power for Land, Sea and Air, Atlanta, Georgia, USA, June 2003. ASME.

[153] T. Schuller, S. Ducruix, D. Durox, and S. Candel. Modeling tools for the prediction of premixed flame transfer functions. *Proceedings of the Combustion Institute*, 29(1):107–113, 2002.

[154] T. Schuller, D. Durox, and S. Candel. A unified model for the prediction of laminar flame transfer functions: comparisons between conical and V-flame dynamics. *Combustion and Flame*, 134:21–34, 2003.

[155] Shreekrishna, S. Hemchandra, and T. Lieuwen. Premixed flame response to equivalence ratio perturbations. *Combustion Theory and Modelling*, 14(5):681–714, 2010.

[156] C. W. Shu and S. Osher. Efficient Implementation of Essentially Non-oscillatory Shock-Capturing Schemes. *Journal of Computational Physics*, 77:439–, 1988.

[157] Chi-Wang Shu. Essentially non-oscillatory and weighted essentially non-oscillatory schemes for hyperbolic conservation laws. 1998.

[158] Swiss Propulsion Laboratory (SPL). `http://www.spl.ch/news/`, January 2015.

[159] E. Stein and R. Shakarchi. *Complex Analysis*. Princeton University Press, 2003.

[160] G. Stephanopoulos. *Chemical process control: An introduction to theory and practice*. Prentice-Hall, Englewood Cliffs, New Jersey, 1984.

[161] S. R. Stow and A. P. Dowling. Low-order modelling of thermoacoustic limit cycles. Number GT2004-54245 in Proc. of ASME Turbo Expo 2004 Power for Land, Sea and Air, Vienna, Austria, June 2004.

[162] L. Strobio Chen, S. Bomberg, and W. Polifke. Propagation and Generation of Acoustic and Entropy Waves Across a Moving Flame Front. *Combustion and Flame*, 166:170–180, 2016.

[163] P. Subramanian, R. S. Blumenthal, W. Polifke, and R. I. Sujith. Distributed time lag response functions for the modelling of combustion dynamics. *Combustion Theory and Modelling*, 19(2):223–237, 2015.

[164] P. Subramanian, S. Mariappan, R. I. Sujith, and P. Wahi. Bifurcation analysis of thermoacoustic instability in a horizontal rijke tube. *International Journal of Spray and Combustion Dynamics*, 2(4):325–355, 2010.

[165] P. Subramanian and R. I. Sujith. Non-normality and internal flame dynamics in premixed flame-acoustic interaction. *Journal of Fluid Mechanics*, 679:315–342, 2011.

[166] P. Subramanian, R. I. Sujith, and P. Wahi. Subcritical bifurcation and bistability in thermoacoustic systems. *Journal of Fluid Mechanics*, 715:210–238, 2013.

[167] T. Sugimoto and Y. Matsui. An experimental study on the dynamic behavior of premixed laminar flames. *Symposium (International) on Combustion*, 19(1):245–250, 1982.

[168] H. J. Sussmann and P. V. Kokotovic. The peaking phenomenon and the global stabilization of nonlinear systems. *Automatic Control, IEEE Transactions on*, 36(4):424–440, 1991.

[169] A. K. Tangirala. *Principles of System Identification: Theory and Practice*. Taylor & Francis, 2014.

[170] L. Tay Wo Chong, S. Bomberg, A. Ulhaq, T. Komarek, and W. Polifke. Comparative Validation Study on Premixed Flame Transfer Function Identification. *Journal of Engineering for Gas Turbines and Power*, 134(2):021502, 2012.

[171] P. Testud, Y. Aurégan, P. Moussou, and A. Hirschberg. The whistling potentiality of an orifice in a confined flow using an energetic criterion. *Journal of Sound and Vibration*, 325(4-5):769–780, 2009.

[172] L. N. Trefethen and David Bau III. *Numerical linear algebra*, volume 50. Siam, 1997.

[173] L. N. Trefethen and M. Embree. *Spectra and Pseudospectra*. Princeton University Press, 2005.

[174] J. M. Varah. On the separation of two matrices. *SIAM Journal on Numerical Analysis*, 16(2):216–222, 1979.

[175] H. Y. Wang, C. K. Law, and T. Lieuwen. Linear response of stretch-affected premixed flames to flow oscillations. *Combustion and Flame*, 156(4):889–895, 2009.

[176] I. Waugh, M. Geuss, and M. Juniper. Triggering, bypass transition and the effect of noise on a linearly stable thermoacoustic system. *Proceedings of the Combustion Institute*, 33(2):2945–2952, 2011.

[177] I. C. Waugh and M. P. Juniper. Triggering in a thermoacoustic system with stochastic noise. *International Journal of Spray and Combustion Dynamics*, 3(3):225–242, 2011.

[178] J. B. Weiss. Coordinate invariance in stochastic dynamical systems. *Tellus Series A*, 55:208, 2003.

[179] K. Wieczorek, C. Sensiau, W. Polifke, and F. Nicoud. Assessing non-normal effects in thermoacoustic systems with mean flow. *Physics of Fluids*, 23(10):107103, 2011.

[180] J. C. Willems. Dissipative dynamical systems part I: General theory. *Archive for rational mechanics and analysis*, 45(5):321–351, 1972.

[181] J. C. Willems. Dissipative dynamical systems. *European Journal of Control*, 13(2):134–151, 2007.

[182] F. A. Williams. *Combustion Theory: the fundamental theory of chemical reacting flow systems*. Addison-Wesley, 1965.

[183] D. You, Y. Huang, and V. Yang. A generalized model of acoustic response of turbulent premixed flame and its application to gas-turbine combustion instability analysis. *Combustion Science and Technology*, 177(5-6):1109–1150, 2005.

[184] S. Zhang and C.-W. Shu. A New Smoothness Indicator for the WENO Schemes and Its Effect on the Convergence to Steady State Solutions. *Journal of Scientific Computing*, 31:273–305, 2007.

[185] B. T. Zinn and T. C. Lieuwen. Combustion instabilities: Basic concepts. *Progress in Astronautics and Aeronautics*, 210:3, 2005.

A Commentary on the G-Equation Flame

The G-equation model describing the laminar premixed flame dynamics is derived in Sec. 3.1 in a laboratory-fixed reference frame. As depicted in Fig. 3.2(b), the flame displacement η extends in the direction of the mean flow x, and is thus only a function of the radial component y and time t, $\eta = \eta(y,t)$ (see also the step in the derivation from Eq. (3.2) to Eq. (3.3)). This stands in contrast to some of the previous studies on the 1-D G-equation flame, which employ a flame-fixed reference (for example, [1, 12, 19, 32, 154, 165]). There, the flame displacement ξ is perpendicular to the mean flame sheet (see Fig. 3.2(b)).

The reason why the present study employs a laboratory-fixed reference is due to the fact that the *nonlinear* flame sheet kinematics cannot be represented correctly in the flame-fixed reference. This is because the flame sheet either misses a portion or overlaps for large positive and negative values of flame displacement at the flame tip, respectively. Both effects are clearly not physical and alter the response in heat release rate fluctuations $\dot{q}_1$, which in turn is determined from the fluctuating flame surface area A_1. The error is more pronounced for wedge flames, where the flame tip lies one flame radius away from the axis of rotation, and thus has a large effect on the overall flame surface area. Preetham *et al.* [138] have equally used the laboratory-fixed reference to study the nonlinear flame response of the G-equation flame.

As mentioned at the end of Sec. 3.1.4, the situation is different for the *linearized* 1-D G-equation flame, where the magnitude of flame displacement is assumed to be small. In this case, it does not matter which reference frame is used, as will be shown in the following.

The linearized G-equation flame is treated in Sec. 3.3.1 under fully premixed conditions. The equations governing the fluctuations in flame displacement

η_1 and in heat release rate $\dot{q}_1$ are given in Eqs. (3.21). Using Eq. (3.4), the heat release rate fluctuations $\dot{q}_1$ are expressed in terms of fluctuations in flame surface area A_1. Equations (3.21) can then be written as

$$\frac{\partial \eta_1}{\partial t} = -S_{L,0} \cos\alpha \frac{\partial \eta_1}{\partial y} + v_1 \,, \tag{A.1a}$$

$$A_1 = 2\pi \cos\alpha \begin{cases} \displaystyle\int_0^{R_F} \eta_1 \,\mathrm{d}y & \text{conical flame} \\ \left\{ R_F \eta_1(R_F) - \displaystyle\int_0^{R_F} \eta_1 \,\mathrm{d}y \right\} & \text{wedge flame} \end{cases} . \tag{A.1b}$$

In a linear framework, the flame displacement variables of the laboratory-fixed and the flame-fixed reference frames, η_1 and ξ_1, respectively, are related by $\xi_1 \approx \eta_1 \sin\alpha$ (see also the inset in Fig. 3.2(b)). Substituting this relation into Eqs. (A.1), the latter become

$$\frac{\partial \xi_1}{\partial t} = -S_{L,0} \cos\alpha \frac{\partial \xi_1}{\partial y} + v_1 \sin\alpha \,, \tag{A.2a}$$

$$A_1 = \frac{2\pi}{\tan\alpha} \begin{cases} \displaystyle\int_0^{R_F} \xi_1 \,\mathrm{d}y & \text{conical flame} \\ \left\{ R_F \xi_1(R_F) - \displaystyle\int_0^{R_F} \xi_1 \,\mathrm{d}y \right\} & \text{wedge flame} \end{cases} . \tag{A.2b}$$

Equation (A.2b) is the same as derived by Schuller *et al.* in Eqs. (21) and (29) in [154] (mind that the radial coordinate is defined as x in [154]).

Further, the radial coordinates of the laboratory-fixed and the flame-fixed references, y and Y, respectively, are related by $Y = y/\sin\alpha$ (see Fig. A.1), which substituted into Eqs. (A.2), and keeping in mind that $S_{L,0} = v_0 \sin\alpha$, yields

$$\frac{\partial \xi_1}{\partial t} = -v_0 \cos\alpha \frac{\partial \xi_1}{\partial Y} + v_1 \sin\alpha \,, \tag{A.3a}$$

$$A_1 = 2\pi \cos\alpha \begin{cases} \displaystyle\int_0^{R_F/\sin\alpha} \xi_1 \,\mathrm{d}Y & \text{conical flame} \\ \left\{ \dfrac{R_F}{\sin\alpha} \xi_1\left(\frac{R_F}{\sin\alpha}\right) - \displaystyle\int_0^{R_F/\sin\alpha} \xi_1 \,\mathrm{d}Y \right\} & \text{wedge flame} \end{cases} . \tag{A.3b}$$

Equations (A.3) correspond to the governing equations found in most studies employing a flame-fixed reference for the 1-D G-equation flame (for example, [1, 19, 154], and with minor differences [12, 165]).

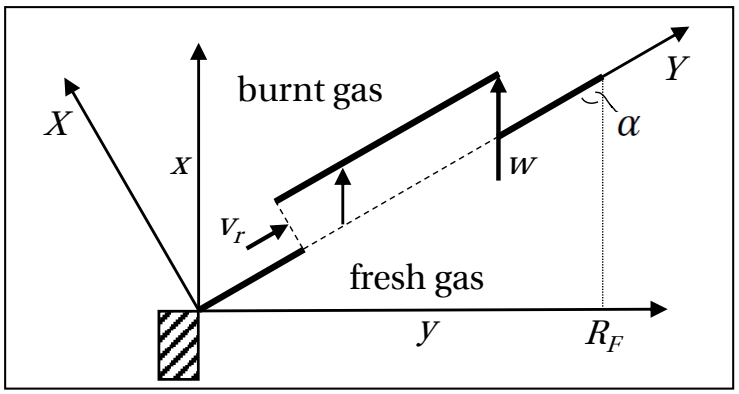

Figure A.1: Sketch of the *G*-equation flame as it should be according to physical arguments.

To conclude the present commentary, we return to the discussion on the two competing response mechanisms of the *G*-equation flame given in Sec. 3.3.1. As explained with the help of Fig. 3.5(b), the first process of convection locally displaces the flame sheet in the direction of mean flow. The corresponding perturbation is advected downstream at the convective velocity w (see also Fig. A.1). In parallel, the other process of flame response restores the unperturbed flame shape starting from the flame base. This causes a second discontinuity in the flame shape, which travels downstream at a rate of v_r.

As stated in Sec. 3.3.1, restoration happens because a "new flame sheet develops from the flame holder as soon as the flame is displaced. The displaced flame sheet downstream is gradually deprived of fresh premixture and extinguishes." In Fig. 3.5(b), the resulting flame displacement is oriented in the direction of mean flow due to the reference frame used. However, following the physical arguments cited above, the process of restoration leads to a flame displacement that is perpendicular to the mean flame sheet, as depicted in Fig. A.1. This kind of flame displacement is not representable in terms of η_1 in the laboratory-fixed reference, but instead would require to be modeled in terms of ξ_1 in the flame-fixed reference (as is done in [12]). On the other hand, the convective displacement, which is clearly oriented in the direction of mean flow, cannot be represented by ξ_1, but only by η_1.

The framework of the 1-D *G*-equation flame thus faces a dilemma, which is visible from Fig. A.1: Each of the reference frames can represent the flame dis-

placement of only one of the two processes of flame response in a physically correct manner. The laboratory-fixed reference can represent the convective process in a physically meaningful manner, but fails to do so for the restorative process. For the flame-fixed reference, it is vice versa. From a mathematical point of view, the dilemma at least does not exist in the linear regime, as we have shown above that in this case both frames of reference yield equivalent results. However, the situation is certainly different in the nonlinear regime.

The above dilemma raises general questions regarding the 1-D *G*-equation flame. Is it simply a modeling framework that happens to decently mirror the experimentally observed linear response characteristics of laminar premixed flames? And how much physical interpretability does the 1-D framework offer in the first place? Are the linear response characteristics of the 2-D *G*-equation flame the same as those obtained in the 1-D case? The present study makes no attempt to resolve these issues. They rather contribute to an even greater sense of sympathetic wonderment on the fact that the 1-D *G*-equation model is nonetheless a powerful low-order modeling tool in the field of thermoacoustics.

B Non-Dimensionalizing the Equations Governing the Simple Acoustic Model

The dimensional set of equations governing the respective conservation of momentum and of energy and mass of the simple acoustic system treated in Sec. 4.2 read

$$\frac{\partial \tilde{v}}{\partial \tilde{t}} = -\tilde{v}_0 \frac{\partial \tilde{v}}{\partial \tilde{\xi}} - \tilde{v} \frac{\partial \tilde{v}_0}{\partial \tilde{\xi}} + \tilde{\zeta}_v \tilde{v} - \frac{1}{\tilde{\rho}_0} \frac{\partial \tilde{p}}{\partial \tilde{\xi}} , \tag{B.1a}$$

$$\frac{\partial \tilde{p}}{\partial \tilde{t}} = -\gamma \tilde{p}_0 \frac{\partial \tilde{v}}{\partial \tilde{\xi}} - \tilde{v}_0 \frac{\partial \tilde{p}}{\partial \tilde{\xi}} - \gamma \tilde{p} \frac{\partial \tilde{v}_0}{\partial \tilde{\xi}} + K_0 \frac{(\gamma - 1)}{\tilde{A}_A} \tilde{q}\, \tilde{d} , \tag{B.1b}$$

where $\tilde{}$ denotes dimensional quantities. With the reference scales given in Eq. (4.6), Eqs. (B.1) can be transformed to express the non-dimensional temporal evolution of acoustic velocity and pressure, respectively. Keeping in mind that the speed of sound $\tilde{c}_0 = \tilde{c}_0(\tilde{\xi})$ is a function of space, and with the definitions of β, M and K as given in Eqs. (4.8), (4.9) and (4.10), respectively, Eqs. (B.1) become

$$\frac{\partial v}{\partial t} = -M \frac{\partial v}{\partial \xi} - \left(2 \frac{M}{\beta} \frac{\partial \beta}{\partial \xi} + \frac{\partial M}{\partial \xi} - \zeta_v \right) v - \frac{\partial p}{\partial \xi} , \tag{B.2a}$$

$$\frac{\partial p}{\partial t} = -\frac{\partial v}{\partial \xi} - \frac{1}{\beta} \frac{\partial \beta}{\partial \xi} v - M \frac{\partial p}{\partial \xi} - \left(\gamma \frac{\partial M}{\partial \xi} + \gamma \frac{M}{\beta} \frac{\partial \beta}{\partial \xi} - \zeta_p \right) p + K \dot{q}\, d . \tag{B.2b}$$

From Eqs. (4.8) and (4.9), we find that $M(\xi) = M_u \beta(\xi)$, which substituted into Eqs. (B.2) yields the non-dimensional governing equations shown in Eqs. (4.7).

C Matrices of Discrete Models

C.1 Subsystem Velocity Model $\mathcal{S}_{F,v}$

The matrices describing the discrete model of the linear velocity model subsystem $\mathcal{S}^{(F,v)}$ treated in Sec. 3.2.1 read

$$\mathbf{A}^{(F,v)} = \left(\mathbf{M}_{\mathrm{FE}}^{(F,v)}\right)^{-1} \mathbf{K}_{\mathrm{FE}}^{(F,v)}, \quad \in \mathbb{R}^{N_{F,v} \times N_{F,v}}, \tag{C.1}$$

$$\mathbf{B}^{(F,v)} = \left(\mathbf{M}_{\mathrm{FE}}^{(F,v)}\right)^{-1} \mathbf{B}_{\mathrm{FE}}^{(F,v)}, \quad \in \mathbb{R}^{N_{F,v}}, \tag{C.2}$$

with finite element mass and stiffness matrices, respectively,

$$\mathbf{M}_{\mathrm{FE}}^{(F,v)} = \frac{\Delta x}{6} \begin{bmatrix} 4 & 1 & & & & & & & \\ 1 & 4 & 1 & & & & & & \\ & 1 & 4 & 1 & & & & & \\ & & \ddots & \ddots & \ddots & & & & \\ & & & & 1 & 4 & 1 & & \\ & & & & & 1 & 4 & 1 & \\ & & & & & & 1 & 2 & \end{bmatrix}, \quad \in \mathbb{R}^{N_{F,v} \times N_{F,v}}, \tag{C.3}$$

$$\mathbf{K}_{\mathrm{FE}}^{(F,v)} = \frac{w}{2} \begin{bmatrix} 0 & -1 & & & & & & & \\ 1 & 0 & -1 & & & & & & \\ & 1 & 0 & -1 & & & & & \\ & & \ddots & \ddots & \ddots & & & & \\ & & & & 1 & 0 & -1 & & \\ & & & & & 1 & 0 & -1 & \\ & & & & & & 1 & -1 & \end{bmatrix}, \quad \in \mathbb{R}^{N_{F,v} \times N_{F,v}}. \tag{C.4}$$

$\mathbf{C}^{(F,v)} \in \mathbb{R}^{N_{F,G} \times N_{F,v}}$ is implemented as a time-varying matrix that linearly interpolates the velocity field at the current position of the flame sheet. It is not given explicitly.

C.2 IR-Based Representation of LTI Systems

The matrices of the discrete model describing the IR-based representation of an LTI system defined in Sec. 3.2.2 are defined in the following. For each input-to-output channel, the discrete matrices read

$$\mathbf{A}^{(\mathrm{IR})} = \left(\mathbf{M}_{\mathrm{FE}}^{(\mathrm{IR})}\right)^{-1} \mathbf{K}_{\mathrm{FE}}^{(\mathrm{IR})}, \quad \in \mathbb{R}^{N_{\mathrm{IR}} \times N_{\mathrm{IR}}}, \tag{C.5}$$

$$\mathbf{B}^{(\mathrm{IR})} = \left(\mathbf{M}_{\mathrm{FE}}^{(\mathrm{IR})}\right)^{-1} \mathbf{B}_{\mathrm{FE}}^{(\mathrm{IR})}, \quad \in \mathbb{R}^{N_{\mathrm{IR}}}, \tag{C.6}$$

$$\mathbf{C}^{(\mathrm{IR})} = \Delta\tau\ \check{h}, \quad \in \mathbb{R}^{N_{\mathrm{IR}}}, \tag{C.7}$$

with discretized impulse response function of the input-to-output channel $\check{h}$ and finite element mass and stiffness matrices, respectively,

$$\mathbf{M}_{\mathrm{FE}}^{(\mathrm{IR})} = \frac{\Delta\tau}{6} \begin{bmatrix} 4 & 1 & & & & & & & \\ 1 & 4 & 1 & & & & & & \\ & 1 & 4 & 1 & & & & & \\ & & & \ddots & \ddots & \ddots & & & \\ & & & & & & & & \\ & & & & & 1 & 4 & 1 & \\ & & & & & & 1 & 4 & 1 \\ & & & & & & & 1 & 2 \end{bmatrix}, \quad \in \mathbb{R}^{N_{\mathrm{IR}} \times N_{\mathrm{IR}}}, \tag{C.8}$$

$$\mathbf{K}_{\mathrm{FE}}^{(\mathrm{IR})} = \frac{a_{\mathrm{IR}}}{2} \begin{bmatrix} 0 & -1 & & & & & & & \\ 1 & 0 & -1 & & & & & & \\ & 1 & 0 & -1 & & & & & \\ & & & \ddots & \ddots & \ddots & & & \\ & & & & & 1 & 0 & -1 & \\ & & & & & & 1 & 0 & -1 \\ & & & & & & & 1 & -1 \end{bmatrix}, \quad \in \mathbb{R}^{N_{\mathrm{IR}} \times N_{\mathrm{IR}}}. \tag{C.9}$$

C.3 Acoustics Subsystem $\mathcal{S}_A$

The matrices of the discrete models describing the acoustics subsystem $\mathcal{S}_A$ treated in Chap. 4 are laid out in the following.

C.3.1 Primitive Variables-Based Representation

The primitive variables-based representation of the acoustics subsystem $\mathcal{S}^{(A)}$ is discussed in the first part of Sec. 4.4.1. The corresponding matrices of the discrete model are defined as

$$\mathbf{A}^{(A)} = \begin{bmatrix} \mathbf{A}_{v \to v}^{(A)} & \mathbf{A}_{p \to v}^{(A)} \\ \mathbf{A}_{v \to p}^{(A)} & \mathbf{A}_{p \to p}^{(A)} \end{bmatrix}, \quad \in \mathbb{R}^{(2N_{A,FD}) \times (2N_{A,FD})}, \tag{C.10}$$

$$\left(\mathbf{B}^{(A)}\right)_m = \begin{cases} \check{K\psi}_{q,m-N_{A,FD}-1} & \text{for } m \in \left[(N_{A,FD}+2); 2N_{A,FD}\right] \\ 0 & \text{otherwise} \end{cases},$$

$$\in \mathbb{R}^{(2N_{A,FD})}, \tag{C.11}$$

$$\left(\mathbf{C}^{(A)}\right)_n = \begin{cases} 1 & \text{for } n = n_F \\ 0 & \text{otherwise} \end{cases}, \quad \in \mathbb{R}^{(2N_{A,FD})}, \tag{C.12}$$

where $n_F \Delta\xi = \xi_F$.

It is visible from the structure of the submatrices appearing in Eq. (C.10) that the boundary elements of the submatrices render the state matrix $\mathbf{A}^{(A)}$ non-

normal (see the first and last rows in the following Eqs. (C.13)–(C.16)). The submatrices read

$$\mathbf{A}^{(A)}_{v\to v} = \frac{\mathbf{P}_{vv}}{2\Delta\xi}\begin{bmatrix} -3 & 4 & -1 & & & & & & \\ 1 & 0 & -1 & & & & & & \\ & 1 & 0 & -1 & & & & & \\ & & & \ddots & \ddots & \ddots & & & \\ & & & & & 1 & 0 & -1 & \\ & & & & & & 1 & 0 & -1 \\ & & & & & & -1 & 4 & -3 \end{bmatrix} + \zeta_v \mathbf{I} - \mathbf{R}_{vv}\,, \\ \in \mathbb{R}^{(N_{A,FD}+1)\times(N_{A,FD}+1)}\,, \tag{C.13}$$

$$\mathbf{A}^{(A)}_{p\to v} = \frac{\mathbf{P}_{vp}}{2\Delta\xi}\begin{bmatrix} -4 & 1 & & & & & \\ 0 & -1 & & & & & \\ 1 & 0 & -1 & & & & \\ & & \ddots & \ddots & \ddots & & \\ & & & & 1 & 0 & -1 \\ & & & & & 1 & 0 \\ & & & & & -1 & 4 \end{bmatrix}, \quad \in \mathbb{R}^{(N_{A,FD}+1)\times(N_{A,FD}-1)}\,, \tag{C.14}$$

$$\mathbf{A}^{(A)}_{v\to p} = \frac{1}{2\Delta\xi}\begin{bmatrix} 1 & 0 & -1 & & & & & & \\ & 1 & 0 & -1 & & & & & \\ & & & \ddots & \ddots & \ddots & & & \\ & & & & & 1 & 0 & -1 & \\ & & & & & & 1 & 0 & -1 \end{bmatrix} - \mathbf{R}_{pv}\,, \\ \in \mathbb{R}^{(N_{A,FD}-1)\times(N_{A,FD}+1)}\,, \tag{C.15}$$

$$\mathbf{A}^{(A)}_{p\to p} = \frac{\mathbf{P}_{pp}}{2\,\Delta\xi}\begin{bmatrix} 0 & -1 & & & & & \\ 1 & 0 & -1 & & & & \\ & \ddots & \ddots & \ddots & & & \\ & & & 1 & 0 & -1 & \\ & & & & 1 & 0 & \end{bmatrix} + \zeta_p\,\mathbf{I} - \mathbf{R}_{pp}\,, \\ \in \mathbb{R}^{(N_{A,FD}-1)\times(N_{A,FD}-1)}\,, \tag{C.16}$$

where **I** stands for identity matrices of suitable sizes. The auxiliary matrices of the FD scheme are defined as

$$(\mathbf{P}_{vv})_{mn} = \begin{cases} (1-M_u) & \text{for } m=n=1 \\ M_u\,\check{\beta}_m & \text{for } m=n\in\left[2;N_{A,FD}\right] \\ (1+M_d) & \text{for } m=n=(N_{A,FD}+1) \\ 0 & \text{otherwise} \end{cases}, \tag{C.17}$$

$$\left(\mathbf{P}_{vp}\right)_{mn} = \begin{cases} (1-M_u) & \text{for } m=n=1 \\ 1 & \text{for } m=n\in\left[2;N_{A,FD}\right] \\ (1+M_d) & \text{for } m=n=(N_{A,FD}+1) \\ 0 & \text{otherwise} \end{cases}, \tag{C.18}$$

$$\left(\mathbf{P}_{pp}\right)_{mn} = \begin{cases} M_u\,\check{\beta}_{m+1} & \text{for } m=n\in\left[1;(N_{A,FD}-1)\right] \\ 0 & \text{otherwise} \end{cases}, \tag{C.19}$$

$$(\mathbf{R}_{vv})_{mn} = \begin{cases} 3\,M_u\,\Delta_\beta\,\check{\psi}_{q,m} & \text{for } m=n\in\left[1;(N_{A,FD}+1)\right] \\ 0 & \text{otherwise} \end{cases}, \tag{C.20}$$

$$\left(\mathbf{R}_{pv}\right)_{mn} = \begin{cases} \Delta_\beta\,\dfrac{\check{\psi}_{q,m+1}}{\check{\beta}_{m+1}} & \text{for } m\in\left[1;(N_{A,FD}-1)\right]\wedge n=m+1 \\ 0 & \text{otherwise} \end{cases}, \tag{C.21}$$

$$\left(\mathbf{R}_{pp}\right)_{mn} = \begin{cases} 2\,\gamma\,M_u\,\Delta_\beta\,\check{\psi}_{q,m+1} & \text{for } m=n\in\left[1;(N_{A,FD}-1)\right] \\ 0 & \text{otherwise} \end{cases}. \tag{C.22}$$

The discrete 1-D distribution function regulating the heat addition to the acoustic field is given as a discrete normal distribution function,

$$\check{\psi}_q = \frac{1}{\sigma\sqrt{2\pi}}\exp\left(-\frac{\left(\check{\xi}-\xi_F\right)^2}{2\sigma^2}\right), \quad \in \mathbb{R}^{(N_{A,FD}+1)}\,, \tag{C.23}$$

with discretized spatial coordinate $\check{\xi} = \left[0, \Delta\xi, \ldots, N_{A,FD}\Delta\xi\right]^T$. The standard deviation σ is chosen such that at least 99.9% of the changes in distribution occur within $\xi_F \pm 0.025$. The discrete non-dimensional temperature distribution is accordingly given as discrete cumulative distribution function,

$$\check{\beta} = 1 + \frac{\Delta_\beta}{2}\left[1 + \mathrm{erf}\left(\frac{\check{\xi} - \xi_F}{\sqrt{2}\sigma}\right)\right], \quad \in \mathbb{R}^{(N_{A,FD}+1)}. \tag{C.24}$$

C.3.2 Method of Weighted Residuals

The method of weighted residuals (MWR) is introduced in Sec. 4.4.2. The corresponding matrices of the discrete model read

$$\mathbf{A}_M^{(A)} = \begin{bmatrix} \mathbf{A}_{M,v_M \to v_M} & \mathbf{A}_{M,p_M \to v_M} \\ \mathbf{A}_{M,v_M \to p_M} & \mathbf{A}_{M,p_M \to p_M} \end{bmatrix}, \quad \in \mathbb{R}^{(2N_{A,M})\times(2N_{A,M})}, \tag{C.25}$$

$$\left(\mathbf{B}_M^{(A)}\right)_m = \begin{cases} 2K\sin\left((m - N_{A,M})\pi\xi_F\right) & \text{for } m \in \left[(N_{A,M}+1); 2N_{A,M}\right] \\ 0 & \text{otherwise} \end{cases},$$
$$\in \mathbb{R}^{(2N_{A,M})}, \tag{C.26}$$

$$\left(\mathbf{C}_M^{(A)}\right)_n = \begin{cases} \cos\left(n\pi\xi_F\right) & \text{for } n \in \left[1; N_{A,M}\right] \\ 0 & \text{otherwise} \end{cases}, \quad \in \mathbb{R}^{(2N_{A,M})}, \tag{C.27}$$

where

$$\left(\mathbf{A}_{M,v_M \to v_M}\right)_{mn} = 2M_u\left(n\pi\mathbf{N}_{mn} - 3\Delta_\beta\mathbf{P}_{mn}\right) + \zeta_v\delta_{mn}, \tag{C.28}$$

$$\left(\mathbf{A}_{M,p_M \to v_M}\right)_{mn} = -m\pi\delta_{mn}, \tag{C.29}$$

$$\left(\mathbf{A}_{M,v_M \to p_M}\right)_{mn} = m\pi\delta_{mn} - \frac{2\Delta_\beta}{1+\Delta_\beta}\mathbf{Q}_{mn}, \tag{C.30}$$

$$\left(\mathbf{A}_{M,p_M \to p_M}\right)_{mn} = -2M_u\left(n\pi\mathbf{N}_{nm} + 2\gamma\Delta_\beta\mathbf{R}_{mn}\right) + \zeta_p\delta_{mn}, \tag{C.31}$$

for $m,n \in [1;N_{A,M}]$ and with Kronecker delta δ_{mn}. The auxiliary operators of the MWR are defined as

$$\mathbf{N}_{mn} = \begin{cases} \frac{\Delta_\beta}{4m\pi}\left\{\cos\left(2m\pi\xi_F\right)-1\right\} & \text{for } n=m \\ \frac{1}{\pi(n-m)(n+m)}\Big\{n\left(1-\cos(n\pi)\cos(m\pi)\right) & \\ \quad +\Delta_\beta\Big[m\sin(n\pi\xi_F)\sin(m\pi\xi_F) & \\ \quad +n\left(\cos(n\pi\xi_F)\cos(m\pi\xi_F)-\cos(n\pi)\cos(m\pi)\right)\Big]\Big\} & \text{for } n\neq m \end{cases} \tag{C.32}$$

and

$$\mathbf{P}_{mn} = \begin{cases} \cos^2\left(m\pi\xi_F\right) & \text{for } n=m \\ \cos\left(n\pi\xi_F\right)\cos\left(m\pi\xi_F\right) & \text{for } n\neq m \end{cases}, \tag{C.33}$$

$$\mathbf{Q}_{mn} = \begin{cases} \frac{1}{2}\sin\left(2m\pi\xi_F\right) & \text{for } n=m \\ \cos\left(n\pi\xi_F\right)\sin\left(m\pi\xi_F\right) & \text{for } n\neq m \end{cases}, \tag{C.34}$$

$$\mathbf{R}_{mn} = \begin{cases} \sin^2\left(m\pi\xi_F\right) & \text{for } n=m \\ \sin\left(n\pi\xi_F\right)\sin\left(m\pi\xi_F\right) & \text{for } n\neq m \end{cases}. \tag{C.35}$$

C.4 Thermoacoustic System $\mathcal{S}_T$

The full thermoacoustic model is computed in dimensional time. Unlike the model describing $\mathcal{S}_F$, that describing $\mathcal{S}_A$ is non-dimensionalized by the reference scales given in Eq. (4.6). In combining both models, the reference scales t_{ref}, v_{ref} and $\dot{q}_{\text{ref}}$ thus appear in the assembled state operators $\mathbf{A}^{(T)}$ and $\mathbf{A}_M^{(T)}$, which are detailed in the following.

C.4.1 Primitive Variables-Based Representation

In a primitive variables-based framework, the matrices of the discrete model describing the autonomous thermoacoustic system $\mathcal{S}^{(T)}$ read

$$\mathbf{A}^{(T)} = \begin{bmatrix} \dfrac{1}{t_{\mathrm{ref}}}\mathbf{A}^{(A)} & \dfrac{1}{t_{\mathrm{ref}}\,\dot{q}_{\mathrm{ref}}}\mathbf{B}^{(A)}\,\mathbf{C}^{(F)} \\ v_{\mathrm{ref}}\mathbf{B}^{(F)}\,\mathbf{C}^{(A)} & \mathbf{A}^{(F)} \end{bmatrix}, \quad \in \mathbb{R}^{(2N_{A,FD}+N_F)\times(2N_{A,FD}+N_F)}, \tag{C.36}$$

$$\mathbf{C}^{(T,A)} = \mathrm{chol}\left(\frac{\Delta\xi}{2}\begin{bmatrix} \mathbf{I} & \mathbf{Q}_{vv} \\ \mathbf{Q}_{pp} & \mathbf{I} \end{bmatrix}\right), \quad \in \mathbb{R}^{(2N_{A,FD})\times(2N_{A,FD})}, \tag{C.37}$$

where $\mathbf{I}$ stands for identity matrices of suitable sizes. In the linear case, $N_F = N_{\mathrm{IR}}$, and in the nonlinear case, $N_F = N_{F,v} + N_{F,G} + 1$. The auxiliary operators of the FD scheme are defined as

$$(\mathbf{Q}_{vv})_{mn} = \begin{cases} M_u\,\check{\beta}_m & \text{for } m \in \left[2; N_{A,FD}\right] \wedge n = m-1 \\ 0 & \text{otherwise} \end{cases}, \tag{C.38}$$

$$\left(\mathbf{Q}_{pp}\right)_{mn} = \begin{cases} M_u\,\check{\beta}_{m+1} & \text{for } m \in \left[1; (N_{A,FD}-1)\right] \wedge n = m+1 \\ 0 & \text{otherwise} \end{cases}. \tag{C.39}$$

C.4.2 Method of Weighted Residuals

Using the method of weighted residuals, the matrices of the discrete model describing the autonomous thermoacoustic system $\mathcal{S}^{(T)}$ read

$$\mathbf{A}_M^{(T)} = \begin{bmatrix} \dfrac{1}{t_{\mathrm{ref}}}\mathbf{A}_M^{(A)} & \dfrac{1}{t_{\mathrm{ref}}\,\dot{q}_{\mathrm{ref}}}\mathbf{B}_M^{(A)}\,\mathbf{C}^{(F)} \\ v_{\mathrm{ref}}\mathbf{B}^{(F)}\,\mathbf{C}_M^{(A)} & \mathbf{A}^{(F)} \end{bmatrix}, \quad \in \mathbb{R}^{(2N_{A,M}+N_F)\times(2N_{A,M}+N_F)}, \tag{C.40}$$

$$\mathbf{C}_M^{(T,A)} = \mathrm{chol}\left(\frac{1}{4}\begin{bmatrix} \mathbf{I} & 2M_u\mathbf{N} \\ 2M_u\mathbf{N}^T & \mathbf{I} \end{bmatrix}\right), \quad \in \mathbb{R}^{(2N_{A,M})\times(2N_{A,M})}, \tag{C.41}$$

with identity matrix $\mathbf{I} \in \mathbb{R}^{N_{A,M}\times N_{A,M}}$ and $\mathbf{N}$ as defined in Eq. (C.32).